Surficial Seismology:
Landslides, Glaciers, and Volcanoes in the Pacific Northwest
through a Seismic Lens

Kate Allstadt

A dissertation

submitted in partial fulfillment of the

requirements for the degree of

Doctor of Philosophy

University of Washington

2013

Reading Committee:

John Vidale, Chair

Juliet Crider

Stephen Malone

Ken Creager

Program Authorized to Offer Degree:

Earth and Space Sciences

University of Washington

Abstract

Surficial Seismology: Landslides, Glaciers, and Volcanoes in the Pacific Northwest through a Seismic Lens

Kate Allstadt

Chair of the Supervisory Committee:

Professor John Vidale

Department of Earth and Space Sciences

The following work is focused on the use of both traditional and novel seismological tools, combined with concepts from other disciplines, to investigate shallow seismic sources and hazards. The study area is the dynamic landscape of the Pacific Northwest and its wide-ranging earthquake, landslide, glacier, and volcano-related hazards.

The first chapter focuses on landsliding triggered by earthquakes, with a shallow crustal earthquake in Seattle as a case study. The study demonstrates that utilizing broadband synthetic seismograms and rigorously incorporating 3D basin amplification, 1D site effects, and fault directivity, allows for a more complete assessment of regional seismically induced landslide hazard. The study shows that the hazard is severe for Seattle, and provides a framework for future probabilistic maps and near real-time hazard assessment.

The second chapter focuses on landslides that generate seismic waves and how these signals can be harnessed to better understand landslide dynamics. This is demonstrated using two contrasting Pacific Northwest landslides. The 2010 Mount Meager, BC, landslide generated strong long period waves. New full waveform inversion methods reveal the time history of forces the landslide exerted on the earth that is used to quantify event dynamics. Despite having a similar volume (~10^7 m^3), The 2009 Nile Valley, WA, landslide did not generate observable long period motions because of its smaller accelerations, but pulses of higher frequency waves were valuable in piecing together the complex sequence of events.

The final chapter details the difficulties of monitoring glacier-clad volcanoes. The focus is on small, repeating, low-frequency earthquakes at Mount Rainier that resemble volcanic earthquakes. However, based on this investigation, they are actually glacial in origin: most likely stick-slip sliding of glaciers triggered by snow loading. Identification of the source offers a view of basal glacier processes, discriminates against alarming volcanic noises, and has implications for repeating earthquakes in tectonic environments.

This body of work demonstrates that by combining methods and concepts from seismology and other disciplines in new ways, we can obtain a better understanding and a fresh perspective of the physics behind the shallow seismic sources and hazards that threaten the Pacific Northwest.

Table of Contents

Chapter 1: Landslides triggered by earthquakes:

A scenario study of seismically induced landsliding in Seattle using broadband synthetic seismograms

Summary 1-3
1. Introduction 1-4
2. Background 1-8
3. Methods 1-12
4. Synthetic Seismogram Generation 1-14
5. Incorporating Site Amplification 1-19
6. Model Outputs 1-23
7. Validation of Ground Motions 1-25
8. Validation of Landslide Simulation 1-29
9. Results of Landslide Simulation for Mw 7.0 Seattle Fault Earthquake 1-31
10. Infrastructure Impacts 1-36
11. Discussion 1-38
12. Conclusions 1-44
13. Data and Resources 1-46
14. Acknowledgements 1-47
15. References 1-48

Chapter 2: Seismogenic landslides, a new way to study landslide dynamics:

Part a: Extracting source characteristics and dynamics of the August 2010 Mount Meager landslide from broadband seismograms

Summary 2a-4
1. Introduction 2a-5
2. Data 2a-10
2.1 Seismic data 2a-12
3. Methods 2a-17
3.1 Validation 2a-21

4. Results 2a-23
4.1 Rockslide initiation 2a-26
4.2 Debris flow 2a-30
4.3 "Aftershock" 2a-35
5. Discussion 2a-38
5.1 Improvements to landslide characterization 2a-38
5.2 Limitations 2a-44
6. Conclusions 2a-45
7. Acknowledgements 2a-47
8. References 2a-48

Part b: The seismic story of the Nile Valley landslide

Summary 2b-3
1. Introduction 2b-4
2. Background 2b-5
3. Seismic Data 2b-10
4. Discussion 2b-13
5. Conclusion 2b-15
6. Acknowledgements 2b-16
7. References 2b-16

Chapter 3: Glacier-quakes mimicking volcanic earthquakes:

Swarms of repeating stick-slip glacial earthquakes triggered by snow loading at Mount Rainier

Summary 3-3
1. Introduction 3-4
2. Background 3-8
3. Detection and Characterization 3-12
3.1 Comprehensive Repeating Earthquake Search 3-12
3.1.1 Methods 3-12
3.1.2 Results 3-15
3.2 Correlation with Weather 3-19
3.3 Locations 3-22
3.4 Recurrence Time vs. Event Size 3-28
3.5 Source migration over time - coda wave interferometry 3-31
3.5.1 Methods 3-31
3.5.2 Results 3-36

4. Discussion 3-38
4.1 What is the source mechanism? 3-38
4.2 Why is this behavior transient and triggered by precipitation? 3-43
4.3 Broader Implications 3-52
5. Conclusions 3-55
6. Acknowledgements 3-57
7. References 3-57

Appendices

Appendix 1 Representative Shear Wave Velocity Surficial Profiles for Seattle and Map of Units (Chapter 1)

Appendix 2 High resolution maps (2) of relative seismically induced landslide hazard for a M_w 7.0 Seattle fault earthquake for dry and saturated soil conditions (Chapter 1)

Appendix 3 Details of Inversion Methods (Chapter 2a)

Chapter 1 - Landslides triggered by earthquakes:

A Scenario Study of Seismically Induced Landsliding in Seattle using Broadband Synthetic Seismograms

The content of this chapter was published in:

Allstadt, K., Vidale, J.E., and Frankel, A.D., 2013. A Scenario Study of Seismically Induced Landsliding in Seattle Using Broadband Synthetic Seismograms, Bull. Seism. Soc. Am., 103, No. 6, doi: 10.1785/0120130051

with some added details from:

Allstadt, K., and Vidale, J. E., 2012. Seismically Induced Landsliding in Seattle: A Magnitude 7 Seattle Fault Earthquake Scenario, USGS NEHRP Final Tech Report, Grant #: G11AP20012, 39p.

Table of Contents

Summary 1-3
1. Introduction 1-4
2. Background 1-8
3. Methods 1-12
4. Synthetic Seismogram Generation 1-14
5. Incorporating Site Amplification 1-19
6. Model Outputs 1-23
7. Validation of Ground Motions 1-25
8. Validation of Landslide Simulation 1-29
9. Results of Landslide Simulation for Mw 7.0 Seattle Fault Earthquake 1-31
10. Infrastructure Impacts 1-36
11. Discussion 1-38
12. Conclusions 1-44
13. Data and Resources 1-46
14. Acknowledgements 1-47
15. References 1-48

Summary

We demonstrate the value of utilizing broadband synthetic seismograms to assess regional seismically induced landslide hazard. Focusing on a case study of an M_w 7.0 Seattle fault earthquake in Seattle, WA, we computed broadband synthetic seismograms that account for rupture directivity and 3D basin amplification. We then adjusted the computed motions on a fine grid for 1D amplifications based on the site response of typical geologic profiles in Seattle and used these time series ground motions to trigger shallow landsliding using the Newmark method. The inclusion of these effects was critical in determining the extent of landsliding triggered. We found that for inertially triggered slope failures modeled by the Newmark method, the ground motions used to simulate landsliding must have broadband frequency content in order to capture the full slope displacement. We applied commonly used simpler methods based on ground motion prediction equations for the same scenario and found that they predicted far fewer landslides if only the mean values were used, but far more at the maximum range of the uncertainties, highlighting the danger of using just the mean values for such methods. Our results indicate that landsliding triggered by a large Seattle fault earthquake will be extensive and potentially devastating, causing direct losses and impeding recovery. The high impact of landsliding predicted by this simulation shows that this secondary effect of earthquakes should be studied with as much vigor as other earthquake effects.

1. Introduction

Landslides triggered by earthquakes have caused significant damage and casualties worldwide. For example, seismically triggered landslides were responsible for more than half of the damage caused by the 1964 Good Friday Earthquake in Alaska (Keefer, 1984) and the 2008 Wenchuan earthquake in China triggered about 60,000 landslides that destroyed entire towns and caused tens of thousands of deaths, about a third of the total (Yin *et al.,* 2009; Huang and Fan, 2013). Other recent examples include the 1999 Chi-chi earthquake (Hung, 2000) and the 1994 Northridge earthquake (Harp and Jibson, 1996). Despite these examples, and calls for more focused attention to this secondary earthquake hazard (*e.g.* Huang and Fan, 2000; Wasowski *et al.,* 2000), seismically induced landslide hazard has not been quantitatively investigated or fully incorporated into seismic hazard assessments for many areas that are particularly at risk.

This is not for a lack of methods. Researchers have been developing and implementing methods to assess seismically induced landslide hazard for years. Some of these methods use soil and slope characteristics of landslides triggered by past earthquakes either qualitatively (*e.g.* Stewart, 2005; Keefer, 1984), or through logistic regressions and neural network analysis (*e.g.* Lee and Evangelista, 2006; Keefer, 2000). A limitation is that complete post-earthquake landslide distributions needed for many of these methods are rare (Keefer, 2002), and the applicability of these methods from one area to a different setting that does not have a similar dataset is an issue. More sophisticated methods of estimating coseismic landslide triggering have also been developed, such as those using dynamic finite-element modeling to simulate the permanent slope deformations induced by the input ground motion throughout the potential failure mass (*e.g.* Seed *et al.,* 1973; Lee, 1974; Prevost, 1981). However, these types of methods are both computationally intensive and require dense, high-quality, site-specific soil data in order

for the modeling efforts to be worthwhile (Jibson, 2011; Kramer, 1996). As a result, they are not feasible in most cases, and certainly not for regional hazard mapping studies. As a compromise between the empirical, statistical approaches and detailed numerical models of slope performance, the Newmark method (Newmark, 1965) has emerged as a dominant approach to seismically induced landslide hazard mapping and analysis (*e.g.* Wilson and Keefer, 1983; Jibson *et al.*, 2000; Miles and Ho, 1999, Ambraseys and Menu, 1988, Jibson and Michael, 2009; Saygili and Rathje, 2009). Variations abound, but the core of the method is that slope displacements accumulate each time the ground acceleration exceeds a critical threshold value. This threshold value depends on the slope geometry, material properties, and groundwater conditions. The Newmark method is simple enough that it is well suited to regional seismically induced hazard mapping studies (Jibson *et al.*, 2000).

A major limitation to all of these methods of assessing seismically induced landsliding hazard is that they require ground motion information for future earthquakes. Previous studies have gotten around this by using recordings of past earthquakes if they exist (e.g. Peng *et al.*, 2009; Jibson *et al.,* 1998) or by using ground motion prediction equations to obtain a simplified ground motion parameter for a specific scenario earthquake such as peak ground acceleration (PGA) (*e.g.* Ambraseys and Menu, 1988; Lee and Evangelista, 2006) or Arias intensity (*e.g.* Jibson et al., 1998). This is then coupled with regression equations to estimate the performance of slopes with various characteristics (*e.g.* Jibson, 2007; Rathje and Saygili, 2009). Others take the peak ground acceleration for a specified return period straight from probabilistic seismic hazard maps (*e.g.* Jibson and Michael, 2009; Blake *et al.,* 2002; Saygili and Rathje, 2009). More rigorous solutions include rescaling recordings of earthquakes in other locations, or in the case of Miles and Ho (1999), producing simple stochastic synthetic seismograms for a specific event.

Though some of these methods have ways of approximating site amplifications, they are often generalized – based on recordings of earthquakes all over the world in different settings, not tailored to the peculiarities of a particular location. This means variability, and thus uncertainty, is high, and they are missing the characteristics in the time series such as coherent pulses from the finite fault rupture or increased duration due to basin amplification which can be important to landslide triggering. Furthermore, for studies that use a single ground motion parameter like PGA instead of a time series recording, one more step of approximation with its own uncertainties is required to tie PGA to the slope displacement.

Fortunately, seismological methods and computing power have advanced to the point where it is possible to generate realistic broadband synthetic seismograms for scenario earthquakes. These methods are capable of accounting for finite fault rupture, basin amplification, coherent pulses, and directivity effects specific to a particular event and locale that are poorly approximated by other methods. In this study, we used such methods to generate broadband synthetic seismograms on a fine grid (210-meter) for a scenario earthquake striking the city of Seattle and rigorously adjusted these ground motions for site amplification due to soil layering on an even finer grid (5-meter) using methods from geotechnical earthquake engineering and engineering geology. Then, we used these ground motions and pre-existing static slope stability data throughout the city to simulate seismically induced landsliding based on the Newmark method. We show that using the full time-series recordings that account for the details of ground motion variability such as rupture directivity, basin amplification, and site response makes a substantial difference in determining the extent of landsliding triggered relative to simpler methods.

We focus our efforts on simulating shallow landsliding triggered by a large crustal earthquake within the city limits of Seattle, Washington, in order to develop and test the methodology. The reason we focus on Seattle is that it is a prime example of a city at risk of seismically induced landsliding that has not been thoroughly investigated. The city is highly susceptible to landsliding in general (Harp et al., 2006), and is also located in an area of elevated seismic hazard that has been well quantified (Frankel et al., 2007). We simulate a magnitude 7.0 event on the Seattle fault, a crustal reverse fault that lies directly below the city (Blakely et al., 2002). We focus on this fault because it is a primary contributor to the seismic hazard. Around 900 A.D., an earthquake on this fault sent entire forested hillsides sliding into Lake Washington (Jacoby et al., 1992) and triggered lake-wide turbidity currents (Karlin and Abella, 1992, Karlin et al., 2004), indicating that landsliding was widespread from both this most recent Seattle fault earthquake and previous earthquakes. If such landsliding were to occur today, the consequences could be dire: the steep hillsides along Lake Washington and Puget Sound are now densely populated. In order to be prepared and to build a more resilient city, such hazards must be quantified.

We use the methods described above and detailed in the methods section to demonstrate how they can be used to quantify the hazard posed by landsliding triggered by a scenario shallow crustal earthquake close to the city. We map relative hazard but also take the scenario approach further and assign actual slope failures, estimate areas in potential runout zones, and look at potential intersections with infrastructure. We address the critical questions of where landslides are most likely to occur, how many might be triggered, what effect soil saturation levels will have on the number of landslides triggered, and how many buildings and critical infrastructure are at risk. This scenario approach yields a tangible picture of the extent of landsliding and the

areas and infrastructure that could be at risk, but represents just one of the countless scenarios that are possible. However, now that the framework is established for this scenario-based approach, it can be used to run a suite of likely scenarios that could even eventually be compiled to develop a probabilistic seismically induced landslide hazard map similarly to how urban probabilistic seismic hazard maps are generated (*e.g.* Frankel et al., 2007).

In the following sections, we discuss the background of seismically induced landsliding in Seattle, then present and validate the methods we used to simulate shallow landsliding triggered by a Seattle fault earthquake for the city of Seattle. This is followed by the results of our seismically induced landslide simulation, a discussion of the patterns and extent of landsliding triggered, potential impacts on infrastructure, the importance and sensitivity of various components of our methodology, and a comparison to simpler methods. Finally we conclude and discuss how broadband synthetic seismograms and these scenario-based methods could be refined for application to more scenarios to improve awareness of and preparedness for seismically induced landsliding in Seattle and other cities.

2. Background

Seattle's location near the convergence of the Juan de Fuca and North American plate (Figure 1-1, inset) leaves the city and surrounding region prone to three major earthquake sources: deep earthquakes within the subducted Juan de Fuca plate, offshore megathrust earthquakes on the Cascadia subduction zone, and shallow crustal earthquakes within the North American Plate (Frankel *et al.*, 2007). Locally, the latter type could be the most disastrous of the three if a large shallow crustal earthquake occurred close to the city. The closest crustal fault that threatens Seattle is the Seattle fault, which has not had a large earthquake since western settlement. The zone of south-dipping reverse faults extends east-west across the Puget Lowland

just south of downtown Seattle (Figure 1-1), forming the southern boundary of the Seattle basin (Blakely *et al.*, 2002). Paleoseismic studies have revealed that the last major earthquake on this fault was around 900 A.D. (Bucknam *et al.*, 1992) with an estimated magnitude of 7.5 (ten Brink *et al.*, 2006). This event triggered some of the landslides preserved in Lake Washington and rock avalanches in the Olympic Mountains (Jacoby *et al.*, 1992, Karlin and Abella, 1992, Karlin *et al.*, 2004, Schuster *et al.*, 1992). If the 900 A.D. event is characteristic, the next event could be thousands of years away (Johnson *et al.*, 1999, Pratt *et al.*, 1997), but trenching of a backthrust of the Seattle Fault shows earthquake recurrence intervals in the fault zone range from 200 to 12,000 years (Nelson *et al.*, 2003), and glacial loading and unloading could have disturbed the cycle (Thorson, 1996).

Seattle itself is particularly prone to strong shaking because it was built directly over the Seattle Basin - a deep sedimentary basin that amplifies ground motion, generates strong basin surface waves, and tends to increase the duration of shaking (Frankel *et al.*, 2002). On top of this deeper structure is a veneer of unconsolidated soils: layers of clay, sands, and till primarily deposited by retreating ice sheets at the end of the Pleistocene (Troost *et al.*, 2005). These deposits compose steep slopes of unconsolidated material found throughout the city that have been further destabilized by human activity, stream erosion, and wave erosion along coastal bluffs (Tubbs, 1974). This steep unconsolidated surficial geology coupled with a wet climate make landsliding a frequent issue in Seattle, most commonly triggered by some combination of human activity and heavy precipitation. Landslides triggered by water have been the topic of many investigations specific to Seattle (*e.g.*, Tubbs, 1974, Harp *et al.*, 2006, Baum *et al.*, 2005, Montgomery *et al.*, 2001, Coe *et al.*, 2004, Laprade *et al.*, 2000, Salciarini *et al.*, 2008).

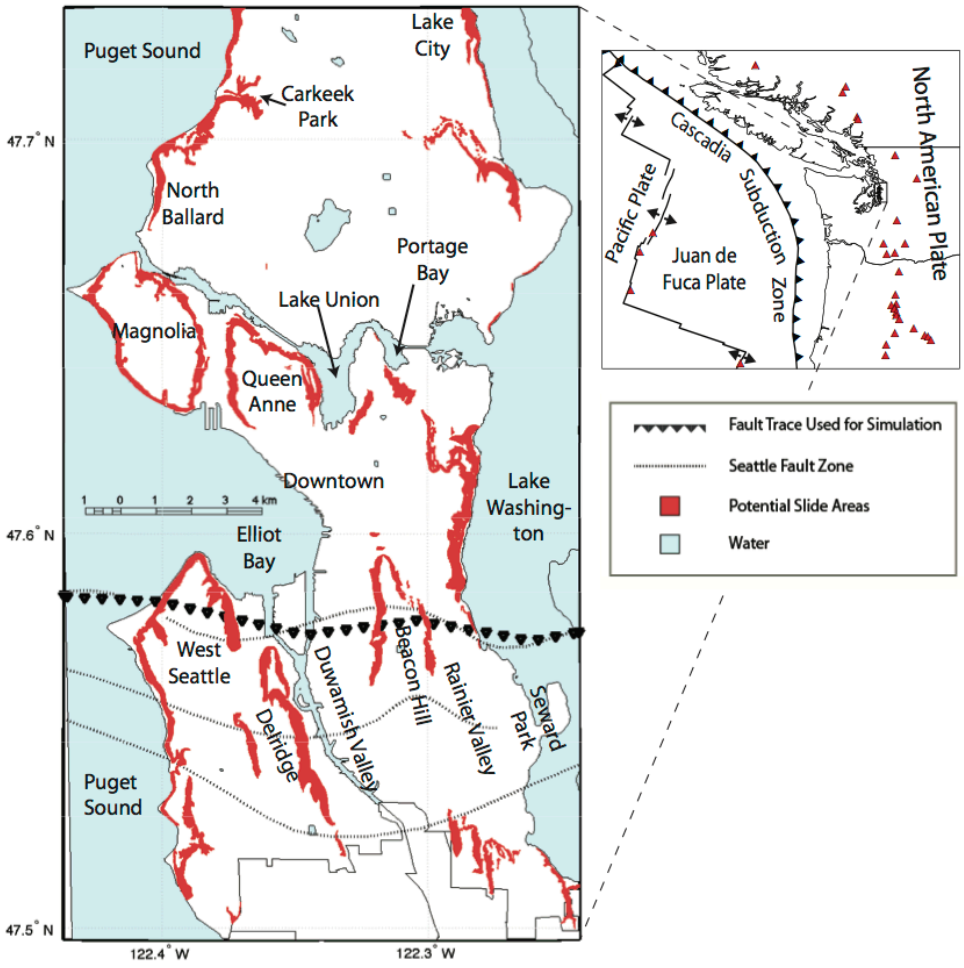

Figure 1-1 Map of Seattle showing location of Seattle Fault Zone (dotted line), frontal fault location used for rupture model for landslide simulation (line of triangles), and potential landsliding areas designated by the City of Seattle. Neighborhoods and landmarks mentioned in the text are labeled. Inset map shows regional tectonic setting and volcanoes (triangles).

Earthquake-triggered landslides, on the other hand, occur only episodically and receive far less attention because of the long intervals between significant earthquakes in western Washington. At least 15 earthquakes have triggered landsliding in the region since the mid-1800's (Chleborad and Schuster, 1998; Noson *et al.*, 1988; Keefer, 1983; Hopper, 1981), but nearly all of the historical examples were moderate earthquakes, and the historical record is short in this part of the country. All three major historical Puget Sound earthquakes (M_w 7.1 in 1949,

M_w 6.5 in 1965 and M_w 6.8 in 2001) caused ground failures throughout Western Washington and Northern Oregon (Chleborad and Schuster, 1998, Highland, 2003), but not extensively because all three were deep Benioff zone earthquakes with relatively moderate ground motions and lower than normal or average antecedent rainfall (Stewart, 2005).

Since its founding, the city has yet to experience its most dangerous earthquakes: large crustal earthquakes on nearby faults, and subduction megathrust earthquakes. It is only when we look further back that we find that seismically induced landsliding has shown the potential to cause as much or more damage than other earthquake effects. Oral traditions of the native Salish tribes report specific locations where earthquake-triggered landsliding or other earthquake effects occurred (Ludwin et al., 2005). Furthermore, as mentioned earlier, there is significant geologic evidence of seismically triggered landslides including sunken forests on giant block landslides, submarine landslides, and lake-wide turbidite layers preserved in Lake Washington (Jacoby *et al.*, 1992, Karlin and Abella, 1992, Karlin *et al.*, 2004). These deposits have been tied to landsliding triggered by as many as seven earthquakes in the last 3,500 years (Karlin *et al.*, 2004).

Despite this, there are few rigorous studies of seismically induced landsliding in Seattle. Of those that exist, most characterize past seismically induced ground failures triggered by historical earthquakes in the area and identify the types of soils that failed (*e.g.*, Chleborad and Schuster, 1998, Noson *et al.*, 1988, Keefer, 1983, Hopper, 1981, Stewart, 2005, Highland, 2003). McCalpin (1997) took a more quantitative approach and used ground motion prediction equations to calculate slope stability for some probabilistic and scenario earthquakes, but did not include the level of detail that we have found to be necessary to accurately assess seismically induced landslide hazard in Seattle.

3. Methods

In this study we focus on shallow disrupted landslides, which are generally the most abundant types of landslides triggered by earthquakes (Keefer, 1984) and are also the most common type of landslide in Seattle (Baum *et al.*, 2005). The failure surface of this type of slide is within a few meters of the ground surface. Deep-seated landsliding and liquefaction-related ground failure are also significant hazards that need to be addressed but are beyond the scope of this study.

We model co-seismic landslide movement using Newmark's method (Newmark, 1965), which approximates a slope as a rigid block sliding against friction down an inclined plane that is subjected to ground motion; the block accumulates downslope displacement each time a threshold acceleration is exceeded. The final displacement is termed the Newmark displacement. Though the model is simplistic, with some modifications it is currently the most widely used tool for looking at regional susceptibility of natural slopes to landsliding triggered by earthquakes (*e.g.*, Miles and Ho, 1999, Ambraseys and Menu, 1988, Jibson *et al.*, 1998, Peng et al., 2009, Jibson and Michael, 2009). For natural slopes, the Newmark displacement is not the actual displacement that will occur, but is instead considered an index for the likelihood of slope failure (Jibson *et al.*, 2000). We take a similar approach.

Some have improved on the Newmark method to make it more realistic by allowing internal deformation within the failure mass (*e.g*. Makdisi and Seed, 1978; Bray and Rathje, 1998; Rathje and Bray, 2000). However, we did not use these modifications because they are too computationally intensive to be applied on a citywide scale.

We discretized the city limits of Seattle into 5-meter cells. To apply the Newmark method, each cell was approximated as a rigid block sitting on a ramp with an incline equal to

the average slope within that cell. The block is initially stable and has a threshold ground acceleration in the downslope direction above which the block starts to slide down the ramp. This value is known as the critical acceleration (a_c), sometimes referred to as the yield acceleration, and is dependent on the slope, the soil properties, and the saturated thickness of the failure mass. As the shaking progresses, whenever the critical acceleration is exceeded, the block accumulates displacement down the ramp. The final Newmark displacement is calculated by integrating time intervals of the seismogram that exceed the threshold acceleration to determine the velocity time-history of the block when mobilized and then by integrating this result to determine the displacement history. In this study, after integrating once to velocity we assumed a symmetrical pulse shape in order to bring the velocity back to zero after each exceedance (as in Goodman and Seed, 1966) and then integrated once more to obtain displacement. In order to speed up calculations, we only calculated Newmark displacement for slopes equal to or greater than 15°, the minimum slope for which shallow disrupted landslides typically occur (Keefer, 1984). We did not calculate Newmark displacement for slopes greater than 64° because only manmade structures are that steep at the resolution of our slope map (5m).

The factor of safety (FS) and slope angle (θ) of each cell was used to calculate the critical acceleration (a_c), which is the acceleration in the downslope direction required to reduce the factor of safety to 1. This can be calculated by the relation $a_c = (FS\text{-}1)g\sin\theta$ where g is the acceleration due to gravity (Newmark, 1965). High-resolution (1.8 m) slope information was available from the Puget Sound LIDAR Consortium. The factor of safety is the ratio of resisting forces to driving forces; thus, a factor of safety of less than 1 means a slope is unstable. Fortunately, Harp *et al.* (2006) conducted a detailed study of slope stability under static conditions in Seattle and calculated the factor of safety for dry and completely saturated soil

conditions on a 2-m grid for the entire city using typical engineering properties for each geologic unit. They assumed a uniform failure thickness of 2.4 m to simulate shallow landslides of the same type we are investigating in this project so we were able to use their results. The factor of safety reported by Harp et al., (2006) was less than 1 for some cells because it was calculated on a large scale using a simple model. For this study, we assumed that all slopes were at least marginally stable prior to the simulated earthquake and raised all cells with a factor of safety below 1 to 1.01.

4. Synthetic Seismogram Generation

To accurately assess landslide hazard in Seattle, it is necessary to use synthetic seismograms that account for rupture directivity and the effects of the Seattle basin. The final input required for the simulation is a set of broadband synthetic seismograms generated on a fine grid throughout the city. We chose to simulate an M_w 7.0 earthquake as a compromise between the estimated maximum magnitude the fault is capable of generating (M_w 7.6 to 7.7, Pratt *et al.*, 1997) and the size of the earthquake that could be generated by the estimated slip accumulated since the last earthquake on the main fault, 75-120 cm (Johnson *et al.*, 1999), which would produce an M_w 6.6 to 6.7 earthquake if completely released (Wells and Coppersmith, 1994).

We used the surface projection of the frontal fault (Figure 1-2A) from Blakely et al. (2002) as the rupture plane. We ruptured a 45-km segment from the middle of the fault from 3-15 km depth. We assumed a rupture dip of 45°, resulting in a rupture width of about 17 km. The rupture plane was divided into 3,150 subevents that were spaced 500 m apart and had a mean M_w of 4.6 (Figure 1-2b). We used methods developed by Frankel *et al.* (2007) to model the slip distribution and the moment distribution among the subevents as a spatial random field with a correlation length for asperities that corresponds to the magnitude of the earthquake (Mai and

Beroza, 2002). To simulate a finite fault rupture, the point source subevents were set to break first at the lower eastern edge of the fault. Then the rupture propagated updip and westward at rupture velocity that was set to 70% of the shear wave velocity so that it slows as the rupture approaches the surface. The rupture velocity is randomized by 25% and constrained to never exceed the shear wave velocity in order to avoid unrealistically large directivity pulses (Figure 1-2c). In addition, the rake of each subevent was varied randomly by ±20°. We deviate from the methods of Frankel *et al.,* (2007) slightly in the calculation of the rise time (T_D) by making it dependent on the shear wave velocity (β) at the point of rupture by $T_D = 16Lf^{0.5}/(7\beta\pi^{1.5})$ (Stein and Wysession, 2003) in which L is the length of the fault, β is the shear wave velocity, and f is the ratio of width to length. By doing so, the source-time function at shallower depths was slightly longer than at greater depths, which caused shallower subevents to radiate lower frequency energy than deeper ones. This step helped maintain realistic ground acceleration levels.

We then used this fault rupture model to generate broadband seismograms by calculating long-period motion (<1 Hz) deterministically, high-frequency motion (>1 Hz) stochastically on a 210-meter grid throughout the city, and combined them using methods developed by Frankel (2009). To compute the deterministic low-frequency ground motions, we used the fault rupture model as input to a finite-difference code developed by Liu and Archuleta (2002) that propagates seismic waves through a 3D velocity model of the Seattle basin developed by Delorey and Vidale (2011). This simulates amplification and surface wave generation in the Seattle basin. To isolate the influence of the Seattle basin on ground motions and consequently on the extent of landsliding triggered, we also generated synthetic seismograms for a 1D velocity model

formulated from the out-of-basin velocities in Delorey and Vidale's (2011) 3D model. Both velocity models had a shear-wave velocity of 600 m/s at the surface.

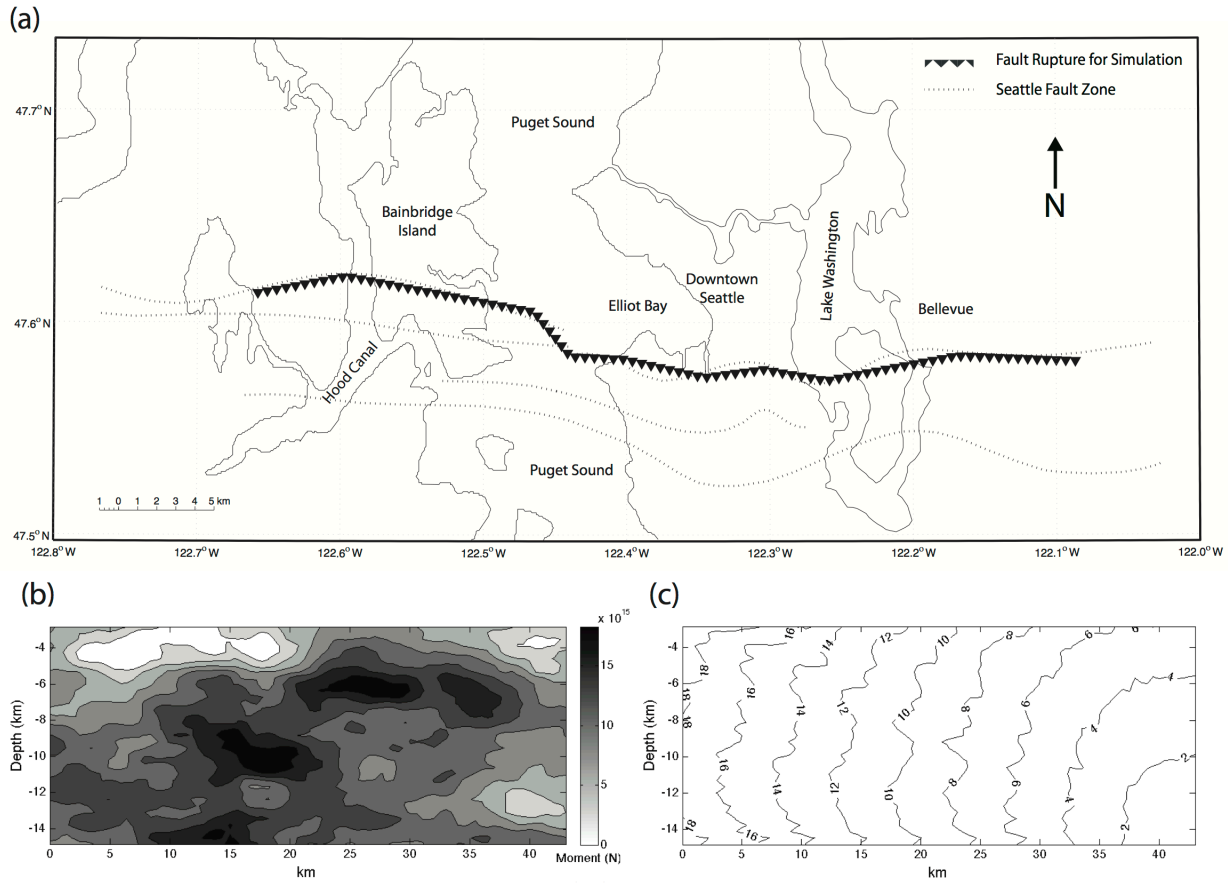

Figure 1-2(a) The surface projection of fault rupture used to generate synthetic seismograms (triangles) corresponds to the frontal fault of the Seattle Fault Zone as defined by Blakely *et al.* (2002). This is just one of the set of faults that make up the entire Seattle Fault Zone (gray dotted lines). (b) Contoured moment distribution of subevents on the fault rupture plane (0 km is westernmost end of ruptured segment) (c) Rupture time in seconds from the start of the earthquake.

Higher frequency portions of the seismogram were computed stochastically using the constant stress-drop model proposed by Frankel (2009), derived from Boore (1983, 1996). Subevents were assigned stress drops using a fractal distribution with a root-mean-square value of 10 MPa. The assigned stress drops were used to calculate a theoretical spectrum for each subevent, which was then multiplied by Gaussian white noise in the frequency domain so that

each subevent had a realistic seismogram when transformed into the time domain and tapered. These subevent waveforms were then adjusted for attenuation, geometrical spreading, and travel times between each source and each station, and summed up at each station. The high- and low-frequency components of the synthetics were combined with a crossover at 1 Hz using a matched filter to form broadband seismograms.

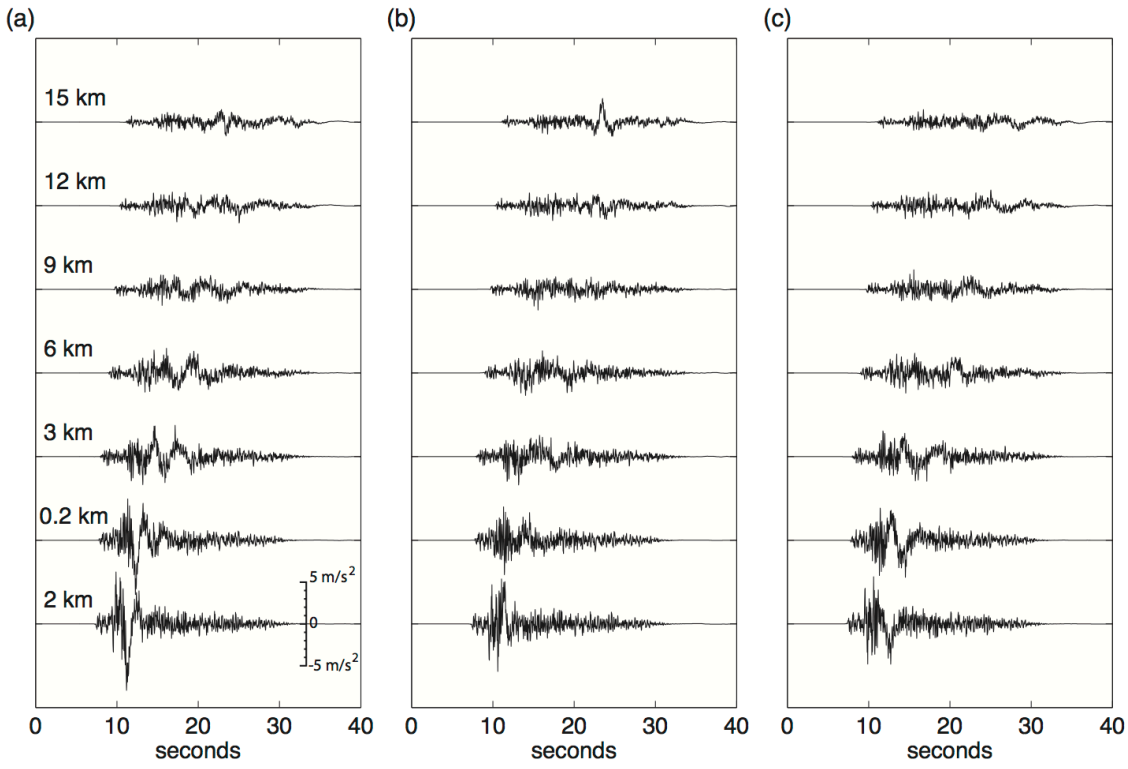

Figure 1-3 Examples of (a) North, (b) East, and (c) vertical component synthetic accelerograms, starting from south of the surface trace of the fault at bottom, moving northward toward the top of the plot. Distance to the closest point on the frontal fault trace is shown to the left of each seismogram. Locations of each synthetic seismometer used are shown as black dots on Figure 4.

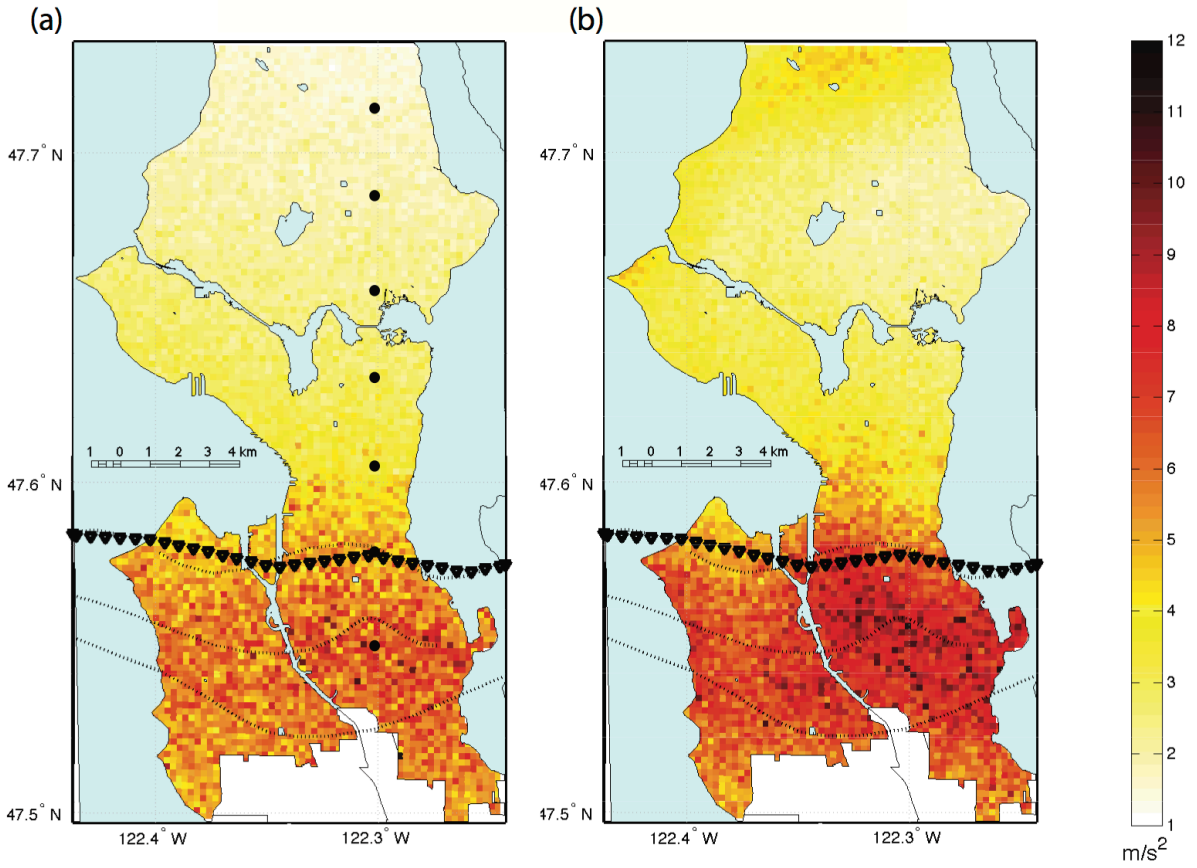

Figure 1-4 Maximum horizontal peak ground accelerations on a 210-m grid of broadband synthetic seismograms of the simulated Mw 7.0 Seattle fault earthquake generated using (a) a 1D velocity model of the Puget Lowland outside the Seattle basin compared with (b) a 3D velocity model (Delorey and Vidale, 2011) that simulates 3D basin amplification. Triangles delineate the rupture used to generate seismograms, dotted lines show the Seattle fault zone.

Sample synthetic seismograms are shown in Figure 1-3. These seismograms contain important features that would not be represented using ground-motion values from average ground-motion prediction equations. For stations within about 5 km of the fault trace, there is a forward rupture directivity pulse that greatly increases the peak acceleration. The synthetics for stations in the Seattle basin also exhibit substantial basin surface waves generated at the edges of the Seattle basin. These basin surface waves increase the amplitude and duration of long-period shaking. The peak horizontal ground accelerations for this earthquake for the 3D velocity model and the 1D velocity model are shown in Figure 1-4. This is a randomized iteration of a possible

Seattle Fault earthquake and represents just one possible scenario. As expected, the synthetics generated using the 3D velocity model that accounted for amplification within the Seattle basin resulted in higher peak ground accelerations and more spatial variability within the basin (north of the Seattle fault) than the 1D velocity model, particularly along the northern edge of the basin.

5. Incorporating Site Amplification

The broadband seismograms we generated by the methods described above represent shaking at the surface with a base shear wave velocity of 600 m/s, but most of the city is underlain by shallow layers of soil with much lower shear wave velocities that can amplify ground motion (Pratt and Brocher, 2006, Frankel *et al.*, 2002, Pratt *et al.*, 2003, Snelson *et al.*, 2007, Hartzell *et al.*, 2000). In order to simulate realistic ground motions, we needed to account for site amplification relative to the 600 m/s base layer. No effective simple methods yet exist for adjusting a full seismogram in the time domain for site effects on a regional scale. Most methods depend on the average shear wave velocity in the top 30 meters (Vs30), which some argue is a poor predictor of site amplification (*e.g.,* Castellaro *et al.,* 2008). They are also developed to adjust response spectra (Choi and Stewart, 2005, Borcherdt, 1994) and are thus not appropriate for adjusting Fourier spectra, which is required to adjust time series seismograms. As an intermediate approach, we developed 67 representative shear wave velocity (Vs) profiles that represent the range of typical surficial geologic profiles in Seattle. The complete profiles are reported in Appendix 1. We then used ProShake, a software package that uses equivalent linear methods to approximate soil non-linearities, to develop 1D site amplification transfer functions for each Vs profile using the base synthetic seismograms as the input ground motion level. This method does not correctly handle the surface waves or P-waves in the waveforms, but at the

frequencies being amplified and for horizontal components, S-waves are dominant, so it should be a good approximation.

We built the representative Vs profiles based on the geologic map of Seattle, cross-sections and typical thicknesses for each unit (Troost *et al.*, 2005), and typical engineering properties, shear wave velocity ranges, and measured shear wave profiles for these units (Savage *et al.*,2000; Williams *et al.*, 1999; Wong *et al.*, 2010; Palmer *et al.*, 2004). The geologic units and the range of engineering properties we used to construct these representative profiles are shown in Table 1-1. For simplicity, all unconsolidated deposits older than the last glaciation (the Vashon stade of Fraser glaciation) were lumped together as Qpf. These units are nearly all classified as very dense and hard because they have been overconsolidated by one or more glaciations so we considered them to be equivalent to the base layer of 600 m/s. We assumed linear behavior of these units because soils of this site class (NEHRP class C) do not generally show much non-linear behavior (Choi and Stewart, 2005). The few soft rock sites, all located in the southern part of the city, were treated similarly. We concentrated our efforts in the development of these representative shear wave profiles on areas that could generate landslides. Consequently, profiles for flat-lying areas, such as the Duwamish valley, Harbor Island, and Interbay, are highly oversimplified and should be improved if used for any other purpose. Figure 1-5 shows the average shear wave velocity in the top 30 meters (Vs30) calculated from these representative profiles.

Table 1-1 Description of geologic units used in the development of the representative Vs profiles and the range of thicknesses and engineering properties they were assigned.

Unit	Typical Thickness range (m)	Vs range (m/s)	Wet density range (kg/m^3)	Description	Age
Qvt	8	400-600	2160-2400	Vashon Till	Fraser Glaciation Vashon Stade (pleistocene)
Qva	10-50	300-600	1920-2160	Advance Outwash Deposits	
Qvr	5	250-350	1680-1800	Recessional Outwash Deposits	
Qvrl	5	250-350	1560-1800	Recessional Lacustrine Deposits	
Qvlc	15-30	200-500	1560-1920	Lawton Clay	
Qpf	NA	450-600	2160-2400	Pre-fraser Deposits	pleistocene
Tb	NA	350-600	2300-2400	Blakely Formation (weakly lithified sandstone)	Tertiary
soil	1	100	1440	Soil	postglacial (holocene)
Qp	10	60	1260	Peat	
Qal	6-30	120-180	1440-1620	Alluvium	
Qt	6	120-130	1440	Terrace deposits	
Qls	3-10	120-140	1440-1500	Landslide deposits	
Fill	2-10	120-140	1440-1500	Artificial Fill	
Qb	8	120-140	1440-1500	Beach	
Ql	3	130-150	1560-1680	Lake Deposits	

Once we applied the corresponding transfer functions that we developed to each 5-meter grid cell, the spatial variability of the ground motions increased significantly (Figure 1-6). The ground motions in some of the low-lying areas with low shear wave velocities were deamplified due to soil non-linearity, particularly areas of fill and alluvium (where liquefaction is more likely than landsliding). Areas that were significantly amplified relative to the base seismograms include (1) old landslide deposits along many of the steep coastal bluffs that overlie higher velocity undisturbed deposits, (2) areas where thin, lower velocity deposits such as recessional outwash or soil overlie pre-Vashon deposits, and (3) soft rock sites that behave linearly. The soft rock sites have a higher Vs30 than much of the city, yet they also have some of the highest amplifications because they behave linearly and high impedance contrasts between the rock and overlying shallow soil and weathered layers can cause amplification at higher frequencies where

there is more seismic energy. Accelerations reach 2g in a few of these localized areas on the hanging wall of the fault.

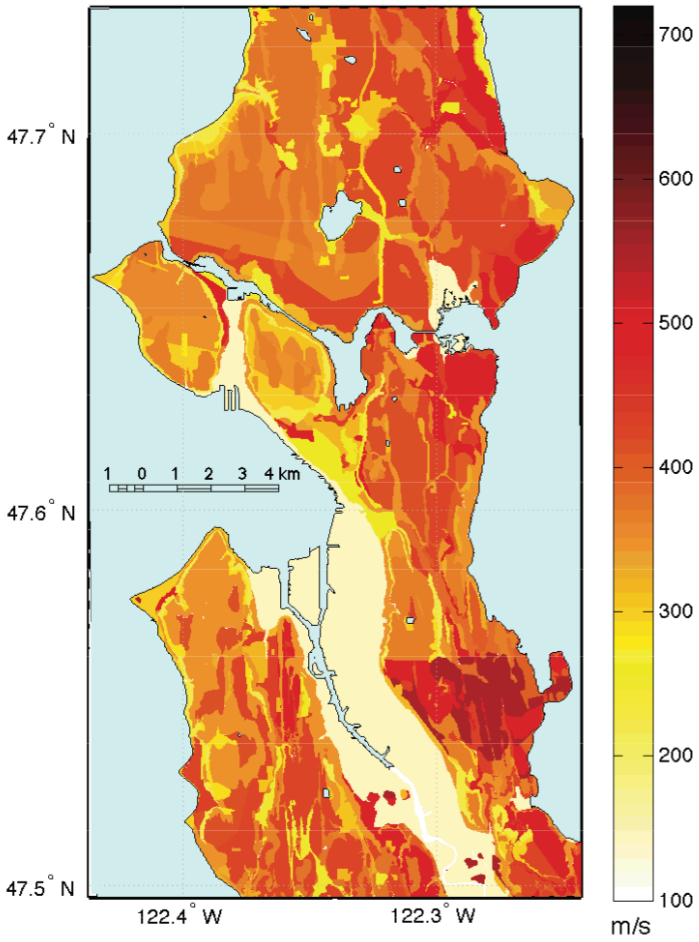

Figure 1-5 Average shear-wave velocity down to 30 m (Vs30) computed from the representative Vs profiles compiled for this study.

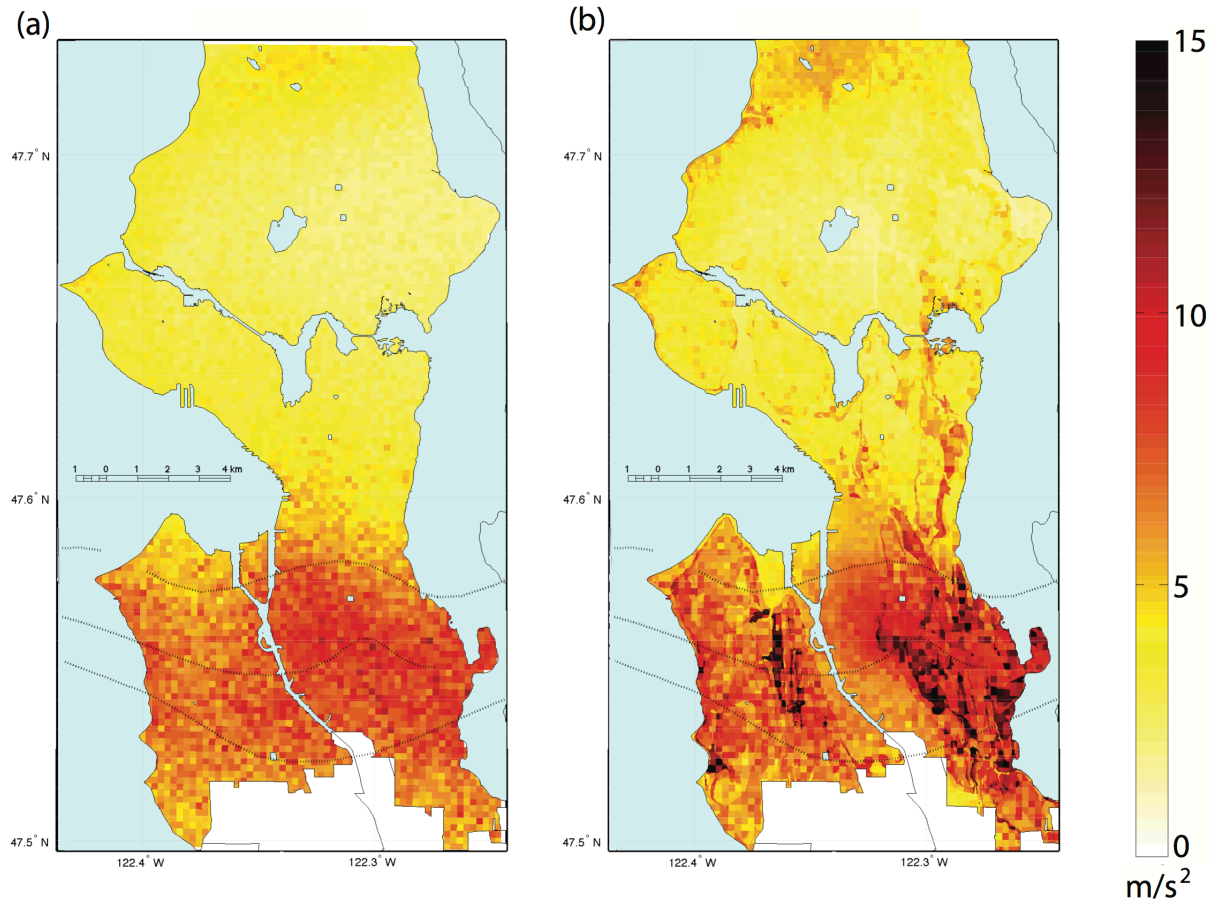

Figure 1-6 Maximum horizontal peak ground acceleration for (a) the base synthetic seismograms generated using the 3D basin velocity model with a surface layer velocity of 600 m/s and (b) the same seismograms adjusted for 1D site amplification due to the shallow surficial soil layers at right. Seattle fault zone is indicated by dotted lines.

6. Model Outputs

Next, the critical acceleration for both dry and saturated soil conditions and ground motions for the scenario earthquake assigned to each cell were used to calculate the Newmark displacement for each cell using the methods described above. We used the final Newmark displacement as an index for the relative likelihood of landsliding, as in Jibson and Michael (2009). We designated seismically induced landslide hazard zones based on an empirical relation between Newmark displacement and probability of failure developed by Jibson *et al.,* (2000). This relation was derived from the landsliding catalog from the Northridge earthquake. While the

soils and rocks that failed in the 1994 Northridge earthquake are different than the soils of Seattle, using the probability curve developed for Northridge is currently the best option available due to the dearth of complete post-earthquake landslide surveys. This is something that needs to be improved upon in future work. We divided hazard into four zones: Low, Moderate, High, and Very High. Cells with more than 0 cm of displacement up to 3.5 cm of displacement, corresponding to a less than 10% chance of failure, were designated as Low seismically induced hazard. The Moderate seismically induced landslide hazard zone corresponds to areas with Newmark displacements between 3.5 and 7 cm, or 10-20% probability of failure, High corresponds to 7 to 12 cm or 20-30% probability of failure, and Very High corresponds to anything with more than 12 cm of displacement, or a probability of failure above 30%. The reason the highest landslide hazard zone cutoff is at a mere 30% probability of failure is because Jibson et al. (2000) found that the probability of failure levels off at 34% beyond about 18 cm of displacement due to natural variability. We generated relative seismically induced landslide hazard maps using these designated landslide hazard zones, but also went one step further towards the scenario approach and designated predicted slope failures to assess the extent of landsliding one might expect. To do this, a random number generator chose a number between 0 and 1 for each cell. If the chosen number was lower than the probability of failure assigned to that cell, the slope represented by that cell fails. Failure is defined as a detachment of the slope. The failure of each cell is independent of all the others. Once the distribution of failed cells throughout the city was determined, adjacent failed cells were clustered together into landslide source areas. Each cluster of adjacent failed cells was counted as one source.

Landslide damage can occur both in the source area and in downslope cells. Deterministic models of runout are not practical on the scale required for this study and

empirical runout estimation methods that currently exist, often based on the travel distance angle (e.g. Hunter and Fell, 2003), are derived from datasets of landslides primarily triggered by water, not ground motion, and are not appropriate for this scenario study where the water content of failed materials could be significantly lower. Therefore, we were not able to estimate runout from each failed cell in the scenario. However, Harp et al. (2006) recommended a runout buffer zone of 60 meters below steep slopes based on the mean runout length of a set of landslides in Seattle. We used this runout distance of 60 meters (or until the slope reached 2º, whichever came first) to quantify the extent of infrastructure and buildings that are potentially at risk.

7. Validation of Ground Motions

In order to validate the methods we used to generate synthetic seismograms, we calculated spectral accelerations (for 5% critical damping) of the synthetic seismograms and compared them to the spectral accelerations predicted for an M_w 7.0 thrust fault earthquake on the Seattle Fault by three of the Next Generation Attenuation (NGA) relations that account for basin depth: Campbell and Borzognia (2008), Chiou and Youngs (2008) and Abrahamson and Silva (2008). There is a directivity pulse in the broadband synthetics because of the updip rupture that appears primarily on the fault-normal (~North) component, so we also included a modification to the NGA relations developed by Shahi and Baker (2011) that accounts for a directivity pulse. We calculated response spectra for the base synthetic seismogram (NEHRP Class C site condition) corresponding to each grid point on the 210-m grid and binned them in 2-km wide bins based on the closest distance to the fault. The mean spectral accelerations (±1 standard deviation) of the synthetics at a range of horizontal distances to the fault are shown in Figure 1-7. Spectral accelerations are shown for synthetics computed using both the 1D and 3D velocity models (left and right, respectively). These are compared with the spectra for three NGA

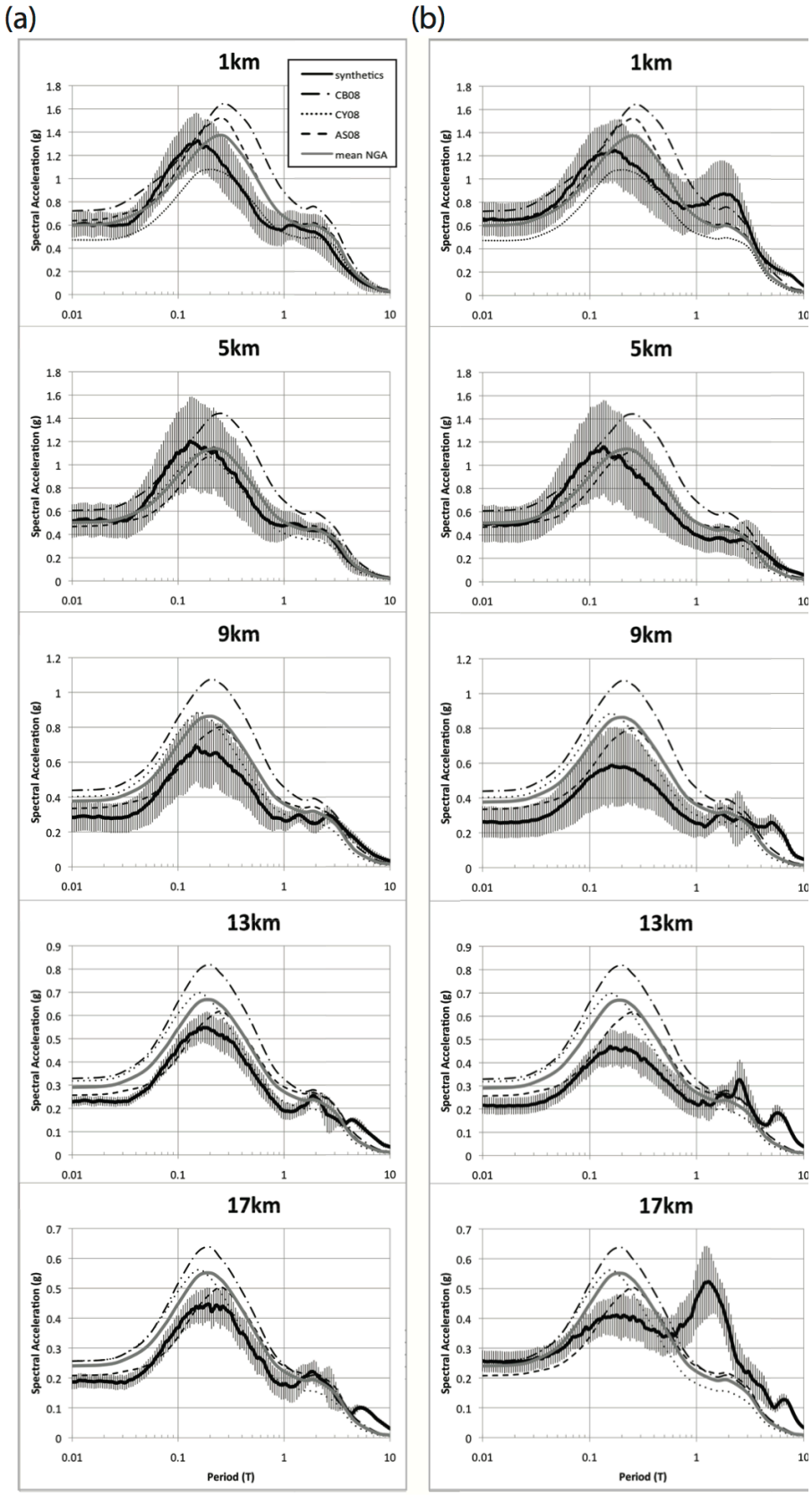

Figure 1-7 Response spectra (5% critical damping) of the broadband synthetics generated with the (a) 1D basin velocity model and the (b) 3D basin model, compared with the mean values for three Next Generation Attenuation relations that are modified to include a directivity pulse using methods developed by Shahi and Baker (2011). Black is the mean of the synthetics at the distance bin noted ±1km with one standard deviation indicated by the error bars. The thick gray line is the mean of the three attenuation relations, CB08 (dash-dot) is the response spectra for Campbell and Borzorgnia (2008), CY08 (dotted) is Chiou and Youngs (2008), and AS (dashed) is Abrahamson and Silva (2008). The bump at about T = 3 seconds is due to the directivity pulse.

relations and the mean of all three combined, assuming the same distance for all types of distances to the fault required for each equation. The fit is quite good, particularly taking into account the large variability between the NGA attenuation relations themselves and their respective uncertainties, the spatial variability within the synthetics as shown by the error bars, and the fact that the y-axis is linear rather than logarithmic. The synthetics made using the 3D model show much higher spectral accelerations at long periods because of basin amplification, particularly around 17 km from the fault where there is strong amplification at the northwestern edge of the Seattle basin. The directivity pulse at a period of 3 seconds in the synthetic seismograms matches the period predicted by Shahi and Baker (2011) for this event. Their predicted pulse also matches the amplitude quite well for the 1D model but is exceeded by the 3D synthetics, suggesting that amplification within the 3D structure also occurs at these frequencies.

To validate the transfer functions that we computed for representative Vs profiles throughout Seattle using ProShake, we generated transfer functions for them using recordings of the 2001 Nisqually earthquake as the input ground motions. We then compared the resulting transfer functions to the spectral ratios of the recorded Nisqually ground motions at several accelerometers located throughout the city, using a soft rock site in Seward Park (SEW) as the reference site. Comparisons between our modeled transfer functions for representative profiles and the spectral ratios of the real data are shown in Figure 1-8. We did not expect to fit the exact peaks and troughs of amplification shown in the spectral ratios because representative profiles cannot replicate site-specific peculiarities. Instead, we aimed to roughly match the frequencies and amplitudes of amplification for most sites. The transfer functions match well for many stations (*e.g.*, WEK, THO, BRI, MAR, SEU), particularly at less than 10 Hz, but they diverge at

higher frequencies where shallow layers dominate the site response (e.g. TKCO, ALO, BHD, CRO, HOLY). Amplifications on this fine scale are beyond our ability to reproduce using representative profiles, but most of the energy in the seismograms is below 10 Hz so this is not detrimental. A few transfer functions do not match the spectral ratios as well (e.g., NOWS, QAW, SEA). These differences could be due to finer scale geological variability than is reflected in the geologic map of Seattle or issues with station or site response. They illustrate the limitations of simplifying shear wave profiles into representative units for such a large region, but the differences are not severe and only occur at a fraction of the sites.

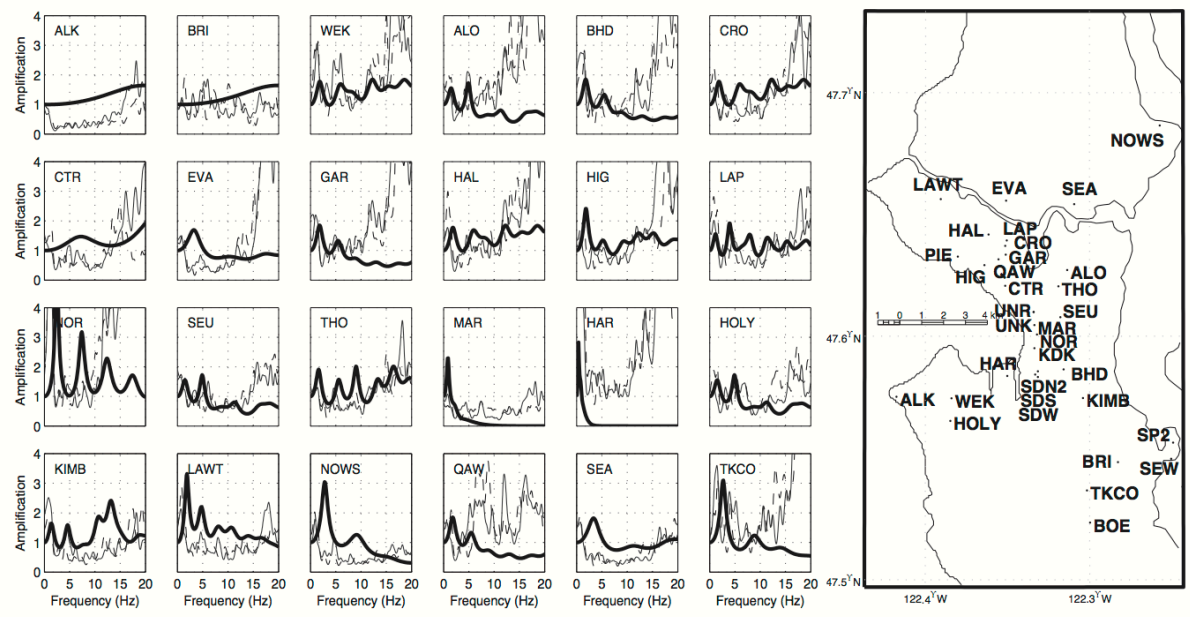

Figure 1-8 The spectral ratio of the recorded ground motions of the Nisqually earthquake at 24 accelerometers using the soft-rock reference station, SEW, shown on the station map at right (thin lines, North is dashed, East is solid) compared to the transfer functions computed in ProShake for the corresponding representative Vs profiles computed using the Nisqually earthquake ground motions as the input ground motions (thick black line).

8. Validation of Landslide Simulation

The 2001 M_w 6.8 Nisqually earthquake, located at 52 km depth with a hypocenter 57 km SSW of Seattle (location from the Pacific Northwest Seismic Network), is the only one of the three large historic Puget Sound earthquakes for which dense ground acceleration records exist. The earthquake triggered about 100 landslides throughout Puget Sound (Stewart, 2005), fewer than expected since the earthquake occurred during a rare winter dry period (Highland, 2003). Only landslides that caused damage and losses were included in a post-quake report on landsliding by Highland (2003). Most of these occurred closer to the epicenter, south of Seattle. Only two of the reported landslides in this report were within city limits: landsliding in one location of West Seattle damaged some houses and lateral spreading caused some damage to a viaduct downtown. No comprehensive landslide survey was done due to the scarcity of significant landsliding within city limits. As the best validation available, we ran the Nisqually ground motions through the seismically induced landslide simulation model using the factor of safety map for dry conditions to see if it reproduced the observed scarcity of landsliding.

To do this, we used 33 strong ground motion records; the locations of these stations are shown on the map in Figure 1-8. In order to infer ground motion throughout the city from this sparse and irregular sampling, we removed site amplification using spectral ratios relative to a reference site on a soft rock site in Seward Park (SEW). Then, each 210-m grid point was assigned the closest actual recording with the recording station's site effects removed and corrected for geometrical spreading. We then readjusted the ground motions for site effects using transfer functions developed in ProShake using actual recordings of the Nisqually earthquake as the ground motion input and the representative Vs profiles we developed. Ground motions during the Nisqually earthquake were much lower than those for the Seattle fault simulation, so

the site amplifications in the simulation for most representative profiles are actually higher for the Nisqually earthquake than for the Seattle fault event because they are not moderated as much by non-linear effects.

The landslide simulation for dry conditions - representative of the conditions during the Nisqually earthquake - predicted 26 landslide sources with a total area of about 1,000 m^2 (Tables 1-2 and 1-3). They are located in ten localities (Figure 1-9) almost exclusively on extremely steep (median slope of 40°) undeveloped coastal bluffs and ravines - nearly half in city parks. The simulation predicted that only 0.001% of the land area of Seattle had high landsliding potential (nmdisp>7cm, >20% probability of failure). We consider this dearth of predicted landsliding and their locations in extremely steep undeveloped areas where they would be unlikely to affect structures or infrastructure, or even be noticed, to be a validation that our earthquake-induced landslide simulation generates realistic results. We also ran the same landslide simulation of the Nisqually earthquake but for saturated soil conditions instead to see what might have happened if the earthquake had occurred after an extended period of heavy rainfall. The results are drastically different: nearly 7,500 landslide sources were triggered, 9 of those greater than 500 m^2 in area. These sources cover 0.3 km^2 of the city, and 0.4% of the land area of the city had high potential for landsliding (nmdisp>7cm, Tables 1-2 and 1-3).

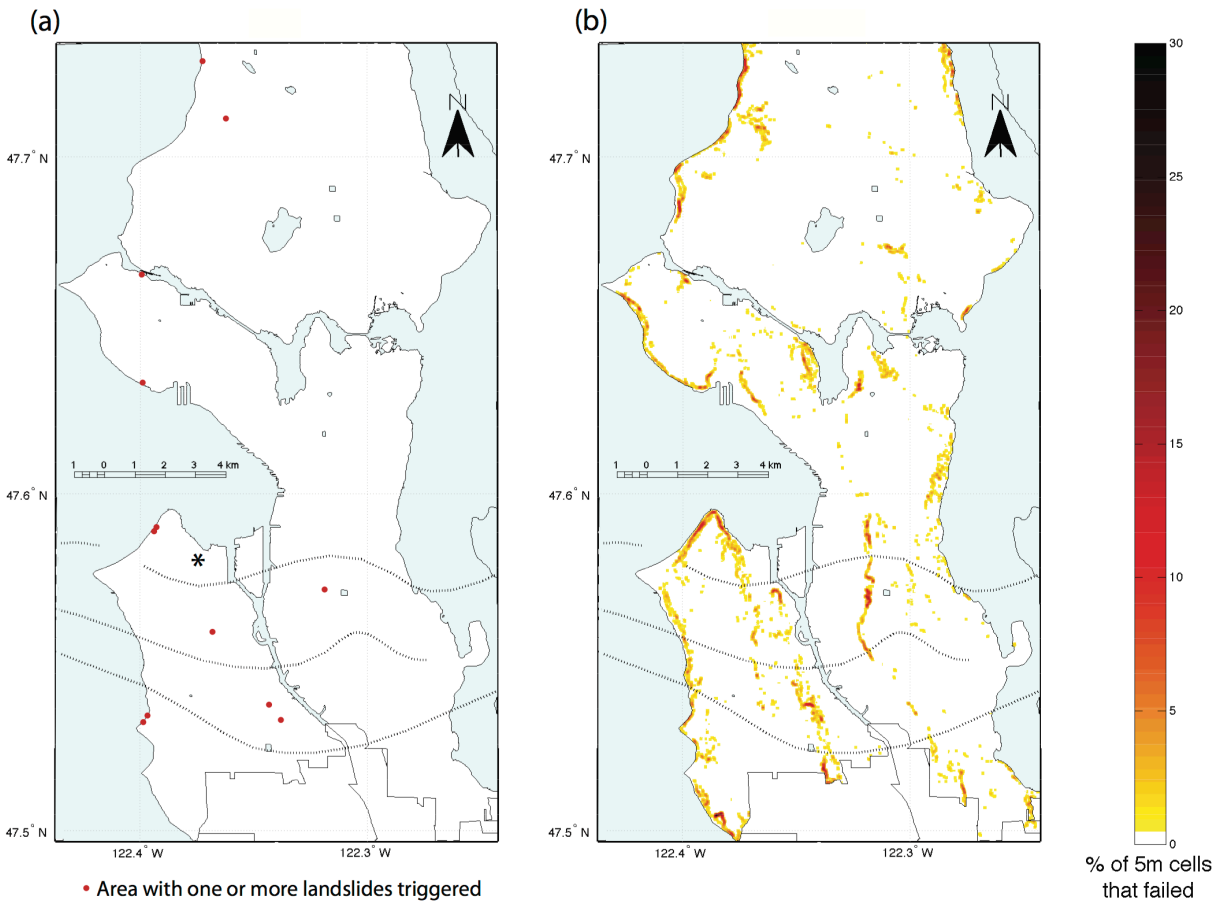

Figure 1-9 Percentage of cells in each area where failures were triggered, as defined in the text for the (a) dry and (b) saturated soil conditions using ground motions from the 2001 Mw6.8 Nisqually earthquake. For visibility, individual failures are indicated for dry soil simulation because there were so few landslides triggered. In reality, so few shallow disturbed landslides were triggered by this quake that no post-quake landslide survey was done, the location of just one damaging landsliding was documented by Highland (2003), which is indicated by an asterisk at left. For the saturated soil simulation, the shading corresponds to the percentage of 5-meter cells in each area that failed in the simulation, smoothed with a 20x20 cell Gaussian kernel.

9. Results of Landslide Simulation for Mw 7.0 Seattle Fault Earthquake

The results of our seismically induced landslide simulation of the scenario M_w 7.0 Seattle fault earthquake for the best- and worst-case scenarios, (dry and saturated soil conditions, respectively) are summarized on Tables 1-2 and 1-3. Individual failures of 5-meter cells are too small to see on a citywide map, so Figure 1-10 instead shows the percentage of cells that failed

in each area of the city smoothed with a 20x20 cell kernel (100 m x 100 m). In addition, high resolution maps of relative seismically induced landslide hazard for a M_w 7.0 Seattle fault earthquake are provided in Appendix 2, Figures A1 and A2. Zoom-ins on a few areas of interest of this map are shown in Figure 1-11. Hazard zone levels are based on Newmark displacement and the corresponding probability of failure as described above.

Table 1-2 Summary of landslide sources triggered by seismically induced landslide simulations

	Mw 6.8 Nisqually Earthquake Simulation*		Mw 7.0 Seattle Fault Earthquake Simulation†	
	Dry Conditions	Saturated Conditions	Dry Conditions	Saturated Conditions
Number of failed 5x5m cells	40	13,720	9,698	77,765
Number of sources††	26	7494	4,977	30,699
Median slope of source cells (degrees)	40	35	29	26

* Results using nearest original ground motion recording of the 2001 Nisqually earthquake for each cell with site effects removed and then adjusted for site amplification using the corresponding transfer functions developed for this study
† Results using broadband synthetic seismograms generated using a 3D velocity model and including site amplification
†† Sources are clustered - adjacent "failed" cells are counted together as one source

Table 1-3 Total land area potentially affected by seismically induced landsliding

	Mw 6.8 Nisqually Earthquake Simulation*				Mw 7.0 Seattle Fault Earthquake Simulation†			
	Dry Conditions		Saturated Conditions		Dry Conditions		Saturated Conditions	
	Area (km^2)	% Land area††	Area (km^2)	% Land area	Area (km^2)	% Land area	Area (km^2)	% Land area
Sources	0.001	0.0004%	0.3	0.1%	0.2	0.1%	1.9	0.8%
nmdisp§ >0cm	0.025	0.01%	3.2	1.4%	2.6	1.2%	10.1	4.4%
nmdisp >3.5cm	0.006	0.001%	1.2	0.5%	0.9	0.4%	6.5	2.8%
nmdisp >7cm	0.003	0.001%	0.9	0.4%	0.6	0.2%	5.6	2.4%
nmdisp >12cm	0.002	0.001%	0.8	0.3%	0.4	0.2%	4.7	2.1%

* Results using nearest original ground motion recording of the 2001 Nisqually earthquake for each cell with site effects removed and then adjusted for site amplification using the corresponding transfer functions developed for this study
† Results using broadband synthetic seismograms generated using a 3D velocity model and including site amplification
†† Percent of total land area of Seattle. Seattle has a land area of ~229 km^2
§ nmdisp = Newmark Displacement

In our simulation for dry soil conditions, 4,977 landslide sources are triggered by the earthquake, covering 0.2 km^2 - 0.1% of the total land area of the city. In addition, 0.2% of the city is in a high landslide hazard zone for this event (nmdisp>7 cm, probability of failure >20%).

Landsliding is concentrated in the southern half of the city along the coastal bluffs of West Seattle, the western side of Beacon Hill, and scattered throughout Delridge. The coastal bluffs of Magnolia and Queen Anne show some less concentrated landsliding, and North Seattle escapes relatively unharmed with the exception of localized landsliding along coastal bluffs in North Ballard, near Carkeek Park, and in Lake City (Figure 1-10, left, locations of places mentioned are shown on Figure 1-1).

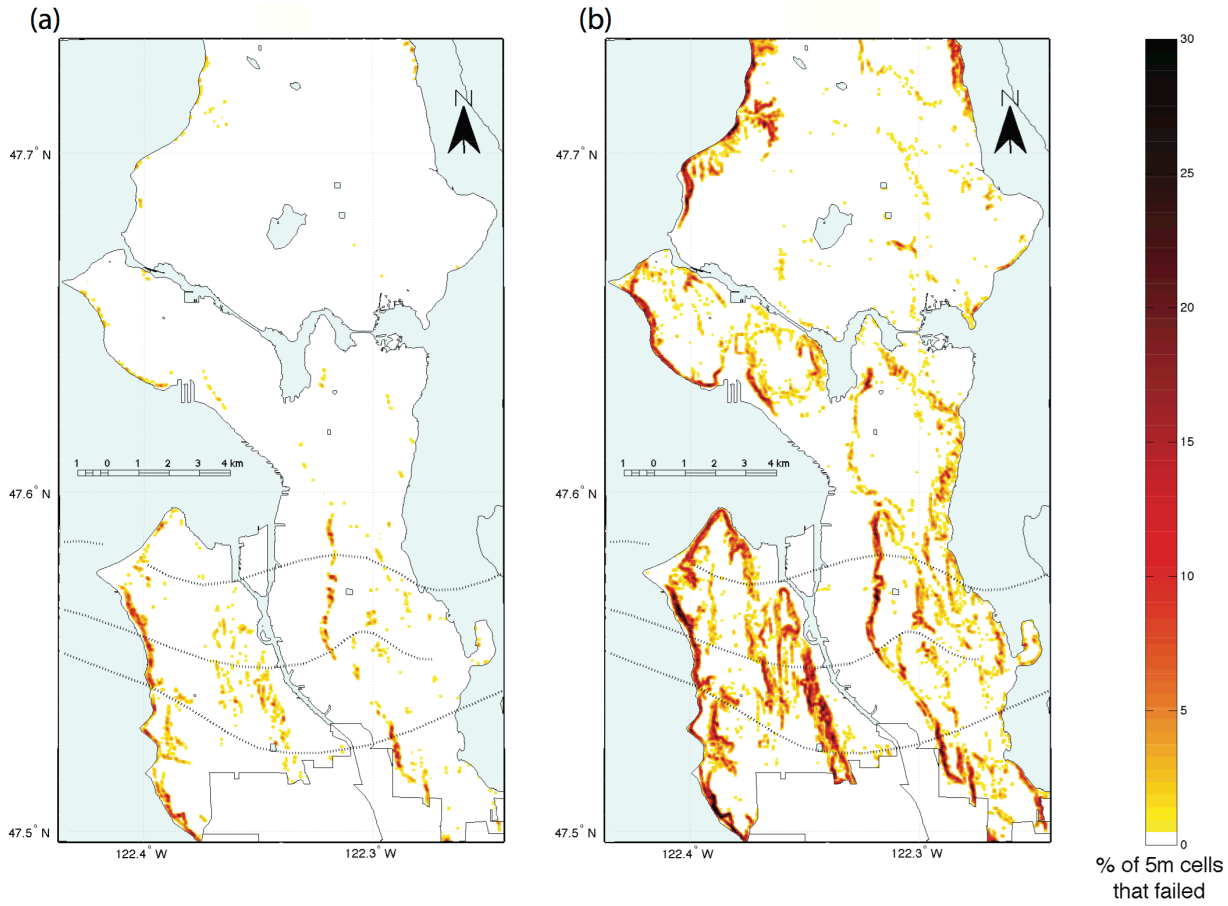

Figure 1-10 Percentage of cells in each area where failures were triggered, as defined in the text for the (a) dry and (b) saturated soil conditions for the Mw 7.0 Seattle Fault earthquake simulation.

For the same exact scenario but using the factor of safety map for saturated soil conditions instead, the results are more drastic. More than 30,000 landslide sources are triggered covering 1.9 km^2, equal to 0.8% of the land area of the city. In this case, 2.4% of the city is in a

high landslide hazard zone (nmdisp>7 cm). Fortunately this simulation represents an unlikely scenario where the water table is effectively at the surface everywhere due to higher than normal seasonal rainfall, followed by an intense precipitation event, followed, in turn, by a low-probability earthquake.

The distribution of landslide sources for saturated conditions contrasts with the dry scenario (Figure 1-10, place names on Figure 1-1). In this simulation, the southern half of Seattle experiences dense landsliding concentrated not only on the coastal bluffs and the slopes bordering the Duwamish river valley but also scattered inland throughout West Seattle, Delridge, Beacon Hill, Seward Park and Rainier Valley. Landsliding rims both Magnolia and Queen Anne hills and extends north all the way to Portage bay along Interstate-5 (I-5). The northern half of Seattle, though less hard-hit than the rest of the city, is more severely affected in this case than in the dry scenario. The coastal bluffs along Puget Sound experience dense landsliding in incised valleys up to 1 km from the coast, particularly in the northwest corner of the city, because of the strong amplification of low frequencies at the edge of the basin. In both cases, areas of steep topography on the hanging wall of the Seattle fault are most severely affected by seismically induced landsliding, consistent with observations of landsliding triggered by other earthquakes worldwide (*e.g.*, Tang et al., 2011).

Overall patterns of predicted landsliding correspond to areas that are generally known to be landslide prone. In fact, 66% of known historical landslides in Seattle (from the City of Seattle dataset) lie within landslide hazard zones predicted by the Seattle fault earthquake simulation for dry conditions; 80% for the saturated soil conditions. However, if we look at existing landslide hazard maps for static (no ground shaking) conditions, a significant percentage of the landslides predicted by the simulation are in areas of low and medium relative hazard

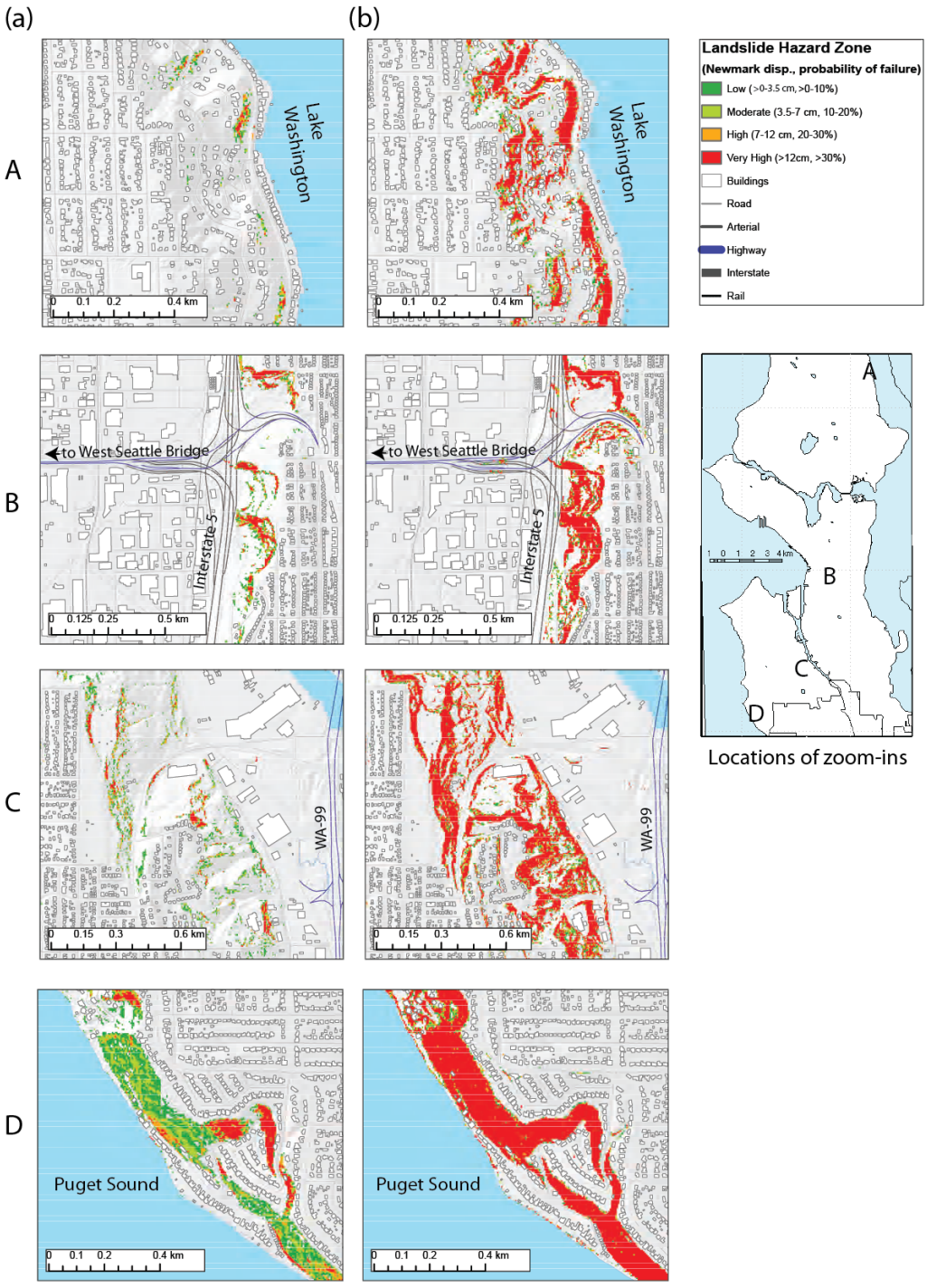

Figure 1-11 Zoom-ins of the relative seismically induced landslide hazard map for (a) dry and (b) saturated soil conditions superimposed on infrastructure and building outlines. Full high resolution versions are included in the electronic supplement, Figures S1 and S2. Locations of each zoom-in are shown on the map of Seattle at right. A) Coastal bluffs in the northern part of Seattle are most affected when soils are saturated. Many single family homes are located within landslide hazard zones, as well as downslope from potential source areas where they could be

affected by runout. B) There are several areas along the I-5 corridor that are highly susceptible to landsliding for all soil saturation levels, such as the area shown here near the access point to the West Seattle bridge. C) The hillsides in West Seattle along the Duwamish valley are at risk of seismically induced landsliding, such as the area shown here. There are industrial as well as residential buildings that could be affected by runout from landsliding in these areas. D) The coastal bluffs along Puget Sound in West Seattle on the hanging wall of the fault, such as the area shown here, are the most highly susceptible areas to landsliding in the city; numerous residential structures are at risk from both potential landslide source areas and runout. North is up on all maps.

based on static slope stability as delineated by Harp *et al.* (2006): 28% of the total landslides triggered by our dry soil conditions simulation occur in medium and low static landslide hazard areas for dry conditions, and 40% for the saturated soil simulation. Similarly, a comparison between the cells that failed in the seismically induced landslide simulation and areas designated as potential sliding areas in the City of Seattle corporate GIS database also shows that a significant percentage of the predicted landsides lie outside the designated areas: for dry conditions 36% of failed cells are outside potential sliding areas, 38% for saturated conditions. The City of Seattle potential sliding areas were designated based on the contact between a permeable and an impermeable geologic unit (Esperance sand and Lawton clay, respectively) where seepage occurs and many historical landslides have been triggered by water. Clearly, these maps are not adequate to delineate areas likely to produce landslides during earthquakes. We cannot assume that seismically induced landslides will only be triggered in areas already designated as hazardous by studies focusing on static slope stability, highlighting the importance of studies dedicated to seismically induced landslide hazard such as this one.

10. Infrastructure Impacts

Our results show that it is not only the relatively undeveloped coastal bluffs that are hit, but landsliding also affects inland slopes that could threaten key transit routes and buildings,

particularly in the saturated soil scenario. To further investigate the infrastructure and buildings that may be at risk from seismically induced landsliding in such a scenario, we calculated the number of buildings and total length of linear infrastructure such as roads and water lines that fall within the four different seismically induced landslide hazard zones as well as within a 60-meter buffer (or until the slope reaches 2°) downslope from these hazard zones to determine susceptibility to potential runout from the triggered landslides as well. Note that the numbers presented here do not mean that every single building and piece of infrastructure within these zones will be negatively affected when a Seattle fault earthquake eventually occurs. The highest probability of failure for any hazard zone is 34% and most are much lower and the runout buffer zone is probably overestimated in most cases. The numbers are simply a measure of the extent of infrastructure and buildings that are potentially at risk.

There are a significant number of buildings that are located directly within the seismically induced landslide hazard zones (Figure 1-12). For dry soil conditions, there are over 1,000 buildings that are within all hazard zones, 400 of those in the two highest hazard designation zones (>20% probability of failure). Twice as many buildings are in the potential runout zones from these landslides. For saturated soil conditions, it is nearly an order of magnitude worse, with 8,000 buildings within all hazard zones, 5,000 of those within the two highest hazard zones. 8,500 more buildings are within the potential runout from all hazard zones. Additionally, hundreds of total kilometers of linear infrastructure (roads, rail, electric, water, and sewer lines) also sit within these hazard zones. The total length in kilometers of each type of infrastructure that is located within the two highest hazard zones (>20% probability of failure) and within the potential runout zone from these hazard zones is shown in Figure 1-13. We found that the majority of the length of linear infrastructure that is at risk is within the potential runout

areas rather than within the potential source areas. For dry soil conditions, with the exception of railroad tracks, on the order of 1 km of each type is at risk from landslide sources, while on the order of 10 km of each are in potential runout areas. For saturated soil conditions, the numbers are bumped up by an order of magnitude, on the order of 10 km of each are within potential source areas and 100 km are within potential runout areas. In any case, the impacts to infrastructure from landsliding will be extensive when a large Seattle fault earthquake occurs for any soil saturation level and this could significantly slow down recovery.

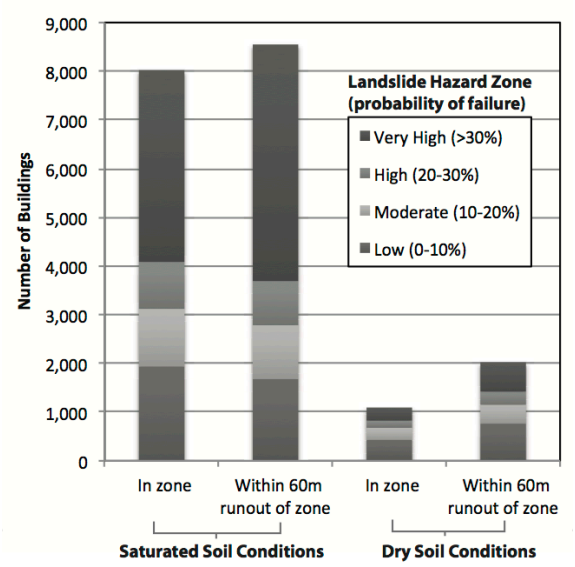

Figure 1-12 The total number of buildings in each landslide hazard zone and also within a 60-meter runout buffer downslope from each hazard zone for both dry and saturated conditions. Each building can only be designated in one hazard zone or potential runout zone, so totals are mutually exclusive.

11. Discussion

The ground motions we developed include a much higher level of detail than is typically used to model seismically induced landsliding. To determine which efforts and effects are most important and which could potentially be neglected without significantly altering the results, we compared the total citywide Newmark displacement for various levels of ground motion complexity for dry conditions (Summary on Figure 1-14).

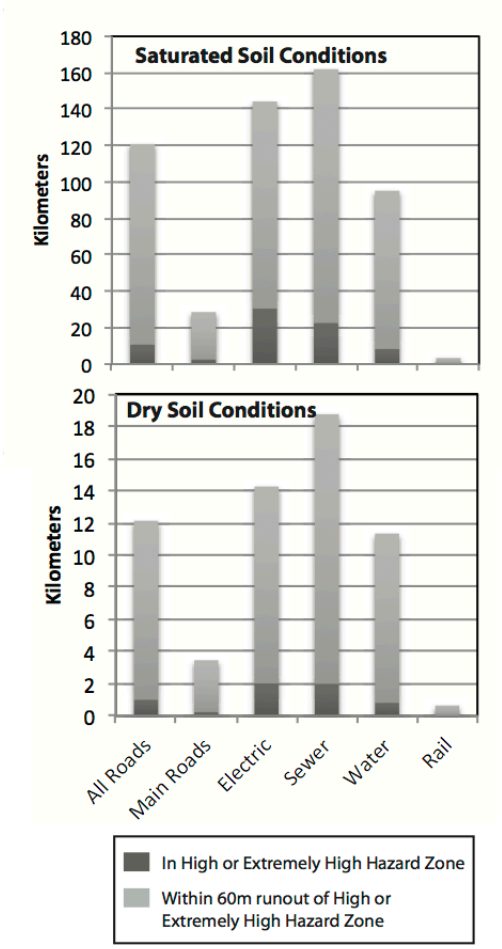

Figure 1-13 Total length of critical linear infrastructure that is located within the high or extremely high landslide zones and within the potential runout areas from these zones for saturated (top) and dry (bottom) soil conditions.

We first ran the simulation with and without site and basin amplification and found that both need to be rigorously accounted for in simulations like this. Ignoring them could result in an under-prediction of seismically induced landsliding hazard. For example, the inclusion of 1D site amplification (site effects) quadruples the number of failed cells for dry soil conditions. On top of that, the inclusion of basin amplification (using a 3D velocity model instead of 1D velocity model) bumps up the number of slope failures by about 35% because the basin amplification is so strong in Seattle. For an area that does not sit on a significant sedimentary basin, the 1D velocity model may be sufficient, but for Seattle, using a 3D basin model to account for basin amplification is critical.

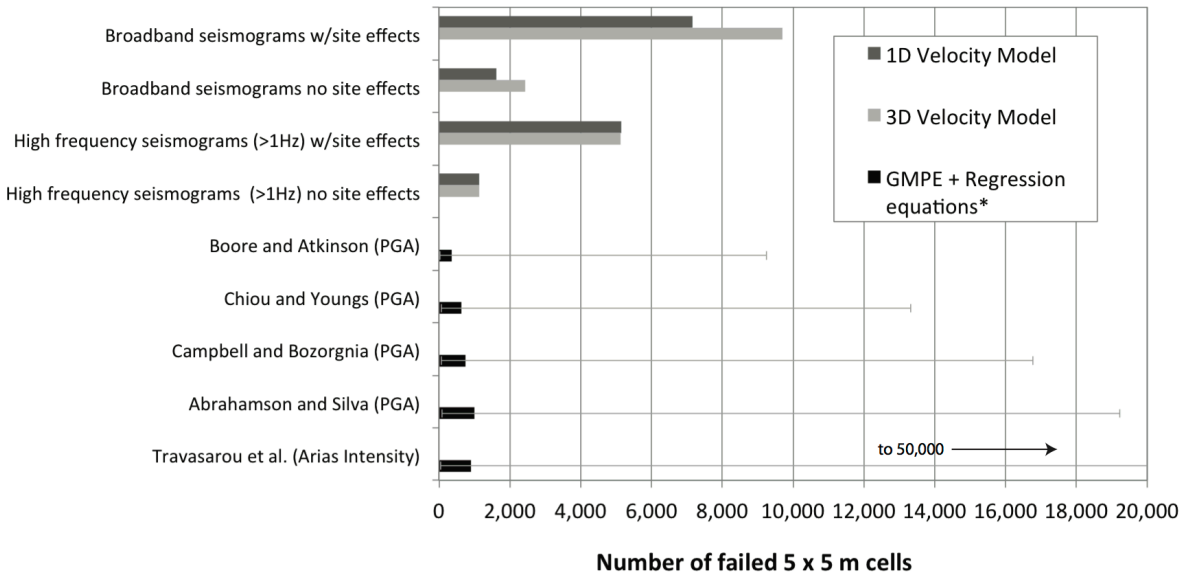

Figure 1-14 Results of seismically induced landslide simulation for dry soil conditions for various levels of complexity. Gray bars indicate the total number of failed cells (as defined in text) from the landslide simulation using both broadband seismograms and just the high frequency portion of the synthetic seismograms (> 1Hz) using the 1D (dark gray) and 3D (light gray) velocity models for simulations that include and exclude 1D site amplification. These results are compared with simpler methods (black) where ground motion prediction equations (GMPE's) are used to estimate ground motion parameters for a Mw 7.0 Seattle fault earthquake instead of synthetic seismograms and the Newmark displacement is calculated using a regression equation developed by Jibson (2007). Four Next Generation Attenuation relations were used to estimate PGA and Travasarou et al., (2003) was used to estimate Arias Intensity. Error bars indicate ± one standard deviation accumulated from both the GMPE's and the regression equations.

Next, we compared the results of this study with what would be predicted by simpler methods. Most previous regional assessments of seismically induced landsliding used empirical regression equations that estimate Newmark displacement as a function of simplified ground motion parameters that are obtained using ground motion prediction equations (GMPE's). We estimated landsliding for our scenario using these methods in order to compare the result with our more detailed simulation.

To do this, we used four Next Generation Attenuation (NGA) relations (Boore and Atkinson, 2008; Abrahamson and Silva, 2008; Chiou and Youngs, 2008; Campbell and

Borzognia, 2008) to estimate peak ground acceleration for each cell throughout the city for the same scenario earthquake. All the NGA relations account for site effects by NEHRP site class that is based on the Vs30 of each site, which we take from the Vs30 of the representative shear wave profile assigned to each cell. The latter three NGA relations also require the depth to a defined shear wave velocity contour to account for basin depth. We extracted those values from Delorey and Vidale's (2011) 3D velocity model for each cell. Once we obtained PGA, we used the regression equation developed by Jibson (2007) that relates earthquake magnitude and PGA to Newmark displacement. The mean number of failures triggered by each of the four NGA equations used is shown on Figure 1-14, along with error bars that span plus or minus one standard deviation for both the NGA predicted PGA values and the Newmark displacement predicted from it combined. The four relations predict a similar number of ground failures between them, but Boore and Atkinson (2008) predict the lowest values, possibly because their methods do not account for basin amplification at all. Arias intensity, which depends on both shaking intensity and duration, is considered a superior ground motion parameter for predicting landslide triggering (Miles and Keefer, 2000; Jibson, 2007), so we computed it for each cell using the attenuation relationship developed by Travasarou et al. (2003) and then used the regression equation developed by Jibson (2007) that relates Arias intensity to Newmark displacement. The downside to this approach is that the uncertainties are much higher for Arias intensity than for PGA, which explains why the positive error bar is literally off the charts.

The most obvious conclusion from Figure 1-14 is that the methods based on simplified ground motion parameters that are commonly used for seismically induced landslide hazard analyses predict far fewer failed cells than the full time series approach used in this study if just the mean values are used. One possible explanation is that the ground motion prediction

equations are not able to account for 1D site amplification, basin amplification, and directivity as completely as we can with our synthetic seismograms that are specifically tailored to the city of Seattle. But the error bars, compounded from uncertainties in the attenuation relations used to predict the ground motion parameters and in the regression equations used to predict Newmark displacement, exceed the number of failures calculated for the final results of our most detailed seismically induced landslide simulation. This shows that approximating landsliding hazard using ground motion prediction equations and regression equations can be useful and is certainly simpler and less time consuming, but the uncertainties are huge and must be taken into account. Using just the mean values can severely underestimate the extent of landsliding.

Finally, to test whether the most time consuming part of generating the synthetic seismograms - the long period deterministic portion of the synthetic seismograms - was important or could be neglected; we ran the landslide simulation using only the stochastic portion of the synthetic seismograms (>1 Hz). This removes any directivity pulses, basin surface waves, and other coherent long period pulses. For the synthetics calculated using the 3D velocity model, removing the long periods cut the number of failed cells nearly in half. For the 1D velocity model that does not account for basin amplification, it cut the number of failed cells by about a quarter. While theoretically, the Newmark method depends on the absolute slope-parallel acceleration irrespective of the frequency of ground motion, this finding illustrates that it does have some inherent frequency dependence. Though the long period energy is too low in amplitude to cause much Newmark displacement on its own, when combined with higher frequency energy, final Newmark displacements are significantly increased because the long period motion boosts the higher frequency motion higher above the critical acceleration.

This finding raises questions about the frequency dependence of seismically induced landslide triggering, because if shallow landslide triggering is not sensitive to longer period ground motion, then this simulation could be significantly overpredicting the seismically induced landslide hazard. For example, Jibson *et al.* (2004) suggested that landslides triggered by earthquakes might be most sensitive to frequencies between 1 and 10 Hz based on field observations. On the other hand, laboratory studies have shown that the Newmark sliding block approximation is most valid when the resonant frequency of the landslide is much higher than the ground motion (Wartman *et al*., 2003), which would be the case in this study because these landslides are only a few meters thick and would have resonant frequencies between 20 Hz and 60 Hz, much higher than most of the energy in the seismograms.

Clearly, this is a topic that demands more research. If shallow seismically induced landslides are solely triggered by inertial forces as modeled by the Newmark method, then this study demonstrates that the ground motions used to simulate landsliding must have broadband frequency content in order to capture the full displacement, particularly in areas with potentially strong long-period ground motion, like the sedimentary basin underlying Seattle. However, if shallow landslide triggering is dependent on the frequency content of the ground motion, whether due to site-specific amplifications in pre-weakened slopes (*e.g.*, Allstadt, 2009; Moore *et al.*, 2011), or another mechanism such as the wavelength and coherence of ground motion, then seismically induced landslide studies should only use band-limited ground motions. This could simplify the calculation of synthetic seismograms significantly, but introduces the issue of what frequency cutoff to use and whether the frequency cutoff varies depending on the size or shear wave profile of the potential failure mass. This is not an insignificant decision. In this study, for example: if we highpass filter the seismograms at 1 Hz, the total citywide Newmark

displacement is decreased by 50%. However, if we increase the frequency cutoff to just 2 Hz, it is instead decreased by 80%, hence the selection of a frequency cutoff cannot be chosen arbitrarily because it controls the results. At this point in time, the research on the matter is too feeble to justify using a band-limited version of the synthetic seismograms for this study, so our final results are those generated using the full broadband synthetic seismograms.

12. Conclusions

This study shows that seismically induced landsliding will significantly impact Seattle's residents and its infrastructure when the next large earthquake occurs on the Seattle Fault. The southern half of the city, which is on the hanging wall of the fault, will be particularly hard hit while North Seattle is less exposed with the exception of localized areas primarily along coastal bluffs. Several hundred to thousands of buildings could be affected citywide; many kilometers of roads could be obstructed, including some key transit routes such as Interstate-5 and access roads to West Seattle. If the groundwater table is low and shallow soils dry when the earthquake hits, as simulated by the dry scenario, the total area of landslide sources will be about an order of magnitude smaller than if soils are completely saturated. We found that the geology of Seattle, particularly on the hanging wall of the fault and over the Seattle basin, as well as site amplification in the shallow unconsolidated subsurface, played a dominant role in determining the final pattern of landsliding predicted.

The high impact of landsliding predicted by this simulation for a Seattle Fault earthquake shows that this secondary effect of earthquakes can be a significant contributor to overall earthquake hazard and should be studied on an equal level to other earthquake effects in landslide-prone areas. In this paper we present the results of just one scenario event for Seattle to develop and demonstrate the methodology, but now that the methods are compiled it would be

relatively easy to develop a library of plausible earthquake scenarios and the predicted extent of landsliding triggered by each to better quantify the seismically induced landslide hazard in the Seattle area and to assist emergency managers. An ultimate goal could be to run hundreds of possible scenarios on various faults and for a range of ground saturation levels and use them to develop a probabilistic seismically induced landslide hazard map. Another potential application is to set up the landslide triggering simulation to run automatically after an earthquake occurs to obtain a rapid estimate of affected areas, similar to what was done in Godt *et al.* (2008), using real ground motions from our ever-densifying urban strong ground motion networks such as the dense NetQuakes network recently installed in Seattle. There are other cities nationwide and worldwide threatened by seismically induced landsliding that could also benefit from such an approach.

However, in order to make such results more accurate and refined, we have identified some areas that require further research. First, in order to better quantify uncertainties, we need to develop a more robust relation between Newmark displacement and the probability that the slope will fail and the extent of that failure (*e.g.* cracking vs. complete detachment). The relation we use in this study (Jibson *et al,* 2000), the only of its kind thus far, is based on just one seismically induced landslide inventory. However, more complete post-earthquake landslide inventories are now available from more recent earthquakes and this relation should be improved for wider application. Second, there are currently no scientifically justifiable methods to estimate runout from seismically induced landslides. Existing empirical runout estimation methods are based on datasets from water-induced landsliding, whereas landslides triggered by earthquakes can be significantly drier and thus may have shorter runout lengths. Since runout is often what causes the most damage because it covers more area and can reach less steep areas downslope

that are more likely to be developed, we need to develop methods to estimate runout and its uncertainties for seismically induced landslides beyond the simple potential runout buffer-zone approach we used in this study. Finally, we found that the combination of high- and low-frequency ground motions together results in much higher Newmark displacements and thus more slope failures than using the higher frequency ground motions alone. However, there has been little research on the frequency dependence of shallow seismically triggered landslides and it is not well understood. Some suggest that these shallow landslides are not sensitive to longer-period motions, which would have important implications in the accuracy of assessing seismically induced landslide hazard in areas like Seattle where high long-period ground motions are expected. The frequency dependence of seismically induced landslide triggering requires further investigation.

In conclusion, in-depth scenario studies using broadband synthetic seismograms such as this one are becoming more practical with ever faster computing power, the increasing availability of detailed geologic and geotechnical GIS databases, evolving understanding of earthquake and landslide hazard, and improving methods. This type of study that integrates methods and data across disciplines to obtain a tangible final result serves as a good complement to the more thorough, but less intuitive, probabilistic hazard maps and can help us more effectively prepare for future earthquakes.

13. Data and Resources

Ed Harp and John Michael of the U.S. Geological Survey provided GIS files for the factor of safety maps developed for the Harp *et al.* (2006) study that we used. Andy Delorey provided us with the 3D velocity model of Seattle from Delorey and Vidale (2011). Ground motion recordings from the 2001 Nisqually earthquake were provided by the Pacific Northwest

Seismic Network and the USGS Seattle urban seismic array. Strong motion records from PNSN stations are available via the Nisqually Earthquake Information Clearinghouse at http://www.ce.washington.edu/~nisqually/seis/observations.html# last accessed May 2013, and data from the USGS array are available from ftp://ftpext.usgs.gov/pub/cr/co/golden/hazards/Carver/Seattle/ last accessed May 2013. The City of Seattle GIS files used to calculate intersections between landslides and infrastructure were accessed from the Washington State Geospatial Data Archive available through the University of Washington library and from the publicly available Data.Seattle.Gov website (last accessed October 2012). Public domain LIDAR GIS files were obtained through the Puget Sound LIDAR consortium. Software packages used for this study include MATLAB from MathWorks, ProShake from EduPro Civil Systems, Inc., ArcGIS from ESRI. We also used MATLAB codes developed by the Baker Research Group at Stanford to compute the ground motions required using Next Generation Attenuation (NGA) relations, these codes were accessed at http://www.stanford.edu/~bakerjw/attenuation.html in July 2012.

14. Acknowledgements

Research supported by the U.S. Geological Survey (USGS) under USGS award number G11AP20012. Randy Jibson and Ed Harp reviewed the manuscript. We thank the associate editor of the Bulletin of the Seismological Society of America and anonymous reviewers for their helpful comments. In addition, many thanks to Randy Jibson, Steve Kramer, Ed Harp, Andy Delorey, Kathy Troost, John Michael, Tim Walsh, Isabelle Sarikhan, and the City of Seattle, for sharing data, ideas, and advice.

15. References

Allstadt, K., and J. E. Vidale (2012). Seismically Induced Landsliding in Seattle: A Magnitude 7 Seattle Fault Earthquake Scenario, Final Technical Report, USGS under the National Earthquake Hazards Reduction program - grant G11AP20012, 46p. earthquake.usgs.gov/research/external/reports/G11AP20012.pdf last accessed May 2013

Allstadt, K. (2009). Study of Site Effects in Landslides using Weak Ground Motion, Avignonet and Séchilienne Landslides, French Alps, M.S. Thesis, Université Joseph Fourier and ROSE School. 87p.

Abrahamson, N., and W. Silva (2008). Summary of the Abrahamson & Silva NGA Ground-Motion Relations, Earthquake Spectra 24 67-97.

Ambraseys, N. N., and J. M. Menu (1988). Earthquake-induced ground displacements, Earthquake Eng. Struct. Dynam. 16 (7) 985-1006.

Baum, R. L., J. A. Coe, J. W. Godt, E. L. Harp, M. E. Reid, W. Z. Savage, W. H. Schulz, D. L. Brien, A. F. Chleborad, J. P. McKenna, and J. A. Michael (2005). Regional landslide-hazard assessment for Seattle, Washington, USA, Landslides 2 266-279.

Blake, T.F., Hollingsworth, R.A. and Stewart, J.P. (2002). Recommended procedures for implementation of DMG special publication 117 Guidelines for analyzing and mitigating landslide hazards in California. Southern California Earthquake Center, Los Angeles, CA. 127 p.

Blakely, R. J., R. E. Wells, C. S. Weaver, and S. Y. Johnson (2002). Location, structure, and seismicity of the Seattle fault zone, Washington: evidence from aeromagnetic anomalies, geologic mapping, and seismic-reflection data, Bull. Geol. Soc. Am. 114 169-177.

Boore, D. M. (1983) Stochastic simulation of high-frequency ground motions based on seismological models of the radiated spectra, Bull. Seism. Soc. Am. 73 1865-1894.

Boore, D. M. (1996) SMSIM-Fortran programs for simulating ground motions from earthquakes: version 1.0, USGS Open-File Rept. 96-80-A, 73p.

Boore, D. M., and G. M. Atkinson (2008). Ground-Motion Prediction Equations for the Average Horizontal Component of PGA, PGV and 5%-damped PSA at Spectral Periods between 0.01 s and 10.0 s., Earthquake Spectra 24 99–138.

Borcherdt, R. D. (1994). Estimates of Site-Dependent Response Spectra for Design (Methodology and Justification), Earthquake Spectra 10 617-653.

Bucknam, R. C., E. Hemphill-Haley, and E. B. Leopold (1992). Abrupt Uplift Within the Past 1700 Years at Southern Puget Sound, Washington, Science 258 1611-1614.

Bray, J.D. and E. M. Rathje (1998). Earthquake-induced displacements of solid-waste landfills, J. Geotechn. Geoenviron. Eng. 124 242–253.

Campbell, K. W., and Y. Borzorgnia (2008). NGA Ground Motion Model for the Geometric Mean Horizontal Component of PGA, PGV, PGD and 5% Damped Linear Elastic Response Spectra for Periods Ranging from 0.01 to 10 s, Earthquake Spectra 24 139-171.

Castellaro, S., F. Mulargia, and P. L. Rossi (2008). Vs30: Proxy for Seismic Amplification? Seism. Res. Lett. 79 540-543.

Chiou, B. S.-J., and R. R. Youngs (2008). An NGA Model for the Average Horizontal Component of Peak Ground Motion and Response Spectra, Earthquake Spectra 24 173-215.

Chleborad, A. F. and R. L. Schuster (1998). Ground failure associated with the Puget Sound region earthquakes of April 13, 1949, and April 29, 1965, USGS Open-File Report 90-687, 136p.

Choi, Y. and J. P. Stewart (2005). Nonlinear Site Amplification as Function of 30m Shear Wave Velocity, Earthquake Spectra 21 1-30.

Coe, J. A., J. A. Michael, R. A. Crovelli, W. Z. Savage, W. T. Laprade, and W. D. Nashem (2004). Probabilistic assessment of precipitation-triggered landslides using historical records of landslide occurrence, Seattle, Washington, Environ. Eng. Geosci. 10 103-122.

Delorey, A. A. and J. E. Vidale (2011). Basin Shear-Wave Velocities beneath Seattle, Washington, from Noise-Correlation Rayleigh Waves, Bull. Seism. Soc. Am. 101 2162-2175.

Frankel, A. D., D. L. Carver, and R. A. Williams (2002). Nonlinear and Linear Site Response and Basin Effects in Seattle for the M6.8 Nisqually, Washington, Earthquake, Bull. Seism. Soc. Am. 92 2090-2109.

Frankel, A. D., W. J. Stephenson, D. L. Carver, R. A. Williams, J. K. Odum, and S. Rhea (2007). Seismic hazard maps for Seattle, Washington, incorporating 3D sedimentary basin effects, nonlinear site response, and rupture directivity, USGS Open-File Report 07-1175, 77 p., 3 pls.

Frankel, A. D. (2009). A Constant Stress-Drop Model for Producing Broadband Synthetic Seismograms: Comparison with the Next Generation Attenuation Relations, Bull. Seism. Soc. Am. 99 664-680.

Godt, J. W., B. Sener, K. L. Verdin, D. J. Wald, P. S. Earle, E. L. Harp, and R. J. Jibson (2008). Rapid Assessment of Earthquake-induced Landsliding, Proceedings of the First World Landslide Forum, United Nations University, Tokyo, Japan, 4 p.

Goodman, R.E., and H. B. Seed (1966). Earthquake-induced displacements in sand embankments, J Soil Mech. Found. Div. 92, 125-146.

Harp, E. L., and R. W. Jibson (1996). Landslides Triggered by the 1994 Northridge, California, Earthquake. Bull. Seism. Soc. Am., 86, S319-S332.

Harp, E. L., J. A. Michael, and W. T. Laprade (2006). Shallow-Landslide Hazard Map of Seattle, Washington, USGS Open-File Report 2006-1139, 18 p., 2 pl.

Hartzell, S., D. Carver, E. Cranswick, and A. D. Frankel (2000). Variability of Site Response in Seattle, Washington, Bull. Seism. Soc. Am. 90 1237-1250.

Highland, L. M. (2003). An Account of Preliminary Landslide Damage and Losses Resulting from the February 28, 2001, Nisqually, Washington, Earthquake, USGS Open-File Report 03-211, 48p.

Hopper, M. G. (1981). A study of liquefaction and other types of earthquake-induced ground failures in the Puget Sound, Washington, region, Virginia Polytechnic and State University M.S. thesis, 131 p.

Huang, R. and X. Fan (2013). The landslide story, Nat. Geosci., 6 325-326.

Hung, J.-J. (2000). Chi-chi Earthquake Induced Landslides in Taiwan, Earthquake Eng. and Eng. Seismol. 2 25-33.

Hunter, G. and R. Fell (2003). Travel distance angle for “rapid” landslides in constructed and natural slopes, Can. Geotech. J. 40 1123-1141.

Jacoby, G. C., P. L. Williams, and B. M. Buckley (1992). Tree Ring Correlation Between Prehistoric Landslides and Abrupt Tectonic Events in Seattle, Washington, Science 258 1621-1623.

Jibson, R. W., E. L. Harp, and J. A. Michael (1998). A Method for Producing Digital Probabilistic Seismic Landslide Hazard Maps: An Example From the Los Angeles, California, Area, USGS Open-File Report 98-113, 17 p.

Jibson, R. W., E. L. Harp, and J. A. Michael (2000). A method for producing digital probabilistic seismic landslide hazard maps, Eng. Geol. 58 271-289.

Jibson, R. W., E. L. Harp, W. Schulz, and D. K. Keefer (2004). Landslides Triggered by the 2002 Denali Fault, Alaska, Earthquake and the Inferred Nature of the Strong Shaking, Earthquake Spectra 20 669–691.

Jibson, R. W. (2007). Regression models for estimating coseismic displacement, Eng. Geol. 91 209-218.

Jibson, R. W., and J. A. Michael (2009). Maps Showing Seismic Landslide Hazards in Anchorage, Alaska, Pamphlet to accompany USGS Scientific Investigations Map 3077.

Jibson, R. W. (2011). Methods for assessing the stability of slopes during earthquakes – A retrospective, Eng. Geol. 122 43-50.

Johnson, S. Y., S. V. Dadisman, J. R. Childs, and W. D. Stanley (1999). Active tectonics of the Seattle fault and central Puget Sound, Washington – Implications for earthquake hazards, Bull. Geol. Soc. Am. 111 1042-1053.

Karlin, R. E., and S. E. B. Abella (1992). Paleoearthquakes in the Puget Sound Region Recorded in Sediments from Lake Washington, USA, Science 258 1617-1620.

Karlin, R. E., M. Holmes, S. E. B. Abella, and R. Sylvester (2004). Holocene landslides and a 3500-year record of Pacific Northwest earthquakes from sediments in Lake Washington, Bull. Geol. Soc. Am. 116 94-108.

Keefer, D. K. (1983). Landslides, soil liquefaction, and related ground failures in Puget Sound earthquakes, in Proceedings of Workshop XIV, Earthquake hazards of the Puget Sound region, Washington, October 13–15, 1980, Lake Wilderness, Wash. J.C. Yount and R. S. Crosson (editors), USGS Open-File Report 83–19, p. 280–299.

Keefer, D. K. (1984). Landslides caused by earthquakes, Bull. Geol. Soc. Am. 95 406-421.

Keefer, D. K. (2000). Statistical analysis of an earthquake-induced landslide distribution – the 1989 Loma Preita, California event, Eng. Geol. 58, 231-249.

Keefer, D. K. (2002). Investigating Landslides Caused by Earthquakes – A Historical Review, Surv. Geophys. 23 473-510.

Kramer, S. L. (1996). Geotechnical Earthquake Engineering, Prentice Hall, Upper Saddle River, NJ. 653 pp.

Laprade, W. T., T. E. Kirkland, W. D. Nashem, and C. A. Robertson (2000). Seattle landslide study, Shannon and Wilson, Inc. Internal Report W-7992-01, 83 p.

Lee, K. L. (1974). Seismic permanent deformations in earth dams, School of Engineering and Applied Science, Univ. California at Los Angeles, Report No. UCLA-ENG-7497, 31 p.

Lee, S. and D. G. Evangelista (2006). Earthquake-induced landslide-susceptibility mapping using an artificial neural network, Nat. Hazards Earth Syst. Sci. 6, 687-695.

Liu, P. C., and R. J. Archuleta (2002). The effect of a low-velocity surface layer on simulated ground motion, Seismol. Res. Lett. 73 267.

Ludwin, R. S., C. P. Thrush, K. James, D. Buerge, C. Jonientz-Trisler, J. Rasmussen, K. Troost, and A. de los Angeles (2005). Serpent Spirit-power Stories along the Seattle Fault, Seismol. Res. Lett. 76 426-431.

Makdisi, F. I., and H. B. Seed (1978). Simplified procedure for estimating dam and embankment earthquake-induced deformations, J. Geotech. Eng. Div. ASCE. 104 849-867.

Mai, P. M., and G. C. Beroza (2002). A spatial random field model to characterize complexity in earthquake slip, J. Geophy. Res.107 No.B11, 2308.

McCalpin, J.P. (1997). An improved procedure for mapping earthquake-induced landslide potential using a geographic information system, with applications to the Puget Sound region, Final Technical Report, USGS under the National Earthquake Hazards Reduction program - grant 1434-95-G-2550, 53p.

Miles, S. B., and C. L. Ho (1999). Rigorous landslide hazard zonation using Newmark's method and stochastic ground motion simulation, Soil Dynam. Earthquake Eng. 18 305-323.

Miles, S. B., and D. K. Keefer (2000). Evaluation of Seismic Slope-Performance Models Using a Regional Case Study, Environ. Eng. Geosci. VI (1) 25-39.

Montgomery, D. R., H. M. Greenberg, W. T. Laprade, and W. D. Nashem (2001). Sliding in Seattle: test of a model of shallow landsliding potential in an urban environment, in Land use and watersheds: Human influence on hydrology and geomorphology in urban and forest areas: Water Science and Application. M. S. Wigmosta and S. J. Burges (editors) American Geophysical Union, Washington, D.C., p59-73.

Moore, J. R., V. Gischig, J. Burjanek, S. Loew, and D. Fah (2011). Site Effects in Unstable Rock Slopes: Dynamic Behavior of the Randa Instability (Switzerland), Bull. Seism. Soc. Am. 101 3110-3116.

Nelson, A. R., S. Y. Johnson, H. M. Kelsey, R. E. Wells, B. L. Sherrod, S. K. Pezzopane, L-A. Bradley, R. D. Koehler III, and R. C. Bucknam (2003). Late Holocene earthquakes on the Toe Jam Hill fault, Seattle fault zone, Bainbridge Island, Washington, Bull. Geol. Soc. Am. 115 1388-1403.

Newmark, N. M. (1965). Effects of earthquakes on dams and embankments, Geotechnique 15 139-160.

Noson, L. L., A. I. Qamar, and G. W. Thorsen (1988). Washington State earthquake hazards: Washington Division of Geology and Earth Resources Information Circular 85, 77 p.

Palmer, S.P., S. L. Magsino, E. L. Bilderback, J. L. Poelstra, D. S. Folger, and R. A. Niggemann (2004). Liquefaction Susceptibility and Site Class Maps of Washington State, By County. Washington Department of Natural Resources Open file report 2004-20, 45 p.

Peng, W-F., C-L. Wang, S-T. Chen, and S-T. Lee (2009). A seismic landslide hazard analysis with topographic effect, a case study in the 99 Peaks region, Central Taiwan, Environ. Geol. 57 537-549.

Pratt, T. L., S. Johnson, C. Potter, W. Stephenson, and C. Finn (1997). Seismic reflection images beneath Puget Sound, western Washington State: The Puget Lowland thrust sheet hypothesis, J. Geophys. Res. 102 27,469-27,489.

Pratt, T. L., T. M. Brocher, C. S. Weaver, K. C. Creager, C. M. Snelson, R. S. Crosson, K. C. Miller, and A. M. Trehu (2003). Amplification of Seismic Waves by the Seattle Basin, Washington State, Bull. Seis. Soc. Am. 93 533-545.

Pratt, T. L., and T. M. Brocher (2006). Site Response and Attenuation in the Puget Lowland, Washington State, Bull. Seis. Soc. Am. 96 536-552.

Prevost, J.H. (1981). DYNAFLOW: a nonlinear transient finite element analysis program, Department of Civil Engineering, Princeton University, Princeton, NJ.

Rathje, E.M., and J. D. Bray (2000). Nonlinear coupled seismic sliding analysis of earth structures, J. Geotech. Geoenviron. Eng. 126 1002–1014.

Rathje, E. M. and Saygili, G. (2009). Probabilistic assessment of earthquake-induced sliding displacements of natural slopes, Bull. N.Z. Soc. Earthquake Eng. 42 18-27.

Salciarini, D., J. W. Godt, W. Z. Savage, R. L. Baum and P. Conversini (2008). Modeling landslide recurrence in Seattle, Washington, USA, Eng. Geol. 102 227-237.

Savage, W. Z., M. M. Morrissey, and R. L. Baum (2000). Geotechnical Properties for Landslide-Prone Seattle-Area Glacial Deposits, USGS Open file report 00-228, 5p.

Saygili, G. and E. M. Rathje (2009). Probabilistically based seismic landslide hazard maps: An application in Southern California, Eng. Geol. 109 183-194.

Schuster, R. L., R. L. Logan, and P. T. Pringle (1992). Prehistoric Rock Avalanches in the Olympic Mountains, Washington, Science 258 1620-1621.

Seed, H. B., K. L. Lee, I. M. Idriss and R. Makdisi (1973). Analysis of the slides in the San Fernando dams during the earthquake of Feb. 9, 1971. Earthquake Engineering Research Center, University of California, Berkeley, Report No. EERC 73-2, 150 pp.

Shahi, S. K., and J. W. Baker (2011). An Empirically Calibrated Framework for Including the Effects of Near-Fault Directivity in Probabilistic Seismic Hazard Analysis, Bull. Seis. Soc. Am. 101 742-755.

Snelson, C. M., T. M. Brocher, K. C. Miller, T. L. Pratt, and A. M. Trehu (2007). Seismic Amplification within the Seattle Basin, Washington State: Insights from SHIPS Seismic Tomography Experiments, Bull. Seis. Soc. Am. 97 1432-1448.

Stein, S., and M. Wysession (2003). An Introduction to Seismology, Earthquakes, and Earth Structure, Blackwell Publishing, Malden, MA.

Stewart, M. (Editor) (2005). Scenario for a Magnitude 6.7 Earthquake on the Seattle Fault: Earthquake Engineering Research Institute and Washington Military Department Emergency Management Division.

Tang, C., J. Zhu, X. Qi and J. Ding (2011). Landslides induced by the Wenchuan earthquake and the subsequent strong rainfall event: A case study in the Beichuan area of China, Eng. Geol. 122 22-33.

ten Brink, U. S., J. Song, and R. C. Bucknam (2006). Rupture models for the A.D. 900-930 Seattle fault earthquake from uplifted shorelines, Geology 34 585-588.

Thorson, R. M. (1996). Earthquake recurrence and glacial loading in western Washington, Bull. Geol. Soc. Am. 108 1182–1191.

Travasarou, T., J. D. Bray, and N. A. Abrahamson (2003). Empirical attenuation relationship for Arias Intensity, Earthquake Eng. Struct. Dyn. 32 1133-1155.

Troost, K. G., D. B. Booth, A. P. Wisher, and S. A. Shimel (2005). The geologic map of Seattle - a progress report, USGS Open-File Report 2005-1252, plate 1.

Tubbs, D. W. (1974). Landslides in Seattle, Washington Dept. of Natural Resources division of geology and earth resources information circular no.52.

Wartman, J., J. D. Bray and R. B. Seed (2003). Inclined Plane Studies of the Newmark Sliding Block Procedure, J. of Geotech. Geoenviron. Eng. 129 673-684.

Wasowski, J., D. K. Keefer, and R. W. Jibson (2000). Preface to Special Issue from the Symposium on Landslide Hazards in Seismically Active Regions, Eng. Geol. 58 v-vi.

Wells, D. L., and Coppersmith, K. J. (1994). New Empirical Relationships among Magnitude, Rupture Length, Rupture Width, Rupture Area, and Surface displacement, Bull. Seis. Soc. Am. 84 974–1002.

Williams, R. A., W. J. Stephenson, A. D. Frankel, and J. K. Odum (1999). Surface Seismic Measurements of Near-Surface P- and S-wave Seismic Velocities at Earthquake Recording Stations, Seattle, Washington, Earthquake Spectra 15 565-584.

Wilson, R. C. and D. K. Keefer (1983) Dynamic analysis of a slope failure from the 6 August 1979 Coyote Lake, California earthquake, Bull. Seism. Soc. Am. 73 863-877.

Wong, I., K. H. Stokoe II, B. R. Cox, Y-C. Lin, and F-Y. Menq (2010). Geotechnical Characterization and Evaluation of Site Amplification at Selected PNSN Strong Motion Sites, Seattle, Washington, Final Technical Report submitted to USGS under the National Earthquake Hazards Reduction Program. 38p.

Yin, Y., F.Wang and P. Sun (2009). Landslide hazards triggered by the 2008 Wenchuan earthquake, Sichuan, China, Landslides 6 139-151.

Chapter 2 – Seismogenic landslides, a new way to study landslide dynamics:

Part a: Extracting Source Characteristics and Dynamics of the August 2010 Mount Meager Landslide from Broadband Seismograms

Part b: The Seismic Story of the Nile Valley Landslide

Chapter 2a: Extracting Source Characteristics and Dynamics of the August 2010 Mount Meager Landslide from Broadband Seismograms

The content of this chapter was published in:

Allstadt, K., 2013, Extracting Source Characteristics and Dynamics of the August 2010 Mount Meager Landslide from Broadband Seismograms, J. Geophys. Res., 118, p.1-19, doi: 10.1002/jgrf.20110

Table of Contents

Summary 2a-4
1. Introduction 2a-5
2. Data 2a-10
2.1 Seismic data 2a-12
3. Methods 2a-17
3.1 Validation 2a-21
4. Results 2a-23
4.1 Rockslide initiation 2a-26
4.2 Debris flow 2a-30
4.3 “Aftershock” 2a-35
5. Discussion 2a-38
5.1 Improvements to landslide characterization 2a-38
5.2 Limitations 2a-44
6. Conclusions 2a-45
7. Acknowledgements 2a-47
8. References 2a-48

Summary

Seismic methods can substantially improve the characterization of the dynamics of large and rapid landslides. Such landslides often generate strong long period seismic waves due to the large-scale acceleration of the entire landslide mass, which, according to theory, can be approximated as a single-force mechanism at long wavelengths. I apply this theory and invert the long period seismic waves generated by the 48.5 Mm^3 August 2010 Mount Meager rockslide-debris flow in British Columbia. Using data from five broadband seismic stations 70 to 276 km from the source, I obtain a time-series of forces the landslide exerted on the earth, with peak forces of 1.0×10^{11} N. The direction and amplitude of the forces can be used to determine the timing and occurrence of events and subevents. Using this result, in combination with other field and geospatial evidence, I calculate an average horizontal acceleration of the rockslide of 0.39 m/s^2 and an average apparent coefficient of basal friction of 0.38±0.02, which suggests elevated basal fluid pressures. The direction and timing of the strongest forces are consistent with the centripetal acceleration of the debris flow around corners in its path. I use this correlation to estimate speeds, which peak at 92 m/s. This study demonstrates that the time-series recording of forces exerted by a large and rapid landslide derived remotely from seismic records can be used to tie post-slide evidence to what actually occurred during the event, and can serve to validate numerical models and theoretical methods.

1. Introduction

Direct time-dependent observations of natural landslides are critical to improving our understanding of landslide dynamics and hazard. However, such observations can be hard to come by due to the destructive nature of landsliding events, uncertainty about when and where they will occur, and their sometimes-remote locations. Seismology is a potential tool to span this observational gap. Assuming the landslide under investigation radiates enough seismic energy to be recorded at existing seismic stations and the seismograms can be correctly interpreted, seismic data can provide a time series recording of landsliding events that can be used to extract information about landslide dynamics and source characteristics. This approach is comparable to how seismologists have been using seismograms to study earthquakes for over a century - but landslide seismology has the added benefits of being able to access the source area and of knowing the driving stress – gravity. When combined with field investigation, theoretical methods, and numerical landslide modeling, a much clearer interpretation of the event being investigated can emerge [e.g. *Favreau et al.,* 2010, *Moretti et al.,* 2012, *Guthrie et al.,* 2012].

In order to correctly interpret seismic signals of landslides, one must first understand how landslides radiate seismic energy. Energy is radiated on two scales: coherent long-period waves at periods of tens to hundreds of seconds generated by the acceleration and deceleration of the failure mass as a whole [*Kanamori and Given,* 1982; *Eissler and Kanamori,* 1987], and a more stochastic higher frequency signal at periods from a few seconds to frequencies of tens of Hz generated by momentum exchanges on smaller scales such as flow over smaller scale topographic features, frictional processes [e.g. *Schneider et al.*, 2010], and impacts of individual blocks [e.g. *Huang et al.,* 2007].

Large and rapid landslides, in particular, are effective at generating strong long period seismic waves, particularly surface waves, which attenuate slowly and can be detected at seismic stations for hundreds to thousands of kilometers. These long period seismic waves are not sensitive to heterogeneities in the crust on much shorter scales than their wavelengths, so they can be studied using simplified earth velocity models and are thus easier to work with than higher frequency seismic energy. The long period seismograms generated by such large landslides are often recorded at great distances and have been used for decades to study landslides.

Some authors have directly interpreted the timing of pulses and variations in amplitude in long-period landslide seismograms to determine the occurrence, duration, speed, and timing of events [*Berrocal et al.,* 1978; *Weichert et al.,* 1994; *McSaveney and Downes*, 2002; *Guthrie et al.,* 2012].

Others have taken analysis further and used the long period seismic waves to study the source process directly. In contrast to the double-couple mechanism of earthquakes, the equivalent force mechanism of a landslide is a single force applied to the surface of the earth proportional to the acceleration and mass of the moving material. This is what generates the long period seismic waves [*Kanamori and Given*, 1982; *Eissler and Kanamori*, 1987; *Hasegawa and Kanamori*, 1987; *Kawakatsu,* 1989; *Fukao,* 1995*; Julian et al.,* 1998]. Many authors have used forward modeling to determine the amplitude and duration of the forces exerted on the earth that could generate the observed seismic waves, and used the result to estimate the mass or the acceleration of the landslide and to interpret the sequence of events [e.g. *Kanamori and Given,* 1982; *LaRocca et al.,* 2004]. These methods have even been used to argue that what was thought to be an earthquake was actually a landslide [e.g. *Eissler and Kanamori,* 1987; *Hasegawa and*

Kanamori, 1987]. Others have used this approach to constrain rheological characteristics. For example, *Brodsky et al.* [2003] estimated the coefficient of friction beneath three large volcanic landslides based on the forces they exerted on the earth. *Favreau et al*. [2010] used long period seismic observations of the 2004 Thurweiser landslide in Italy to determine the rheological parameters to use in a numerical landslide model. *Moretti et al.* [2012] used the long period seismic signals generated by the 2005 Mount Steller landslide in Alaska to invert for the forces it exerted on the earth and used both to constrain details about the flow dynamics in a numerical model. Most recently, *Ekström and Stark* [2013] inverted seismic waves generated by 29 large and rapid landslides recorded by the Global Seismographic Network. They used their catalog of landslide force inversions combined with field data to build empirical relations between maximum forces and mass, momentum, potential energy loss, and surface wave magnitude. These relations allow for rapid order of magnitude estimates of landslide size without having to wait for other evidence.

However, the long period seismic signals generated by the acceleration of the landslide as a whole that can be approximated as a single-force mechanism are not always observed. If the mass is too small and/or the average acceleration of the landslide too slow, the forces the landslide exerts on the earth will be smaller [*Kanamori and Given*, 1982] and less likely to generate a long period signal above the noise level on nearby seismometers. Furthermore, the period of the waves generated depends on the duration of the forcing [*Kanamori and Given*, 1982], so a slow landslide with an extended duration may not emit waves at seismic frequencies. The higher frequency signal generated by smaller scale processes, on the other hand, has been often observed for a wide range of landslide sizes and many authors have used this type of signal to study landslides as well. Often referred to as emergent, cigar-shaped, or spindle-shaped, the

higher frequency seismic energy typically builds up gradually, emerging from the noise without a clear onset or obvious phase arrivals, and then tapers back into the noise afterwards [*e.g. Norris,* 1994; *Dammeier et al.,* 2011; *Deparis et al.,* 2008; *La Rocca et al.,* 2004; *Schneider et al.,* 2010; *Suriñach et al.,* 2005].

Such signals are useful for determining the occurrence, duration, and timing of landslides [*e.g., Norris,* 1994; *Helmstetter and Garambois*, 2010]. It is more challenging to use these signals to obtain quantitative landslide characteristics such as failure volume, fall height, or runout distance because only a small percentage of the energy is transmitted seismically for all landslides [*Berrocal et al.,* 1978*; Deparis et al.,* 2008; *Hibert et al.,* 2011], and higher frequency waves attenuate rapidly and are much more affected by smaller scale heterogeneities in the crust. Despite this, several authors have been successful in estimating landslide characteristics, such as volume and runout length, within an order of magnitude or better, particularly in the presence of dense nearby seismic networks [*Norris*, 1994; *Deparis et al.,* 2008; *Hibert et al.,* 2011; *Helmstetter and Garambois*, 2010; *Dammeier et al.,* 2011]. *Schneider et al.* [2010] investigated the physical basis for variations in amplitude in the higher frequency seismic signal and found that increases in the relative amplitude could be attributed to increases in the loss of power due to frictional processes – the frictional work rate. The frictional work rate can be elevated, for example, after a sudden increase in speed after passing a step in the path, or when the sliding material hits a flatter area at high speeds and begins to decelerate as frictional resistance increases [*Schneider et al.*, 2010]. Thus, the relative amplitude of the high frequency seismic signature can be used to tie the timing of the seismic signal to the passage of material over particular sections of the sliding path.

In this study, I inverted the long period seismic signals generated by the August 2010 Mount Meager rockslide and debris flow in British Columbia to solve for the source process that generated them - the forces the landslide exerted on the earth over time. I built on the initial characterization of the landslide by *Guthrie et al.* [2012] and show that the characterization of the dynamics and source process of the landslide can be substantially improved by these methods. The time-series recording of forces exerted on the earth during the landslide can be used to significantly reduce the level of interpretation required to tie post-slide observations to what actually happened during the event. Though this study is based on the same seismic records *Guthrie et al.* [2012] used as part of their characterization, they used just the raw seismograms of this event to qualitatively interpret the timing of events from peaks in amplitude of the signal. By inverting the seismic signals, I take a much more direct and quantitative approach to obtain information about the source process by determining what forces actually generated the observed seismic waves at the source location. This is comparable to the inversion of seismic signals generated by earthquakes to obtain information about the source history of an earthquake. Just as this type of analysis has advanced our understanding of earthquake physics, such an analysis of the seismic signals generated by landslides can contribute to a greater understanding of the landslide physics.

In the following sections I first detail the known characteristics of the Mount Meager landslide and the seismic data available. Then I describe the inversion methods used, test these methods with synthetic data, and invert the long period (T = 30 to 150 s) seismic signals to determine the forces exerted on the earth by the landslide with time. I compare this result to the envelope of the higher frequency portion of the signal and piece together the sequence and timing of events. I also calculate the speed of the landslide with higher certainty than was

possible using just the raw seismic data. This provides a validation for other less-direct landslide speed estimation methods. I use this result to discern the direction of failure of subevents, extract the coefficient of dynamic friction during the rockslide, and observe changes in the behavior of the debris flow over time - characteristics that are otherwise difficult to determine in the absence of seismic analysis. This case study illustrates the benefits of including a seismic source analysis in landslide investigations and its potential to improve numerical models, an option that is becoming more readily available as seismic networks become denser and high quality digital data more accessible.

2. Data

On 6 August 2010 at about 10:27 UTC, 3:27 a.m. local time, the secondary peak (gendarme) and southern flank of Mount Meager, part of the Mount Meager Volcanic Complex in British Columbia, collapsed in a massive rockslide that quickly mobilized into a debris flow [*Guthrie et al.,* 2012]. A rockslide is a failure of bedrock where sliding occurs dominantly on a single failure surface [*Cruden and Varnes*, 1996], while a debris flow is a poorly sorted, internally disrupted, and saturated flowing mass controlled by both solid and fluid forces [*Iverson et al.,* 1997]. According to the interpretation of the event by *Guthrie et al.* [2012], once the rockslide converted to a debris flow, it traveled down Capricorn Creek valley, turning two corners, sloshing up the sides of the valley and plowing down swathes of trees. When it reached the end of the 7.8 km long valley, the debris flow burst out into the adjacent Meager Creek valley and ran 270 vertical meters up the opposing valley wall. It then split and flowed up and downstream 3.7 and 4.9 km respectively, where it finally stopped, leaving vast fields of deposits and temporarily blocking the Lilloet River and its tributary, Meager Creek. This sequence of events is illustrated on Figure 2a-1. Field evidence showed that some deposition began almost

immediately below the initiation zone, though most material was deposited after the convergence with Meager Creek. Very little material was entrained along the path, though later activity incised into the primary deposits [*Guthrie et al.,* 2012].

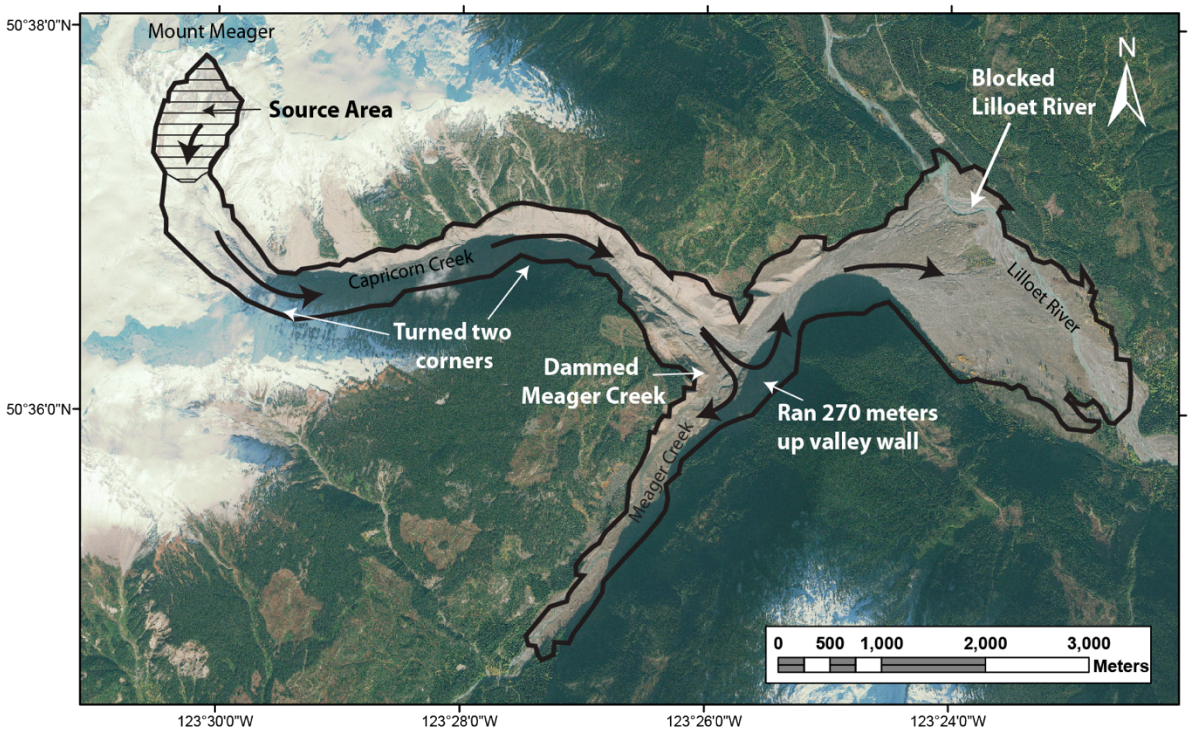

Figure 2a-1 Overview of the sliding path overlain on a post-landslide satellite image with approximate boundaries outlined. Refer to inset map on Figure 2a-3 for regional location of Mount Meager.

The source material was an estimated 48.5 million cubic meters of highly fractured and hydrothermally altered rhyodacite breccias, tuffs, and flows, with a porphrytic dacite plug in the steeper areas [*Guthrie et al.,* 2012]. Additionally, the source mass was highly saturated, evidenced by the rapid mobilization of the rockslide to a debris flow, requiring the availability of a lot of water, as well as surface seepage and large springs observed along the failure surface [*Guthrie et al.,* 2012]. Assuming a density range of 2000-2500 kg/m^3, representative of typical values for these types of rocks, the total mass was 1.0-1.2 x 10^{11} kg.

2.1 Seismic data

This highly energetic event generated strong seismic signals that were visible above the noise level at over 25 three-component broadband seismometers throughout Canada, Washington State, and Alaska. A record section of the seismograms of this event recorded across British Columbia and Washington State by the Canadian National Seismograph Network (CNSN) and the Pacific Northwest Seismic Network (PNSN) (Figure 2a-2) shows that the entire seismic signal lasted about 5 minutes before fading into the noise. The onset of the seismic signal is dominated by long period pulses, which are then overtaken by a more chaotic short-period signal. The two distinct frequency bands, corresponding to the two types of signals radiated by landslides described earlier, are apparent in the spectrum of the signal, and their distinct characters are made more apparent by high- and low-pass filtering the same signal around 0.2 Hz (Figure 2a-3). Note that it is impossible to pick out the P and S wave arrivals separately because the amplitudes of the body waves in the higher frequency signal are below the noise at the start of the event (Figure 2a-3b).

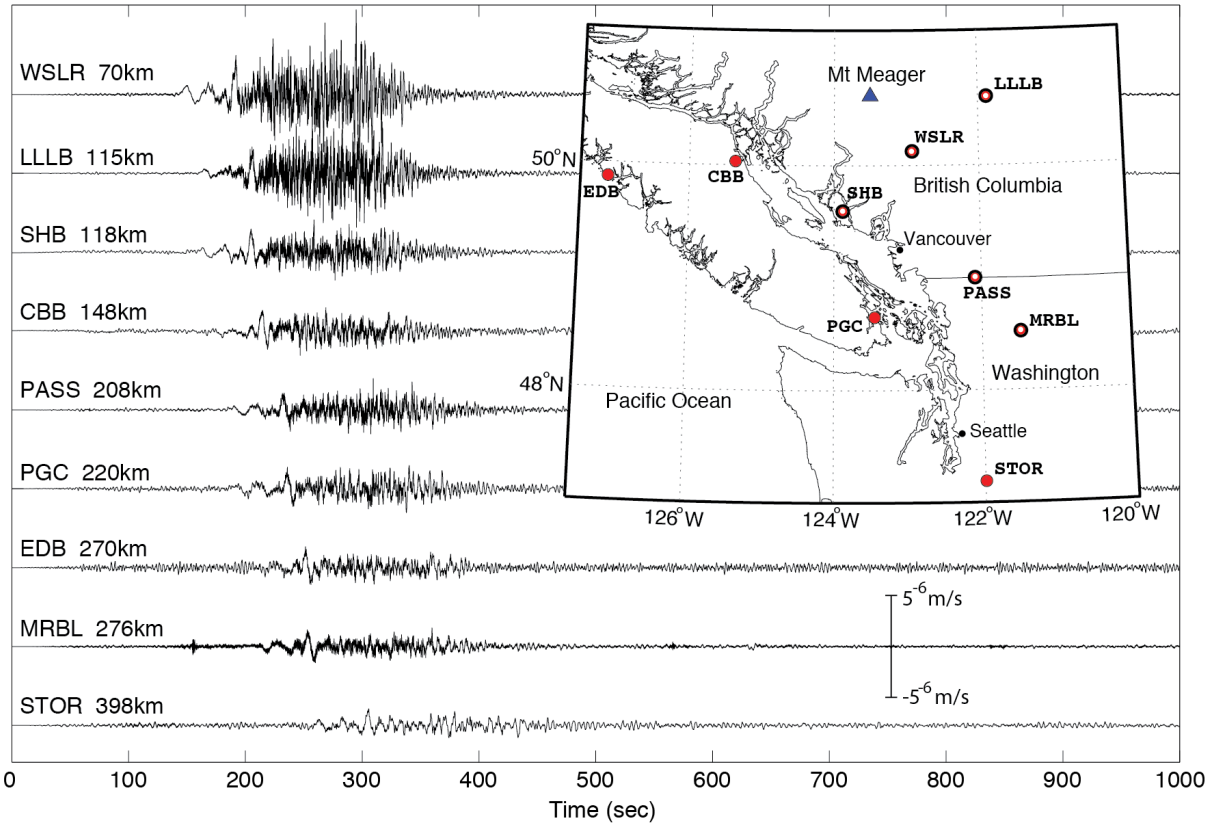

Figure 2a-2 Record section of vertical component broadband velocity seismograms generated by the Mount Meager rockslide and debris flow. Seismograms are corrected for station response and are all plotted on the same vertical scale, which is shown under the inset map. The inset map shows station locations relative to Mount Meager, ring-shaped symbols indicate stations used in the inversion of long period seismograms.

The consistency in the signal between distant stations (Figure 2a-2) demonstrates that both the low and high frequency portions of the signal largely reflect source effects and not path effects or site effects at individual stations. However one interesting difference is that the amplitudes of the higher frequency ground motion are significantly stronger at station LLLB than station SHB, though it is only 3 km further from the source area. This could be due to lower attenuation rates east of the source area, site amplification at the location of LLLB, or both. Another contributing factor could be that the landslide moved towards station LLLB and away from SHB. This change in location would affect the amplitudes of the shorter period waves more

than the longer periods because anelastic attenuation is strongly frequency dependent. Therefore the movement of the source 10% closer to LLLB could result in a noticeable reduction in the attenuation of higher frequency waves over the course of the event. *Suriñach et al*. [2005] observed a similar effect for smaller landslides. In this study, landslide speeds are almost two orders of magnitude slower than the seismic wave velocities, so this is probably not true directivity as observed during earthquakes, which is related to the Doppler effect [*Douglas et al*., 1988].

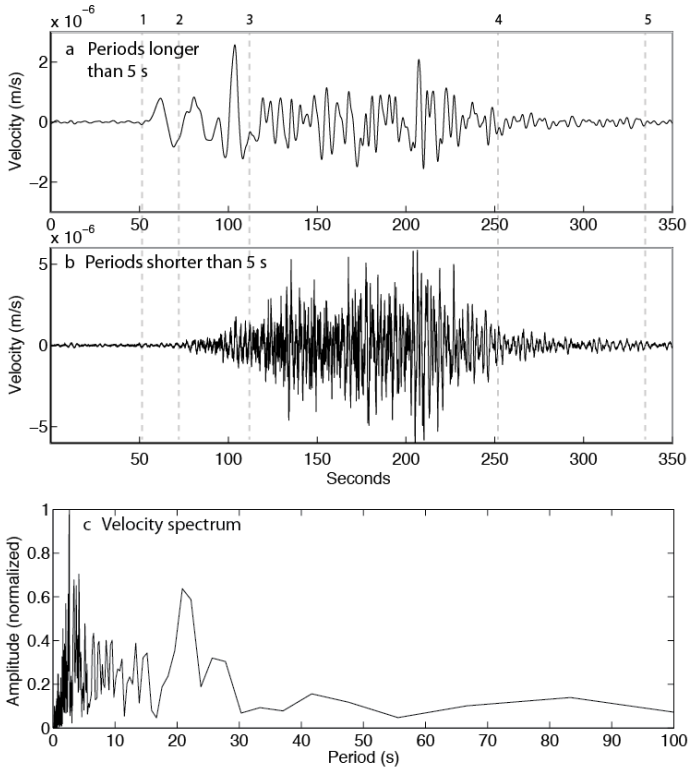

Figure 2a-3 The vertical component velocity seismogram recorded at WSLR a) lowpass filtered below 0.2 Hz to isolate the long period pulses that start first at point 1, and b) highpass filtered above 0.2 Hz to isolate the shorter period signal that emerges from the noise about 20 seconds later at point 2. c) The two distinct frequency bands are apparent as two separate broad peaks on the velocity spectrum of the entire signal. By point 3 the long period signal shifts to shorter periods. By point 4 the seismic signal is largely over but does not fade completely back into the noise until point 5, nearly 5 minutes after the start of the signal.

From the seismic data available, I selected those that had the best signal quality in the frequency band of interest by visual inspection. Five of the seismic stations had significantly better signal quality than the rest. Rather than using more data with questionable signal quality, I used just the data from these five stations because test inversions (detailed in section 3) showed that high quality seismic signals from just a few seismic stations should be more than sufficient to recover the force-time function. The seismic stations used for the inversion are shown in relation to the location of the landslide on the map on Figure 2a-2 and are detailed on Table 2a-1. At least one component of each station had a signal to noise ratio (SNR) above 8 in the frequency band used in the inversion (T=30-150s). The highest SNR was 57. The noise characteristics of each component of each station used are displayed on Table 2a-1.

Table 2a-1 Broadband seismic stations used in the inversion

	Latitude	Longitude	Distance (km)	Source to station azimuth (clockwise from N)
WSLR	50.1265°	-122.9212°	70	142˚
LLLB	50.6090°	-121.8815°	115	90˚
SHB	49.5930°	-123.8805°	118	192˚
PASS	48.9983°	-122.0852°	208	150˚
MRBL	48.5183°	-121.4845°	276	149˚

I prepared the seismic data by deconvolving the instrument response, integrating the seismograms from ground velocity to ground displacement, and rotating the horizontal components to the radial and transverse direction for each station. The radial component refers to motion directly towards or away from the source and transverse is perpendicular to radial. I then bandpass filtered the data between periods of 30 and 150 seconds using a second order minimum-phase (causal) Butterworth bandpass filter. Using shorter period waves in the inversion would require a detailed velocity model of the region because shorter period seismic waves are more sensitive to smaller scale heterogeneities and topography. Periods longer than

150 seconds couldn't be used because such long periods are beyond the fall-off in the response curves of all of the seismic stations and including them amplified the noise at these longer periods and overwhelmed the signal. The data were weighted for the inversion by the inverse of the root mean squared (rms) value of the noise before the signal at the periods used. These weights are reported on Table 2a-2.

Table 2a-2 Noise characteristics and solution misfit at each station

station name	Component*	Signal to noise ratio (amplitude)	% noise	weight (1/rms noise x 100)	rms noise (nm)	rms misfit solution (nm)
WSLR	Z	23	2%	2.5	40	124
	R	4	11%	0.2	530	1002
	T	4	9%	0.3	316	434
LLLB	Z	8	4%	2.0	51	131
	R	7	5%	1.2	86	168
	T	57	2%	4.7	21	66
SHB	Z	8	8%	0.6	157	170
	R	8	18%	0.4	282	657
	T	3	12%	0.5	206	416
PASS	Z	31	6%	1.1	89	105
	R	4	10%	0.9	110	266
	T	7	16%	0.4	239	232
MRBL	Z	23	3%	3.2	32	88
	R	8	26%	0.5	220	306
	T	7	7%	1.1	93	191

*Z, R, T refers to vertical, radial, and transverse components respectively

3. Methods

For a landslide simplified as a block of constant mass m sliding down a slope, the magnitude of the slope parallel force $F_{//}$ comes from the driving force of gravity opposed by the frictional force F_f:

$$F_{//} = mg \sin\theta - F_f \qquad (1)$$

where g is the magnitude of the acceleration due to gravity, θ is the slope angle and bold font indicates a vector quantity. The magnitude of the frictional force on the block is equal to:

$$F_f = \mu' F_n \qquad (2)$$

where μ' is the apparent dynamic coefficient of friction, which accounts for both friction and the basal pore fluid pressures, and F_n is the magnitude of the normal force. The sum of forces in the direction perpendicular to the slope is zero because the landslide does not accelerate into or out of the slope, so the magnitude of the normal force is equal to:

$$F_n = mg \cos\theta \qquad (3)$$

This also means that the magnitude of the net force F_{net} is equal to the magnitude of the slope parallel force $F_{//}$ and equation 1 can be rewritten as:

$$F_{net} = mg (\sin\theta - \mu' \cos\theta) \qquad (4)$$

If the frictional force and gravitational driving force are unbalanced, as they are in the case of a mobilizing landslide, the block will begin to accelerate. According to Newton's second law, the net force acting on an object is equal to its mass times its acceleration, a, so equation 4 becomes:

$$F_{net} = ma = mg (\sin\theta - \mu' \cos\theta) \qquad (5)$$

According to Newton's third law, the forces of two bodies on each other are equal and opposite. Therefore, at the long wavelength limit, as the sliding block feels a force due to its gravitational

acceleration the earth feels an equal point force, $\boldsymbol{F}_e$, in the opposite direction. $\boldsymbol{F}_e$ is a 3-component vector that can be written more explicitly as a time dependent phenomenon:

$$\boldsymbol{F}_e(t) = -m\boldsymbol{a}(t) \qquad (6)$$

where bolding indicates a vector. This is the equivalent force system that is responsible for generating the observed long period energy generated by large rapid landslides [*Kanamori and Given*, 1982; *Eissler and Kanamori*, 1987; *Hasegawa and Kanamori*, 1987; *Kawakatsu,* 1989; *Fukao,* 1995; *Julian et al.,* 1998]. $\boldsymbol{F}_e(t)$ is comparable to the source-time function of an earthquake so I refer to it as the force-time function in this study. Friction and slope angle control the acceleration of the sliding mass (equation 5), which in turn determines the forces exerted on the earth (equation 6). Equation 6 dictates that the force felt by the earth will be in the opposite direction to the landslide acceleration. So as the source mass accelerates downslope, the earth feels a single force applied in the upslope direction. Then, as the mass decelerates (accelerates upslope), the earth feels a single force in the same direction as the sliding mass, *i.e.* downslope. When the landslide banks a curve, the acceleration is towards the center of the curve (centripetal acceleration), and thus the equivalent force points away from the center of the curve. *Julian et al.* [1998] also describes the torque due to lateral displacement of the landslide mass as a potential source of seismic radiation. However *Brodsky et al.* [2003] did not find it to be a significant contributor of seismic waves in their analysis of similarly large and rapid landslides. For this study, the inclusion of torque as a seismic source was not required to fit the data and was not incorporated into the analysis.

In this study, I inverted the seismic data to determine $\boldsymbol{F}_e(t)$. Once obtained, the force-time function can be used with equations 5 and 6 combined with the field evidence, imagery, and geospatial calculations compiled by *Guthrie et al.* [2012] to extract information about the source

characteristics and dynamics of the landslide. However, there are a few caveats to using equations 5 and 6 directly for interpretation: the rigid block model of a landslide is of course a simplification of reality and these equations do not account for all spatio-temporal dependencies. First, the area of application of the force will migrate with the landslide mass and will change in total area over time. In spite of this, the landslide can still be treated as a stationary single force point source for long period (and thus long wavelength) seismic waves even though, in this case, the sliding mass moved more than 12 km. This is because the shift in arrival times between waves generated at the start and the end of the sliding path would be less than 2 seconds at all stations for the slowest waves in the frequency band used: Rayleigh waves of a 30 second period. Two seconds is a negligible fraction of the wavelength. The difference in arrival times would be even smaller for the faster longer period waves.

Secondly, the mass may vary with time. Mass may be added due to erosion and entrainment and removed due to deposition. Significant changes in mass over time are important for inferring acceleration from force (equation 6) and must be taken into account in the interpretation. Further, the failure mass spreads out in space and becomes internally disturbed and agitated when it transforms from a rockslide to a debris flow. To be a pure single force, the dislocation of the sliding mass needs to be spatially uniform; otherwise higher order force components can contribute seismic radiation [*Fukao,* 1995]. The complexities of debris flow motion and its elongation over its sliding path can hinder the straightforward interpretation of the force-time function. This is particularly true in the case of Mount Meager where there are several sharp bends in the sliding path and segments of the debris flow may be accelerating in different directions simultaneously resulting in opposing forces.

In order to invert the seismograms to obtain $F_e(t)$, I first set up the forward problem relating how the source process translates to the observed seismograms. The seismogram recorded at each station (after the station response has been removed) represents the effects of the source itself as well as its path through the earth. To a good approximation, at long periods the earth is a linear system that can be characterized by the seismogram that would be recorded at the seismometer location from an impulse force applied at the source location. The set of impulse responses between each source and station pair are known as the Green's functions and they account for all types of seismic waves as well as attenuation along the wave path. The seismograms for a realistic source can then be obtained by convolving the Green's functions with a source-time function that describes the evolution of the source process over time [*e.g Stein and Wysession*, 2003]. In the case of a landslide, this is the force-time function $\boldsymbol{F}_e(t)$.

Green's functions can be calculated if the velocity structure of the material the seismic waves are passing through is known. The periods used in this study (T = 30 – 150 s) have wavelengths on the order of hundreds of kilometers and a low sensitivity to smaller scale heterogeneities in the regional velocity structure or topography. For this reason, a generalized earth model was sufficient to use in the calculation of the Green's functions. In this study I used the 1D ak135Q earth velocity and anelastic attenuation model [*Kennett et al*., 1995]. I calculated the Green's functions between each station and the landslide location using the wavenumber integration method [*Bouchon,* 1981] as implemented in Computer Programs in Seismology (CPS) [*Hermann*, 2002]. Only the source to station distance and the velocity and anelastic attenuation model were required for this step of the calculation. The radiation patterns of the seismic waves were accounted for in the inversion equations based on the source to station azimuth as explained in the Appendix. The source to station distance did not change over time in

the inversion because the location of the single force applied to the earth by the landslide is assumed to be a stationary point source for reasons explained earlier in this section. Once the forward problem was set up, I inverted for the force-time function using damped least squares [*e.g. Aster et al.,* 2005]. Complete details of the inversion process are located in the Appendix.

3.1 Validation

To validate the robustness of this inversion method, I first tested it with synthetic data to see if it was capable of recovering an input force-time function and to test the noise tolerance. I started by using the forward model (equation A1) to generate three-component synthetic seismograms for an arbitrary force-time function. I then progressively increased the noise in the synthetic seismograms by adding Gaussian noise with a standard deviation equal to a percentage of the maximum absolute peak of the noise-free synthetic data (Figure 2a-4). I then used these data to invert for the force-time function using the process described in the Appendix to see how well it returned the original signal after the addition of noise. The results of this inversion for a range of noise levels first using a single three-component station (WSLR) and then three three-component stations (WSLR, LLLB, SHB) are shown on Figure 2a-5 and 2a-6 respectively.

The success of the inversion in retrieving the input test signal confirms that a force-time function very close to the original can be retrieved using data from just a few high quality three-component stations if the noise levels are low and random. Even with just one three-component station and a significant amount of noise, this inversion method recovered a force-time function close to the actual input model. The ability of the inversion to recover the signal starts to break down when noise levels reach 30 - 40%, but the noise levels for the real seismic signals of the landslide in the time immediately before the earthquake were mostly below 10% (Table 2a-2).

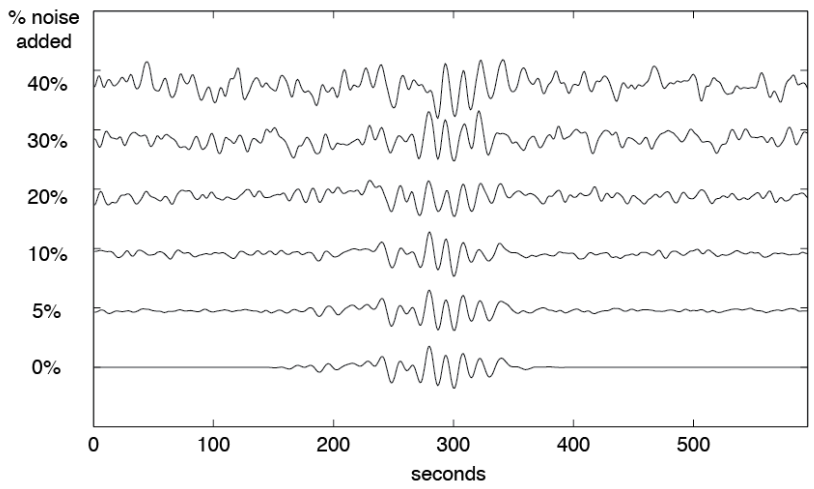

Figure 2a-4 The vertical component of one station (WSLR) of the synthetic seismograms generated for an arbitrary force-time function with 0 to 40% Gaussian noise added to illustrate the range in signal quality used in the test inversions.

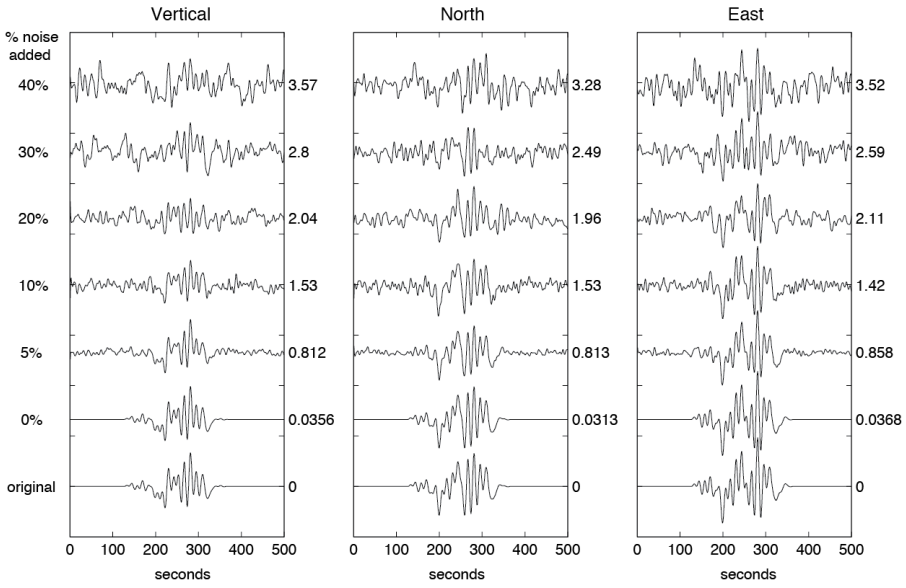

Figure 2a-5 The three-component force-time function recovered by the test inversion of synthetic seismograms for a single three-component station (WSLR) with 0 to 40% noise added. The original force-time function that was used to generate the synthetic seismograms (bottom line) is shown for comparison. All force-time functions are scaled identically. The relative root mean squared errors (in arbitrary units) between the force-time functions obtained by the inversions and the original are indicated at the right of each signal.

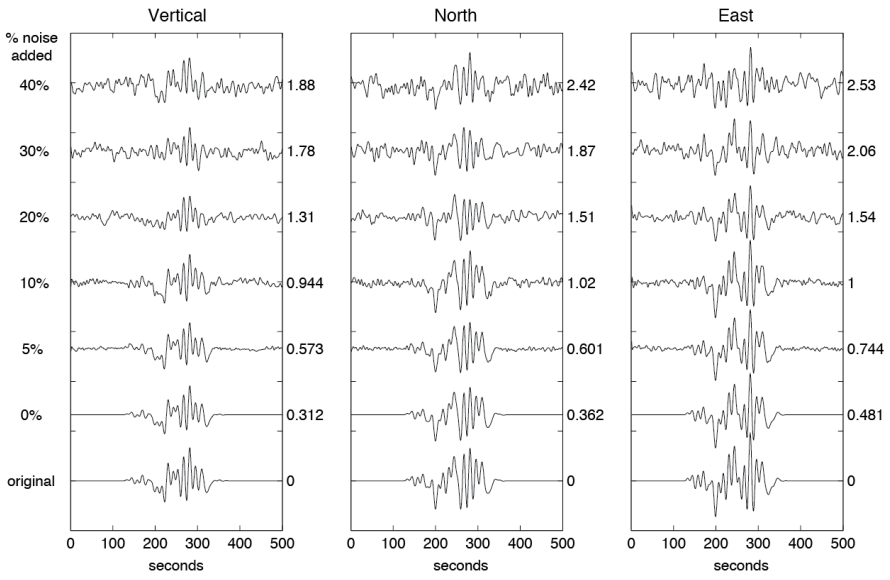

Figure 2a-6 Same as Figure 2a-5 but for the inversion of synthetic data for three three-component seismic stations (WSLR, LLLB, SHB) with varying amounts of noise added to the signal.

4. Results

Using the methods described above and in the Appendix, I inverted the seismic data to solve for the force-time function of the Mount Meager landslide. The result is shown in Figure 2a-7 A-C. This is compared to the raw seismogram from the closest station (Figure 2a-7D) and the azimuth of the force vector at each point in time (Figure 2a-7E). To quantify the fit of the resulting force-time function, I generated synthetic seismograms from the inversion solution by plugging the force-time function back into the forward model. The synthetic seismograms fit the real data remarkably well (Figure 2a-8) with a variance reduction of 80%. The model can even closely reproduce data that was not used in the inversion (EDB, bottom of Figure 2a-8). The worst misfits were for the stations and components that had strong long period noise in the signal, so it was encouraging that the solution did not fit that noise when it was present before and after the landslide signal. The root mean squared (rms) errors between the original and synthetic

seismograms are comparable to the rms of the noise prior to the signal (Table 2a-2), though the rms errors are nearly all higher than the rms of the noise. This is because the forward model is approximate, I am fitting 15 channels of noisy data simultaneously, and the noise may not be entirely random as it was in the test inversions.

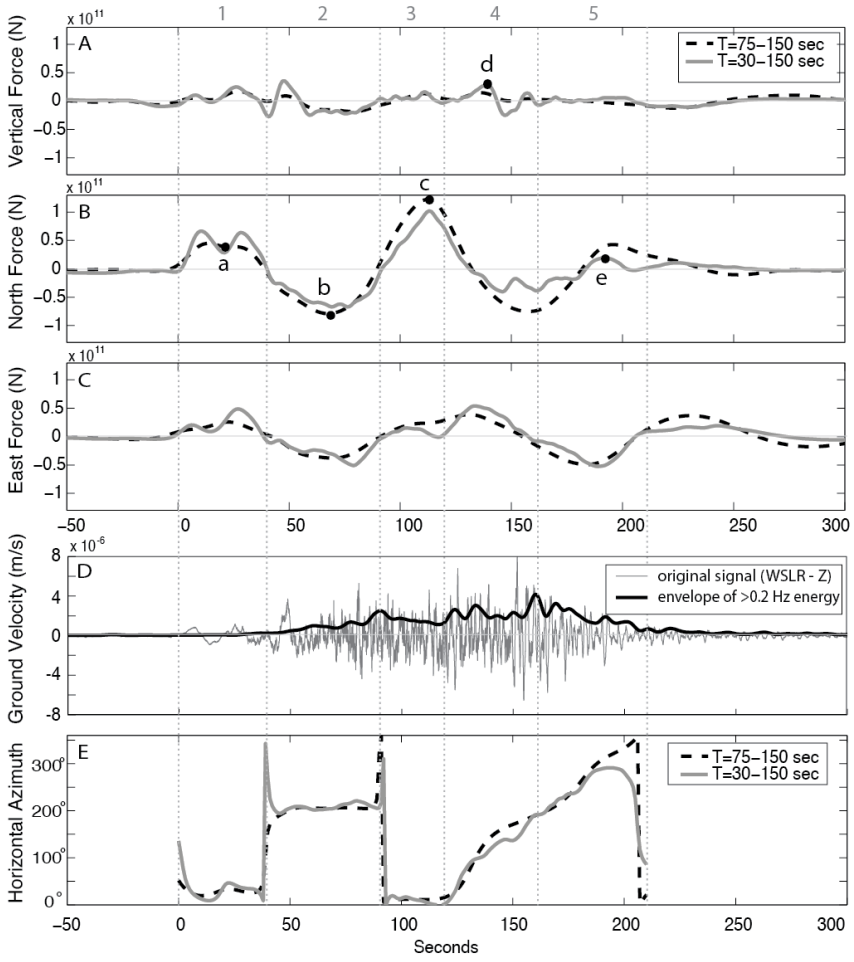

Figure 2a-7 (A-C) The three-component force time function for both the broadband five-station inversion and the solely long period inversion. The vertical force is positive up and the zero of the time scale corresponds to the start of the landslide. (D) the vertical component of the original unfiltered broadband seismic signal at the closest station (WSLR) and the envelope of the energy above 0.2 Hz in the signal, shifted to line up in time with the force-time function. Intervals 1-5 correspond with events described in text. Points a-e indicate the peak in the force-time function within each interval that was used to tie the arrival of the center of mass of the landslide with arrival at points of peak forcing along the path. The location and horizontal direction of the force at each of these points is plotted on Figure 2a-10. (E) The azimuth of the force vector over time

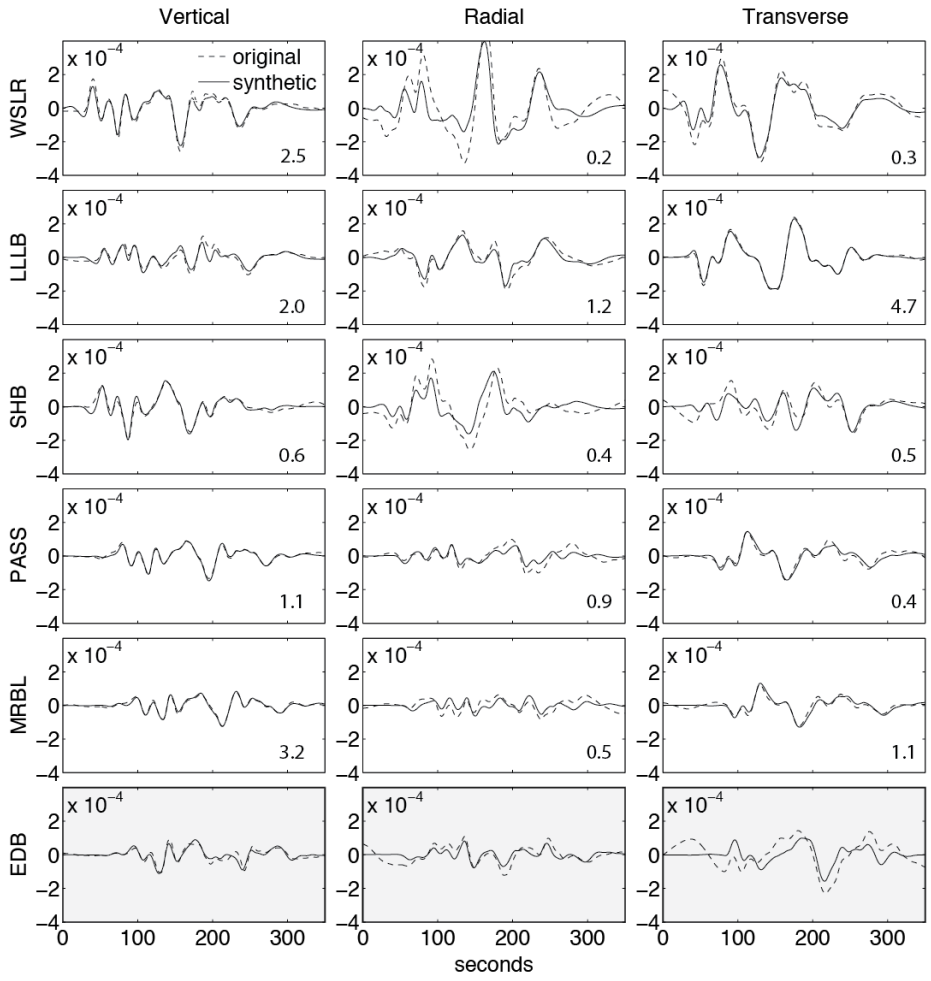

Figure 2a-8 Comparison of observed displacement seismograms (dashed line) with the synthetic seismograms generated by the force-time function obtained in the broadband inversion (T = 30-150 s) when plugged back into the forward model (solid line). The number in the right corner of each box indicates the relative weighting of the original data used in the inversion. Data from EDB (shaded), 270 km from the source, is shown to demonstrate how well the model reproduces data from a station not used to develop the model. Vertical units are centimeters.

The force-time function of the Mount Meager landslide starts at 10:26:55 UTC, has a duration of about 215 seconds and peak force amplitudes on the order of 10^{11} N. This is of the same order of magnitude as the forces generated by the similarly sized Mount Steller landslide [*Moretti et al.,* 2012], but one to two orders of magnitude smaller than some much larger landslides in other volcanic areas [*Kanamori and Given*, 1982; *Brodsky et al.,* 2003], and four orders of magnitude smaller than some huge submarine landslides [*Hasegawa and Kanamori*,

1987; *Eissler and Kanamori*, 1987]. This is to be expected because force scales linearly with mass (equation 6).

The forces are primarily horizontal, consistent with the findings of other studies of landslide single-forces [*e.g. Kanamori and Given*, 1982; *Brodsky et al.,* 2003]. The amplitudes of the vertical forces are much lower and more prone to noise in the solution. In particular the dip in the amplitudes prior to the start of the landslide, an artifact that only occurs on the vertical component, suggests the overall amplitudes may be reduced by an unknown amount. As a result, I focused on the horizontal components in the quantitative interpretation requiring absolute amplitudes. I use the vertical component of force only for the relative direction (up or down) of the horizontal forces and timing of events along the path.

With knowledge about the sliding path, the timing and changes in direction of the force vector can be attributed to events along the path. The initiating rockslide is well approximated as a sliding block allowing us to make first order calculations about landslide dynamics using equations 5 and 6 directly. The subsequent debris flow is not well approximated by a sliding block, but we can also make some inferences about the debris flow behavior and estimates speeds based on the timing of changes in direction of the forces relative to the debris flow path. Numerical landslide modeling might be necessary to fully interpret the features of the force-time function, but that is beyond the scope of this study.

4.1 Rockslide initiation

The Mount Meager rockslide failed toward the south, and according to theory, the direction of the initiating single force should be in the opposite direction: northward and upslope. That is, in fact, what occurs first in the force-time function, but instead of one wide pulse, there are two pulses superimposed on each other with about 20 seconds between their peaks (Interval 1,

Figure 2a-7). The acceleration direction of the first pulse had an azimuth of 191±3°, followed by another pulse of failure in a more southwesterly direction (217±3°). The errors in azimuth are estimated as the standard deviation of the slope angle in interval 1 on Figure 2a-7E. This sequence suggests a progressive mobilization of the flank of the mountain. Based on the shape of the source volume (Figures 2a-1), the landslide may have started with the release of material lower down on the flank of the slope toward the south, generating the first pulse. As this started to mobilize, it may have destabilized the material above, the bulk of which is to the northeast of the lower flank and may have failed in a more southwesterly direction, as the azimuth of the second pulse suggests. This two-part failure is consistent with the report of two loud cracks heard at the start of the landslide by campers nearby [*Guthrie et al.,* 2012].

Though this indicates the flank mobilized in two pulses, they occur close enough in time to act as one bulk movement in the generation of the longest period seismic waves, which are not sensitive to shorter-timescale subevents. This is apparent in the force-time function obtained by inverting only the longer period waves (T=75-150 s, Figure 2a-7 A-C). In this result, the overall mobilization of the rockslide now appears as a longer period single pulse with an overall acceleration towards 213±5° (Figure 2a-7).

After these initiating pulses, at t = 40 seconds, the force vector starts to point downwards and towards the south, possibly due to the rockslide starting to decelerate, but this is interrupted by a sharp upward and then downward force suggesting a rapid vertical collapse and impact (start of interval 2, Figure 2a-7). This could signify the collapse of part of the secondary peak (gendarme) of Mount Meager or other steep material from the headwall that was left unsupported as the flank below mobilized. It is probably not the entire secondary peak, however, because its total volume was estimated as 8 to 10 Mm^3 (N. Roberts, pers. comm., 2013), which would

generate a vertical force of about 2 x 10^{11} N if it collapsed vertically (using equation 6 and assuming a density of 2300 kg/m^3), much higher than that observed. The vertical force observed has an amplitude of 4-6 x 10^{10} N, depending on what point is taken as its starting point, so it's volume would be more on the order of 1 Mm^3 if the collapse was nearly vertical.

According to *Varnes* [1978] classification, the sliding surface of a rockslide is along one or a few shear surfaces within a narrow zone, and though the source material is disintegrating, it is moving en masse and is not yet elongated in space and flowing. This type of behavior can be approximated as a sliding block, which allows for a few simple calculations. First, equation 6 can be used to determine the acceleration of the block and determine the trajectory of the mobilizing flank as a whole, assuming the mass is relatively constant. Using the longer-period version of the force-time function (T=75-150 s) to represent the whole-scale mobilization of the rockslide, I calculated the horizontal acceleration of the mass at each second in time. Unfortunately it is not possible to calculate the acceleration of the subevents separately because their respective masses are unknown. I integrated the acceleration twice to obtain the displacement of the center of mass of the landslide at each moment in time and fit the displacement curve with the equation of motion: $d(t)=d_o + v_o t + 0.5at^2$ to obtain a best estimate of the average horizontal acceleration of the rockslide (a), where $d(t)$ is the horizontal displacement with time t. The initial horizontal displacement d_o and initial velocity v_o were set to zero. The best fit was an average horizontal acceleration of 0.39 m/s^2 (Figure 2a-9). The median slope angle of the source area from the post-slide digital elevation model (15 m resolution) resolved in the azimuth of slope failure (231±5°) was θ=23±1° so the vertical acceleration corresponding to the horizontal acceleration calculated above should have been 0.17 m/s^2 and the total slope-parallel acceleration, 0.43 m/s^2. By this

calculation, the rockslide as a whole mobilized slowly, taking 36 seconds to accelerate to a speed of 15 m/s, traveling about 250 meters horizontally, and dropping about 110 meters in that time.

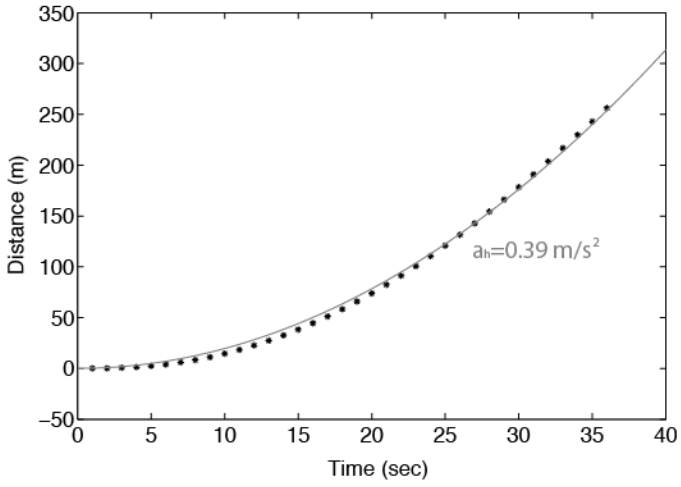

Figure 2a-9 The horizontal trajectory of the rockslide calculated from the long period (T = 75-150 s) force-time function assuming a mass of 48.5 million m^3. The solid line shows a quadratic fit to the trajectory to the form of the equation of motion relating displacement, acceleration, and time. The best fitting average acceleration was 0.39 m/s^2.

Using a rigid sliding block approach, it is also possible to estimate the areally averaged apparent dynamic friction at the base of the rockslide given the angle of the sliding plane. Using a rearrangement of equation 5

$$\mu' = (\sin\theta - a/g)(\cos\theta)^{-1} \qquad (7)$$

yields a best estimate of the apparent friction coefficient of μ'=0.38±0.02 assuming a slope-parallel acceleration of 0.43 m/s^2 and a slope angle of θ=23±1°. The apparent friction coefficient accounts for the effects of both friction and basal fluid pressure, and this value suggests high basal fluid pressures. To quantify this, the apparent coefficient of friction can be related to the true coefficient of friction, μ, that would be felt in the absence of pore fluids by:

$$\mu'\sigma_n = \mu(\sigma_n - P) \qquad (8)$$

where P is the mean basal pore pressure and σ_n is the mean normal stress at the base of the sliding mass. When rearranged, equation 8 relates the difference between the apparent and true coefficient of friction to the ratio of basal pore pressure over basal normal stress:

$$\mu - \mu' = P/\sigma_n \qquad (9)$$

While we don't know what the actual dynamic coefficient of friction in the absence of basal fluids was for the rocks composing Mount Meager, we know from lab experiments that μ is nearly always greater than 0.6 for dry rocks of a wide variety of lithologies [*Byerlee,* 1978], so equation 9 indicates that basal fluid pressures were at least 22% of the basal normal stress during the rockslide for μ'=0.38. This is corroborated by the large springs and surface seepages found throughout the source area after the landslide [*Guthrie et al.,* 2012], suggesting that groundwater was instrumental in triggering this slide and its rapid mobilization to a debris flow. The value obtained here is within the bounds on the coefficients of friction of μ'=0.2 to 0.6 that *Brodsky et al.* [2003] found for three large landslides also in volcanic environments, but significantly higher than the value used by *Guthrie et al.* [2012] to numerically model this part of the event, μ'=0.06. The reason for this discrepancy is addressed in the discussion section.

4.2 Debris flow

After the initiating pulses, two longer period, horizontal oscillations dominate the force-time function (Figure 2a-7 A-C, intervals 2 and 3). Based on the direction of these vectors (Figure 2a-7E), they are most likely the manifestation of centripetal accelerations of the debris flow material turning the two major corners in its sliding path. Unfortunately, it is not possible to take the same approach as above and use equation 6 to estimate the trajectory of the debris flow directly because a debris flow is poorly approximated as a sliding block. The flow becomes

elongated in space, which could result in differing flow directions amongst segments of the failure volume, and the material is flowing and agitated, and can have complicated flow patterns [*Iverson et al.,* 1997; *Zanuttigh and Lamberti*, 2007]. However, under the assumption that the timing of peaks in the force-time function correspond to the times when the center of mass reached points of maximum forcing, the timing of peaks can be tied to points along the sliding path to estimate the debris flow speeds. I defined the starting point as the center of mass of the landslide, calculated from the depleted thickness map from *Guthrie et al.* [2012] (marked with an x on Figure 2a-7) and placed the location of the first peak, point a, 75 meters downslope from there, corresponding with the distance traveled by the rockslide by the time it reached its peak at t=21 s (Figure 2a-9).

For intervals 2 and 3 on Figure 2a-7, I assumed that the peak in the force-time function corresponded to the time that the center of mass of the debris flow passed the portion of the path with the highest curvature (*i.e.* highest centripetal acceleration). To find these points quantitatively, I fit a polynomial to the horizontal sliding path that was delineated by *Guthrie et al.* [2012] and calculated the curvature of this polynomial analytically. I then placed the peak force vectors for each curve at these peak points of curvature (Figure 2a-10, points b and c). If the assumption that the peak force corresponds to the center of mass arriving at the location of peak forcing is valid, the direction of the acceleration should point towards the center of a circle tangent to the point of maximum curvature. To test this, I placed circles with radii equal to the radius of curvature tangent to the point of maximum curvature, and the peak acceleration vectors do point to within a few degrees of the center of these circles, as expected for a centripetal acceleration (Figure 2a-10).

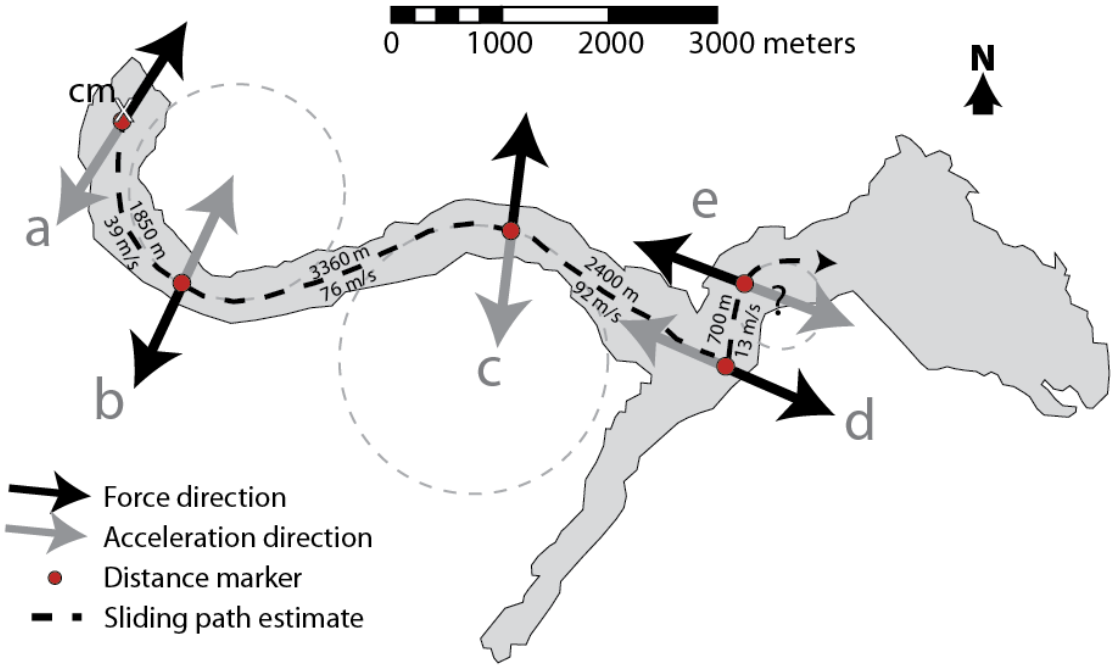

Figure 2a-10 Outline of sliding path with the azimuth of the major peaks in the force-time function from Figure 2a-8 placed at locations of maximum forcing (black arrows). The acceleration is in the opposite direction (gray arrows). The path trace (dashed line) is from *Guthrie et al*. [2012], except from segment d to e, which was estimated from satellite imagery. The x marks the approximate location of the start of the center of mass. Peaks in the force-time function correspond to the arrival of the center of mass of the landslide at the designated locations and were used to estimate the average speed of the landslide between these intervals, as summarized on Table 2a-3 and labeled along the path.

The next interval (interval 4) is characterized by an eastward and upward force that I interpreted as the debris flow decelerating rapidly upon reaching the confluence with Meager creek and running into the opposing valley wall (point d). At this point, the debris flow split and flowed both up and downstream and also left significant deposits at the confluence of the two valleys. This complicated the interpretation of the force-time function in interval 5 because there were opposing accelerations and a significant decrease in moving mass. However, the distinct pulse of force toward the northwest (point e) is consistent with another centripetal acceleration of some of the debris as it sloshed up the side of a steep hill before making its final turn to the

northern depositional area (point e, Figure 2a-7 and 2a-10). I placed the location of this peak force vector at the estimated point of maximum curvature of this turn and used it to estimate the speed for this last segment.

To conservatively account for uncertainties in the determination of distances between points, I assumed a possible distance interval range of ±400 meters. I assumed a timing error range of ±2 seconds. The location assigned to each major peak labeled on Figure 2a-7 is shown on Figure 2a-10. The direction of the force vector at each of these peak times is also plotted along with the corresponding acceleration vector pointing in the opposite direction. I estimated the errors in the azimuth of the peak force as the standard deviation of the angle within the interval containing the peak force (Figure 2a-7E). All error ranges are within a few degrees except for point d, probably due to the opposing flow directions of the material at this confluence (Table 2a-3).

Table 2a-3 Distances and speeds between points along path and corresponding azimuth of the force at each point

Point*	Distance from previous point (m)	Time from previous point (s)	Average speed, best estimate (m/s)	Possible range (m/s)	Azimuth of Force
a	75	21 ± 2	4	3-4	33° ± 5
b	1850 ± 400	48 ± 2	39	32-45	205° ± 5
c	3360 ± 400	44 ± 2	76	64-90	7° ± 4
d	2400 ± 400	26 ±2	92	71-117	114° ± 29
e	700 ± 350	52 ±2	13	6-22	290° ± 3

*Refer to Figure 2a-7 for the timing and Figure 2a-10 for the location of points a-e

The average speed of the center of mass of the landslide between each of these points, calculated by simply dividing the distance over the time, is reported on Table 2a-3 and plotted as the solid black line on Figure 2a-11. By this analysis, the average speed from the starting point to the first curve was 39 m/s, increasing to 76 m/s going into the second curve and to 92 m/s as the

debris flow traversed the third segment and burst into the adjacent valley. After reaching the opposing valley wall at point d, the average speed decreased significantly and the portion of debris that continued downstream slowed to an estimated 13 m/s before turning the final curve to main depositional area.

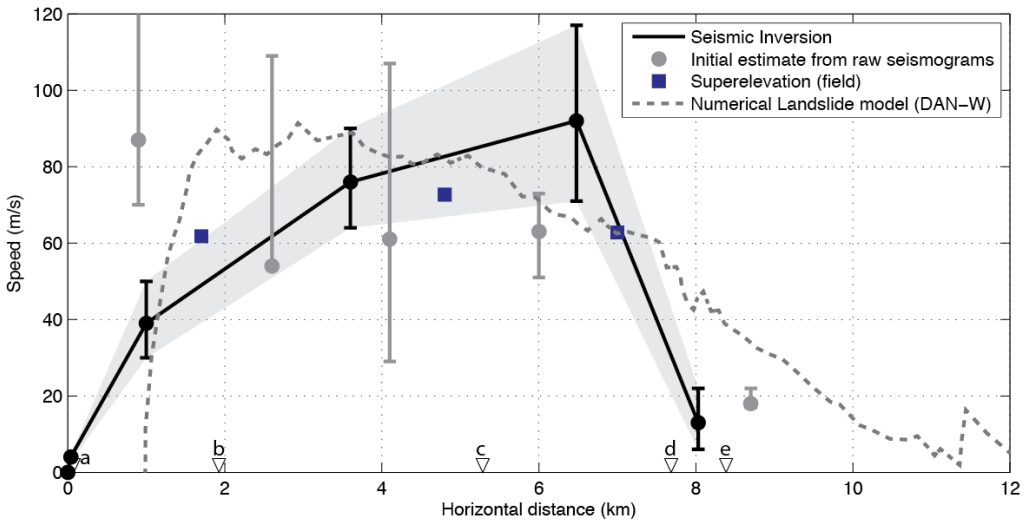

Figure 2a-11 The average speed of the center of mass along path distance from this study (black dots with error bars). The average speed estimates are plotted halfway between the distance markers defining each interval. The solid line shows a linear interpolation to these points, shading shows the error range. The zero point corresponds to the location of the center of mass of the source area and the average speed estimates were plotted halfway between the distance markers used. This result is compared to speed estimates by the three methods used by *Guthrie et al.* [2012].

Schneider et al. [2010] showed that the relative amplitude of the envelope of the high frequency seismic signal correlates well with the total frictional work rate. Frictional forces will be higher than the gravitational forces when the landslide reaches a slope shallower than the arc tangent of the coefficient of friction [*Schneider et al.,* 2010]. For the apparent coefficient of friction determined in this study, μ'=0.38, that angle would be 21˚. The slope of the sliding path is consistently less than 21˚ just past the toe of the source area so there should have been an increase in the amplitude of the higher frequency signal almost immediately after the rockslide

left the source area. This is, in fact, what occurred: the envelope of the higher frequency (>0.2 Hz) energy started to build up about 20 seconds after the start of the landslide (Figure 2a-7D). As the mass started to disintegrate, flow, and reach high speeds, the random kinetic energy should have increased as well. This, in turn, should have increased the frictional resistance due to higher shearing rates and thus higher seismic amplitudes. This is observed: the envelope of the higher frequency energy rose and reached a plateau after turning the first curve in the path (interval 2-3). This is the part of the sliding path where the debris flow reached high speeds (~76 m/s) over a relatively straight interval and random kinetic energy should have been high. After passing the second curve (point c, Figure 2a-7), the amplitude of the envelope reached an even higher plateau, this is where the estimated speeds reached their highest point but were followed by a rapid deceleration as the debris hit the wall, was deflected, and slowed down as it spread over the depositional area. This section (interval 4) has the highest amplitudes of high frequency shaking, most likely due to high frictional resistance forces as the mass rapidly decelerated.

4.3 "Aftershock"

About 2 minutes after the end of the main landslide event, there was an "aftershock," a smaller landslide that occurred after the main event. This landslide also generated a long period seismic pulse. I inverted the long period seismograms of this event to obtain its force-time function (Figure 2a-12). I had to use shorter period seismic waves (T = 20 – 50 seconds) in the inversion to capture this smaller event. The shortest period waves used are too short to be accurately represented by the Green's functions so this is a more approximate inversion than the main event. I also only used the closest three stations in the inversion because their mean signal to noise ratio (SNR) was 4, while the two more distant stations had a mean SNR of 2, with the lowest component having an SNR less than 1. The force-time function for this event indicates a

primarily vertical collapse towards the south-southeast, probably off the now over-steepened headscarp. The collapse quickly took on a more horizontal trajectory in the southeast direction. The absence of a strong subsequent downward force suggests that there was no impulsive vertical impact so the material may have disintegrated along the slope as it fell. The force of the vertical collapse is an order of magnitude smaller than the main event, peaking around 6×10^9 N. The second vertical pulse, occurring about 30 seconds after the first, could have been a second collapse or could be forces generated along the sliding path of the first collapse. Since there is no way of estimating the volume of this secondary landslide from satellite data because it occurred just minutes after the main event, I used the result of this inversion to estimate the volume solely from the seismic data. To do this, I assumed the same frictional value found for the main event, μ'=0.38, and took the arc tangent of the vertical over the horizontal forces at the peak of the vertical collapse to estimate a slope of θ=72°. This results in an acceleration of 8.2 m/s^2 by equation 7. Since the magnitude of the forces at this point was 5.8×10^9 N, using equation 6, this yielded an estimated mass of 7×10^8 kg, or a volume of 0.3 million m^3 assuming a density of ~2300 kg/m^3. This volume of material is two orders of magnitude smaller than the main event, yet the forces are only one order of magnitude smaller, probably because accelerations were higher due to the near-vertical failure direction.

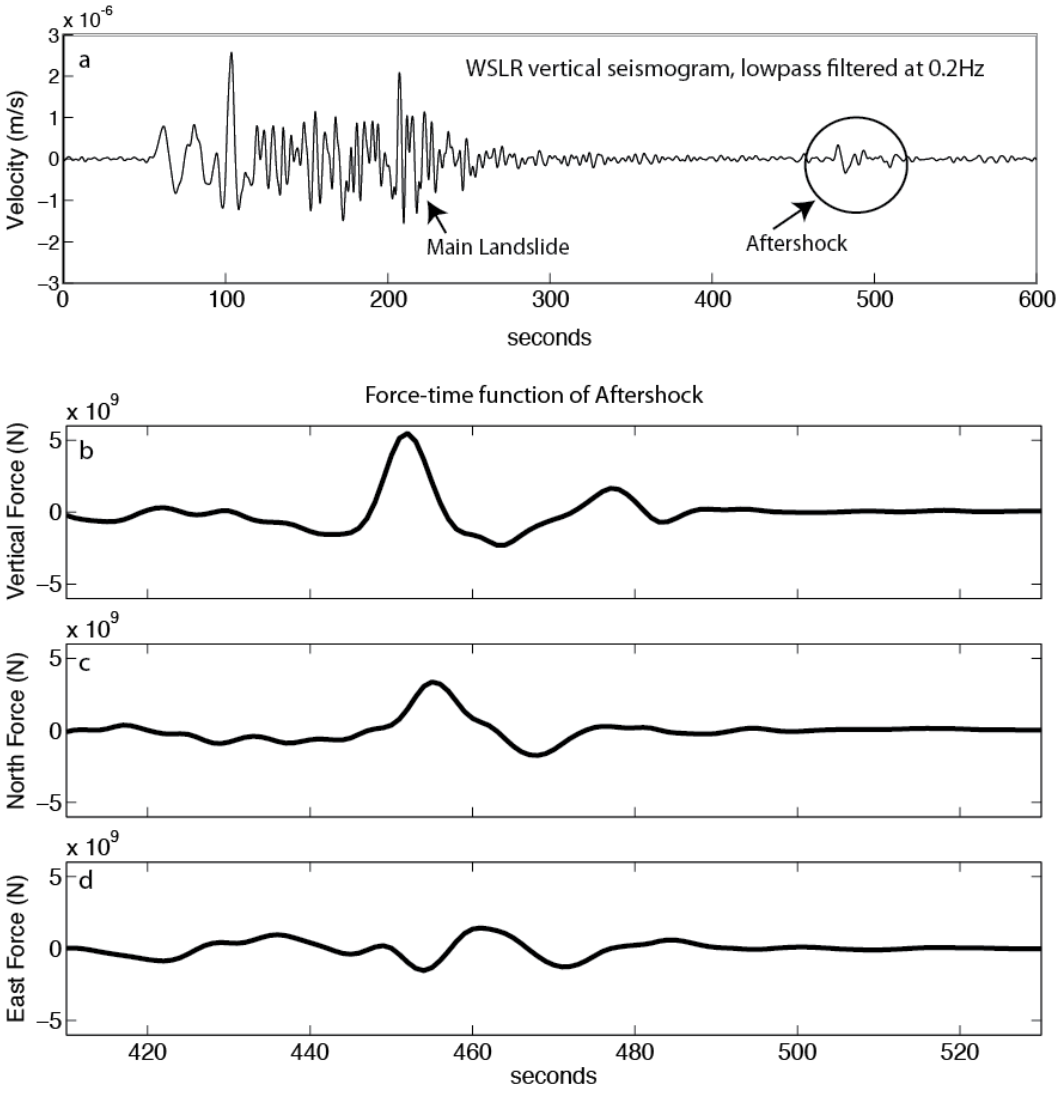

Figure 2a-12 a) A second smaller landslide, an "aftershock," occurred a few minutes after the end of the main landslide, as shown in the seismic data. (b-d) Three components of force of the aftershock obtained by inverting seismic data at periods of 20 to 50 seconds from the three closest three-component stations (WSLR, LLLB, SHB). The time scale is consistent between all four plots.

5. Discussion

5.1 Improvements to landslide characterization

The time series recording of the forces exerted by the landslide allowed for significant improvements in the characterization of the dynamics of this event, particularly when combined with the extensive field evidence and geospatial data compiled by *Guthrie et al*. [2012]. In particular, the availability of the force-time function reduces the qualitative interpretation typically required to tie post-slide evidence to what happened during the event. It also eliminates guesswork required to interpret the source of pulses in the raw seismograms directly by using the seismograms to find what the source was quantitatively.

As mentioned, the force-time function showed that the rockslide initiation occurred in two pulses, which I interpreted as a progressive failure of the flank of the mountain. These events were followed soon after by a nearly vertical collapse that was smaller in volume. This sequence of events is in contrast with the interpretation of *Guthrie et al.* [2012]. They proposed that the near-vertical collapse of the steep gendarme occurred first and its impact onto the shallower slopes below caused the flank to mobilize due to undrained loading and rapidly turn into a debris flow. This is a reasonable interpretation from the evidence that was available at the time, but with the additional information provided by the force-time function, it is clear that the failure of the flank of the mountain started first and was likely the cause of the vertical collapse - though the collapse of this material onto the already-mobilizing flank still could have been responsible for its rapid disintegration and mobilization to a debris flow. This is a reasonable argument given that the higher frequency portion of the signal attributable mainly to the debris flow rises quickly after the vertical collapse.

The results of this study also improve on the interpretation of Ekström and Stark [2013], who included the 2010 Mount Meager landslide in their inversion of long period seismograms from 29 catastrophic landslides worldwide recorded on the Global Seismographic Network. Though they do not include the entire force-time function in their results, they reported peak forces of 1.48×10^{11} N for this event, comparable but higher than the peak magnitude of the force found in this study of 1.0×10^{11} N. However, the start time they reported for the start of the event was two minutes later than the start time found in this study and reported by *Guthrie et al.* [2012]. Their start time corresponds instead to the time of the peak at point d (Figure 2a-7 and 2a-10). This suggests they interpreted what this study found to be a centripetal acceleration of the debris flow around the second curve in the path as the initiation of the rockslide. This discrepancy may explain why their estimated runout of 4.6 km was much shorter than the actual runout (>12 km) and highlights the care that must be taken when interpreting the force-time functions of landsliding events.

Though the methods used to estimate the speed of the landslide from the force-time function in this study still required some interpretation, they are the closest to a direct measurement of the options available. *Guthrie et al.* [2012] used two common methods of estimating landslide speeds: a theoretical method called superelevation [*Chow*, 1959] and a numerical landslide model, DAN-W [*Hungr, 1995; Hungr and McDougall, 2009*]. I validated these methods against the more physically based measurement available from the results of this study, since the opportunity is not often available for natural landslides. As mentioned, *Guthrie et al.* [2012] also used features of the raw seismograms to estimate speeds, and I include that result in the comparison as well. The four methods are plotted for comparison on Figure 2a-11 and were all adjusted to the same path starting point used in this study.

The speeds predicted by the numerical model presented by *Guthrie et al.* [2012] are much higher at the start of the debris flow than that determined in this study. The initial acceleration in the first 20 seconds was about 4.5 m/s^2, which should have generated a force an order of magnitude higher than that observed in the force-time function, so the speeds cannot have been that high at the onset. The exceptionally low coefficient of friction they used in this simulation (μ'=0.06, compared to 0.38 determined in this study) may partially explain the difference. Guthrie et al. [2012] chose this value to best fit the runout distance and velocities of the landslide interpreted from the raw seismograms, and did not fit the superelevation estimates well. This low value for μ' is probably because they were trying to match initial speed estimates that were too high. This mismatch highlights the potential of using the force-time functions and other information derived from seismic waves to validate and calibrate numerical models and tie them to the physical world, as *Moretti et al.* [2012] did in their study. The limitation is that for complicated events - such as this one, with subevents of unknown relative masses and a complex path causing opposing forces at times - numerical models may be needed to fully interpret the force-time function. So in reality, the comparison between numerical models and landslides may be more of an iterative process that may not necessarily have a unique solution.

The landslide speeds estimated roughly from the raw seismograms in *Guthrie et al.* [2012] also had a much higher estimate of the initial speed (Figure 2a-11). This is due to the aforementioned difference in their interpretation of mobilization sequence. They assumed that the majority of the landslide mass - the flank of the mountain - did not mobilize until the secondary peak collapsed on it about 45 seconds after the start of the landslide. With this interpretation, there is very little time between the mobilization of the flank of the mountain and its arrival at the first corner, thus resulting in the extremely high initial speeds they report. As

explained above, the force-time function shows the reverse sequence of events: the flanks of the mountain mobilized first, followed by a vertical collapse. If they had this information in the initial interpretation of the seismograms, the initial speed estimate would have been much closer to the speeds obtained by this study. Though the uncertainties are higher, the best estimates of the speeds from the raw seismograms are close to those estimated in this study: between 10 and 30% lower but with error bars that overlap. The main benefit of using the results of the seismic inversion to estimate speeds is the elimination of most of the guesswork involved in correlating pulses in the seismic record to exact locations of events along the path.

The speeds determined in this study compare most favorably with the values determined using the superelevation method [*Chow*, 1959], a theoretical method of determining speed by how much higher the debris flow reaches on the outside corners of turns than the inside corners. The three superelevation measurement points are between 5 and 11% different from the projection of the speeds calculated in this study, and are well within the error bars (Figure 2a-11), providing a validation of this theoretical method with real data. The main discrepancy is the average speed for the path segment between points c and d coming out of the last corner in the valley, where the average speed from this study exceeds the projection line between superelevation estimates by 35%. However, it is not possible to conclude whether this discrepancy is real or not because the superelevation measurements are effectively point measurements at the points before and there is no information in between.

There is a possibility that the continuous increase in the debris flow speed until point d found in this study could be erroneous. However, the uncertainties incorporated in the calculation of the error bars of the speeds for this study were conservatively wide. The main source of error would have to be a misinterpretation of the force-time function in this study due

to the complexity of flow at this junction. This is possible, but it is difficult to conceive where the pulse of eastward forces observed in interval 4 would come from if not from the material running up against the adjacent primarily west-facing valley wall (point d), so I consider this unlikely.

Assuming this late peak in speeds is real and the other methods are either erroneous or cannot resolve this peak, there are a few potential explanations. According to field evidence, there was very little entrainment of material along the path, in fact deposition started immediately below the initiation zone, but most material was deposited beyond the Capricorn creek valley [*Guthrie et al.,* 2012] so the mass was relatively constant during the fastest intervals along the landslide path. A landslide of constant mass will continually increase in velocity if the angle of friction ($\tan^{-1} \mu'$) is shallower than the slope angle [*Iverson,* 2012]. The apparent coefficient of friction at the base of the rockslide estimated in this study to be μ'=~0.38, which translates to an angle of friction of about 21°. The slope of the debris flow path is shallower than this, averaging around 10°, which means the coefficient of friction must have dropped below 0.18 (tan 10°) during the debris flow in order to still be accelerating along this path. A drop in the coefficient of friction of a debris flow can occur due to undrained loading of wet bedded sediments by the overriding debris flow that causes an increase in the pore pressures at the bed [*Iverson et al.,* 2011]. This often also results in an increase in entrainment [*Iverson et al.,* 2011], but entrainment was not observed in this case, possibly because of the exceptionally high speeds, which actually make entrainment less likely to occur [*Iverson*, 2012].

Another contributing factor to the late high peak in speeds estimated in this study could be due to a common behavior of debris flows: the development of surging, also referred to as roll waves. As explained by *Zanuttigh and Lamberti* [2007], debris flow surges develop when

smaller flow instabilities grow and form surface waves that overtake each other with growing wavelengths and amplitudes. As these instabilities progress downstream and continue to overtake each other, they can coalesce into bigger surges, often eventually forming one dominant first surge characterized by a concentration of boulders at the front, sometimes followed by subsequent smaller surges. Debris flow depths are often significantly higher in surge waves and the waves can travel up to three times faster and exert forces more than an order of magnitude higher than the rest of the regularly flowing mass.

The development of one or more large coalesced surges along the flow path of the Mount Meager debris flow could have moved the speed of the center of mass of the debris flow forward faster than the average flow, but the forces exerted by the surges themselves were likely too short period and too low-amplitude to be resolved in the force-time function. The timing of the speedup is consistent with the observation that larger coalesced surges tend to preferentially appear further down the flow path because it takes time for the instabilities to grow large enough and overtake each other [*Zanuttigh and Lamberti*, 2007]. If the surge started to develop prior to reaching point c, the speed estimate between b and c could also be higher than the regular non-surging flow. There is even a hint of what could be interpreted as two separate surges visible in the vertical component of the force-time function. The vertical component of the force at point d has a shorter duration than the eastward component and is followed by a second smaller upward pulse (Figure 2a-7A). This could indicate that the bulk of the debris flow material did not run up vertically, but was primarily deflected horizontally, and it could have been the arrival of these two or three subsequent surges that were faster, deeper, and higher energy than the rest of the flow that was responsible for the high runup observed in the field. The surges do not appear as discrete events on the east component of the force-time function, however, though this could be

because their masses are not large enough to contrast with the rest of the regular flow being deflected primarily horizontally.

5.2 Limitations

One major limitation to the application of the methods used in this study to other events is that there is a whole spectrum of landslide types and behaviors [*Varnes,* 1978], but these methods can only be used to study the small percentage that generate the required long period waves: exceptionally large and rapid landslides. Scaling these methods down to more common shorter duration, smaller rapid landslides would require a detailed characterization of the velocity and attenuation structure of the study area and better seismic coverage because they would generate lower amplitude and shorter period seismic waves. Even if this can be done, it doesn't address the problem of potential overlap in the frequency domain between the coherent pulses from the bulk mobilization of the landslide mass and the signal generated by stochastic smaller scale processes. For larger landslides, the two sources of seismic radiation are manifested in distinct frequency bands (*e.g.* Figure 2a-3c), but this may not be the case in a scaled down scenario and if they overlap the two can no longer be isolated with simple filtering. On the other side of the spectrum, slower events that may have large masses but slow accelerations and long durations, such as large slumping events, may be too slow to generate waves of short enough period to be observed by seismic methods, though subevents or smaller scale forcing may be resolvable.

Another limitation is that the force-time function alone cannot be used directly to estimate useful information about the dynamics of the landslides. Other information is required. For example, even if the landslide under investigation can be approximated as a coherent sliding block, equation 6 dictates that the trajectory of the sliding block can only be calculated from the

force-time function if the mass is known. Likewise, the mass can only be calculated if the trajectory is known. However, even if neither is known, order of magnitude estimates of mass can still be obtained due to physical limitations on acceleration.

I showed that the methods used in this study can be used to determine the sequence of events and the occurrence of subevents. However, this can also be a limitation because subevents can complicate the force-time function and thus make straightforward interpretation and calculations from it challenging. In this study, I was able to get around the fact that the rockslide initiation occurred in two subsequent failures because the two subevents were close enough in time and space that they acted as a single failure mass at the long period limit. Care must be taken to correctly assess when and where the rigid sliding block approximation is valid, and when it breaks down. For example, the approximation breaks down if subevents are too far apart in time or space to be considered one failure mass at long periods, or when the failure mass is not moving coherently enough, such as during the debris flow of this event, where the material became elongated in space and internal agitation and complex flow patterns dominated.

6. Conclusions

In this study, I inverted the long period seismic signals generated by the Mount Meager landslide to solve for the forces it exerted on the earth as the failure mass accelerated, turned curves along its path, and decelerated. I used this result, the force-time function, to track landslide behavior over time. This analysis is useful not only for unraveling the sequence of events and facilitating a more direct interpretation than is typically possible between post-slide evidence and what actually happened during the event, but can also be used to make first order calculations about landslide dynamics.

Using the three component force-time function, I was able to identify the directions of the slope collapse and discern that the slope failure was progressive, with the massive flank of the mountain starting to mobilize first in two discrete but closely timed subfailures, followed by a much smaller nearly vertical collapse that might have been the collapse of part of the gendarme of the secondary peak of Mount Meager left unsupported as the flank mobilized. The addition of this new information clarified the sequence of events, suggesting that the initial interpretation made by *Guthrie et al.* [2012], where they proposed that the vertical collapse occurred first and caused the flank to mobilize, was actually reversed.

Using the mass of the failure determined from satellite imagery by *Guthrie et al.* [2012], I was able to use the force-time function directly to estimate the trajectory of the center of mass of the rockslide, showing that it had an average horizontal acceleration of 0.39 m/s^2, and estimated the apparent coefficient of friction at the base of the rockslide to be μ'=0.38, a low value that suggests basal fluid pressures were high – at least 22% of the normal stresses at the base of the slide, assuming a minimum coefficient of friction of 0.6 for dry rocks.

Following the sequence of forces generated by the rockslide initiation, the direction and timing of the primarily horizontal forces were consistent with the debris flow turning two corners in its path and then running up the wall of an adjacent river valley. The horizontal forces from these centripetal accelerations were actually the highest forces overall. A debris flow is poorly approximated as a sliding block so I could not make calculations or estimate the trajectory directly from the force-time function, but instead tied the timing and direction of peak forces to points of peak forcing along the path to estimate the speed of the center of mass of the debris flow. I found that speeds increased continuously as the debris flow progressed down the first valley, peaking at 92 m/s before rapidly decelerating upon reaching the adjacent Meager Creek

valley. The speeds I found by this method were very close to the speeds predicted by superelevation, providing a physically based validation to that theoretical method. The force-time function also provided a test of other speed estimation methods applied by *Guthrie et al.* [2012]. The initial speeds they estimated by numerical modeling were much higher than those estimated in this study, and would have required forces an order of magnitude higher than those observed in the force-time function. Their estimates of speed from the raw seismograms were close to those estimated in this study, though with higher uncertainties, but their speed estimates were also too high at the onset of the landslide because of their reverse interpretation of the sequence of initiating events. The differences show that the addition of the information provided by the force-time function can significantly clarify landslide characterization.

Though the calculations I presented in this study are rough and large scale due to the long period nature of the seismic waves used, and direct interpretation is difficult due to the complexities of debris flow behavior, it is remarkable that using data from five broadband stations 70 to 276 km from the source it was possible to reconstruct details of this event that are unobtainable by other methods but nonetheless important for understanding landslide physics and improving numerical models. As there are currently networks of broadband seismometers worldwide for which data are freely available, the techniques I described could be applied to study other large landslides that occurred both in the past and to come.

7. Acknowledgements

Many thanks to Ken Creager who provided indispensable guidance on what started as a project for his Inverse Theory course, and to my advisor John Vidale. Also to Emily Brodsky, Dick Iverson, Rick Guthrie, John Clague, Anne Mangeney, and Hiroo Kanamori for helpful

feedback, reviews, and discussions, Nicholas Roberts for helping with some geospatial calculations, the Pacific Northwest Seismic Network and Canadian National Seismograph Network for providing the seismic data and Sharon Watson for tolerating frigid fast flowing river crossings and quicksand to accompany me on a field visit of the landslide. Additionally, reviews by Jackie Caplan-Auerbach, Agnes Helmstetter and two anonymous reviewers helped improve the manuscript significantly.

8. References

Aster, R. C., B. Borchers, and C. H. Thurber (2005), Parameter estimation and inverse problems, Elsevier, Amsterdam.

Berrocal, J., A. F. Espinosa and J. Galdos (1978), Seismological and geological aspects of the Mantaro landslide in Peru, Nature, 275(5680), 532-536.

Bouchon, M. (1981), A simple method to calculate Green's functions for elastic layered media, Bull. Seism. Soc. Am. 71, 959-971.

Brodsky, E. E., E. Gordeev and H. Kanamori (2003), Landslide basal friction as measured by seismic waves, Geophys. Res. Lett., 30(24), 2236, doi:10.1029/2003GL018485

Byerlee, J. (1978), Friction of rocks, Pure and Appl. Geophys., 116(4-5), 615-626.

Chow, V.T. (1959), Open-channel hydraulics, McGraw-Hill, New York.

Cruden, D. M. and D. J. Varnes (1996), Landslide types and processes, in Landslides Investigation and Mitigation, Transportation Research Board Special Report 247, pp.36-75, National Research Council, National Academy Press, Washington, D.C.

Dammeier, F., J. R. Moore, F. Haslinger and S. Loew (2011) Characterization of alpine rockslides using statistical analysis of seismic signals, J. Geophys. Res., 116, F04024, doi:10.1029/2011JF002037.

Deparis, J., D. Jongmans, F. Cotton, L. Baillet, F. Thouvenot, and D. Hantz (2008), Analysis of rock-fall and rock-fall avalanche seismograms in the French Alps, Bull. Seismol. Soc. Am., 98(4), 1781-1796, doi: 10.1785/0120070082.

Douglas, A., J. A. Hudson, and R.G. Pearce (1988), Directivity and the Doppler effect, Bull. Seism. Soc. Am., 78, 1367-1372.

Eissler, H. K and H. Kanamori (1987), A single-force model for the 1975 Kalapana, Hawaii, Earthquake, J. Geophys. Res., 92(B6), 4827-4836.

Ekström, G. and C. P. Stark (2013), Simple scaling of catastrophic landslide dynamics, Science, 339, 1416-1419.

Favreau, P., A. Mangeney, A. Lucas, G. Crosta, and F. Bouchut (2010), Numerical modeling of landquakes, Geophys. Res. Lett. 37(15), L15305, doi:10.1029/2010GL043512.

Fukao, K. (1995), Single force representation of earthquakes due to landslides or the collapse of caverns, Geophys. J. Int., 122, 243-248.

Guthrie, R.H., P. Friele, K. Allstadt, N. Roberts, K. Delaney, S. G. Evans, D. Roche, M. Jakob. and J. Clague (2012), The 6 August 2010 Mount Meager rock slide-debris flow, Coast Mountains, British Columbia: characteristics, dynamics, and implications for hazard and risk assessment, Nat. Hazards Earth Syst. Sci., 12(5), 1277-1294, doi: 10.5194/nhess-12-1277-2012

Hasegawa, H. S., and H. Kanamori (1987), Source mechanism of the magnitude 7.2 Grand Banks earthquake of November 1929: double couple or submarine landslide? Bull. Seism. Soc. Am., 77(6), 1984-2004.

Helmstetter, A., and S. Garambois (2010), Seismic monitoring of Sechilienne rockslide (French Alps): Analysis of seismic signals and their correlation with rainfalls, J. Geophys. Res., 115(F3), F03016, doi: 10.1029/2009JF001532.

Hermann, R. B. (2002), Computer Programs in Seismology, An Overview of Synthetic Seismogram Computation, Version 3.30, Dept. of Earth and Atmospheric Sciences, Saint Louis University. Accessed at: http://www.eas.slu.edu/eqc/eqc_cps/CPS/CPS330.html

Hibert, C., A. Mangeney, G. Grandjean, and N. M. Shapiro (2011), Slope instabilities in Dolomieu crater, Reunion Island: From seismic signals to rockfall characteristics, J. Geophys. Res., 116(F4), F04032, doi: 10.1029/2011JF002038.

Huang, C. J., H. Y. Yin, C. Y. Chen, C. H. Yeh, and C. L. Wang (2007), Ground vibrations produced by rock motions and debris flows, J. Geophys. Res., 112, F02014, doi: 10.1029/2005JF000437.

Hungr, O. (1995), A model for the runout analysis of rapid flow slides, debris flows, and avalanches, Can. Geotech. J., 32, 610-623.

Hungr, O., and S. McDougall (2009), Two numerical models for landslide dynamic analysis, Comp, Geosci., 35, 978-992.

Iverson, R. M., M. E. Reid, and R. G. LaHusen (1997). Debris-flow mobilization from landslides, Annu. Rev. Earth Planet. Sci., 25(1), 85-138.

Iverson, R.M., M. E. Reid, M. Logan, R. G. LaHusen, J. W. Godt, and J. P. Griswold (2011), Positive feedback and momentum growth during debris-flow entrainment of wet bed sediment, Nat. Geosci., 4(2), 116-121, doi: 10.1038/ngeo1040.

Iverson, R.M. (2012) Elementary theory of bed-sediment entrainment by debris flows and avalanches, J. Geophys. Res., 117, F03006, doi: 10.1029/2011JF002189.

Julian, B.R., A. D. Miller and G. R. Foulger (1998), Non-double couple earthquakes, Rev. Geophys., 36(4), 525-549.

Kanamori, H. and J. W. Given (1982) Analysis of long-period seismic waves excited by the May 18, 1980 eruption of mount St. Helens – a terrestrial monopole?, J. Geophys. Res., 87(B7), 5422-5432.

Kawakatsu, H. (1989) Centroid single force inversion of seismic waves generated by landslides, J. Geophys. Res., 94(B9), 12,363-12,374.

Kennett, B. L. N., E. R. Engdahl, and R. Buland (1995), Constraints on seismic velocities in the earth from travel times, Geophys. J. Int., 122(1), 108-124.

La Rocca, M., D. Galluzzo, G. Saccorotti, S. Tinti, G. B. Cimini, and E. Del Pezzo (2004), Seismic signals associated with landslides and with a tsunami at Stromboli Volcano, Italy, Bull. Seismol. Soc. Am., 94(5), 1850-1867.

McSaveney, M. J., and G. Downes (2002), Application of landslide seismology to some New Zealand rock avalanches, in Landslides, J. Rybar, J. Stemberk, and P. Wagner (Eds.) pp.649-654. Balkema, Lisse, Netherlands.

Moretti, L., A. Mangeney, Y. Capdeville, E. Stutzmann, C. Huggel, D. Schneider, and F. Bouchut (2012). Numerical modeling of the Mount Steller landslide flow history and of the generated long period seismic waves, Geophys. Res. Lett., 39(16), L16402, doi: 10.5167/uzh-68355.

Norris, R. D. (1994), Seismicity of rockfalls and avalanches at three Cascade Range volcanoes: Implications for seismic detection of hazardous mass movements, Bull. Seismol. Soc. Am., 84(6), 1925-1939.

Schneider, D., P. Bartlet, J. Caplan-Auerbach, M. Christen, C. Huggel, and B. W. McArdell (2010), Insights into rock-ice avalanche dynamics by combined analysis of seismic recordings and a numerical avalanche model: J. Geophys. Res. 115(4), F04026, doi: 10.1029/2010JF001734.

Stein, S., and M. Wysession (2003), An Introduction to Seismology, Earthquakes, and Earth Structure, Blackwell, Malden, MA.

Suriñach, E., I. Vilajosana, G. Khazaradze, B.Biescas, G. Furdada, and J. M. Vilaplana (2005), Seismic detection and characterization of landslides and other mass movements: Nat. Haz. And Earth. Syst. Sci., 5, 791-798.

Varnes, D. J. (1978). Slope movement types and processes, in: Landslides analysis and control Transportation Research Board Special Report 176, R. L. Schuster, R. J. Krizek (Eds.), pp.11-33 National Research Council, Washington, DC.

Weichert, D., R. B. Horner and S. G. Evans (1994), Seismic signatures of landslides: the 1990 Brenda Mine Collapse and the 1965 Hope Rockslides, Bull. Seismol. Soc. Am., 84(5), 1523-1532.

Zanuttigh, B., and A. Lamberti (2007), Instability and surge development in debris flows, Rev. Geophys., 45(3), RG3006, doi: 10.1029/2005RG000175

Chapter 2b: The Seismic Story of the Nile Valley Landslide

Most of the content of this chapter was presented at:

Allstadt, K., Vidale, J., Thelen, W. and Bodin, P., 2010, The Seismic Story of the Nile Valley Landslide, Poster Session presented at: Seismological Society of America Annual meeting 2010, 2010 Apr 21-23; Portland, OR.

Table of Contents

Summary 2b-3
1. Introduction 2b-4
2. Background 2b-5
3. Seismic Data 2b-10
4. Discussion 2b-13
5. Conclusion 2b-15
6. Acknowledgements 2b-16
7. References 2b-16

Summary

The Nile Valley landslide of October 11th, 2009, was one of the largest in recent Washington state history. This translational slide involved a volume on the order of 10^7 cubic meters and destroyed 2 houses, a portion of highway, and flooded several houses when it partially dammed a stream. Residents in the area reported noises and deformation starting 2 days beforehand and evacuated safely. The main sliding sequence occurred over about 6 hours and two regional seismic stations 12 and 29 km away captured some of the signals generated by it. Distinct seismic pops began to appear about 3 hours before a partial slope failure generated a continuous 2-minute signal with an emergent onset. After this, the pops became more frequent and evolved into the largest sliding event. This appeared as a 13-minute broadband rumble centered on 4.5Hz with an emergent onset and spindle shaped signal. Diminishing rumbling followed for another hour.

After the landslide occurred, we installed 12 vertical geophones and 4 three-component seismic stations around the perimeter. More than 60 small events were recorded at these stations in the days after the slide and are likely due to settling and continued deformation. One particularly large movement 9 days after the main event generated a signal that also appeared on the more distant permanent stations. This event had a similar shape to the main event but lasted only 15 seconds with about 25% of the amplitude. Smaller events recorded on the seismic stations at the site showed a buildup in amplitude hours before this event.

This case adds to the body of knowledge on the seismic manifestation of landslides and gives more clues as to what happens before, during, and after a landslide of this type. In addition, our observations indicate that landslides may show precursory patterns that seismic monitoring can detect, if they can be reliably identified.

1. Introduction

The Nile Valley landslide of October 11th, 2009 (Figure 2b-1), located on the east side of the Cascades along Highway 410, was one of the largest in recent Washington State history. This translational slide involved a volume on the order of 10^7 cubic meters of material. It destroyed a portion of state highway, damaged several houses and diverted a river, causing flooding. Fortunately no one was injured because the landslide gave warning signals in the days and hours beforehand.

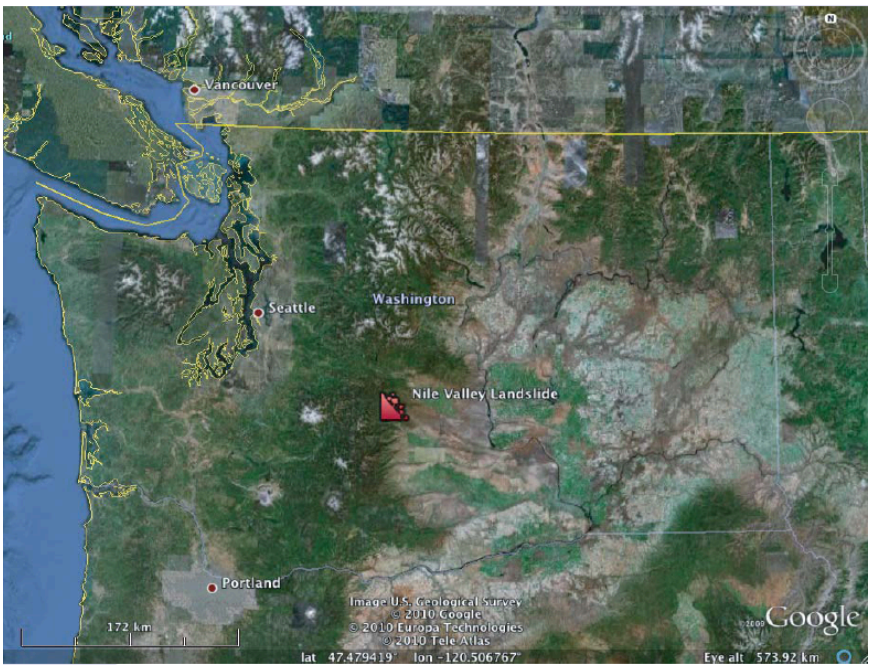

Figure 2b-1 Location of Nile Valley Landslide in Washington State on Google earth basemap.

The slopes failed over the course of about 24 hours in a complex series of events of various sizes and velocities. Some of the more energetic events generated seismic signals that were captured by the Pacific Northwest Seismic Network (PNSN) regional stations 12 and 29 km away (NAC and ELL, Figure 2b-2). This highly precise seismic timeline, in combination with detailed eyewitness reports provided to the Washington State Department of Transportation (WSDOT) and studies of the geology of the landslide conducted by the Washington State

Department of Natural Resources (DNR) resulted in a detailed account of the unfolding of a landslide unlike any other.

This study focuses mainly on the seismic manifestation of movements on the slide and how this case study can contribute to the sparse existing body of knowledge on landslide seismology. Complementary details from eyewitness accounts and landslide geology are included.

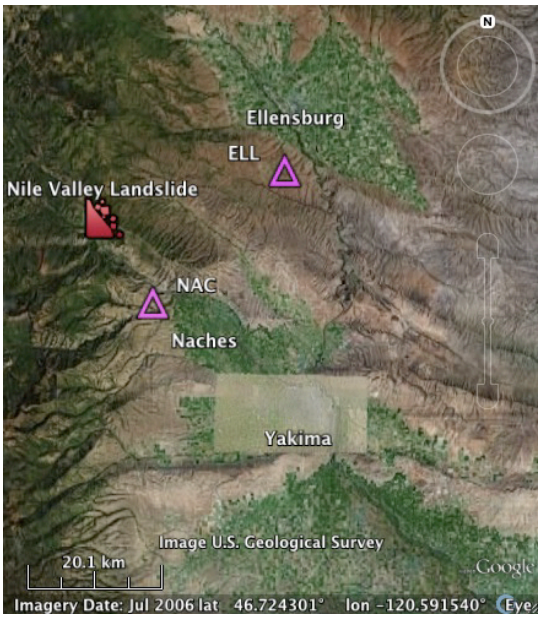

Figure 2b-2 Location of nearby PNSN stations in relation to Nile Valley Landslide (Google Earth basemap)

2. Background

The Nile Landslide may be related to, or occur in deposits of, the much larger ancient Sanford Pasture Landslide (Figure 2b-3), which covers an area of over 50 square kilometers. The Sanford Pasture Landslide is on a southern face of an oversteepened anticline. The Nile Thrust fault approaches the surface inside this ridge. Weak Ellensburg Formation interbeds (siltstone, volcaniclastics, and sandstone) created a perfect failure plane for the landslide. The Sanford Pasture landslide is at most 2 million years old, but the actual age is not well known. The

present-day scar from this slide is apparent on Figure 2b-3. After failure, erosion split the Sanford Pasture landslide and formed a river valley between the deposit area and the main body of the landslide, now known as the Nile Valley. Smaller blocks continued to move; at least two major movements flow into the valley area and to the location of the Nile slide (Hammond, 2009a,b).

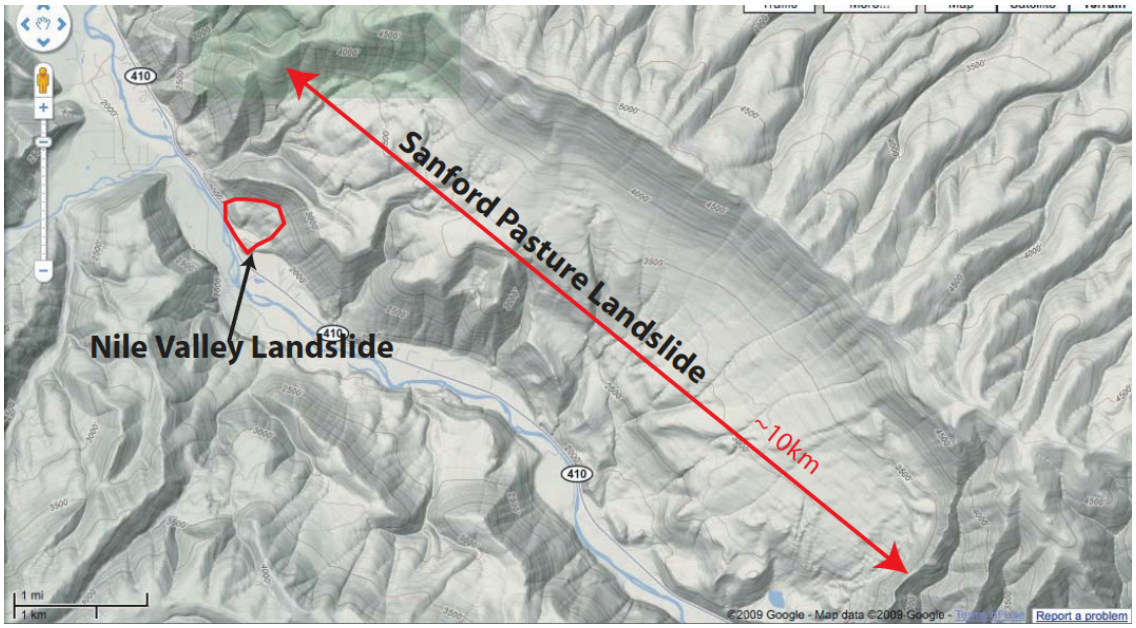

Figure 2b-3 The size of the scar of the ancient Sanford Pasture Landslide dwarfs the Nile Valley Landslide, circled in red (basemap from Google maps).

A cross-section of the Nile Valley landslide of October 2009 is shown on Figure 2b-4 and a map view showing the different failures, adapted based on interpretation by the WSDOT, is shown on Figure 2b-5, the timing of the different failures depicted on this map will be discussed in the next section. The headscarp of the Nile Valley Landslide formed along the contact with a separate landslide block of basalt beds. Movement occurred on two failure planes located on interbeds between basaltic flows. The upper failure plane is composed of sandstone and siltstone at an approximate depth of 20 meters. Movement along this plane was translational, with localized rotational blocks and flows and, resulted in the main surface movement that covered

Highway 410 and diverted the Naches River. The deeper failure plane was at a depth of around 60 meters and borehole drilling afterwards revealed high confining water pressures in this failure plane, most likely confined by a clay-rich sedimentary layer overlying the basalt (Badger, 2010, pers. comm.). This failure block moved into the valley, creating deformation and folding and movement of the soft sediments at the toe of the landslide, including shifting an entire intact block with a house on top of it (eastern hill of uplifted areas labeled on Figure 2b-5).

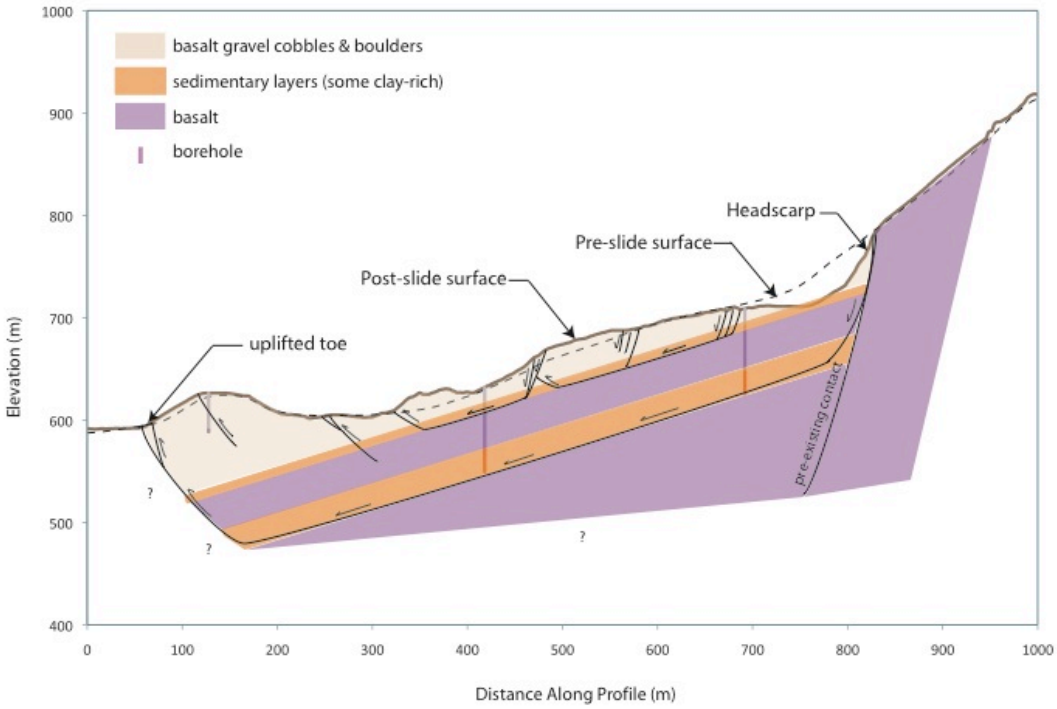

Figure 2b-4 Simplified cross section through the Nile Valley landslide showing two translational failure planes with rotational surface components. Based on borehole data and LiDAR DEM collected by WSDOT, and interpretation by WA DNR. Location of Cross Section shown on Figure 2b-5.

The following account of the sequence of events was compiled by the WSDOT (Nile, 2010). Signs that slopes were reawakening began up to one month before the main event: A fisherman observed clouds of dust coming from high on the slopes that would later fail. Two days before the slide, a local couple reported that their driveway was narrowing and occasional

rocks were tumbling down the slope. The day before the main event, nearby PNSN stations (Figure 2b-2) picked up a faint low frequency rumble coming from the direction of the slide area coinciding with eyewitness reports of increased rockfall and thunder-like sounds coming from the ground. Later that afternoon a small lobe of talus 10 to 15 meters wide, marked initial slide on Figure 2b-5, mobilized. This "foreshock" stopped short of the nearby houses by the late afternoon. After this, all was quiet and the slide seemed to be over.

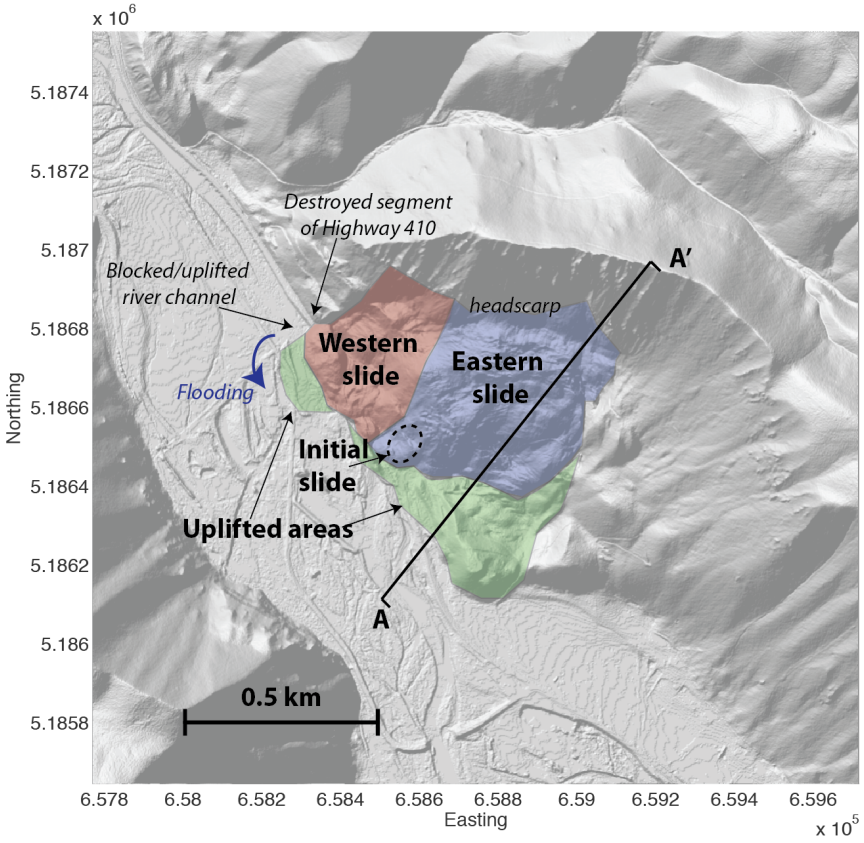

Figure 2b-5 Overview of Nile Valley landslide, cross-section A-A' shown on Figure 2b-4.

Then, in the middle of the night: rockfall and rumbling recommenced. Rumbling at 4-6Hz began to appear on the PNSN stations and started to increase in amplitude and the main sliding sequence began. The rest of the sequence is illustrated on the timeline (Figure 2b-6).

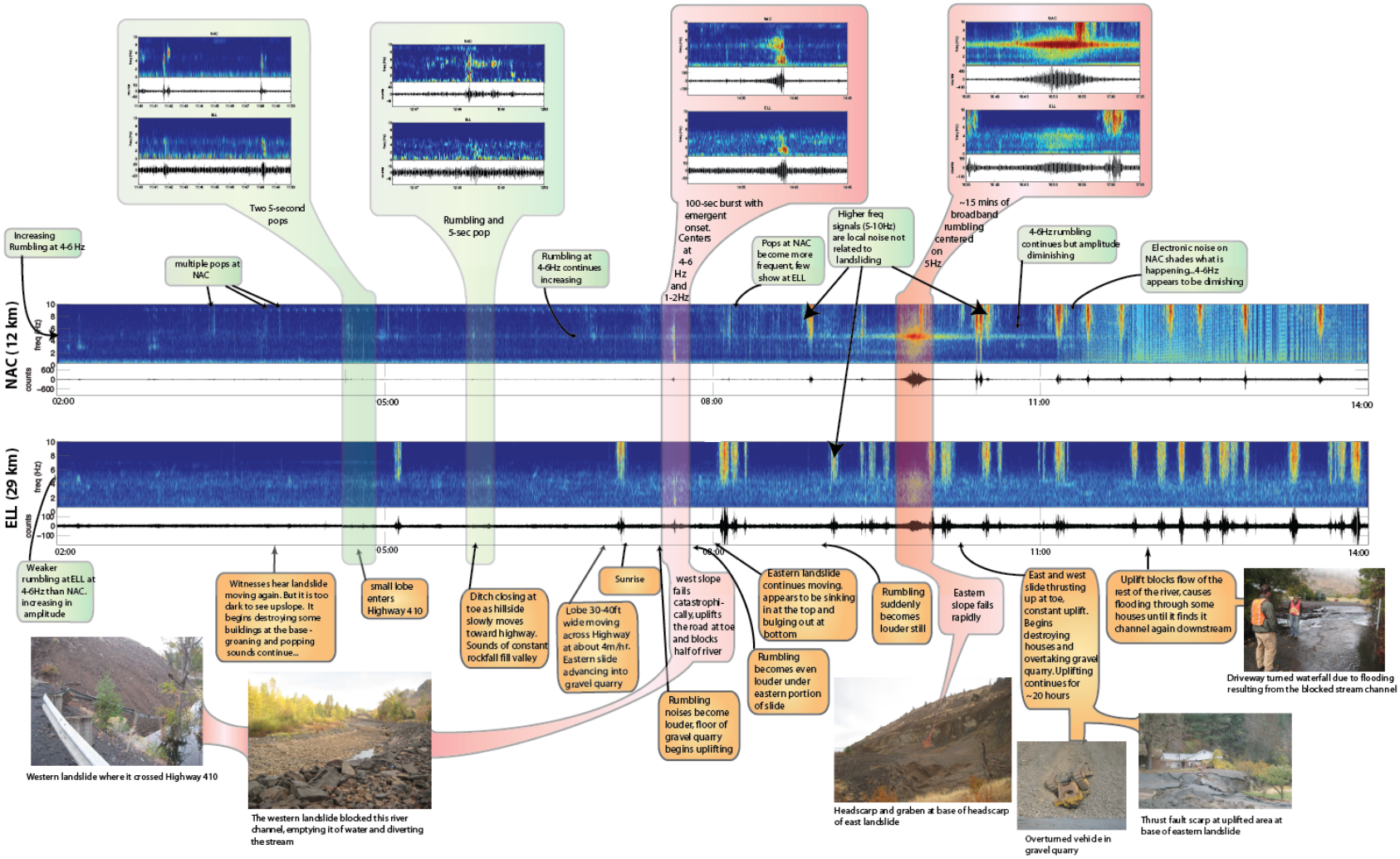
Two 5-second pops
Rumbling and 5-sec pop
100-sec burst with emergent onset. Centers at 4-6 Hz and 1-2Hz
~15 mins of broadband rumbling centered on 5Hz
Increasing Rumbling at 4-6 Hz
multiple pops at NAC
Rumbling at 4-6Hz continues increasing
Pops at NAC become more frequent, few show at ELL
Higher freq signals (5-10Hz) are local noise not related to landsliding
4-6Hz rumbling continues but amplitude diminishing
Electronic noise on NAC shades what is happening...4-6Hz appears to be dimishing
NAC (12 km)
ELL (29 km)
freq (Hz)
counts
02:00
05:00
08:00
11:00
14:00
Weaker rumbling at ELL at 4-6Hz than NAC, increasing in amplitude
Witnesses hear landslide moving again. But it is too dark to see upslope. It begins destroying some buildings at the base - groaning and popping sounds continue...
small lobe enters Highway 410
Ditch closing at toe as hillside slowly moves toward highway. Sounds of constant rockfall fill valley
Lobe 30-40ft wide moving across Highway at about 4m/hr. Eastern slide advancing into gravel quarry
Sunrise
west slope fails catastrophi-cally, uplifts the road at toe and blocks half of river
Rumbling noises become louder, floor of gravel quarry begins uplifting
Eastern landslide continues moving, appears to be sinking in at the top and bulging out at bottom
Rumbling becomes even louder under eastern portion of slide
Rumbling suddenly becomes louder still
Eastern slope fails rapidly
East and west slide thrusting up at toe, constant uplift. Begins destroying houses and overtaking gravel quarry. Uplifting continues for ~20 hours
Uplift blocks flow of the rest of the river, causes flooding through some houses until it finds it channel again downstream
Driveway turned waterfall due to flooding resulting from the blocked stream channel
Western landslide where it crossed Highway 410
The western landslide blocked this river channel, emptying it of water and diverting the stream
Headscarp and graben at base of headscarp of east landslide
Overturned vehide in gravel quarry
Thrust fault scarp at uplifted area at base of eastern landslide

Figure 2b-6 This timeline, in UTC, shows the spectrograms from 1 to 10 Hz and the corresponding seismograms filtered from 1 to 7 Hz for the nearby vertical component short period PNSN stations NAC (Naches, WA) and ELL (Ellensburg, WA). Their locations relative to the landslide are indicated on Figure 2b-2. The seismic timeline is narrated along the top of this and the corresponding eyewitness timeline, paraphrased from the WSDOT compilation (Nile, 2010) is explained along the bottom.

3. Seismic Data

Due to attenuation of higher frequencies, only signals below 7 Hz appeared at NAC and ELL, the two nearby short period vertical component PNSN stations. Several early pops and rumbles (highlighted in green on Figure 2b-6) coming from the direction of the landslide could not be tied to specific movements of the slide observed by eyewitnesses because it was dark at the time. Two clear signals, (highlighted in red on the timeline on Figure 2b-6) can be tied directly with eyewitness reports of the two separate rapid slope failures.

The first signal, at 14:38 UTC, coincides with the rapid failure of the western portion of the slope (refer to Figure 2b-5 for location). The signal builds slowly up from the background rumbling at 4-6Hz and ends 100 seconds later more abruptly. The spectrogram of this part of the signal shows two separate frequency centers and within each of these are discrete peaks of energy, indicating multiple small sources within a complex failure sequence.

The signal at 16:43 UTC corresponds to the rapid failure of the larger eastern slope (Figure 2b-5). This builds up from an increasing frequency of pops and rumbles apparent on NAC. This signal has a clear center between 4-5Hz on NAC, perhaps due to a site amplification effect at that station. Eyewitnesses observed 10 to 20 seconds of rapid failure of this eastern portion of the slope (Nile, 2010), however the signal lasts for 15 minutes. This, and the fact that uplift began with this signal, suggests that much of this signal may be due to the deeper movements on the sliding plane at ~60 m depth. Due to the shallow nature of the source and their

slower attenuation, the seismometers probably recorded mainly surface waves, but they are just vertical component instruments so we cannot confirm by looking at particle motions.

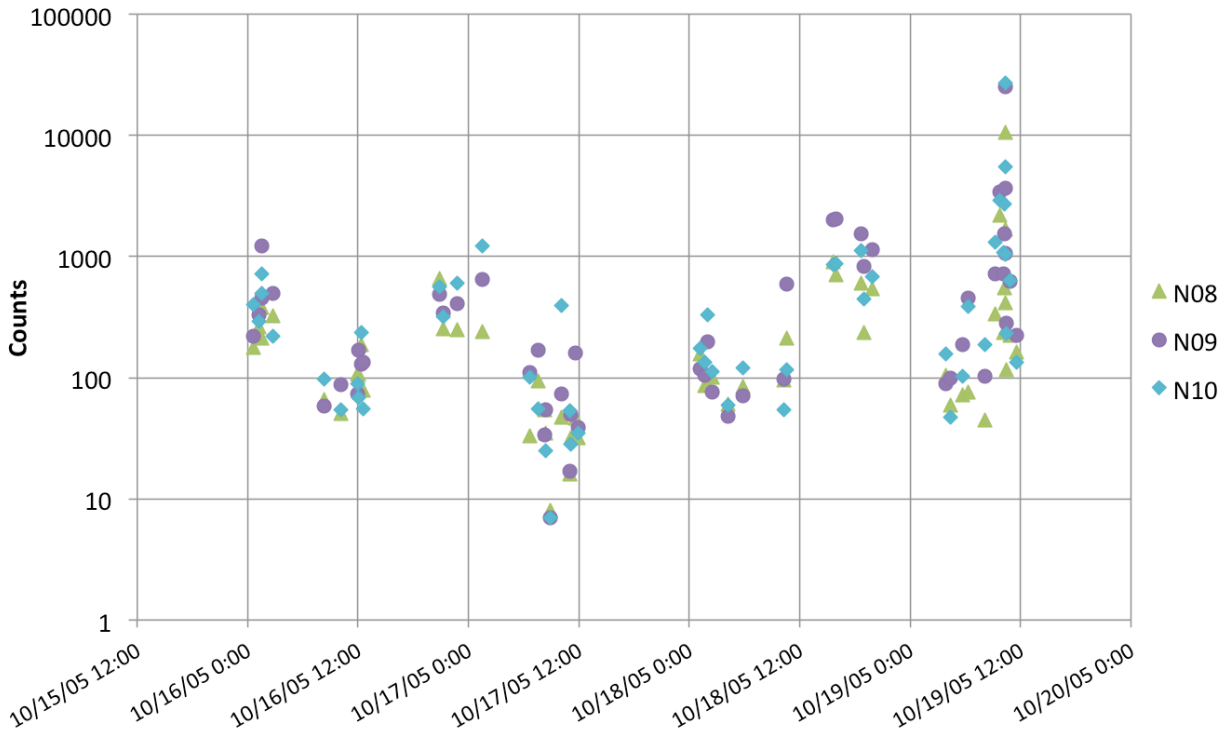

Figure 2b-7 Amplitudes (in counts) of post-slide landslide-related seismic events as recorded on the three stations closest to the activity. Amplitudes are in counts, and have not been corrected for station corrections. The diurnal pattern is because construction noise drowned out any seismic signals during the day.

One week after the main sliding event, we installed 12 vertical geophones and 4 three-component seismic stations around the perimeter to capture the near-source seismic records of any further movements of the slide. Station locations are shown on a post-slide DEM of the area on Figure 2b-8. No further widespread movements occurred during the monitoring period, but more than 60 small events were recorded at these stations in the days after the slide (Figure 2b-7), likely due to settling and continued deformation of the slide mass. One movement 9 days after the main event generated a strong signal that also appeared on the more distant regional stations. Smaller events recorded on the seismic stations at the site showed a buildup in

amplitude hours before this event. The locations of these signals and other strong signals, located by zero-lag cross correlation (Almendros et al., 1999) are shown on Figure 2b-8

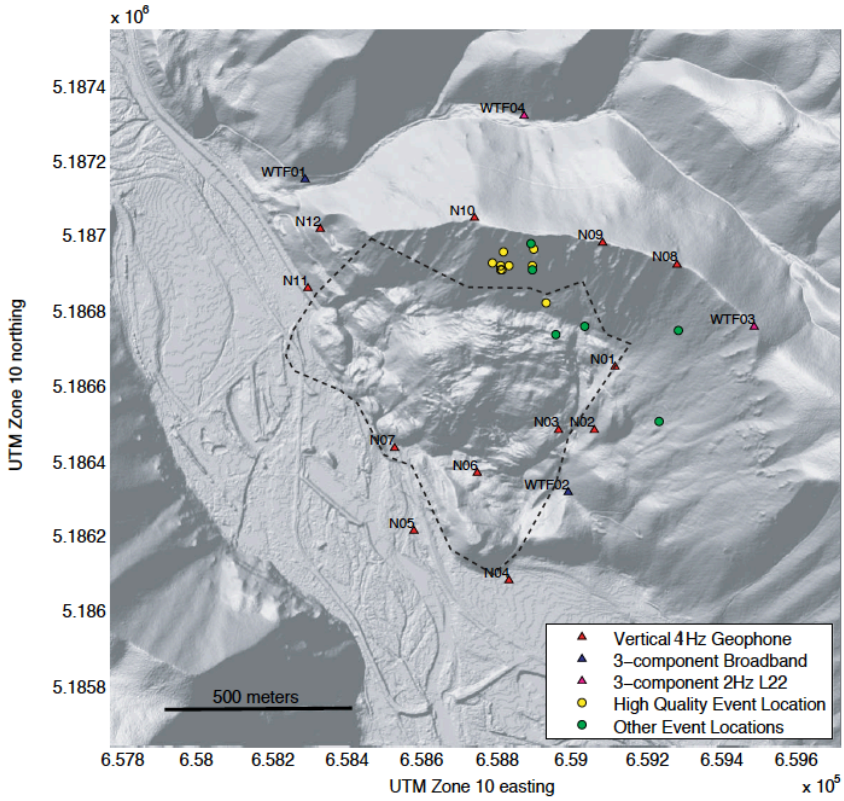

Figure 2b-8 Location of stations installed after the landslide (triangles) and best-fit post-slide event locations (circles). Dashed line outlines approximate slide area.

The locations are all clustered in the same area located above the headscarp, perhaps due to failure of slopes above the newly formed headscarp. WTF2 was telemetered in real-time, and 3-component stations were left out for two months to assist the WSDOT in monitoring and to ensure that the much larger Sanford Pasture landslide wasn't reawakening. Two shallow earthquakes (Md <1.4) were detected in the valley during this time, but further WSDOT investigations did not find any signs that the Sanford Pasture slide was moving.

4. Discussion

The seismic signals generated by the Nile Valley landslide share similar characteristics to other landslide seismograms. Landslide seismic signals typically share emergent, non-impulsive onsets, low maximum amplitudes in relation to duration, no distinct phases, and multiple peaks due to the contribution of many smaller events (Norris, 1994). Some other large landslides emitted long period signals that were recorded by seismographs hundreds to thousands of kilometers away (Berrocal et al., 1978; Kanamori and Given, 1982; Weichert et al., 1994) due to the forces exerted on the earth from the coherent accelerations and decelerations of large volumes over the surface, but there were no noticeable long period signals coming from the Nile Landslide area on any of the PNSN broadband stations. This is particularly apparent when comparing the Mount Meager landslide (Chapter 2a) to the Nile Valley landslide. Both had comparable failure volumes (~10^7 m^3), but the Mount Meager landslide was recorded at long periods up to thousands of kilometers away, whereas the Nile Valley landslide was only recorded as far as 29 km away. A comparison of their waveforms, corrected for station response, is shown on Figure 2b-9. What accounts for this enormous contrast in the seismic manifestation of these two events?

Despite their similar failure volumes, the amplitudes of the seismic recording of the Mount Meager landslide are an order of magnitude larger than the amplitude of the Nile Valley landslide seismogram. Additionally, the frequency content of the Mount Meager landslide is highly concentrated at long periods, whereas the Nile valley landslide is focused more at ~5 Hz, a frequency that attenuates much more rapidly. The peak of amplitude close to 0 Hz is just noise in that case. The long period signal in the Mount Meager landslide comes from the acceleration and deceleration of the failure mass as a whole, the event was so rapid that changes in the forcing

exerted on the earth were fast enough that it could generate waves at high enough amplitudes and short enough periods to be observed seismically, whereas the Nile Valley landslide had much smaller accelerations over a longer period of time, so the force-time function of this event is too elongated in time to generate observable seismic waves.

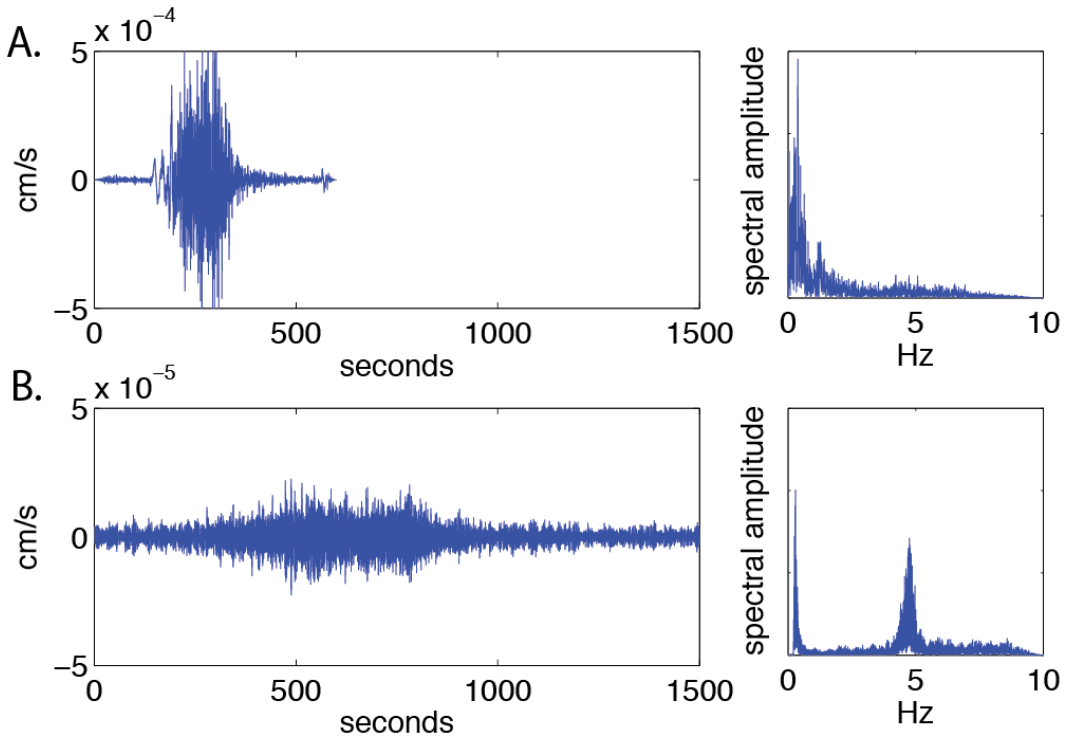

Figure 2b-9 Comparison between recording of Mount Meager landslide at a seismometer 70 km from the source, to the Nile Valley landslide, recorded 12 km from the source. Seismograms are corrected for station response. Left column shows the time series and right column shows the frequency spectra.

To test this idea, we generated synthetic seismograms using the methods of Chapter 2a, but forward modeling rather than an inversion, for a force-time function that could be representative of what occurred during the eastern failure of the Nile Valley landslide: a 15-minute slide of 10^{11} kg of material over a distance of 150 meters as it would have been recorded at the closest broadband station, LTY, located 52 km away (Figure 2b-10). The result was a

maximum displacement of 4 x 10^{-8} cm, 4x lower amplitude than that observed for Mount Meager, at a period of ~0.001 seconds. At these periods, most broadband seismic instruments have rolled off in their sensitivity by 3 orders of magnitude, so these seismic waves would essentially be unobservable by modern methods. The accelerations and time scale of the large-scale failure of the Nile Valley landslide were too low, and too long period, for the landslide to generate observable long-period seismic waves. This is why we only observe the shorter period seismic waves that come from smaller scale processes like the impacts of individual blocks and frictional processes (Chapter 2a), and seismic waves at these frequencies attenuate rapidly, particularly for events located at or near the surface.

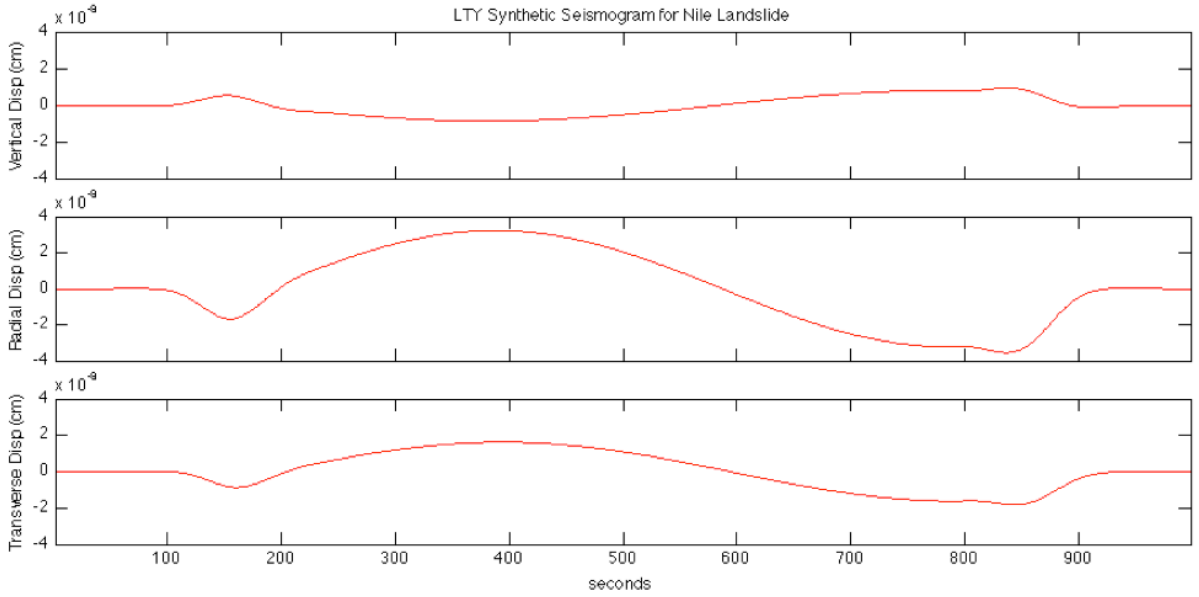

Figure 2b-10 Synthetic seismogram generated for the eastern failure of the Nile Valley landslide as it would have been recorded at the closest broadband seismic station, LTY, 52 km from the landslide source area.

5. Conclusion

This case adds to the sparse catalog of landslide seismograms. It can help in the recognition of landslide signals detected by seismic networks, and in better understanding the

potential uses and limitations of seismically monitoring slope failures. The unfolding of events of this landslide is accompanied by a timeline observed by eyewitnesses and timestamped by seismograms. This landslide showed precursory signs of activity, though in this case the seismic stations were too distant to record much. A few studies (Senfaute et al., 2009; Caplan-Auerbach, and Huggel, 2007; Huggel et al., 2008) have found other landslides that show precursory seismic activity. A better understanding of this phenomenon has the potential to be used to forecast imminent slope failure.

6. Acknowledgements

Thanks to the WA State Department of Transportation, particularly Tom Badger as well as Doug Anderson and Gabe Taylor who pieced together the timeline from eyewitnesses, and the WA Dept of Natural Resources for working with us and sharing information to piece together the story. In addition, thanks to IRIS PASSCAL for leading us equipment on short notice and Agnes Helmstetter from the Laboratoire de Géophysiqe Interne et Tectonophysique at L'Université Joseph Fourier, Grenoble for sharing her event location methods.

7. References

Almendros, J., J.M. Ibanez, G. Alguacil and E.D. Pezzo (1999). Array analysis using circular-wave-front geometry: an application to locate the nearby seismo-volcanic source, Geophys. J. Int., 136, 159-170.

Berrocal, J., A.F. Espinosa and J.Galdos (1978). Seismological and geological aspects of the Mantaro landslide in Peru. Nature. 275, 533-536.

Caplan-Auerbach, J. and C. Huggel (2007). Precursory seismicity associated with frequent, large ice avalanches on Iliamna volcano, Alaska, USA, J. of Glaciology, 53, 128-140.

Hammond, P.E. (2009a). Geologic map of the Meeks Table and western two-thirds of the Nile 7.5-minute quadrangles, Yakima (County, Washington: Washington Division of Geology and Earth Resources Geologic Map GM-74, 1 plate, 12 p. text.

Hammond, P.E. (2009b). Supplement to GM-74, geologic map of the Meeks Table and western two-thirds of the Nile 7.5-minute quadrangles, Yakima County, Washington: Washington Division of Geology and Earth Resources Open File Report 2009-3, 1 DVD.

Nile Landslide Timeline Narrative Report (2010). Washington State Department of Transportation, Unpublished Report 5

Huggel, C., J. Caplan-Auerbach and R. Wessels (2008). Recent Extreme Avalanches: Triggered by Climate Change? EOS 89, 469-470.

Kanamori, H., and J.W. Given (1982). Analysis of Long-Period Seismic wave Excited by the May 18, 1980, eruption of Mount St. Helens – A Terrestrial Monopole? J.Geophys. Res. 87, 5422-5432.

Norris, R.D. (1994). Seismicity of rockfalls and avalanches at three cascade range volcanoes: Implications for seismic detection of hazardous mass movements, Bull. Seis. Soc. Am., 84, 1925-1939.

Senfaute, G., A.Duperret and J.A. Lawrence (2009). Micro-seismic precursory cracks prior to rock-fall on coastal chalk cliffs: a case study at Mesnil-Val, Normandie, NW France, Nat. Haz and Earth Sys. Sci.. 9, 1625-1641.

Weichert, D., R. B. Horner and S. G. Evans (1994). Seismic signatures of landslides: the 1990 Brenda Mine Collapse and the 1965 Hope Rockslides, *Bull. Seismol. Soc. Am*., *84*(5), 1523-1532.

Chapter 3 – Glacier-quakes mimicking volcanic earthquakes:

Swarms of repeating stick-slip glacial earthquakes triggered by snow loading at Mount Rainier

Table of Contents

Summary 3-3

1. Introduction 3-4

2. Background 3-8

3. Detection and Characterization 3-12
   3.1 Comprehensive Repeating Earthquake Search 3-12
      3.1.1 Methods 3-12
      3.1.2 Results 3-15
   3.2 Correlation with Weather 3-19
   3.3 Locations 3-22
   3.4 Recurrence Time vs. Event Size 3-28
   3.5 Source migration over time - coda wave interferometry 3-31
      3.5.1 Methods 3-31
      3.5.2 Results 3-36

4. Discussion 3-38
   4.1 What is the source mechanism? 3-38
   4.2 Why is this behavior transient and triggered by precipitation? 3-43
   4.3 Broader Implications 3-53

5. Conclusions 3-56

6. Acknowledgements 3-58

7. References 3-58

Summary

We have detected over 150,000 low-frequency (~1-5 Hz) repeating earthquakes over the past decade at Mount Rainier volcano by scanning archived continuous seismic data from the permanent seismic network. Most of these were previously undetected due to their small size (M<1), shallow locations, and emergent waveforms. The earthquakes are located high (>3000 m) on the steep glacier-covered part of the edifice, primarily beneath hanging glaciers and icefalls. They occur primarily in week- to month-long swarms of activity that are composed of simultaneous distinct families of events. A given family can be composed of up to thousands of nearly identical earthquakes repeating at regular intervals, as often as every few minutes. The swarms strongly correlate with precipitation, namely snowfall, with a lag averaging a day or two. By stacking several thousand repeats of the same earthquake, we found that at least the largest families have mostly mixed polarity first motions, suggesting a shear source. On short timescales, there is a linear relationship between inter-event repeat time and the size of the subsequent event - consistent with slip-predictable stick-slip behavior. These observations suggest the source is stick-slip basal sliding of glaciers, and that the additional load imparted by the sudden added weight of snow during winter storms triggers a temporary change from smooth aseismic sliding to seismic stick-slip sliding in locations where basal conditions are favorable to frictional instability. The lag in response to snow loading suggests that the redistribution of basal water is responsible rather than the loading directly. Using coda wave interferometry, we estimated source migration over time for several of the largest event families and found they all moved at glacial speeds, suggesting the sources are dirty basal patches that move with the ice rather than stationary asperities. Speeds start out faster than typical sliding velocities and slow down over time suggesting that the trigger of stick-slip motion is a sudden increase in sliding

velocity. The reappearance of some event families up to several years apart suggests that certain areas at the base of certain glaciers are prodigious producers of conditions favorable to this behavior. Identification of the source of these frequent signals offers a view of basal glacier processes, discriminates against alarming volcanic noises, documents short-term effects of weather on the cryosphere, and has implications for repeating earthquakes in tectonic environments.

1. Introduction

Mount Rainier, a 4,392-meter glacier-clad stratovolcano in Washington State (Figure 3-1), is one of the most dynamic landscapes in the world, making it also one of the seismically noisiest. Clear identification of seismic events and assessment of source mechanisms is a fundamental aspect of both volcano monitoring and understanding landscape dynamics. Researchers must be able to distinguish seismicity generated by volcanic activity from ice movement, wind, rock fall, debris flows, and human activity. This is not always straightforward. Benign events related to glacier activity, like surface crevassing, serac collapse, and basal sliding, can mimic subtle signals that are often associated with volcanic fluid or gas movement (Weaver and Malone, 1976; West et al., 2010; Thelen et al., 2013). Nowhere is this more obvious, perhaps, than at Mount Rainier. Mount Rainier is the most glacier-clad mountain, by volume, in the conterminous United States (Hoblitt et al., 1995) and is also an active volcano with the largest at-risk population in the country (Ewert et al., 2005). The convergence of these factors makes timely and accurate identification of seismic events at Mount Rainier both difficult and an issue of great public concern.

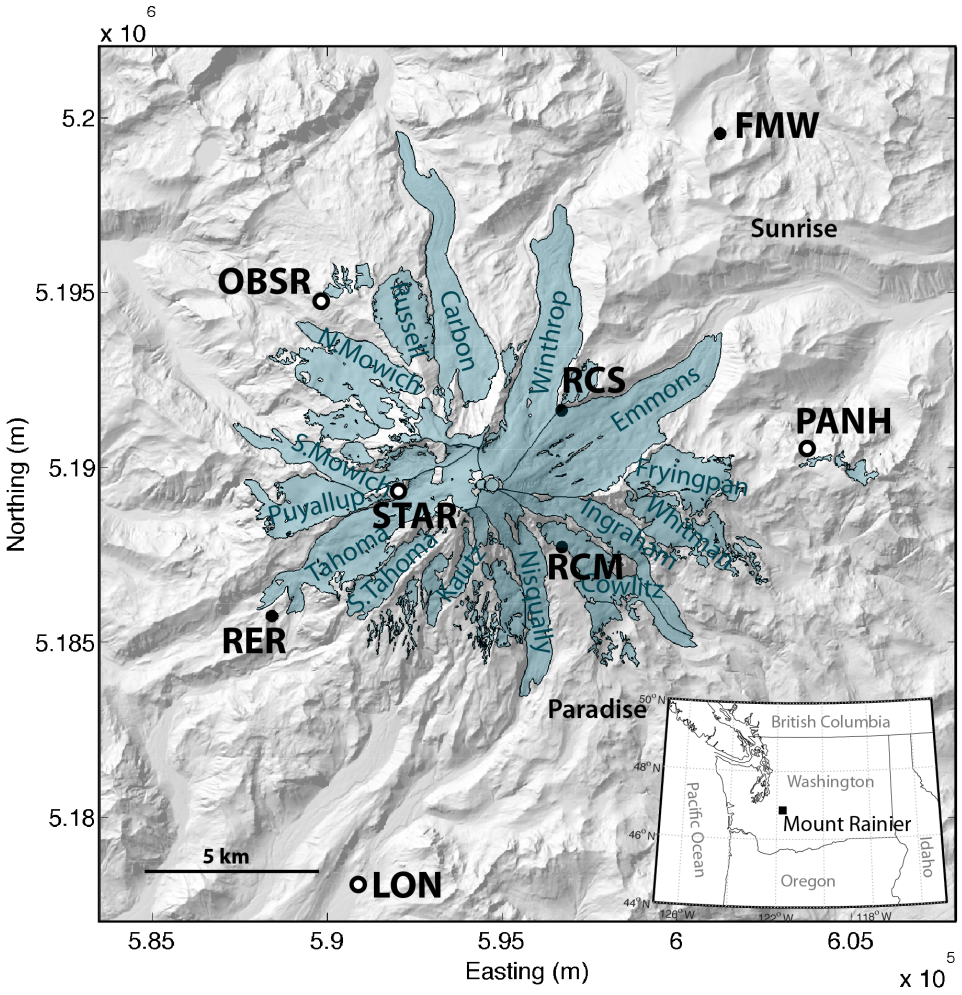

Figure 3-1 Seismic stations and glaciers at Mount Rainier. White dots indicate three-component station. Inset map shows regional location of Mount Rainier. The approximate locations of the Paradise and Sunrise visitor centers are indicated.

This challenge came to light in May and June 2010 when analysts at the Pacific Northwest Seismic Network (PNSN) and USGS Cascade Volcano Observatory (CVO), responsible for monitoring the volcano, observed a swarm of low-frequency (<5Hz) repeating earthquakes. Too small to trigger automated event detection algorithms, the earthquakes were instead detected visually on seismic records due to their regular recurrence intervals and nearly identical waveforms. This activity was of concern because repeating low-frequency seismicity often accompanies, and has been a precursor to, volcanic activity at volcanoes worldwide (Chouet et

al., 1994). However low-frequency and repeating earthquakes have also been attributed to glacial activity (e.g., Jonsdottir et al., 2009, Carmichael et al., 2012). After fully characterizing the swarm, Thelen et al. (2013) concluded that the swarm was actually glacial in origin, most likely basal stick-slip sliding. The main line of evidence was the correlation between two bursts of repeating earthquake activity that coincided with the timing of two passing storms. Glaciers are more likely to respond to weather forcing than the volcano. Thelen et al. (2013) attributed the appearance of the swarm to a glacial speedup triggered either by the rapid input of water in the Spring (e.g. Harper et al., 2007), or snow loading since the events were located high on the mountain where it was still snowing at that time of year.

However, the study by Thelen et al. (2013) left many questions unanswered. Spring melts and snowfall happen every year, and Mount Rainier is always covered in glaciers. Why, then, did we not see these repeating earthquakes all the time? The only other time this type of activity had been documented at Mount Rainier were three much shorter-lived swarms of repetitive earthquakes in the 1990's. Is the behavior of glaciers at Rainier changing? Or does this type of seismic activity occur all the time but we just didn't know to actively look for it?

Secondly, assuming the source mechanism is in fact glacial in origin, what exactly are the glaciers doing and what is triggering this change in behavior? Repeating earthquakes generated by glaciers elsewhere have been documented before (e.g. Carmichael et al., 2012; Jonsdottir et al., 2009; Wiens et al., 2008; Caplan-Auerbach and Huggel, 2007), but to our knowledge, not in this setting nor triggered by short-term weather forcing. Understanding the glacial processes responsible can contribute to our knowledge of glacier dynamics. Furthermore, as put forth by Walter et al. (2013), we need to understand basal seismicity fully before using it as a proxy for glacier sliding, subglacial erosion, or other processes near the bed of glaciers. Mount Rainier

provides a good setting to accomplish this because it has been seismically monitored continuously for decades, with archived continuous data stretching back about 12 years. Weather records stretch back even further. This long time series of observations allows us to look at secular trends as well as seasonal changes, whereas most seismicity studies of glaciers are done using temporary arrays and/or during the summer field season, which means much of the picture can be missed.

Third, assuming Thelen et al. (2013) was correct in hypothesizing that the source is basal stick-slip sliding of glaciers, what causes the sliding behavior to transition from aseismic smooth sliding to seismic stick-slip sliding? This has ramifications not only for understanding the basal processes of glaciers (e.g. Zoet et al., 2013b), but also as an analog for understanding why and when the same transition takes place for slip on tectonic faults. Repeating earthquakes have been observed over a wide range of scales and environments, from the aforementioned glacial and volcanic environments, to crustal faults (Nadeau et al., 1995, Dreger et al., 2007) and during episodic tremor and slip (e.g., Shelley et al., 2007). Some have observed that seismic behavior in these settings is also modulated by minor stress changes such as tidal stresses (Sweet et al., 2012; Rubenstein et al., 2008; Nakata et al., 2008) or dynamic triggering from teleseismic waves (e.g., Peng et al., 2009). The same laws of physics apply to all of these environments, so understanding how small variations in stress from snow loading and/or basal fluid pressures can cause a glacier to change from aseismic to stick-slip sliding and why these earthquakes repeat can lend insight to similar processes in other environments.

Finally, the recognition that the particular swarm characterized by Thelen et al. (2013) was glacial in origin was a start toward improving volcano monitoring abilities, but we still need ways to discriminate benign glacially generated repeating earthquakes from those related to

volcanic activity. How can we reliably tell the difference? This problem was identified decades ago (e.g. Weaver and Malone, 1976, 1979), yet little progress has been made since. However, with the onset of improved methods, continuous data, more seismic stations, and ever-increasing computing power, the outlook for making real progress is positive. This has ramifications beyond just Mount Rainier. There are numerous glacier-covered volcanoes in the world that face similar monitoring challenges (e.g. Metaxian et al, 2003).

With these motivations in mind, we embarked on the current study. In the first section, we detail the study area and describe the characteristics of the low-frequency repeating earthquakes that are the focus of this investigation. Next, we describe the catalog of repeating earthquake activity over the past decade at Mount Rainier that we compiled by developing methods to search through the entirety of the archived continuous seismic data. We then use this catalog to investigate how these earthquakes behave over time, correlate with and react to weather forcing, where they are located, and how their source locations migrate over time. Finally, we discuss what these observations can tell us about the source processes responsible for generating these earthquakes and discuss the wider implications in terms of understanding glacier dynamics, the physics of stick-slip behavior, and repeating earthquakes in general.

2. Background

Mount Rainier is an active stratovolcano located about 90 km southeast of Seattle. It is contained within Mount Rainier National Park and receives 1.5 million visitors to its flanks every year (National Park Service, 2013a). The mountain is almost completely covered in glaciers, having the highest concentration of glacial ice in the coterminous United States (Driedger and Kennard, 1986). There are 23 major glaciers (Figure 3-1). As of 2008, Mount Rainier glaciers cover 87 km^2 (Sisson et al., 2011). Most of the glaciers are thinning and

retreating, having lost a total of 13-15% of the ice volume from 1970 to 2008 (Sisson et al., 2011). The glaciers are thin in the steep upper sections, ranging from about 30 to 80 meters, and become thicker at lower elevations, with the thickest glacier being the Carbon glacier that reaches about 200 meters (Driedger and Kennard, 1986). Mount Rainier's glaciers are characterized as temperate alpine glaciers, meaning they are at their melting point from surface to bed throughout the year. Their movement is dominated by basal sliding (Hodge, 1974).

In part because of the large amount of frozen water stored on its flanks, Mount Rainier is the most hazardous volcano in the U.S., designated for this reason as a "decade volcano" by the National Academy of Sciences (Swanson et al., 1994). Recent estimates put 2.5 million people and $40 billion in assets at risk from lahars originating at the volcano (Cakir and Walsh, 2012). Lahars are debris flows that often occur because of the rapid melting of ice and snow during eruptive activity. The largest lahars in the past have reached as far as Puget Sound, and many densely populated areas overlie old lahar deposits (Hoblitt et al., 1998). Mount Rainier experienced minor eruptive activity a few times in the mid to late 1800's (Mullineaux et al., 1969), but the last major eruptive period was about 1000 years ago (Sisson and Vallance, 2009).

Because there is so much at stake, Mount Rainier is monitored in near real-time for signs of volcanic activity, primarily through seismic monitoring. The seismic monitoring network (Figure 3-1) consists of 10 total stations within 20 km of the summit. Three short-period high-gain stations, RCM, RCS and STAR, are located high on the mountain, at around 3000 meters elevation. All are vertical component sensors except STAR, which has three components. The rest of the stations are a mix of broadband three-component stations (OBSR, PANH, LON) and vertical component short period stations (RER, FMW, LO2, RVC (not shown)). The data from these stations is telemetered and earthquake activity is monitored jointly by the PNSN and CVO.

Mount Rainier is known for its high annual snowfall, receiving an average of 16.3 meters of snow at the Paradise Visitors Center each year (National Park Service, 2013b). Weather, including precipitation, is monitored hourly in near real-time at several weather stations run by the Northwest Weather and Avalanche Center (NWAC, www.nwac.us) and the National Weather and Climate Center (http://www.wcc.nrcs.usda.gov/). We use data from station PVC (Figure 3-1) an NWAC weather station operated by the near the Paradise Visitor Center.

The low-frequency repeating earthquakes that are the focus of this study have several general characteristics. They are small, with magnitudes ranging from -1 to 0, and they are located at high elevations (>3000 m) at shallow depths (Thelen et al., 2013). They often occur at regularly spaced intervals, with some scatter around a mean (Figure 3-2A), and have highly similar waveforms between events in the same family (Figure 3-2B). In this study, we use family to refer to a set of earthquakes that all share a similar waveform, and swarm to refer to an uptick in earthquake activity of any type that is not a mainshock/aftershock sequence. Though recurrence intervals are regularly spaced and waveforms are highly similar in the short term, sometimes there are gradual evolutions and sudden jumps in both factors over the duration of a family (Thelen et al., 2013). We characterize these events as "low-frequency" because their frequency content is much lower than a similarly sized tectonic earthquake occurring deeper in the volcano, and the first arrivals are emergent, meaning the signal emerges gradually from the noise rather than having a clear and sharp first motion (Figure 3-2C).

We estimate the mean frequency content of each event using the dominant frequency, $\bar{f}$, which is computed by:

(3-1) $$\bar{f} = \frac{1}{2\pi}\sqrt{\frac{\int_0^t \dot{u}^2(t')dt'}{\int_0^t u^2(t')dt'}}$$

where u is the waveform, $\dot{u}$ is its derivative, and each is integrated from the first motion to the end of the signal, 0 to t (Snieder, 2006). A typical low-frequency repeating earthquake has a dominant frequency of ~5 Hz (Figure 3-2D).

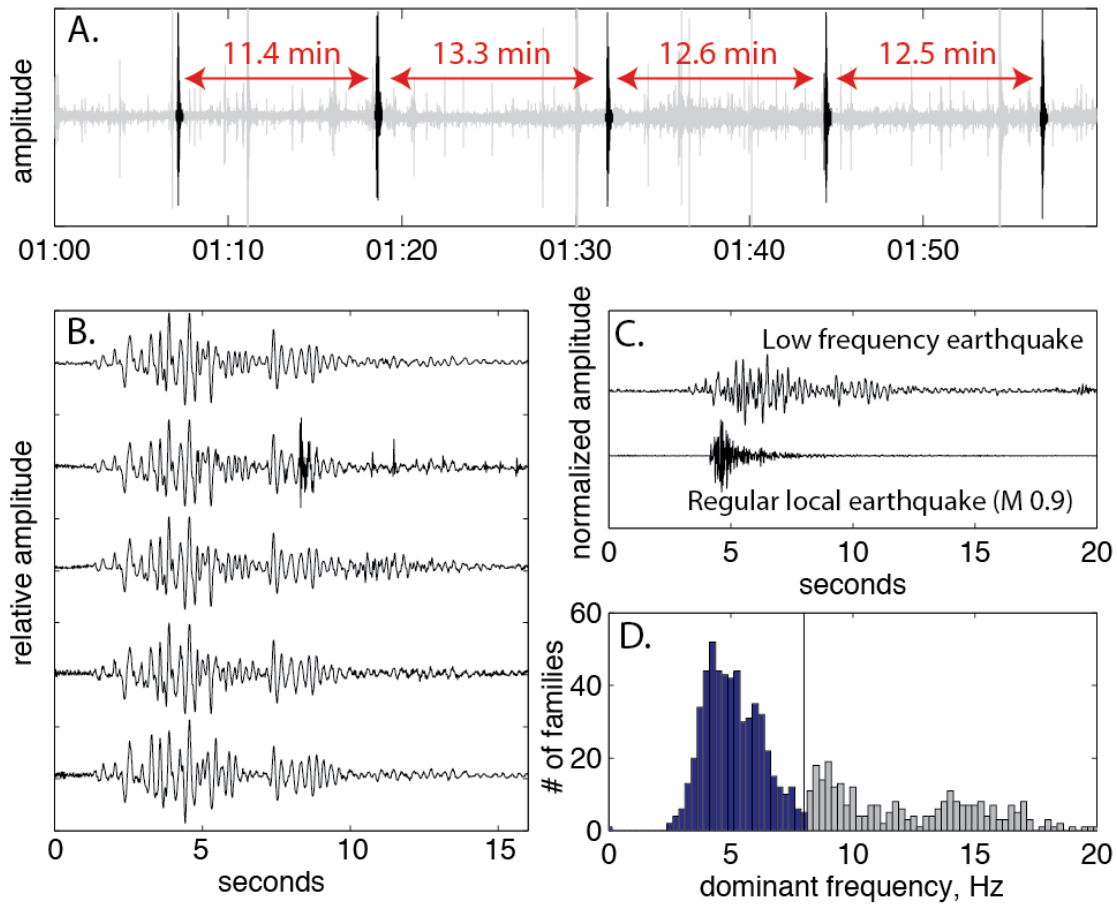

Figure 3-2 Characteristics of the low-frequency repeating earthquakes at Mount Rainier: (A.) The earthquakes repeat at semi-regular intervals with (B.) nearly identical waveforms. These 5 events are the repeating waveforms highlighted in A., plotted on the same amplitude scale (C.) The frequency of these events (top) is lower than regular volcano-tectonic earthquakes (bottom). (D.) A histogram of the dominant frequency of all repeating event families detected since 2003 shows that most have a dominant frequency below 8 Hz (blue), the cutoff used in this study (vertical line). Those with higher frequencies are most likely due to crevassing.

In some cases, the longer period waveforms of glacial earthquakes have been attributed to a slower source process (e.g. Ekstrom et al., 2003), but for the events at Rainier, Thelen et al., (2013) argues that the low amplitudes and low frequency content are a result of path effects: strong alteration and attenuation of the waves as they travel through the shallow, heterogeneous subsurface. This is a typical alteration that occurs to waveforms of all shallow earthquakes in stratigraphically complex volcanic terrains. This is because the wave paths of shallow events travel more horizontally primarily through the heterogeneous, low-velocity shallow layers. Higher frequency waves are attenuated much more rapidly than lower frequency waves (Stein and Wysession, 2003). Shallow waves graze the surface when propagating to seismic stations at lower elevations resulting in the development of surface waves that attenuate less rapidly and can have lower frequency content (Neuberg and Pointer, 2000). The case for strong path effects causing the low-frequency waveforms observed for these events at Mount Rainier is supported by active and passive source studies on Cascade Volcanoes including Mount Rainier (Weaver and Malone, 1976, 1979; Allstadt et al., 2012). They found that when glacial earthquakes were recorded by seismic stations located nearby on the ice, the waveforms were impulsive and had broadband waveforms, but the same event recorded on rock further away yielded the low-frequency emergent waveforms typical of these repeating earthquakes.

3. Detection and Characterization

3.1 Comprehensive Repeating Earthquake Search

3.1.1 Methods

In order to determine whether there have been other repeating earthquake sequences in the past that went undetected, we conducted a comprehensive repeating earthquake search through

all the archived seismic data. Archived data goes back to 2001 for some seismic stations, but we started the search in 2003 because there are a lot of gaps in the data until that point. We conduct the search using codes modified from those developed by Carmichael (2013). Carmichael's (2013) methods are unsupervised, meaning the user does not need to define template events to detect repeating earthquakes. The methods are also set up to detect repeating earthquakes using the simultaneous correlation of data from an entire seismic array, but we found that was not practical at Mount Rainier because if one station was not operating or was saturated by noise (e.g. wind), a frequent occurrence at these rugged high mountain stations, the noise reduced the array correlations such that repeating earthquakes that were still recorded clearly on other stations were not detected. So instead we detected repeating earthquakes for data from each seismic station independently and combined detections at the end. Individual repeating earthquakes are typically low in amplitude and only appear on the three edifice stations (RCS, RCM and STAR). However, STAR, was not installed until 2008 and archived data is only available starting in 2010, so we only present detection results from RCS and RCM, which have remained relatively unchanged since before 2003 in order to present a consistent picture of patterns in activity over time.

In order to search for repeating earthquakes, we started by loading in each day of data, filtering it between 1 and 10 Hz, and using a short term average/long term average (STA/LTA) pick detector (short window of 0.8 seconds, long window of 7 seconds, STA/LTA ratio of 4) to find event pick times. We extracted 25 seconds of data around each pick time, starting 5 seconds before. It is common to get several thousand event detections per day on each station by this method because Mount Rainier is such a seismically noisy place. This number of events overwhelmed the repeating earthquake detection algorithms so in order to cut out picks that are

unlikely to contain a real event we excluded events with a signal width (Meier and Lee, 2009) greater than 15 seconds. We found this excluded longer rumbly events like wind noise without eliminating the low-frequency repeating earthquakes.

Once the data for all the picks detected in a day were extracted, we then cross correlated every event with every other event in that day and grouped them into families. To be grouped together, all events must have a normalized cross correlation of >0.7 with all other events in the family. Any ungrouped events within each day were discarded. This means that in order to be detected, a repeating earthquake must repeat at least once within the same day - a condition easily met for the repeating earthquakes we are searching for. Next, we computed a median stack (line all waveforms up in time and take the median at each time interval) for each family of events detected in each day to suppress noise and condense the family into a single representative waveform. Then we compared the stacks from each day to every other day within that month and grouped them again into larger families. Families with more than 5 repeats in a month were saved. All event families were visually examined and any false families like calibration pulses, data spikes, and repeating waveforms from events originating from nearby Mount St. Helens were deleted. The remaining families were then restacked and compared with all the families detected in the adjacent 3 months on either side and regrouped again. At this step, because we were comparing stacks and noise is suppressed, we used a higher correlation coefficient of 0.8 to combine families.

These larger families were then restacked again, and then each stacked waveform was scanned through the data as a template, pulling out any missed detections within one month on either side of the first and last event detection of that family. We used a lower cross correlation threshold of 0.6 in order to pull out even noisy events. This template search resulted in some

individual events being grouped into more than one family if two families were similar enough for that event to have a correlation above 0.6 with both of them, so we found any events that were grouped into more than one family and deleted all instances of that event except for the one with the highest correlation. Finally, once this catalog was completed for both RCS and RCM, we compared the two catalogs and families for which at least 10% of the total events overlapped between the two stations were considered to be the same family. All these steps except for the visual inspection of waveforms were automated using MATLAB coding. The entire search took about a week to run; the biggest time limitation was downloading the archived seismic data.

3.1.2 Results

The results of this search are shown in Figure 3-3, events detected by at least one station are shown in red, those detected on both RCS and RCM are shown in blue. We only show events with a dominant frequency of less than 8 Hz on this figure. We consider 8 Hz a cut-off for a "low-frequency" repeating earthquake. We choose this cutoff because there is a clear clustering of the dominant frequency of repeating earthquakes families below 8 Hz (Figure 3-2D), and families with a higher dominant frequency typically do not appear on more than the closest station, do not repeat at regular intervals, and occur just as often or even more often in the summer as in the winter (Allstadt et al., 2012), suggesting they are related to a different source, probably localized crevassing (e.g. Neave and Savage, 1970). We do not address these events in this study.

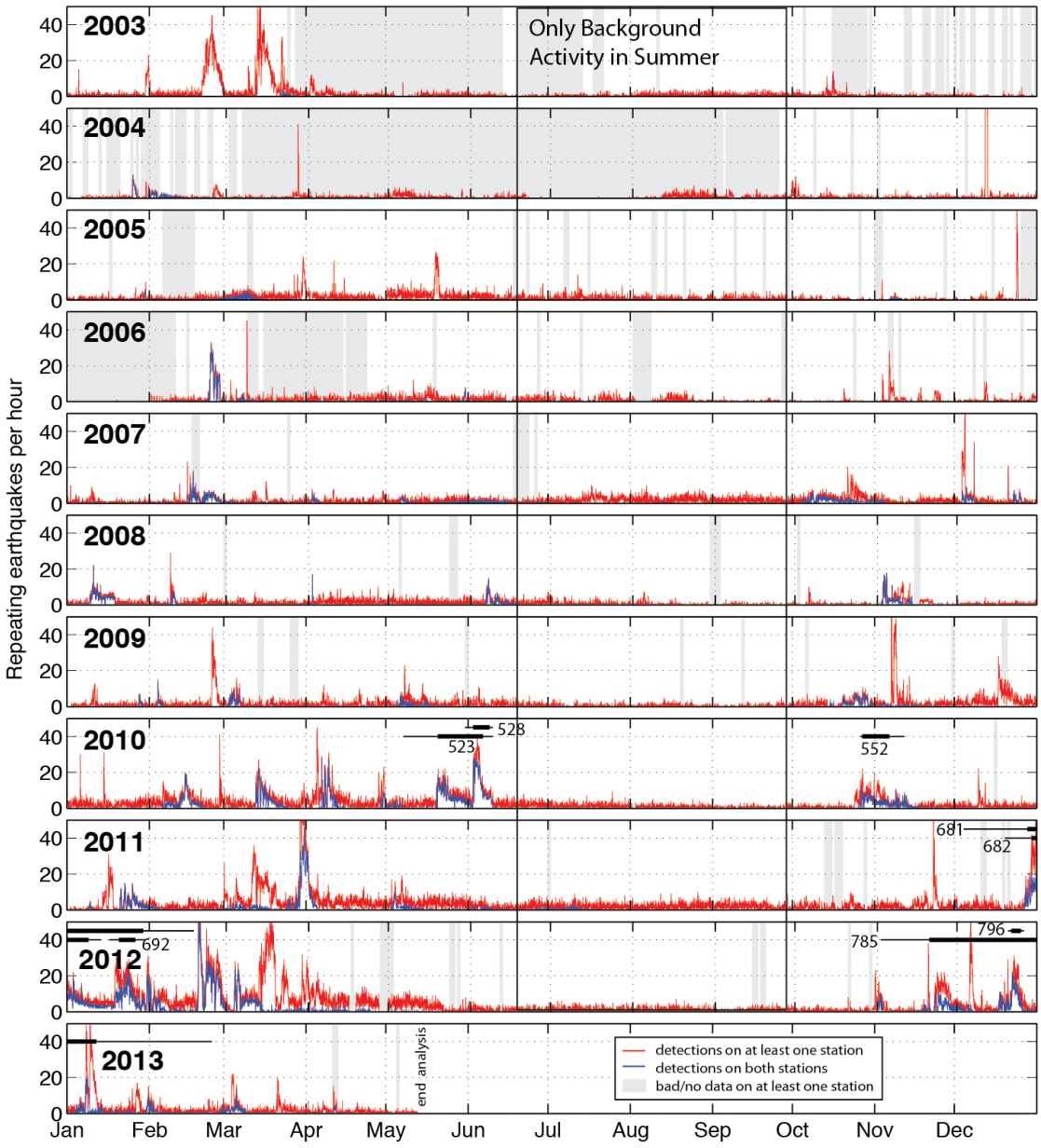

Figure 3-3 Repeating low-frequency earthquakes detected per hour by stations RCS and RCM. Blue indicates detections that occurred on both stations, gray shading indicates when at least one station had an abnormal signal RMS (i.e. wasn't functioning properly). Black lines indicate the span of select families; the thick line delineates the span of 90% of the events in that given family.

RCS had less downtime and seems to record more repeating earthquakes than RCM, probably because it is immediately adjacent to two major glaciers, so its catalog is more complete. We detected 299,558 repeating earthquakes grouped in 840 families at RCS. Of these

families, 559 families containing 150,271 events had a dominant frequency of less than 8 Hz. At RCM, we detected 61,772 repeating earthquakes in 372 families, 369 of these families had a dominant frequency below 8Hz, containing 61,398 events. Far fewer higher-frequency crevassing events were detected at RCM, probably because it is not as close to major glaciers as RCS. 87 families were shared between RCS and RCM. The rest of the families that were not shared either were too low energy to appear above the noise on the other station, or one of the stations was either not working or saturated with noise, for example, signals at RCM are often drowned out by high wind noise, and RCM was not functioning for significant portions of the study period.

An initial glance at Figure 3-3 reveals that low-frequency repeating earthquakes have in fact been happening all along; we just didn't know to look for them so we didn't find them. Individual events often only show up at the three highest stations, so the seismic network does not detect them automatically, and visual detection is difficult because these high mountain stations are extremely noisy. For this reason, only the most obvious sequences were noticed in the past.

Secondly, Figure 3-3 shows that though there is always a background level of low-frequency earthquake activity that hovers around ~5 events per hour, the big swarms of activity like the ones that originally attracted attention to this phenomenon (e.g. Thelen et al., 2013) only occur from late Fall to early Spring - essentially the accumulation season. Most swarms reach at least 20 events per hour, but the repeating earthquake activity sometimes exceeds 50 events per hour, meaning there is an event nearly every minute.

A third conclusion one can make from Figure 3-3 is that there is a secular increase in low-frequency repeating earthquake activity starting in the autumn of 2009. This cannot be attributed

to changes in the seismic stations. The changes that have occurred at RCM include a change in the type of sensor from a Kinemetrics Ranger SS-1 to a Mark Products L-4 on 6 Aug 2006, and a replacement of the L-4 on 13 Aug 2010. The gain was halved on 1 April 2008 and then increased by half on 13 Aug 2008 and has stayed stable since. RCS has been a Mark L4 sensor since 2003, the only change was that it was replaced with a new one on 7 July 2005 and moved to a quieter location a few meters away on 26 July 2006. The only gain change since 2003 was when the gain was halved on 1 April 2008. None of these changes correspond to obvious changes in the number of repeating earthquakes detected except for a reduction in the outage time staring mid-2006.

To clarify the complex behavior of these swarms, we focus on a time period containing a few consecutive swarms and plot a timeline of repeating earthquake activity (Figure 3-4). The swarms are typically composed of more than one dominant family that all start around the same time, typically coinciding with an increase in the snow depth recorded at PVC. Each family tends to start out with large variability in the correlation between individual events and the stack of all events in the family, but after a few hours or days, the waveforms become more consistent (i.e. highly correlated). Then, the correlation and event rate gradually drifts and the family ends. When another storm passes through and drops more snow, old families tend to shut off (though there are some important exceptions, like family 681 on Figure 3-4, which will be discussed later) and new families appear and follow a similar pattern. There are exceptions to these general observations. Some event families, such as families 704 and 721 on Figure 3-4, do not follow these trends, but the families that contribute most to the swarm-like character of the repeating earthquake activity do.

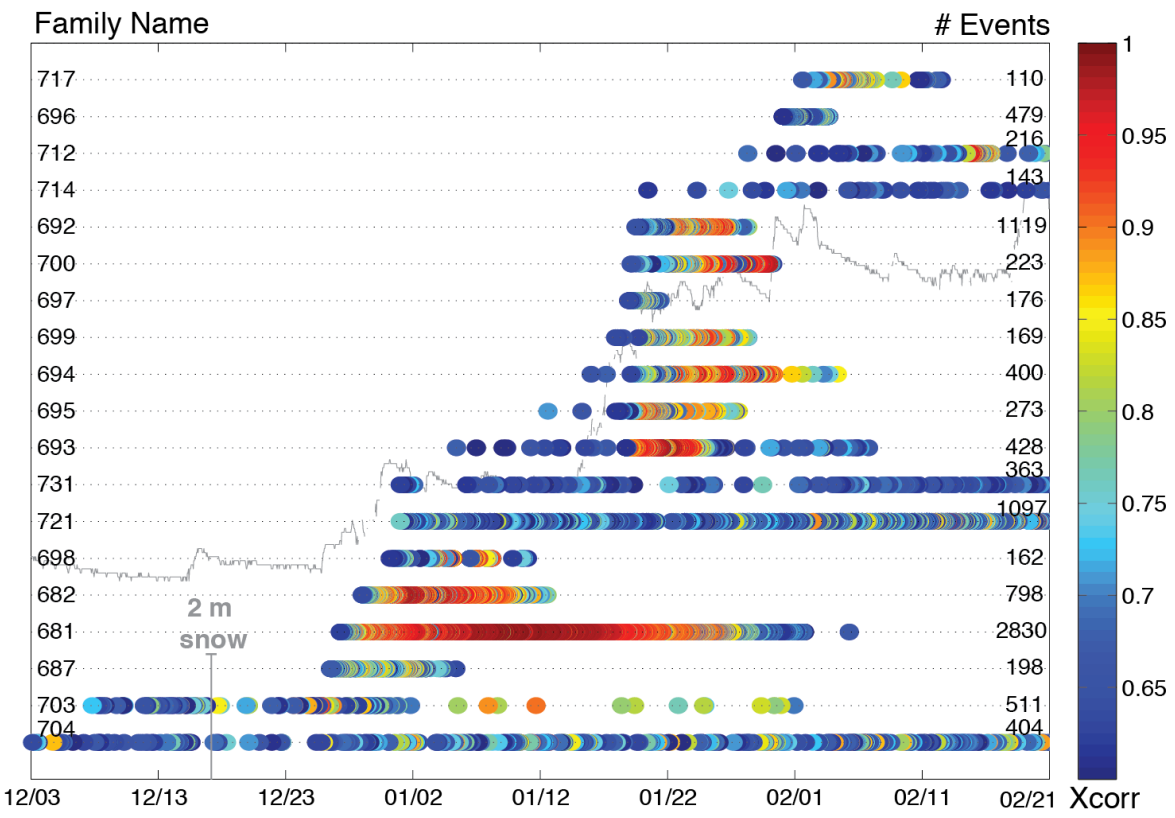

Figure 3-4 Timeline showing the evolution of repeating earthquake families with at least 100 repeats during two snowstorms. Each individual earthquake is a circle plotted on a line corresponding to its event family. The family name is labeled at left. The number of earthquake occurrences contained in each event family is labeled at right. The color of each circle corresponds to the cross correlation between that individual event and the stack of all the events in that family. The snow depth measured at Paradise is shown in the background.

3.2 Correlation with Weather

In order to look more explicitly at the apparent correlation between weather and repeating earthquake swarms, we compared temperature and precipitation to low-frequency repeating earthquake activity over several years in Figure 3-5. This figure clearly shows that the start of each swarm of earthquake activity coincides with a period of intense precipitation in almost every case. This is particularly apparent in the stormy winter of 2011-2012; each clear step up in the snow level coincides with a clear peak in earthquake activity.

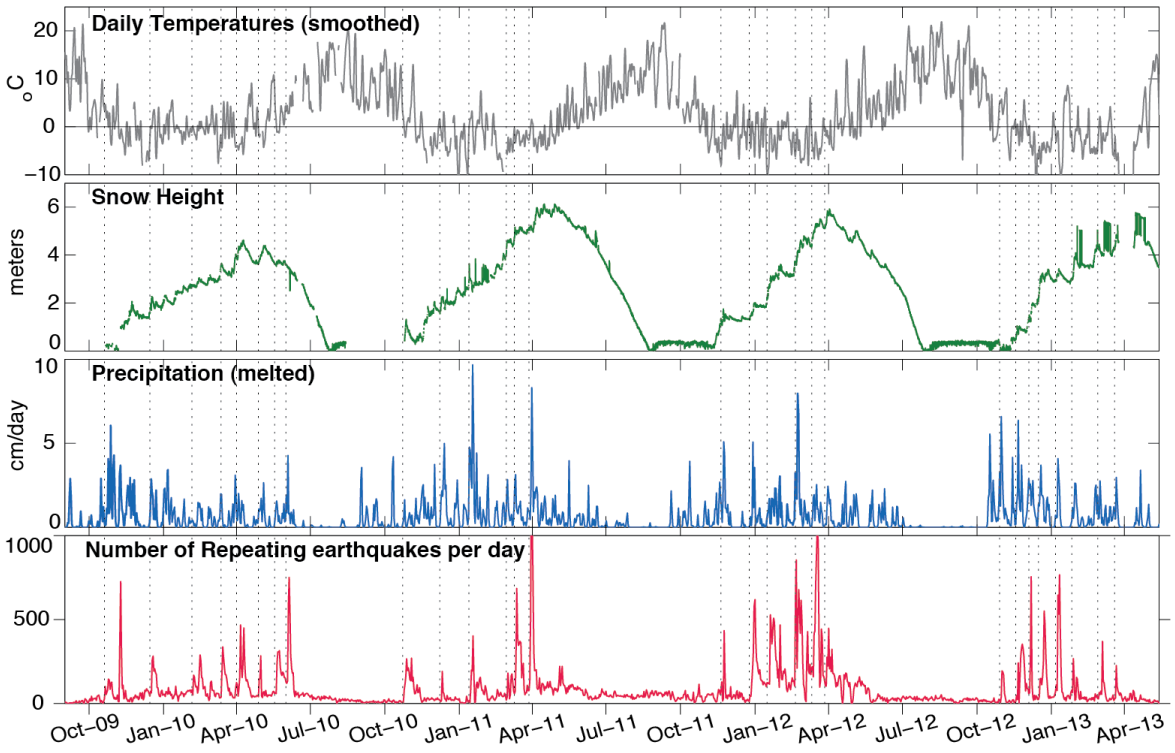

Figure 3-5 Daily temperatures recorded near seismic station RCM and snow height and precipitation (rain & melted snow) recorded at Paradise, compared with repeating earthquake activity. Dotted lines show that peaks in repeating earthquake activity correspond to peaks in precipitation in most cases.

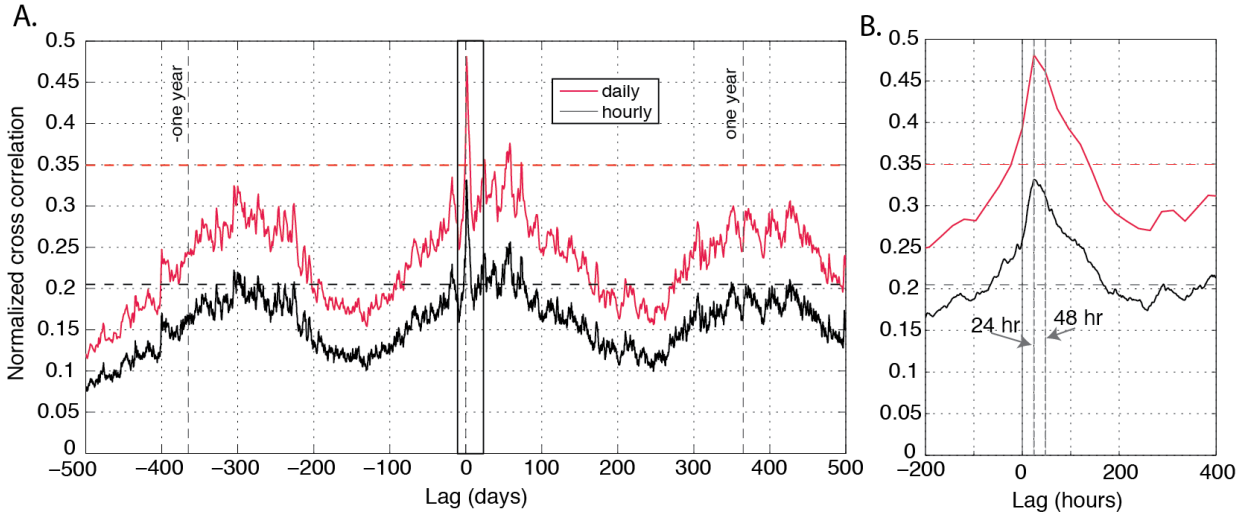

Figure 3-6 (A.) Normalized cross correlation between daily (red) and hourly (black) repeating earthquake activity and precipitation. The boxed area is shown on (B.) showing the clear peak that occurs around 1-2 days lag. Dashed lines indicate the maximum correlation obtained when the precipitation data was randomized and correlated against earthquake occurrence 10,000 times.

To quantify this relationship, we performed a normalized cross correlation between precipitation (liquid equivalent) recorded at PVC and repeating low-frequency earthquake activity (Figure 3-6). We did this for both hourly and daily time series, discretizing the two time series in time exactly the same way. To understand the significance of a correlation between these two distinct processes, we adopted methods similar to those used by Martini et al. (2009) by generating randomized precipitation data and performing the cross correlation between this random data and the vector of repeating earthquakes per day or hour 10,000 times to determine the maximum correlation value that could be obtained if the data were completely random. These maxima are shown as dashed horizontal lines on Figure 3-6. We generated the random data by creating a vector of random numbers with the same mean and standard deviation using the lognormal distribution of the actual precipitation data.

The resulting correlation oscillates with a period of about one year (Figure 3-6A) because both processes are seasonal, though there is a lag in the oscillation of about a month, probably because the repeating earthquake activity does not start to appear until a few weeks into the accumulation season, as is apparent in Figure 3-5. The most significant correlation is obtained when the repeating earthquake activity lags 1-2 days behind the precipitation, indicating a delay time between when precipitation falls and when the repeating earthquake activity appears. The peak, which far exceeds the correlation value that could be obtained randomly, has a broad base, particularly on its right side, indicating that there is variability in the lag time skewed towards longer times by a few days. The correlation is higher for the daily time series comparison than the hourly time series – most likely because there is more variability in precipitation on an hourly time scale than in repeating earthquake activity, but both are smoother on daily timescales.

3.3 Locations

Knowing the location of these events is crucial to understanding their source. Yet locating individual events is nearly impossible because the signals only appear on, at most, the three edifice stations, not enough to determine the location. Also, precise timing of the first P-wave arrivals, required for traditional earthquake location methods, is impossible because the signal doesn't emerge from the noise until some time after the first P-wave arrival. These limitations are apparent in Figure 3-7, where a record section of the vertical components of an individual event is plotted in the left column.

Fortunately, these earthquakes repeat up to several thousand times, so we can line the seismograms up in time and stack the signals to suppress noise and augment the signal. We obtained the time lags to apply to data from all seismic stations using the station with the clearest waveforms, typically RCS. If there were sufficient repeats of an event, a clear signal emerges on the three highest stations, with essentially no noise, and a less clear but still usable signal emerges on the more distant stations where before there was no observable signal whatsoever (Figure 3-7, middle column). In this study, we use the median stack rather than the mean stack to avoid the influence of outliers like spikes in the data.

The clarification of the signal is such that clear P- and S-wave arrival times are sufficient in number to use traditional location methods for families that have hundreds to thousands of repeats, and we were also able to determine the direction of the first motion on the three closest stations. The are significantly smaller than the subsequent waves, and are not even visible on Figure 3-7, even in the virtual absence of noise, unless we zoom in, explaining why individual events appear to emerge from the noise. Almost all families have mixed first motions on the vertical components, though for some families, some of the first motions are too small and

uncertain to say for sure. Unfortunately we cannot go further and estimate the focal mechanisms from these first motions because we only have three stations on which we can reliably recognize first motions, if that, and cannot estimate take-off angles well-enough in this complex terrain to provide good control of focal mechanisms.

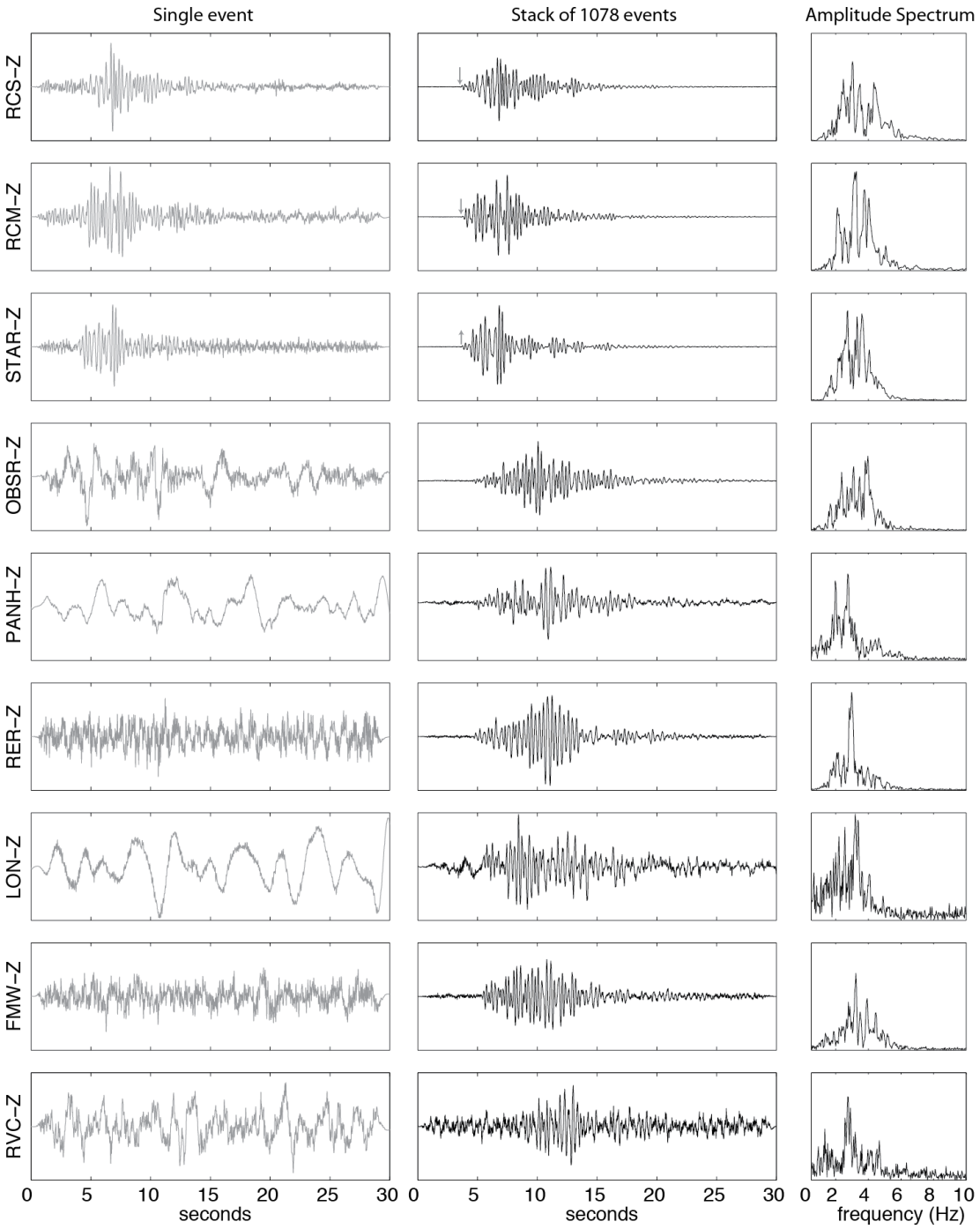

Figure 3-7 Record section demonstrating that a single occurrence of one of these earthquakes (in this case, from family 796) only appears above the noise level at the three summit stations (left column), but when data from hundreds of events are lined up in time and stacked, the noise is suppressed and the signal emerges at stations as far as 20 km from the summit. This processing allows events to be located and the first motions to be determined on the closest stations. First motions are indicated with gray arrows (middle column). The spectrum of these stacks shows that there is very little energy above 6Hz, there aren't clear shared spectral peaks between stations, and higher frequencies are more attenuated further from the volcano (right column).

We only attempted to locate families that had enough repeats to clarify the signal sufficiently upon stacking to be locatable. We focused on families that had more than 700 repeats and a dominant frequency of <6 Hz that occurred since 2010 because that is the earliest date archived data is available for three of the seismic stations (STAR, OBSR, and PANH). We further eliminated families if stacking did not clarify the signal on enough stations to allow at least 8 clear P and S wave picks. This left 8 event families. The stacked waveforms of these eight select families, as recorded on RCS, are shown in Figure 3-8, along with an arrow indicating the direction of the first motion. The characteristics of each family are summarized on Table 3-1, and black bars on Figure 3-2 show when each of these families occurred. The number of days and amount of precipitation that occurred prior to the onset of each event are also reported on Table 3-1. We estimated the precipitation at the location of each family by taking the ratio between the long term average annual precipitation at that location and annual precipitation at PVC, as predicted by the PRISM climate model (PRISM, 2004), and multiplying the precipitation recorded at PVC by that ratio. Two event families, 523 and 528, are very similar but sufficiently different, particularly in their frequency content, that we separated them into two families. In Thelen et al., (2013), they were combined as the main repeating earthquake family examined in that study (multiplet 5).

Table 3-1 Characteristics of select event families

Family Number	Number of events	Median recurrence interval (mins)	Dominant frequency (Hz)	Antecedent precip (cm)	Snow height increase at Paradise (m)	Days of antecedent precip
523	1750	11.3	3.6	2.6	No data	2.6
528	2205	2.9	5.1	3.2	No data	0.7
552	918	10.6	4.4	No data	0.9	2.8
681	2839	19.0	3.8	1.4	0.2	1.5
682	824	16.6	3.6	8.0	0.3	3.2
692	1146	5.9	4.0	7.9	0.9	4.9
785	949	13.4	3.7	5.8	0.4	5.7
796	1051	4.4	3.6	11.3	1	4.8

Once we picked the phase arrivals, to locate earthquakes we used the program SPONG, an adaption of FASTHYPO (Herrmann, 1979), which has been benchmarked against HYPOINVERSE (Klein, 1985), and was used for many years for routine earthquake locations at the PNSN. The program estimates travel ties using a 1D velocity model and applies station corrections to adjust for differences in station elevation – very important for a 4392-meter volcano – and to account for variability in the real velocity structure, as manifested as typical travel time residuals observed at each station. We revised the R4 velocity model developed by the PNSN, which is an adaptation of the C velocity model used by the PNSN to locate earthquakes in the entire Cascade mountain range. The C model is based on 1D velocity inversions using many recorded earthquakes and station corrections were determined using very high quality earthquakes and known explosions (Malone and Pavlis, 1983; Leaver, 1984). The R4 model varies from the C model mainly in the upper layers, with modifications based on seismic tomography of Mount Rainier by Moran et al. (1999). We modified the R4 model by thickening the first layer and moving the zero datum to the summit of the volcano to allow

events to be located at high elevations. We embedded the seismic stations at the correct elevations within the top layer of the model, and adjusted the station corrections slightly for the very localized events high on the mountain. This velocity model, R8, is shown in Table 3-2.

Table 3-2 R8 velocity model used to locate select event families

P wave velocity (km/s)	Depth range, from summit (km)
4.4	0 – 4.4
5.6	4.4 -7.4
6	7.4 - 12.4
6.4	12.4 - 20.4
6.7	20.4 – 38.4
7.1	38.4 - 47.4
7.8	47.4+

The results of locating the 8 select families in this manner are reported on Table 3-3 and shown in map view on Figure 3-9. The root mean squared errors are very low (0.02 to 0.16 seconds) and formal errors are low as well (0 to 0.34 km horizontal, 0.5 to 0.7 km vertical). Of course, uncertainties are actually higher because we are using a 1D velocity model to locate earthquakes in a highly 3D medium, but this is ameliorated somewhat by the station corrections, so although the actual errors are higher, they are likely of the correct order of magnitude. Maximum horizontal errors are larger for families located on the periphery of the triangle connecting the three edifice stations while the families located in the middle of all these three stations have horizontal errors smaller than the size of the dot they are plotted with because of station geometry. The depths of all locations are very shallow, within a few hundred meters or less of the surface elevation at the event locations, which is also reported on Table 3-3. In some cases, the location program fixed the depth very close to the zero elevation (i.e. the summit) to stabilize the solution when it cannot converge on a depth, then the other three parameters are

allowed to adjust. In those cases, which are indicated on Table 3-3, we know that the events were shallow because the depth was fixed near the surface, but the vertical depths reported are unreliable.

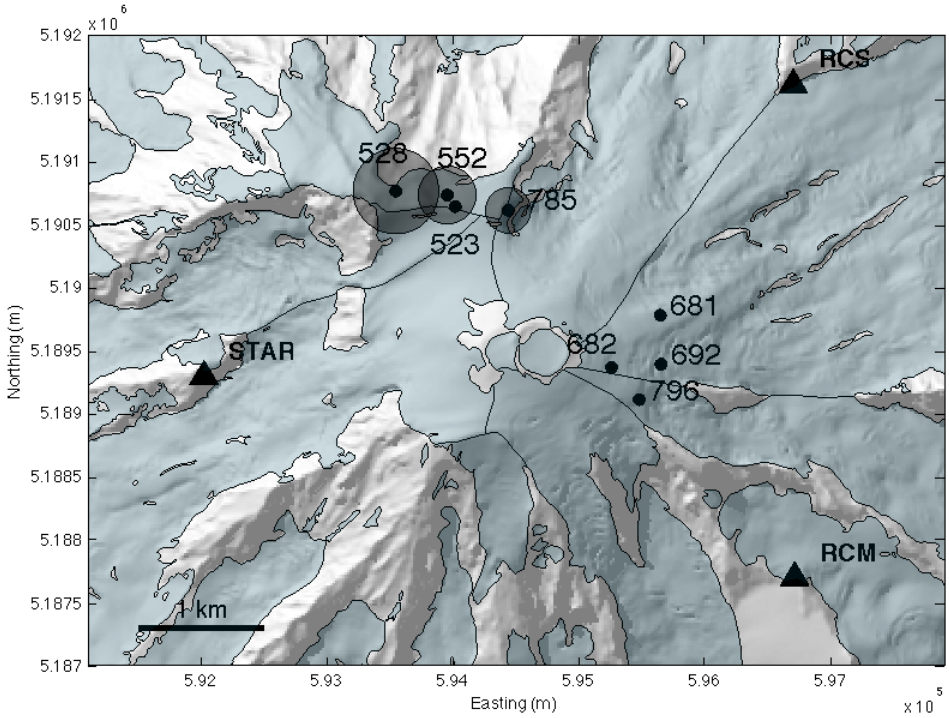

Figure 3-9 Locations of the select families, the gray circle indicates the maximum formal horizontal errors. Families that do not appear to have any location errors actually have formal errors so small they are smaller than the location marker.

There are two clusters of locations. Three families from the north cluster (523, 528, 552) are located at a hanging glacier. Ice moves from this hanging glacier to the Carbon glacier below by detaching and falling down the cliff below. The location of these three families close to each other is consistent with the similarity of the first few seconds of their waveforms (Figure 3-8), but the codas are different, indicating that they are not identically located. Family 785 also has a waveform that is similar to the other three families in the cluster, but its best fitting location is on a different hanging glacier but the horizontal errors are large enough that it could actually be located on the same glacier as the other three. If these are indeed glacial stick-slip, this could be because it would have a different azimuth of slip if it was actually beneath a different glacier

than the other three. The waveforms of the eastern cluster (681, 682, 692 and 796) are not nearly as similar to each other, suggesting they are more distributed in their locations. All locations are in very steep areas, ice falls and hanging glaciers, with surface slopes (reported on Table 3-3) of more than 30° in most cases, with the steepest surface slope as high as 46°.

Table 3-3 Locations and source movement of select event families

Family Number	Latitude	Longitude	RMS (sec)	Number of Phases used in location	Max horizontal error (km)	Vertical error (m)	Elevation of location (m)	Elevation of surface at location	Slope (within 100m radius)
523	46° 51.75'	-121° 45.98'	0.03	9	0	N/A	4382*	4175	13°
528	46° 51.83'	-121° 46.37'	0.08	8	0.34	700	3952	4206	29°
552	46° 51.82'	-121° 46.04'	0.10	11	0.23	600	4072	4174	36°
681	46° 51.29'	-121° 44.72'	0.08	8	0.01	N/A	4362*	3842	30°
682	46° 51.06'	-121° 45.04'	0.16	9	0.03	N/A	4382*	4079	30°
692	46° 51.07'	-121° 44.72'	0.02	8	0	N/A	4388*	3794	40°
785	46° 51.75'	-121° 45.66'	0.08	11	0.18	500	4042	4025	46°
796	46° 50.92'	-121° 44.87'	0.14	10	0.02	N/A	4382*	3844	39°

* Event depth fixed by location program

3.4 Recurrence Time vs. Event Size

Figure 3-4 suggests that the behavior of event families, such as their inter-event correlation and recurrence intervals, change over time. In order to look more closely at these changes plotted the time since the last earthquake (recurrence interval) against a proxy for energy called pseudoenergy, which is the sum of the squared uncorrected velocity seismogram, using just the catalog from RCS for consistency. We also added a third variable to the plot, the date of each event, to see how the previous two variables change over time. We computed pseudoenergy using only the highest amplitude part of the signal (a 4-7 second window) to minimize noise pollution since signal to noise ratios are low. We plotted the data in two different ways to better

visualize what is occurring. Figure 3-10 illustrates results for three of the event families with the highest energy (and thus the least scatter due to noise), and the most interesting behavior.

There are some very clear systematic patterns that emerge, but not a clear dominant pattern, suggesting that several factors are at play. For short periods of time, psuedoenergy scales linearly with recurrence interval: the shorter the time since the last earthquake, the smaller the next event will be. However, the slope of this line (fit to discrete time periods in gray on Figure 3-10, left) changes systematically over time in all three cases. All three families start with a lot of scatter, then after a day or two, form a distinct linear trend that gradually drifts or suddenly jumps after a few days to steeper slopes and higher energies. This then gradually drifts back down to more shallowly sloped linear trends, but tending towards higher recurrence intervals until the family disappears. If we look at the same data in a different way, at the evolution of recurrence interval over time (Figure 3-10, right), we see that the sudden jumps in the slope of the lines actually correspond to the addition of more snow in most cases, and the reaction to additional snow is more immediate, unlike the delayed reaction to snowfall exhibited at the initiation of each family. However, there are also times when additional snow falls and there is no change in the behavior of any of the variables so the story is not simple, though this could be in part because the snowfall was recorded at lower elevations and it may not always be snowing up high when it's snowing down low. Generally, there is a trend toward either having more frequent smaller events or less frequent bigger events, and the recurrence interval generally increases over time.

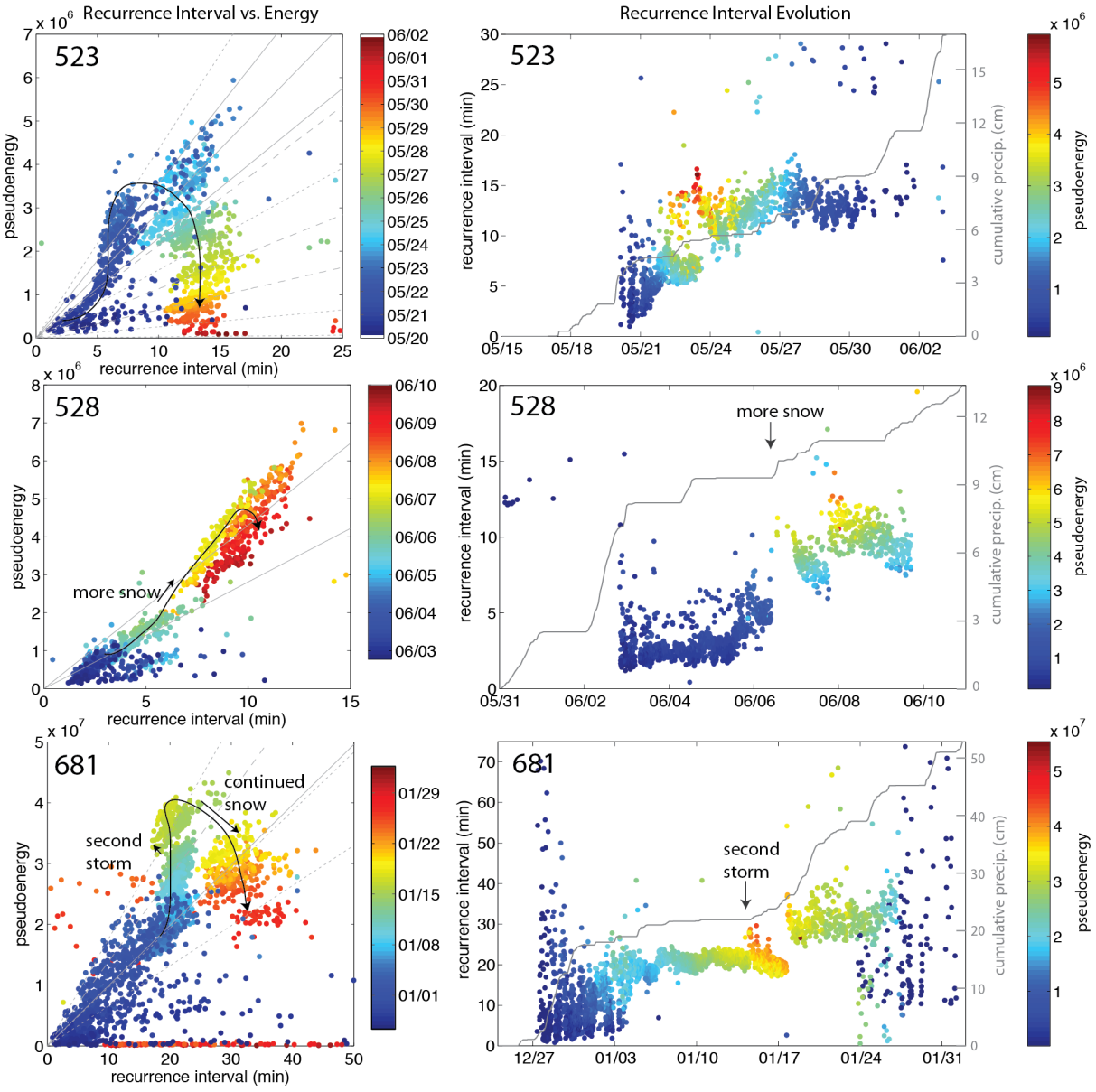

Figure 3-10 Variations of recurrence interval (time since the last quake) and pseudoenergy over time for three families (523, 528, 681) plotted in two different ways. The first column shows the relation between recurrence interval and pseudoenergy. The color of each dot corresponds to event time. Gray lines show a least squares fit to datapoints from discrete time intervals showing that the slope of the line relating the two variables changes over time. The R^2 is above 0.5 for solid lines, above 0 for dashed, dotted is a visual fit. The second column show the same information, but plots changes in recurrence interval over time and the color corresponds to the pseudoenergy. Cumulative precipitation recorded at Paradise is plotted in gray to show that some of the sudden changes in behavior correspond to additional snowfall. See text for further discussion of behavior patterns.

3.5 Source migration over time - coda wave interferometry

3.5.1 Methods

The gradual evolution of the waveforms of each family over time as evidenced by gradual decorrelations (Figure 3-4), suggests incremental changes in the source mechanism, seismic velocities, or the source location. The latter is the most likely of the three given the other evidence for a glacier-related source, because glaciers move. A source either within the ice or related to material embedded at its base would be expected to move with the glacier at the same speed. Determining whether the source is moving and if so, how fast, can help further illuminate the source process. Though it is effectively impossible to use traditional methods with enough accuracy to determine if the sources are moving, and the low number of stations and low signal to noise levels on which individual events appear makes double difference relocation difficult (Waldhauser and Ellsworth, 2000), we can instead use coda wave interferometry to determine the source separation between earthquakes that are located near each other (Snieder and Vrijlandt, 2005). This enables tracking the movement of the source of each event family over time and can be done even using a single station, though we are able to use three for a more robust solution.

Coda wave interferometry exploits changes in the coda of the waveform (the end of the signal), which is composed of scattered waves, to determine source offsets. When the source position of an earthquake moves from the original "unperturbed" location to a new "perturbed" location, some of the wave path lengths become longer and some become shorter, and thus the contribution from some wave trajectories comes early and some later. The change in arrival times summed over all wave trajectories is approximately zero, but the variance of the changes in arrival times increases the further the source location moves. This can be harnessed to estimate

the movement of the centroid of a repeating earthquake over time (Snieder and Vrijlandt, 2005). The variance σ_τ^2 of a given window of the coda can be calculated by:

(3-2) $$\sigma_\tau^2 = \frac{2-2R_{max}^{(t,t_w)}}{\overline{\omega^2}}$$

where $R_{max}^{(t,t_w)}$ is the maximum time-shifted normalized cross correlation coefficient between the unperturbed and the perturbed waveform codas at center time t within window width $2t_w$, and $\overline{\omega^2}$ is the square of dominant angular frequency, which is equal to $\left(2\pi\bar{f}\right)^2$ where $\bar{f}$ is computed by equation 3-1. The relation between the travel time variance and movement of the source depends on the type of source mechanism (Snieder and Vrijlandt, 2005). The waveforms of the repeating earthquakes recorded at Mount Rainier are too low in amplitude and altered by path effects to determine the source mechanism from the seismograms. However, assuming the hypothesis of Thelen et al., (2013), that these are basal stick-slip earthquakes, is correct and that source displacement is along the fault plane, a fair assumption for basal slip, the source displacement δ for a double couple source can be calculated by:

(3-3) $$\delta = \sqrt{\frac{7\left(\frac{2}{\alpha^6}+\frac{3}{\beta^6}\right)\sigma_\tau^2}{\left(\frac{6}{\alpha^8}+\frac{7}{\beta^8}\right)}}$$

where α and β are the P and S wave velocities of the volume around the source, respectively (Snieder and Vrijlandt, 2005). A different source mechanism or different seismic velocities will just change the overall magnitude of the source movement, but not the shape of its movement over time.

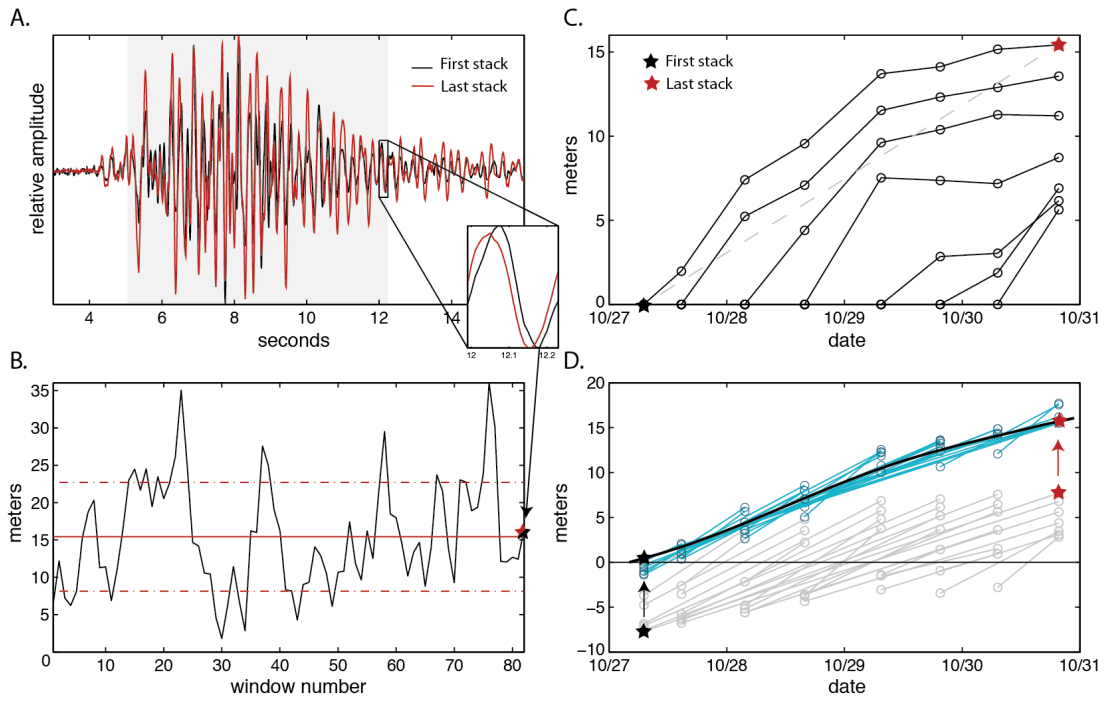

Figure 3-11 Demonstration of how coda wave interferometry was used in this study using family 552. (A.) Each waveform stack representing events from a certain time interval is compared to each other waveform stack by dividing the coda (shaded in gray, starting 2 seconds after the first arrival, 6 seconds long) into 0.24 second windows and taking the normalized cross correlation between the two waveforms in each of those windows, this gives (B.) an independent estimate of source movement for each sliding time window using equation 3. For example the inset time window gives a source movement estimate indicated with a star, the mean of all of these independent estimates (red line) is taken as the source location offset between the two stacks. The dashed line is the standard deviation. (C.) Once every stack is compared in this way to every other stack, the result is the offset over time relative to the starting location of each stack, shown as lines with data points indicated as circles. The offset between the pair of stacks shown in A and B is indicated with a dashed line. (D.) Since there are uncertainties in these results, the offsets over time relative to each starting stack do not line up perfectly, so instead we do a least squares inversion to solve for the overall source offset over time that best fits the observed relative offsets between each stack and every other stack. The light gray segments connect each segment to every other segment, centered around a zero offset, the blue segments show these same segments but migrated to the best fitting overall offset model, shown in black. The stars indicate the migration of the segment connecting the first and last stack from A-C to the model.

Figure 3-11 illustrates the use of coda wave interferometry in this study. We focus on the select families chosen earlier (Table 3-2, Figure 3-9). The seismic signals of individual events are too noisy in the coda to apply this technique so we instead stack 50 to 75 consecutive events to suppress the noise in the signal. We require the events to all occur within half a day of each

other to avoid stacking events together that have significantly different waveforms. These strict requirements for stacking mean that we cannot observe source movements at the start and end of event families in some cases because not enough earthquakes are occurring close enough together in time. We then computed cross correlations between every stack and every other stack for each 0.24 second window in the coda, t_w = ±0.12 seconds (Figure 3-11A). We apply the corrected normalized cross-correlation (Douma and Snieder, 2006), which uses the characteristics of the noise prior to the start of the event to reduce the bias in the cross correlation due to noise contamination. We found this to be very important in this study because offsets between stacks were so small (i.e. true correlations were so high) that not correcting for noise resulted in an overestimate of the source offset because noise biases correlations downwards.

In order to compute source offsets uniformly, we defined the coda as starting 2 seconds after the first arrival and lasting for six seconds past that point. We excluded the first arrivals because their inclusion can result in an underestimate of the source movement (Robinson et al., 2011). We chose a short window length in order to avoid cycle skipping (Robinson et al., 2011), and we allowed the windows to overlap by 75% between adjacent windows to recapture information lost at the edges of each window due to the 25% taper. Each time window results in an independent estimate of σ_τ^2 (and thus independent estimates of the source separation δ once equation 3-3 is applied). We take the mean offset μ_δ as the best estimate of the offset between the pair of stacks being compared, and use the standard deviation σ_δ to estimate uncertainties (Figure 3-11B).

In order to apply equation 3-3 to get source displacement δ from σ_τ^2, we need to know the average seismic velocities of a volume around the source location. The velocity structure of the edifice of Mount Rainier is highly heterogeneous and unknown, so we instead make a best estimate of the mean seismic velocities at the source and also calculate upper and lower bounds.

Active source tests at Mount St. Helens, a neighboring stratovolcano, yielded an estimate of β = 200 - 650 m/s for lava flows and block and ash flows near the surface (W.Thelen, pers. comm., 2013) and α = 800 -1500 m/s for the shallow layers of the edifice (Weaver and Malone, 1976). Mount Rainier is composed primarily of andesite lava flows (Fiske et al., 1988), while Mount St. Helens is composed more of lower velocity ash and block flows, so we used the larger values observed at Mount St. Helens as a lower bound for the shallow subsurface of Mount Rainier: α = 1300 m/s and β = 650 m/s. As the upper bound, we used the seismic velocity of glaciers at Mount St. Helens (prior to the 1980 eruption) measured by Weaver and Malone (1976) to be α = 3150 m/s, and assume α/β = 2 because the shallow surface is probably filled with fluids and fractured to obtain an upper limit on β of 1600 m/s. The true values are most likely somewhere between these bounds, we make a best estimate of α = 2000 m/s and β = 1000 m/s.

Since coda wave interferometry does not allow us to resolve the direction of motion, only the absolute offset, we make the assumption that the source is continuously moving further away from the location of the first stack, a fair assumption for a glacier sliding down a mountain. We compute estimates of the source separation between each stack and every other stack, so the initial result can be framed as separate estimates of movement over time relative to the location of each different stack (Figure 3-11C). If there were no uncertainties, most of this information would be redundant, but there are uncertainties and the relative offsets between other pairs are not perfectly consistent with each other. We performed a least squares inversion in order to determine the overall source movement over time that best fits all the observations using a modification of methods developed by Hotovec-Ellis et al., (2013, submitted). The inversion determined the absolute source migration over time (relative to the first stack) that best fit the relative offsets observed between all pairs (Figure 3-11D).

We weighted each pair by half of the standard deviation of the offset estimate. We regularized the solution using both first and second order Tikhonov regularization, corresponding to a flat and smooth model, respectively, giving twice as much weight as the first order regularization. Since we assumed offsets are always positive, the inversion is biased towards always increasing source offsets. In order to ensure the results are particularly robust and not just showing movement because of this bias, we required that the variance reduction of the solution be more than two standard deviations higher than the mean variance reduction of the inversion of the same data randomly scrambled 30 times. This can be considered equivalent to 95% confidence that the variance reduction of the inversion of the real data is significantly different than the variance reduction of the randomized data. We only include results that pass this test.

We do this inversion separately for each component of each edifice station (RCS, RCM, STAR) in order to achieve up to 5 independent estimates of the source movement over time for each event family (5 because STAR has 3 components), though in most cases only a few of the components yielded results that passed the test for robustness. When different stations and components yield similar estimates of source offset over time, the result is strongly validated.

3.5.2 Results

The results of the inversion of the coda wave interferometry results for source migration are shown graphically in Figure 3-12 and the mean speeds, computed by taking the mean slope of all segments from all robust solutions are reported in Table 3-4. Variance reductions range from 79 - 93%, but are above 85% in most cases. The results show that all select families (except 682 which had no robust solutions) are moving. Their movement rates range from 0.8 to 4.3 meters per day for our best estimate of seismic velocities at the source (0.5-2.8 and 1.3-6.8 m/day for upper and lower bounds, respectively). These are realistic velocities for alpine glaciers (Kamb,

1964), though perhaps higher than typical small alpine glaciers and more representative of steep thick valley glaciers. In most cases, separate components and stations, which provide independent estimates of source movement over time, yield similar or even nearly identical results, including showing the same kinks and bends in the trajectory. For example, results obtained separately for both RCS and RCM show a sudden slowing in the velocity for event 681 on 6 Jan 2012 and for family 796 they show the same flattening and then increase in movement rate. Family 552 has the most solid result, with all 5 components yielding the same movement rate of about 3.5 meters per day. In a few cases, the shape of the movement over time is different between stations (e.g. families 523, 692 and 785) suggesting these solutions are not as reliable and should be more lightly interpreted. Family 681 lasts far longer than any of the other families, and also is the slowest on average; the upper bound estimate of velocity is lower than the lower bound estimate for almost all other families.

Table 3-4 Mean source movement speeds estimated using codawave interferometry

Family Number	Best estimate (m/day)	Lower bound (m/day)	Upper bound (m/day)
523	1.6	1.1	2.6
528	2.6	1.7	4.2
552	3.5	1.9	5.5
681	0.8	0.5	1.3
692	2.9	2.4	6.0
785	3.8	2.7	6.5
796	4.3	2.8	6.8

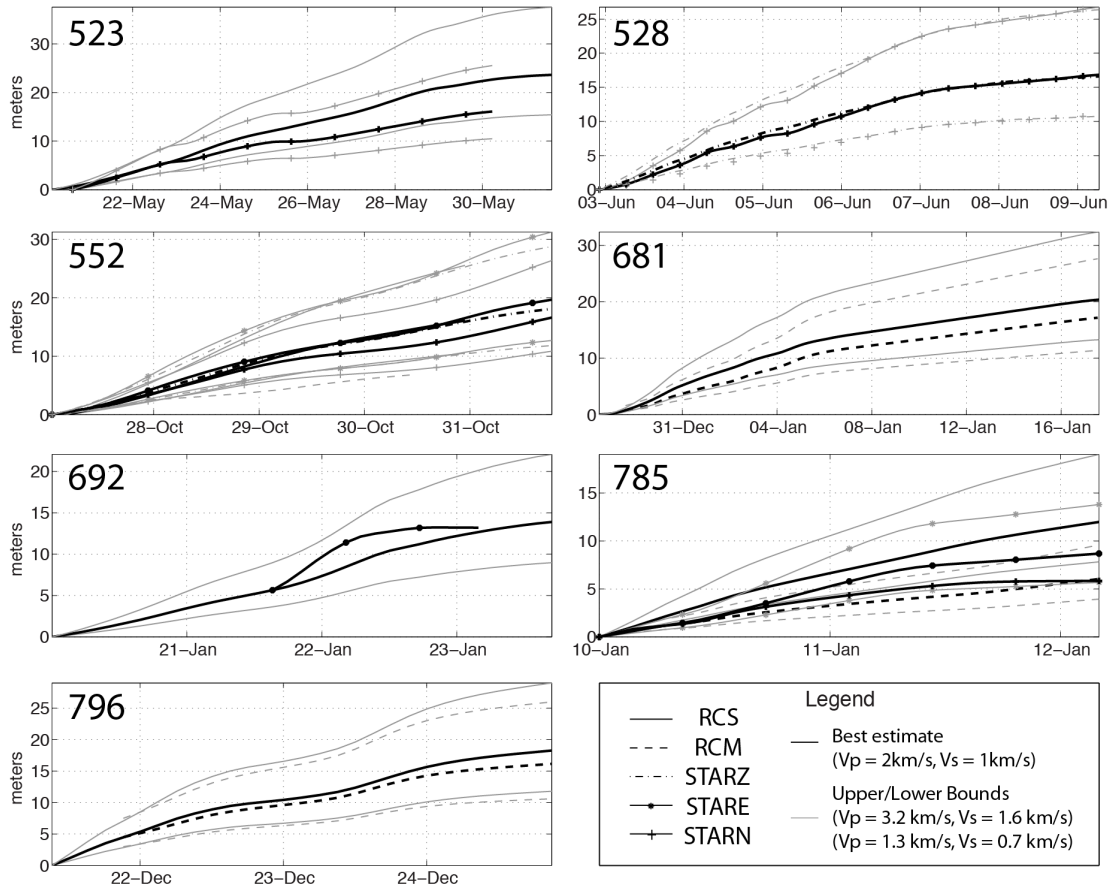

Figure 3-12 Source movement over time for select event families derived from coda wave inteferometry. The black lines indicate the best estimates and gray lines indicate the upper and lower bounds on the possible offsets based on the range of possible seismic velocities. There is not a rigorous solution (see text for definition) for every component of every station for each family. In many cases, the seismic data was too noisy for most of the duration of the event family and we were only able to obtain a rigorous solution for movement over a few days time rather than the whole duration. Solutions for which the start time of the good data was later than the results from other station components are migrated to the mean offset at their starting point.

4. Discussion

4.1 What is the source mechanism?

Using the observations above, we can narrow down the potential source mechanisms of these events. First of all, the occurrence of swarms of these repeating earthquakes every year for at least the past decade without any subsequent volcanic activity, together with the high

correlation of activity with precipitation (Figure 3-6), strongly suggest a non-volcanic source for the majority, if not all, of the low-frequency repeating earthquakes that we detected. We can also rule out a hydrothermal source, at least for the select families, because they move several meters per day, while a hydrothermal source would be stationary. Nevertheless, there is the possibility that a few of the several hundred thousand low-frequency repeating earthquakes we detected could be related to hydrothermal activity.

Having settled on a glacial source as the most likely option, there are many different glacial seismic sources that have been documented to choose from. A few are easy to rule out. Surface crevassing (tensile failure) is the most common type of alpine glacier seismic source (Neave and Savage, 1970; Deichmann, 2000; Walter et al., 2009) and this source can repeat and occur in swarms of activity if extensive crevassing is occurring in the same area (e.g. Neave and Savage, 1970). However, crevassing is unlikely to explain the observed low-frequency earthquakes because seismic events generated by crevassing typically have higher frequency content and can only be detected at seismic stations directly on the ice or on rock very close by (Thelen et al., 2013; Weaver and Malone, 1979). This is due, in part, to the fact that steep glaciers are poorly coupled to their bed (Kamb, 1970) and thus do not transmit seismic waves efficiently from ice into rock (Weaver and Malone, 1979). The most convincing argument against crevassing is the fact that pure tensile cracking is volumetric and all first motions should be the same (Walter et al., 2013), but we observe a mix of up and down first motions for most families, indicating that the source has at least some shear component.

Falling ice, like calving and serac collapses, also can generate low-frequency earthquakes (Qamar, 1988; O'Neel et al., 2007; Roux et al., 2008; Tsai et al. 2008; Thelen et al., 2013), and this source can repeat if ice falls in the same location over and over again (e.g. Jonsdottir et al.,

2009), but it is highly unlikely that this is the source of the events in this study because ice is unlikely to fall exactly the same way thousands of times at regular intervals.

Another often-invoked source interpretation for glacier seismicity is hydraulic transients resonating in fluid-filled cracks and fluid-driven cracking, the same source mechanism often proposed for low-frequency earthquakes related to volcanic activity (St. Lawrence and Qamar, 1979; Metaxian et al., 2003; West et al., 2010). This type of source could repeat if a water-filled crack opened in discrete incremental events, or if hydraulic transients were repeatedly excited by flowing water, for example. But sources of this type typically have a harmonic waveform dominated by a few discrete frequencies that would appear as shared spectral peaks on multiple seismic stations. This is not observed for any of the select families (e.g. Figure 3-7, right column). The resonant character of the signal could be lost due to the alteration of the signal in the shallow heterogeneous subsurface (Thelen et al., 2013). Stronger evidence against this source mechanism is the fact that the events from this study have mixed-polarity first motions. An opening crack is a volumetric source and unsteady fluid flow (hydraulic transients) involves net forces exerted on the earth. In both cases, all first motions should be the same. Though in exceptional cases this type of source could result in mixed polarity first motions if the fluid-driven crack is a shear failure rather than tensile, for some complex combination of multiple source mechanisms (Julian et al., 1998), or if a CLVD mechanism were invoked, which has been used as evidence for earthquakes generated by magma injection (e.g. Kanamori et al., 1993) but to our knowledge, never for glacial earthquakes. In addition, there is no clear physical explanation for why events involving flowing water would occur more often in winter when less water is flowing through the system, or why such events should correlate with snowfall, so we

consider this source also unlikely as the main source, though it is possible that some of the hundreds of thousands of repeating events detected in the past decade could be of this origin.

Walter et al. (2013) proposed a new source for deep glacial earthquakes involving opening and closing bed-parallel cracks in response to basal water pressure changes that can also have some shear component. Though we cannot rule this out because we are unable to solve for focal mechanisms, we do not favor it as the source mechanism here because it is hard to conceive this type of event being repeatable thousands of times at regular intervals. Furthermore, as discussed earlier, events that are completely in the ice at steep mountain glaciers are not well recorded on rock stations because the ice is poorly coupled to its bed on average (Weaver and Malone, 1979), so these events would have to be large in order to be recorded at the observed distances.

This leaves basal stick-slip sliding as the source mechanism that best fits the observations. This mechanism has been observed for glaciers of a range of types and sizes through seismic observations (e.g. Ekstrom et al., 2003; Zoet et al., 2012; Weaver and Malone, 1976, 1979; Caplan-Auerbach and Huggel, 2007), geodetic methods (Wiens et al., 2008; Winberry et al., 2013) and direct observation (e.g. Vivian and Bocquet, 1973).

The mixed polarity first motions that we observe are consistent with shear failure, such as basal stick-slip. A stick-slip source can be non-destructive and repeatable, as required to fit the observations as well. Stick-slip basal sliding occurs at the interface between rock and/or till and thus is better coupled to the ground: it is not limited by the low seismic energy transmission between steep mountain glaciers and their bed as events completely in the ice would be (Weaver and Malone, 1979) which could explain why these events can be observed on distant seismic stations (i.e. a few km away). Furthermore, stick-slip events could move with the glacier, as observed, if the asperity failing elastically is a patch of dirty ice rather than a stationary asperity

like a bedrock bump. This is very feasible because laboratory tests show that dirty ice is much more favorable to stick-slip behavior than clean ice (Zoet et al., 2013a).

Finally, these earthquakes exhibit behavior that suggests healing is taking place (Figure 3-10), a fundamental requirement for stick-slip behavior (Scholz, 1998), i.e. the longer the time since the last earthquake, the larger the earthquake. In fault mechanics, this behavior is referred to as slip-predictable, (Shimazaki and Nakata, 1980; Scholz, 1998), and can be considered a sign that healing is taking place between events (Zoet et al., 2012). The physical explanation is that the two sides of the fault are held together longer so more healing can occur and more stress can accumulate that can then be released in the next event. Energy (and thus pseudoenergy) is linearly proportional to magnitude, and therefore also linearly proportional to average slip if the fault area remains stable. Therefore, for a pure slip-predictable model with a constant loading rate, a linear trend should emerge between pseudoenergy and recurrence interval, as observed (Figure 3-10), at least for short time periods when external loading was relatively constant. Time-predictable behavior is an alternate theory to slip-predictable that is also applicable to stick-slip earthquakes. The theory states that the larger the slip of previous earthquake, the more time there will be until the next earthquake (Shimazaki and Nakata, 1980; Scholz, 1998). To see if a time-predictable model could better explain the observations, we would plot the time until the next quake against pseudoenergy instead of the time since the last earthquake. Linear trends still emerge when we do this, but they are much messier with a lot of scatter, so it is likely that these trends emerge just because the recurrence interval varies smoothly. The time since the last quake is often similar to the time until the next one, thus a trend in the slip-predictable model could also appear as a trend for the time-predictable model.

4.2 Why is this behavior transient and triggered by precipitation?

Assuming our interpretation thus far is correct, the question remains: how such a small additional load as that due to a new layer of snow can trigger this activity and why it is temporary. Glaciers are complex systems and a number of possible scenarios could be invoked, but we present our favored hypothesis that we believe best fits the observations and the current state of knowledge about glacier sliding. Our hypothesis is that a sudden increased snow load increases total glacier velocity partially by an increase in shear stress but primarily via a time-delayed decrease in areally-averaged effective normal stress. This occurs because the increased load squeezes water out of poorly connected, poorly drained water-filled cavities at the glacier bed, spreading it over a larger area at a rate limited by the hydraulic conductivity of basal areas. The increase in velocity pushes sliding behavior in patches of the bed that are favorable to stick-slip sliding (dirty basal ice and well-drained or porous substrate) into a stick-slip, slip-predictable sliding regime. As the basal hydraulic system readjusts and excess fluid pressures drain, the glacier slows down, reducing the seismic moment rate too. However, once a surge has started, additional snow loads do not again speed the glacier up but rather almost immediately cause larger and less frequent stick-slip events temporarily. The rest of this section is devoted to making the case for this hypothesis.

Stick-slip sliding is the result of frictional instability. Theory dictates that for a sliding plane to be capable of stick-slip sliding, two conditions must be met: the material of the sliding plane must be 'velocity weakening' (i.e. friction decreases as sliding velocity increases), and the fault plane must 'heal' over time (i.e. static friction on the plane increases with hold time) (Scholz, 1998). We know, based on Figure 3-10, that at least the latter is true here. However, whether or not stick-slip sliding occurs in a medium that meets these characteristics depends on the external

loading. A stable sliding regime, like the aseismic sliding of ice over rock that is typically modulated by plastic flow and pressure melting and refreezing (Kamb, 1964), can transition into an unstable (stick-slip) sliding regime in two ways: 1) if the effective normal stress is increased or 2) if there is a sudden jump in the sliding velocity, also known as dynamic loading (Scholz, 1998). It is possible that the added load of snow causes one of these changes to occur, and the change is high enough to transition the sliding regime from conditionally stable (smooth, aseismic sliding) to unstable sliding (stick-slip) temporarily.

So which is it here, a sudden velocity increase or an increase in effective normal stress? A load of snow could conceivably cause either to occur, but the evidence suggests that the initiation of these event families is best explained by a sudden increase in sliding velocity. The coda wave interferometry results (Figure 3-12) indicate that the sources start out moving fast; even the lower bound on the velocity estimates, in most cases, exceeds the highest average daily glacier surface velocities measured at several glaciers at Mount Rainier using ground-based radar interferometry of 2 m/day, but slower in most locations (Allstadt et al., 2013). The velocities estimated by the coda wave interferometry also exceed longer-term average surface ice velocities observed by Hodge (1974) at Nisqually glacier. The fastest surface velocity he observed was 0.8 m/day near the equilibrium line.

Almost all of the select families gradually slow down after a few days until they disappear (Figure 3-10), suggesting that the glaciers were perturbed to a higher velocity initially, and then gradually return to normal. This pattern is stable, no matter what seismic velocities are chosen. We would expect this change in sliding velocities over time to be reflected in the plots of the relation between recurrence interval and pseudoenergy (Figure 3-11). The slope of the relation between recurrence interval and pseudoenergy is directly proportional to the moment rate, and

assuming the fault area is stable, it is therefore also directly proportional to slip rate (i.e. sliding velocity, Stein and Wysession, 2003). So we would expect that as the glacier slows down over time, the angle of this line would drift to shallower slopes. This pattern, does, in fact appear at the tail end of all three families shown on Figure 3-11. However, this simple interpretation is complicated by the fact that when more snow falls, the slope of the linear trend steepens in all three cases. In the absence of other evidence, we would guess this means that the slip rate increases (i.e. the glacier speeds up in response), but the coda wave interferometry results show us that this is not the case, the glaciers actually slow down when more snow falls in all three cases (though not every time snow falls). This suggests that the added normal load of the snow increases the friction on the sliding plane enough to make the events bigger (higher stress drop) but less frequent, but it seems to only be enough to affect event behavior once a family has been initiated. The added normal load is tiny compared to the weight of the ice so this suggests the area experiencing stick-slip sliding is highly sensitive to minor external stress perturbations. This hypothesis is supported by the fact that the reaction to additional snow once a family has already been initiated is immediate, whereas the initiation takes a few days to occur once it starts snowing, something we will address in the next section.

Zoet et al. (2013a) provide physical explanations based on laboratory testing for how increases in sliding velocity can cause a glacier to start stick-slip sliding. They found that if initial lubrication of the patch of glacier bed is low (i.e. the glacier is cold and/or well drained and highly fractured) and a sudden increase in sliding velocity occurs, the increased velocity results in increased frictional melting. The temporary increase in lubrication at this spot causes slip to accelerate and overshoot the strength of the fault, as required for stick-slip (Scholz, 1998), causing the sliding plane to stick and allowing it to heal and rebuild strength. Zoet et al. (2013a)

propose that the healing mechanism for glacial stick-slip is refreezing. This healed fault will be reloaded as the surrounding areas continue to slip around this sticky patch and the cycle will repeat over and over again until another change in external loading sends it back into the stable sliding regime. Zoet et al. (2013a) found that dirty ice is more favorable to stick-slip sliding because frictional melting is higher. The basal ice at Mount Rainier is most likely extremely dirty at its bed because the rocks that compose much of the mountain are weak and easily crumbled, so this is feasible. In fact, beyond just being "dirty," there is likely also much larger debris, even large boulders, embedded in the ice at Mount Rainier as well. Zoet et al. (2013a) also found that for stick-slip sliding to occur, the additional lubrication added due to frictional melting had to have a way to drain away from the sticky patch rather than building up, so the rock must be porous or fractured.

However, if a surge in velocity is in fact the reason for the appearance of these stick-slip events, it is still unclear how the tiny load of added snow causes this to occur, why there is a delay of a day or two, and why is the behavior temporary. Assuming the glaciers are 30 to 60 meters thick, a typical thickness for the glaciers near the summit (Driedger and Kennard, 1986), the added snow weight prior to the appearance of the select families (1.4 – 11.3 cm water equivalent, Table 3-1) is just 0.03-0.4% of the glacier weight.

To get at a potential explanation, we first must consider what the bed of a typical Mount Rainier glacier is like at the time of year the swarms of earthquakes occur. During the winter, the subglacial drainage system of alpine glaciers is characterized by a distributed system of isolated cavities that can be filled with stagnant melt water from geothermal and frictional heating (Fountain and Walder, 1998). These cavities are opened primarily by basal sliding over bumps in the bed and can be closed by ice creep (Nye, 1970). Because these cavities are hydrologically

isolated, and thus poorly drained at this time of year, high fluid pressures can build up. This is why basal fluid pressures are typically higher in winter than in summer (Mathews, 1964). Many glaciers are also underlain by a spatially variable and discontinuous layer of rock debris that can also hold and transport water, though water transport is limited by the hydraulic conductivity of the material and is often less efficient than other means (Fountain and Walder, 1998). Figure 3-13A shows a conceptual model of the starting basal conditions we just described under one of the high and steep hanging glaciers (slope >30°) at Mount Rainier where at least some of the repeating events are originating.

When a load of snow falls on the glacier during a storm, there are a few immediate effects (Figure 3-13B). The driving (shear) stress σ_s and the effective normal stress σ_{Neff} (normal stress minus basal fluid pressure $\sigma_{Neff} = \sigma_N - p_w$) are both increased at a ratio depending on the slope angle:

(3-4) $$\sigma'_{Neff} = \sigma_{Neff} + \rho_s g h_s cos\theta - k$$

(3-5) $$\sigma'_s = \sigma_s + \rho_s g h_s sin\theta$$

where the apostrophe indicates the new value, ρ_s is the density of the new snow, g is the acceleration due to gravity, h_s is the thickness of new snow, θ is the slope angle, and k is the fraction of the increase in load that will be offset by an increase in basal water pressure, which will be spatially variable because the subglacial water system is poorly connected. The increased effective normal stress also results in increased frictional forces that resist the increased driving stresses by an amount proportional to the friction coefficient.

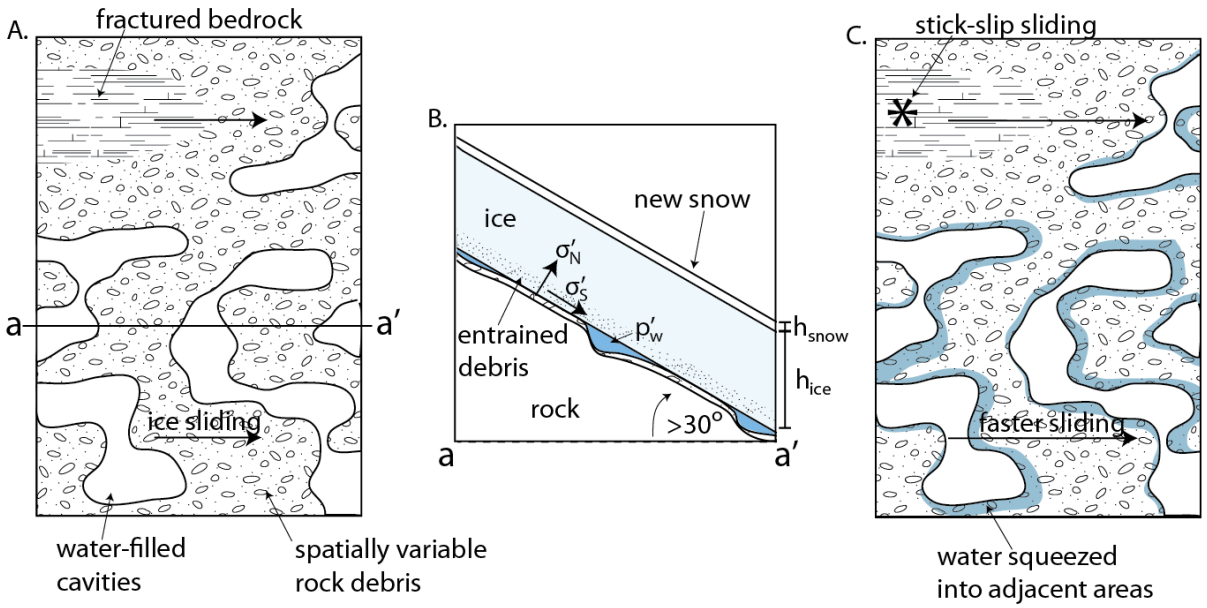

Figure 3-13 Conceptual model of proposed mechanism for velocity increase triggered by snow loading (A.) Typical winter basal configuration in map view: poorly connected distributed basal cavities filled with water with spatial variability. Arrows indicate direction of ice motion. (B.) Cross section of steep upper part of alpine glacier after snow added to surface. (C.) Change in basal configuration several days after the snow loading begins when stick-slip sliding ensues. See text for more detailed explanation.

In any case, the immediate increase in any of these stresses would be just 0.05 - 0.2% (assuming slopes of 30° - 45°) for the amount of snow that occurred prior to any of the select families. This is such a small increase that it could trigger stick-slip sliding only if a particular part of a particular glacier bed was extremely close to a critical state and just a tiny increase in velocity or a tiny increase in effective normal stresses could kick it into an unstable sliding regime. In this case, the 1-2 day lag between peaks in precipitation rate and peaks in repeating event rates (Figure 3-6) could be interpreted as the time it takes for enough snow to build up to push it over the threshold.

However, the sharp peak at a 1-2 day lag time between snow loading and the appearance of repeating earthquakes more strongly suggests that a time-dependent process related to changes in subglacial hydrology is responsible. When the additional normal load from the snow is added to the top of the glaciers, it also squeezes the fluid filled cavities. This increases the fluid pressures,

p_w in each of the isolated basal cavities by the same amount temporarily because they are poorly drained and poorly connected:

(3-6) $$p'_w = p_w + \rho_s g h_s$$

So although the overall shear and effective normal stresses may increase by a fraction of a percent, the initial basal fluid pressures in the isolated cavities may be much lower than the effective normal stresses. Therefore, the fluid pressure could be increased by a larger percentage relative to the initial state, and this would occur over a widespread area since snow falls on the entire glacier. This has the effect of essentially squeezing the water out of the cavities into adjacent areas resulting in the lubrication of a larger area of bed of the glacier (i.e. reducing the areally averaged effective stresses). This could then increase sliding velocities. This change in sliding velocities would take time to occur because the movement of water in response to the pressure increase is limited by the hydraulic properties of the system, providing a potential explanation for the 1-2 day lag. Then, as explained earlier, a sudden increase in sliding velocities in turn could trigger stick-slip sliding (Scholz, 1998) at patches of the bed where conditions are favorable to stick-slip sliding (i.e. colder, dirtier, better drained, Zoet et al., 2013). This could be, for example, a patch of fractured bedrock, and is most likely a different area than those responsible for the increased velocities because it must be poorly lubricated initially (Figure 3-13C). We cannot compute magnitudes because the waveforms are so highly altered, and we do not know the scaling laws to apply in this case to estimate the fault size and amount of slip anyway. Thelen et al. (2013) estimated the size of the seismogenic patch could range from 0.4 to 10^4 m^3, in any case much smaller than the area under any of the glaciers involved, meaning just

part of the glacier bed is seismogenic; the rest may be sliding aseismically. The change in event location over time (Figure 3-12) could be explained by a particularly dirty ice patch moving over an area that favors stick-slip behavior. The family disappearance could occur either when the dirty ice patch moves beyond this area or excess fluid pressures have had sufficient time to drain away and sliding velocities drop back down to previous levels. In most cases, event families die off in about a week or two, which provides a timescale for these processes.

Basal conditions are highly variable (Fountain and Walder, 1998) and there are likely to be places that meet conditions favorable to stick-slip sliding at the base of any glacier (Zoet et al., 2013). If more than one place under a single accelerating portion of a glacier meets the requirements, or if more than one glacier responds in this way, we can get multiple simultaneous event families, as we observed (Figure 3-4). The idea that certain parts of certain glaciers are more prone to the observed behavior is supported by the fact that event families with highly similar waveforms reappear years apart (Figure 3-14). Of course these are not really the same families, but instead, stick-slip sliding occurring again in a very similar location to where it occurred before. This suggests that some areas of some glaciers are much more prone to this behavior than others over long timescales.

Hanging glaciers and icefalls in particular may be prone to transient stick-slip sliding because they are less stable to begin with, which may make them more prone to increases in sliding velocity from minor changes in the system. They also are less likely to have thick layers of deformable basal till beneath them like lower parts of the glaciers might. Deformable till may favor aseismic sliding. These factors may explain why the locations of at least the select event families occur at hanging glaciers and icefalls as opposed to other areas.

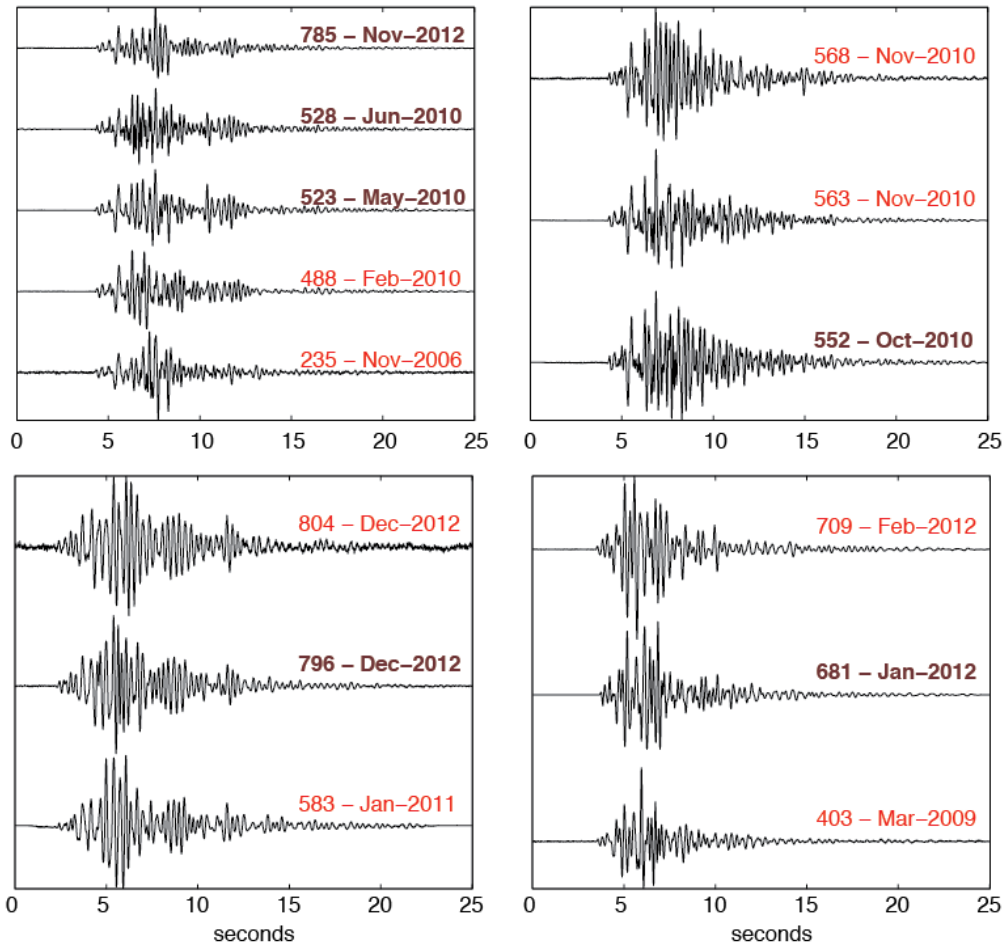

Figure 3-14 Event families that share similar waveforms to the select families (brown text). The month in which each family occurred is labeled. Waveforms shown are the stack of all events recorded at RCS.

One may ask why this behavior doesn't also occur in the late spring and summer when there can be rapid and high volume inputs of water from melt water and rain that can cause sliding velocity increases (e.g. Harper et al., 2007; Fudge et al., 2009). The absence of swarms of repeating low-frequency earthquakes from basal slip in the summer is probably at least in part due to the difference in the configuration of the subglacial drainage system between summer and winter. The summer configuration is efficient and well connected, and thus less favorable for the buildup of high fluid pressures (Fountain and Walder, 1998). The absence of repeating earthquake swarms during the spring melts when the basal configuration may still be distributed

and there can be rapid influxes of rain and melt water could be in part due to the observation by Zoet et al. (2013a) that if the bed of a glacier is already well lubricated, a minor increase in lubrication from a velocity increase is relatively small and is less likely to result in stick-slip sliding. There may just be too much water coming too fast. When there is a lot of basal fluid in the system, widespread bed separation occurs, removing areas of higher drag (Mair et al., 2001). Stick-slip sliding may be triggered for a short time with the initial influx of water, but could quickly be shut off as more and more water enters the system, providing more and more lubrication that can't be drained away fast enough to allow stick-slip sliding to continue. This is consistent with the observations. There are low-frequency repeating earthquakes occurring year round at a background level of about 5 per hour (Figure 3-3). Furthermore, the larger glacial earthquakes observed at Mount Rainier and other Cascade volcanoes by Weaver and Malone (1979) and also at Mount Baker by Moran et al. (2009) were classified as stick-slip events. Those events occurred more often in the summer, indicating that stick-slip sliding probably occurs at some locations of some glaciers year round, just not in the prolonged swarms of repeating earthquakes that seem to rely on winter-like subglacial drainage conditions. Another reason these larger stick-slip events in the summer are not as repeatable as the smaller winter earthquakes of this study could be because the fault area and total slip are larger, so it may require fewer stick-slip cycles for a given patch of entrained debris to move past an area of the bed favorable to stick-slip sliding.

Precipitation does not tend to trigger swarms of repeating earthquakes early in the accumulation season (Figure 3-5). It takes a few weeks of winter conditions for them to start to appear, which may be the amount of time required for the subglacial conduits to collapse viscously and for the drainage system to transition from summer to winter conditions.

There is also the secular trend to explain: the apparent increase in low-frequency repeating earthquake activity over the past ten years (Figure 3-3). This may simply be a function of storminess, for example, the most repeating earthquake activity was detected in the winter of 2011-2012, which also was characterized by fewer storms dropping larger amounts of snow (Figure 3-5). Stormier behavior (i.e. large amounts of snow falling in short amounts of time) would be more likely to trigger sudden velocity increases by the mechanisms we propose than many small storms depositing snow incrementally.

4.3 Broader Implications

Beyond proposing a solution to the puzzle of a peculiar seismic source on one mountain, the findings of this study and our proposed mechanisms have wider implications both in glaciology and beyond. This case adds to the body of knowledge on alpine glacier behavior. We show that some parts of some glaciers can be extremely sensitive to minor changes in external loading. Our observations suggest that if conditions are right, surges in basal sliding velocity can be triggered by surface loading that is a fraction of a percent of the total overburden load, at least in the winter months when the subglacial drainage system is composed of isolated and poorly connected cavities. Furthermore, though stick-slip behavior has been confirmed geodetically for large shallowly sloping ice streams in Antarctica (e.g. Wiens et al., 2008), this is the strongest evidence of seismicity resulting from stick-slip glacial sliding at steep temperate alpine glaciers that we know of. The long-term year round record of repeating earthquake activity provides a window into seasonal differences in the behavior of alpine glaciers, particularly the behavior of the high reaches of alpine glaciers in wintertime – an essentially inaccessible environment that is thus difficult to study with other methods. The behavior documented here adds to the spectrum of known glacier behavior. This may also have ramifications for subglacial morphology, as some

studies suggest stick-slip sliding may have a connection to erosional processes (e.g. Zoet et al., 2012).

Our hypothesis that these events are initiated by a surge in the sliding velocity of hanging glaciers and icefalls also may have implications for ice avalanching hazards. If a velocity increase were to cause sliding to accelerate critically, something we could observe from telemetered seismic data, like the accelerating stick-slip seismicity Caplan-Auerbach and Huggel (2007) observe prior to ice avalanches at Iliamna volcano in Alaska, the end result could be an ice avalanche.

The long-term year-round record of repeating earthquake activity also allowed us to show with more confidence that the majority, if not all, of the observed repeating low-frequency seismicity is not related to volcanic activity. This type of behavior is common and occurs every year. The catalog we compiled also allows us to characterize what is normal behavior, so that when Rainier reawakens, we are better equipped to discriminate harmless glacier-quakes from seismicity related to the volcano. A near real-time method for monitoring repeating earthquake activity that sends alerts when activity is beyond pre-determined bounds on normal behavior, is already under development and testing (Allstadt et al., 2012). These methods could be customized and applied to other glacier-covered volcanoes that present similar monitoring challenges.

These repeating earthquakes at Mount Rainier can provide insight into repeating earthquakes and earthquake behavior in other environments, provided we understand the limitations of the analogy (e.g. ice melts at a much lower temperature than rocks). It is rare to have such an extensive catalog of earthquakes that occur so frequently: nearly 300,000 repeating earthquakes with more occurring every day. This allows us to identify certain seismicity patterns that we do

not typically have enough data to observe for regular earthquakes. For example, we showed that these events show slip-predictable behavior on short timescales, but even minor changes in external loading, such as a tiny increase in the normal load or a gradually decreasing slip rate throw off this relation, but in systematic ways. Shelley (2010) and Shelly and Johnson (2011) observed similarly abrupt changes in the recurrence intervals of small stick-slip earthquakes and non-volcanic tremor on the San Andreas fault near Parkfield that were brought on by stress changes from nearby earthquakes. This is a comparable environment because the repeating earthquakes at this section of the San Andreas are proposed to be sticky spots on a larger plane that is slipping mostly aseismically, similar to the sticky patches at the base of a glacier surrounded by areas that continue to slide aseismically proposed for this study. Ocean and earth tides and even dynamic loading from seismic waves of distant earthquakes also change the normal and shear stresses in the earth by amounts that are a fraction of the total stresses, but have all caused observable changes in the behavior of tectonic events (e.g. Rubenstein et al 2008, Nakata et al 2008; Peng et al., 2009). Apparently, even minor changes in the stress field can alter fault behavior on a range of scales, even for glaciers. The mechanism we invoked as a trigger for the swarms of glacier quakes at Mount Rainier, fluid redistribution and increased aseismic slip around a sticky patch, has been invoked as a trigger for swarms in tectonic environments (e.g. Vidale and Shearer, 2005; Vidale et al., 2006). Though Vidale and Shearer (2005) suggest tectonic swarms are triggered either by the redistribution of fluids or by accelerated aseismic slip, but the mechanism we propose for this study requires both, perhaps both mechanisms are involved in such cases in tectonic environments as well.

5. Conclusions

In this study, we compiled a complete catalog of repeating earthquake activity that occurred over the past decade at Mount Rainier. We found nearly 300,000 repeating earthquakes. About half have dominant frequencies below 8 Hz ("low-frequency") and many of these repeat at regular intervals, the type of event that motivated this study. We found that this type of seismicity has occurred every year for at least the past decade, but previously went undetected. Though low frequency repeating earthquakes occur year round at a background level of about 5 per hour, big swarms of activity occur only in late autumn to early spring.

We used this catalog to fully characterize this type of earthquake to understand the source and to confirm that the source is glacial and not related to volcanic activity. We found that the swarms often are composed of several distinct families occurring at different areas of the mountain simultaneously. Swarms correlate strongly with precipitation, with a normalized cross correlation coefficient of nearly 0.5, peaking sharply around a 1-2 day lag. Within each family, we showed that recurrence intervals, inter-event correlations, and event energy all vary over time, often gradually, but sometimes suddenly, and these sudden changes often correlate with minor changes in loading ($<<1\%$) from snowfall. We also used coda wave interferometry to track the location of these event sources over time, and found that the sources move at glacial speeds, but somewhat faster than average initially, then slowing down over time. We also found evidence of healing occurring between events based on linear relations between recurrence interval and event energy. By stacking hundreds of nearly identical events, we were able to pick out the first P-wave motions at several stations and found that most events show mixed polarities, suggesting a shear source.

These observations are consistent with our hypothesis that most, if not all, of the low-frequency repeating earthquakes we documented are manifestations of stick-slip basal sliding of glaciers, and that the transition from smooth aseismic sliding to stick-slip sliding is triggered by changes in subglacial hydrology in response to snow loading. We hypothesize that the added weight squeezes water out of poorly connected and pressurized subglacial cavities and into adjacent areas, lubricating more of the bed and resulting in a temporary velocity increase. This mechanism could explain the observed time lag between snowfall and earthquake swarm appearance. A basal configuration composed of isolated and distributed cavities is typical of winter, which could partially explain why these events occur primarily in the winter months. We used a range of techniques to locate some families of events with high enough accuracy to identify under which glaciers they occurred, and found that all of the locatable families were located either on steep hanging glaciers or icefalls, suggesting this type of glacier is most sensitive to minor perturbations in external loading.

The behavior of repeating earthquakes at Mount Rainier that we document here provides a particularly complete dataset to provide insight into glacier behavior, and possibly even tectonic fault behavior. The benefit of this dataset that documents the stick-slip sliding of glaciers, is that it a good case for seismology to benefit from the rich body of knowledge from glaciology and vice versa to improve understanding in both cases. In some ways, the glaciers at Mount Rainier provide a giant natural fault laboratory that we have been inadvertently recording for over a decade through seismic and weather monitoring for testing ideas in both disciplines. We have only just begun to analyze the database of repeating earthquakes that we compiled and there is undoubtedly more to be learned.

6. Acknowledgements

This work was funded in part by UW ESS Department Awards and the Colorado Scientific Society, with research assistantship, logistical support, and data from the Pacific Northwest Seismic Network, IRIS Data Management Center, and Cascade Volcano Observatory. It would not have been possible without the help of Mount Rainier National Park Staff and Climbing Rangers, and Steve Malone, John Vidale, and Seth Moran for their advising along the way, Josh Carmichael for sharing his multiplet detection codes, Robert Hahn and Al Rasmussen for meteorological advice, Bernard Hallet, Ed Waddington, TJ Fudge and Adam Campbell for glaciology feedback and everyone who helped with field work, even though the mountain sabotaged most of our efforts, particularly Peter Neff, Kristin Poinar, Max Stevens, Jon Connolly, Doug Gibbons, Eric Sofen, Regina Carns, Stewart Matthiesen, Courtney Moore, David Shean, and Andy Pickering.

7. References

Allstadt, K., S. D. Malone, D. E. Shean, M. A. Fahnestock and J. E. Vidale (2013). Swarms of repeating stick-slip glacier quakes triggered by snow loading at Mount Rainier volcano. AGU Fall Meeting 2013 abstract C54B-06.

Allstadt, K.E., J.D. Carmichael, S.D. Malone, P. Bodin, J.E. Vidale, and S.C. Moran (2012). Glacier Quakes Mimicking Volcanic Earthquakes: The Challenge of Monitoring Ice-clad volcanoes (and some solutions). AGU Fall 2012 Meeting, Poster V21B-2776, San Francisco, CA. available online at: http://fallmeeting.agu.org/2012/eposters/eposter/v21b-2776/, last accessed 3 Nov 2013.

Cakir, R., and T. J. Walsh (2012). Loss estimation pilot project for lahar hazards from Mount Rainier, Washington, Washington Division of Geology and Earth Resources. Information circular 113.

Caplan-Auerbach, J. and C. Huggel (2007). Precursory seismicity associated with frequent, large ice avalanches on Iliamna volcano, Alaska, USA. J. Glaciol., 53 (180), 128-140.

Carmichael, J. D., E. C. Pettit, M. Hoffman, A. Fountain, and B. Hallet (2012). Seismic multiplet response triggered by melt at Blood Falls, Taylor Glacier, Antarctica. J. Geophys. Res., 117, F03004

Carmichael, Joshua D. (2013). Melt-Triggered Seismic Response in Hydraulically-Active Polar Ice: Observations and Methods. PhD thesis, University of Washington.

Chouet, B. A, R. A. Page, C. D. Stephens, J. C. Lahr, and J. A. Power (1994). Precursory swarms of long-period events at Redoubt Volcano (1989-1990), Alaska: Their origin and use as a forecasting tool. J. Volc. and Geothm. Res., 62, 95-135.

Deichmann, N., J. Ansorge, F. Scherbaum, A. Aschwanden, F. Bernardi, and G. H. Gudmundsson (2000). Evidence for deep icequakes in an Alpine glacier. Ann. Glaciol., 31, 85-90.

Douma, H., and R. Snieder (2005). Correcting for bias due to noise in coda wave interferometry. Geophys. J. Int., 164, 99-108.

Dreger, D., R. M. Nadeau, and A. Chung (2007). Repeating earthquake finite source models: Strong asperities revealed on the San Andreas Fault. Geophys. Res. Lett., 34, L23302, 5p.

Driedger, C. L., and P. M. Kennard (1986). Ice volumes on Cascade volcanoes: Mount Rainier, Mount Hood, Three Sisters, and Mount Shasta. USGS Professional Paper 1365, 28 p., 6 plates.

Ekstrom G, Nettles M and Abers GA (2003). Glacial earthquakes. Science, 302(5645), 622–624 (doi: 10.1126/science.1088057)

Ewert J.W., M. Guffanti and T. L. Murray (2005). An assessment of volcanic threat and monitoring capabilities in the United States: framework for a national volcano early warning system. USGS Open File Rep. 2005-1164.

Fiske, R.S., C. A. Hopson, and A. C. Waters (1988). Geologic Map and Section of Mount Rainier National Park, Washington. U.S.G.S Map I-432.

Fountain, A. G. and J. S. Walder (1998). Water flow through temperate glaciers. Rev. Geophys., 36(3), 299-328.

Fudge T.J., J.T. Harper, N.F. Humphrey and W.T. Pfeffer (2009). Rapid glacier sliding, reverse ice motion and subglacial water pressure during an autumn rainstorm. Ann. Glaciol., 50(52), 101–108 (doi: 10.3189/172756409789624247)

Harper J.T., N.F. Humphrey, W.T. Pfeffer and B. Lazar (2007). Two modes of accelerated glacier sliding related to water. Geophys. Res. Lett., 34(12), L12503 (doi: 10.1029/2007GL030233)

Herrmann, R. B. (1979). FASTHYPO -- A hypocenter location program, Earthquake Notes 50, No. 2., 25-37.

Hoblitt R.P., J.S. Walder, C.L. Driedger, K.M. Scott, P.T. Pringle and J.W. Vallance (1995). Volcano hazards from Mount Rainier, Washington. USGS Open File Rep. 95-273

Hodge S.M. (1974). Variations in the sliding of a temperate glacier. J. Glaciol., 13(69), 349–369

Hotovec-Ellis, A., J. Gomberg, J. Vidale and K. Creager (2013). A continuous record of inter-eruption velocity change at Mount St. Helens from coda-wave interferometry. submitted to J. Geophys. Res. Oct 2013.

Jonsdottir K, R. Roberts, V. Pohjola, B. Lund, Z. H. Shomali, A. Tryggvason, and R. Bodvarsson (2009). Glacial long period seismic events at Katla volcano, Iceland. Geophys. Res. Lett., 36(11), L11402 (doi: 10.1029/2009GL038234)

Julian, B.R., A. D. Miller, and G. R. Foulger (1998). Non-double-couple earthquakes 1. Theory, Reviews of Geophysics, 36 (4), 525-549.

Kamb., B. (1964). Glacier Geophysics. Science, 146(3642), 353-365.

Kamb, W. B. (1970). Sliding motion of glaciers: theory and observation. Reviews of Geophysics and Space Physics, 8(4), 673-728.

Kanamori, H., G. Ekstrom, A. Dziewonski, J.S. Barker, and S.A. Sipkin (1993). Seismic radiation by magma injection: an anomalous seismic event near Tori Shima, Japan. J. Geophys. Res., 98(B4), 6511-6522.

Klein, F. W. (1985), User's guide to HYPOINVERSE, a program for VAX and 350 computers to solve for earthquake locations. U. S. Geological Survey, Reston, VA, United States (USA), United States (USA).

Leaver, D. S. (1984). Mixed stochastic and deterministic modeling of the crustal structure in the vicinity of Mount Hood, Oregon, Ph.D. thesis, 193 pp Univ. of Wash., Seattle.

Mair, D., P. Nienow, I. Willis, and M. Sharp (2001). Spatial patterns of glacial motion during a high-velocity event: Haut Glacier d'Arolla, Switzerland. J. Glaciol, 47(156), 9-20.

Malone, S. D., and G. L. Pavlis (1983), Velocity structure and relocation of earthquakes at Mount St. Helens, EOS Trans.Am.Geophys.Union, 64, 895.

Martini, F., C. J. Bean, G. Saccorotti, F. Viverios, and N. Wallenstein (2009). Seasonal cycles of seismic velocity variations detected using coda wave interferometry at Fogo volcano, Sao Miguel, Azores, during 2003-2004. J. Volc. Geothm. Res., 181, 231-246.

Mathews, W. H. (1964). Water pressure under a glacier. J. Glaciol., 5, 235-240.

Meier, M. A. and P. J. Lee (2009). Converted-wave resolution. Geophys., 74 (2), Q1-Q16, doi: 10.1190/1.3074303

Metaxian, J-P., S. Araujo, M. Mora, and P. Lesage (2003). Seismicity related to the glacier of Cotopaxi Volcano, Ecuador. Geophys. Res. Lett., 30(9), 1483.

Moran, S.C., J.M. Lees, and S.D. Malone (1999). P-wave crustal velocity structure in the greater Mount Rainier area from local earthquake tomography. Journal of Geophysical Research, v. 104(B5), p. 10,775-10,786.

Moran S.C., W.A. Thelen, J. Caplan-Auerbach, S.D. Malone and A. Wright (2009). An anomalous swarm of low-frequency events at Mount Baker, Washington, June–August 2009. Abstract V23D-2112 AGU Fall Meeting 2009, available at: http://adsabs.harvard.edu/abs/2009AGUFM.V23D2112M last accessed 13 Nov 2013.

Nadeau, R. M., W. Foxall, and T. V. McEvilly (1995). Clustering and Periodic Recurrence of Microearthquakes on the San Andreas fault at Parkfield, California. Science, 267 (5197) 503-507.

Nakata, R. N. Suda, and H. Tsurouka (2008). Non-volcanic tremor resulting from the combined effect of Earth tides and slow slip events. Nat. Geosci., 1(10), 676-678.

National Park Service (2013a). Mount Rainier Annual Visitor Statistics 1967-2012. Dept. of the Interior, available at: http://www.nps.gov/mora/parkmgmt/upload/vis-stats-1967-2012.pdf, last accessed 9 Nov 2013.

National Park Service (2013b). Annual Snowfall Totals at Paradise, 1920 to 2012. Dept. of the Interior, available at: http://www.nps.gov/mora/planyourvisit/loader.cfm?csModule=security/getfile&pageid=527381 , last accessed 16 Nov 2013.

Neave K.G. and J.C. Savage (1970). Icequakes on the Athabasca Glacier. J. Geophys. Res., 75(8), 1351–1362 (doi: 10.1029/JB075i008p01351)

Neuberg, J. and T. Pointer (2000). Effects of volcano topography on seismic broad-band waveforms. Geophys. J. Int., 143, 239-248.

Nye, J. F. (1970). Glacier sliding without cavitation in a linear viscous approximation. Proc.R . Soc. London, Ser. A, 315, 381-403.

O'Neel, S. H. P Marshall, D. E. McNamara, and W. T. Pfeffer (2007). Seismic detection and analysis of icequakes of Columbia Glacier, Alaska. J. Geophys. Res., 112, F03S23, doi: 10.1029/2006JF000595

Peng, Z., J. E. Vidale, A. G. Wech, R. M. Nadeau and K. C. Creager (2009). Remote triggering of tremor along the San Andreas Fault in central California. J. Geophys. Res., 114, B00A06.

PRISM Climate Group, Oregon State University, http://prism.oregonstate.edu, created 4 Feb 2004, last accessed May 2013.

Qamar, A. (1988). Calving Icebergs: A Source of Low-Frequency Seismic Signals From Columbia Glacier, Alaska. J. Geophys. Res., 93(B6), 6615-6623.

Robinson, D. J., M. Sambridge, and R. Snieder (2011). A probabilistic approach for estimating the separation between a pair of earthquakes directly from their coda waves. J. Geophys. Res., 116, B04309.

Roux P.-F., D. Marsan, J.-P. Metaxian, G. O'Brien and L. Moreau (2008). Microseismic activity within a serac zone in an alpine glacier (Glacier d'Argentiere, Mont Blanc, France). J. Glaciol., 54(184), 157–168 (doi: 10.3189/002214308784409053)

Rubinstein, J. L., M. La Rocca, J. E. Vidale, K. C. Creager, and A. G. Wech (2008). Tidal modulation of nonvolcanic tremor. Science, 319 (5860), 186-189.

Scholz, C. (1998). Earthquakes and friction laws. Nature, 391, 37-42.

Shelley, D. R., G. C. Beroza, and S. Ide (2007). Non-volcanic tremor and low-frequency swarms. Nature, 446, 305-307, DOI 10.1007/s00024-005-0026-6

Shelley, D. R. (2010). Periodic, Chaotic, and Doubled Earthquake Recurrence Intervals on the Deep San Andreas Fault. Science, 328, 1385, doi:10.1007/s00024-005-0026-6

Shelly, D. R., and K. M. Johnson (2011). Tremor reveals stress shadowing, deep postseismic creep, and depth-dependent slip recurrence on the lower-crustal San Andreas fault near Parkfield. Geophys. Res. Lett., 38, L13312, doi: 10.1029/2011GL047863, 6p.

Shimazaki, K. and T. Nakata (1980). Time-predictable recurrence model for large earthquakes. Geophys. Res. Lett., 7, 279-282 doi:10.1029/GL007i004p00279.

Sisson, T. W., J. E. Robinson, and D. D. Swinney (2011). Whole-edifice ice volume change A.D. 1970 to 2007/2008 at Mount Rainier, Washington, based on LIDAR surveying. Geology, 39, 639-642., doi: 10.1130/G31902.1

Sisson T.W. and J.W. Vallance (2009). Frequent eruptions of Mount Rainier over the last 2,600 years. Bull. Volcanol., 71(6), 595–618 (doi: 10.1007/s00445-008-0245-7)

Snieder, R. and M. Vrijlandt (2005). Constraining the source separation with coda wave interferometry: Theory and application to earthquake doublets in the Hayward fault, California. J. Geophys. Res.: 110, B04301, 15 p. doi: 10.1029/2004JB003317.

Snieder, R. (2006). The theory of coda wave interferometry. Pure and Appl. Geophys., 163, 455-473, doi: 10.1007/s00024-005-0026-6

St. Lawrence W. and A. Qamar (1979). Hydraulic transients: a seismic source in volcanoes and glaciers. Science, 203(4381), 654–656 (doi: 10.1126/science.203.4381.654)

Stein, S. and M. Wysession (2003). An introduction to seismology, earthquakes and earth structure. Blackwell, Malden, MA.

Swanson, D.S., S.D. Malone, and T. Casadevall (1994) Mount Rainier, a Decade Volcano. U.S. National Academy of Science Report.

Sweet, J., K.C. Creager, H. Houston, and T. Thomas (2012). Unlocking the secrets of slow slip on the plate interface using low-frequency earthquakes. paper presented at S43I-04 at AGU Fall Meeting 2012.

Thelen, W.A., K. Allstadt, S. de Angelis, S. D. Malone, S. C. Moran, J. Vidale (2012). Shallow repeating seismic events under an alpine glacier at Mount Rainier, Washington. J. Glaciol., 59(214), 345-356.

Tsai, V. C., J. R. Rice, and M. Fahnestock (2008). Possible mechanisms for glacial earthquakes. J. Geophys. Res., 113, F03014, doi:10.1029/2007JF000944

Vidale, J. E. and P. M. Shearer (2006). A survey of 71 earthquake bursts across southern California: Exploring the role of pore fluid pressure fluctuations and aseismic slip as drivers. J. Geophys. Res., 111, B05312, DOI 10.1029/2005JB004034, 12 p.

Vidale, J. E., K. L. Boyle, P. M. Shearer (2006). Crustal earthquake bursts in California and Japan: Their pattern and relation to volcanoes. Geophys. Res. Lett., 33, L20313, doi: 10.1029/2006GL027723, 5p.

Vivian, R. A., and G. Bocquet (1973). Subglacial cavitation phenomena under the Glacier d' Argentiere, Mont Blanc, France. Journal of Glaciology, 12 (66), 439-51.

Waldhauser, F., and W. L. Ellsworth (2000). A double-difference earthquake location algorithm: method and application to the Northern Hayward Fault, California. Bull. Seism. Soc. Am., 90 (6), 1353-1368. doi: 10.1785/0120000006

Walter, F., J. F. Clinton, N. Deichmann, D. S. Dreger, S. E. Minson, and M. Funk (2009). Moment tensor inversions of icequakes on Gornergletscher, Switzerland. Bull. Seism. Soc. Am., 99 (2A), 852-870. doi: 10.1785/0120080110

Walter, F., P. D. Canassy, S. Husen, and J. F. Clinton (2013). Deep icequakes: What happens at the base of Alpine glaciers? J. Geophys. Res., 118, 1720-1728, doi:10.1002/jgrf.20124

Weaver C.S. and S.D. Malone (1976). Mount St. Helens seismic events: volcanic earthquakes or glacial noises? Geophys. Res. Lett., 3(3), 197–200 (doi: 10.1029/GL003i003p00197)

Weaver, C. S. and S.D. Malone (1979). Seismic evidence for discrete glacier motion at the rock-ice interface. J. Glaciol, 23(89), 171-184.

West M.E., C.F. Larsen, M. Truffer, S. O'Neel and L. LeBlanc (2010). Glacier microseismicity. Geology, 38(4), 319–322 (doi:10.1130/G30606.1)

Wiens D.A., S. Anandakrishnan, J.P. Winberry and M.A. King (2008). Simultaneous teleseismic and geodetic observations of the stick–slip motion of an Antarctic ice stream. Nature, 453(7196), 770–774 (doi: 10.1038/nature06990)

Winberry, J. P., S. Anandakrishnan, D. A. Wiens, R. B. Alley (2013) Nucleation and seismic tremor associated with the glacial earthquakes of Whillans Ice Stream, Antarctica. Geophys. Res. Lett., 40(2), 312-315, DOI: 10.1002/grl.50130

Zoet, L. K., S. Anandakrishnan, R. B. Alley, A. A. Nyblade, and D. A. Wiens (2012). Motion of an Antarctic glacier by repeated tidally modulated earthquakes. Nat. Geosci., 5, 623-626.

Zoet, L. K., B. Carpenter, M. Scuderi, R. B. Alley, S. Anandakrishnan, C. Marone and M. Jackson (2013a). The effects of entrained debris on the basal sliding stability of a glacier. J. Geophys Res., 118, 656-666. doi:10.1002/jgrf.20052

Zoet, L.K., R. B. Alley, S. Anandakrishnan, K. Christianson (2013b), Accelerated subglacial erosion in response to stick-slip motion. Geology, 41(2), 159-162, doi: 10.1130/G33624.1

Depth to bottom (m)	Thickness (m)	Vs (m/s)	Dry density (kg/m^3)	Wet density (kg/m^3)	Description	Vs30 (m/s)
Unit 1 - 8m Qvt, 50m Qva, 30m Qvlc, Qpf						
1	1	150	1280	1536	soil	
3	2	400	1800	2160	Qvt	375
5	2	475	1875	2250	Qvt	
7	2	550	1950	2340	Qvt	
8	1	600	2000	2400	Qvt	
12	4	300	1600	1920	Qva	
17	5	350	1680	2016	Qva	
25	8	400	1700	2040	Qva	
35	10	450	1740	2088	Qva	
45	10	500	1760	2112	Qva	
50	5	550	1780	2136	Qva	
58	8	600	1800	2160	Qva	
68	10	400	1500	1800	Qvlc	
78	10	450	1550	1860	Qvlc	
83	5	500	1600	1920	Qvlc	
88	5	550	1650	1980	Qvlc	
	0	600	2000	2400	Qpf	
Unit 2 - 8m Qvt, 15m Qva, 20m Qvlc, Qpf						
1	1	150	1280	1536	soil	
3	2	400	1800	2160	Qvt	369
5	2	475	1875	2250	Qvt	
7	2	550	1950	2340	Qvt	
8	1	600	2000	2400	Qvt	
12	4	300	1740	2088	Qva	
17	5	350	1760	2112	Qva	
25	8	400	1700	2040	Qva	
35	10	400	1500	1800	Qvlc	
45	10	450	1550	1860	Qvlc	
	0	600	2000	2400	Qpf	
Unit 3 - 8m Qvt, 15m Qva, Qpf						
1	1	150	1280	1536	soil	
3	2	400	1800	2160	Qvt	421
5	2	475	1875	2250	Qvt	
7	2	550	1950	2340	Qvt	
8	1	600	2000	2400	Qvt	
16	8	350	1740	2088	Qva	
23	7	450	1760	2112	Qva	
	0	600	2000	2400	Qpf	
Unit 4 - 50m Qva, Qpf						
1	1	100	1280	1536	soil	
5	4	300	1600	1920	Qva	358
10	5	350	1680	2016	Qva	
18	8	400	1700	2040	Qva	
28	10	450	1740	2088	Qva	
38	10	500	1760	2112	Qva	
43	5	550	1780	2136	Qva	
	0	600	1800	2160	Qva	
Unit 5 - 25m Qva, Qpf						
1	1	100	1280	1536	soil	368
5	4	300	1600	1920	Qva	
10	5	350	1680	2016	Qva	
18	8	400	1700	2040	Qva	
25	7	450	1740	2088	Qva	
	0	600	2000	2400	Qpf	
Unit 6 - 10m Qva, Qpf						
1	1	100	1280	1536	soil	403
5	4	300	1600	1920	Qva	
10	5	350	1680	2016	Qva	
15	5	450	1800	2160	Qpf	
20	5	550	1900	2280	Qpf	
	0	600	2000	2400	Qpf	
Unit 7 - 50m Qva, 30m Qvlc, Qpf						
1	1	100	1280	1536	soil	358
5	4	300	1600	1920	Qva	
10	5	350	1680	2016	Qva	
18	8	400	1700	2040	Qva	
28	10	450	1740	2088	Qva	
38	10	500	1760	2112	Qva	
43	5	550	1780	2136	Qva	
50	7	600	1800	2160	Qva	
60	10	400	1500	1800	Qvlc	
70	10	450	1550	1860	Qvlc	

Depth to bottom (m)	Thickness (m)	Vs (m/s)	Dry density (kg/m^3)	Wet density (kg/m^3)	Description	Vs30 (m/s)
80	10	500	1600	1920	Qvlc	
	0	600	2000	2400	Qpf	
Unit 8 - 25m Qva, 25m Qvlc, Qpf						
1	1	100	1280	1536	soil	350
5	4	300	1600	1920	Qva	
10	5	350	1680	2016	Qva	
18	8	400	1700	2040	Qva	
25	7	450	1740	2088	Qva	
35	10	400	1500	1800	Qvlc	
45	10	450	1550	1860	Qvlc	
50	5	500	1600	1920	Qvlc	
	0	600	2000	2400	Qpf	
Unit 9 - 10m Qva, 30m Qvlc, Qpf						
1	1	100	1280	1536	soil	301
5	4	300	1600	1920	Qva	
10	5	350	1680	2016	Qva	
20	10	300	1300	1560	Qvlc	
30	10	350	1400	1680	Qvlc	
40	10	400	1500	1800	Qvlc	
	0	600	2000	2400	Qpf	
Unit 10 - 5m Qvr, 25m Qvlc, Qpf						
1	1	100	1280	1536	soil	
3	2	250	1450	1740	Qvr	230
5	2	350	1500	1800	Qvr	
15	10	200	1300	1560	Qvlc	
25	10	250	1350	1620	Qvlc	
30	5	300	1400	1680	Qvlc	
	0	600	2000	2400	Qpf	
Unit 11 - 30m Qvlc, Qpf						
1	1	100	1280	1536	soil	234
11	10	200	1300	1560	Qvlc	
21	10	250	1350	1620	Qvlc	
26	5	300	1400	1680	Qvlc	
31	5	350	1500	1800	Qvlc	
	0	600	2000	2400	Qpf	
Unit 12 - 15m Qvlc, Qpf						
1	1	100	1280	1536	soil	281
11	10	200	1300	1560	Qvlc	
16	5	250	1350	1620	Qvlc	
21	5	450	1800	2160	Qpf	
26	5	550	1900	2280	Qpf	
	0	600	2000	2400	Qpf	
Unit 13 - 5m Qvr, 8m Qvt, 50m Qva, 30m Qvlc, Qpf						
1	1	100	1280	1536	soil	368
3	2	250	1450	1740	Qvr	
5	2	350	1500	1800	Qvr	
7	2	400	1800	2160	Qvt	
9	2	475	1875	2250	Qvt	
11	2	550	1950	2340	Qvt	
13	2	600	2000	2400	Qvt	
17	4	350	1680	2016	Qva	
22	5	400	1700	2040	Qva	
30	8	450	1740	2088	Qva	
40	10	500	1760	2112	Qva	
50	10	550	1780	2136	Qva	
55	5	600	1800	2160	Qva	
	0	600	1800	2160	Qva	
Unit 14 - 5m Qvr, 8m Qvt, 20m Qva, 25m Qvlc, Qpf						
1	1	100	1280	1536	soil	368
3	2	250	1450	1740	Qvr	
5	2	350	1500	1800	Qvr	
7	2	400	1800	2160	Qvt	
9	2	475	1875	2250	Qvt	
11	2	550	1950	2340	Qvt	
13	2	600	2000	2400	Qvt	
17	4	350	1680	2016	Qva	
22	5	400	1700	2040	Qva	
30	8	450	1740	2088	Qva	
39	9	500	1760	2112	Qva	
49	10	400	1500	1800	Qvlc	
59	10	450	1550	1860	Qvlc	
64	5	500	1600	1920	Qvlc	
	0	600	2000	2400	Qpf	

Depth to bottom (m)	Thickness (m)	Vs (m/s)	Dry density (kg/m^3)	Wet density (kg/m^3)	Description	Vs30 (m/s)
Unit 15 - 5m Qvr, 8m Qvt, 15m Qva, Qpf						
1	1	100	1280	1536	soil	373
3	2	250	1450	1740	Qvr	
5	2	350	1500	1800	Qvr	
7	2	400	1800	2160	Qvt	
9	2	475	1875	2250	Qvt	
11	2	550	1950	2340	Qvt	
13	2	600	2000	2400	Qvt	
17	4	350	1680	2016	Qva	
22	5	400	1700	2040	Qva	
28	6	450	1740	2088	Qva	
	0	600	2000	2400	Qpf	
Unit 16 - 5m Qvr, 50m Qva, 30m Qvlc, Qpf						
1	1	100	1280	1536	soil	
3	2	250	1450	1740	Qvr	420
5	2	350	1500	1800	Qvr	
9	4	350	1680	2016	Qva	
14	5	400	1700	2040	Qva	
22	8	450	1740	2088	Qva	
32	10	500	1760	2112	Qva	
42	10	550	1780	2136	Qva	
47	5	600	1800	2160	Qva	
52	5	600	1800	2160	Qva	
62	10	400	1500	1800	Qvlc	
72	10	450	1550	1860	Qvlc	
77	5	500	1600	1920	Qvlc	
	0	600	2000	2400	Qpf	
Unit 17 - 5m Qvr, 15m Qva, 25m Qvlc, Qpf						
1	1	100	1280	1536	soil	
3	2	250	1450	1740	Qvr	349
5	2	350	1500	1800	Qvr	
9	4	350	1680	2016	Qva	
14	5	400	1700	2040	Qva	
20	6	450	1740	2088	Qva	
30	10	400	1500	1560	Qvlc	
40	10	450	1550	1620	Qvlc	
45	5	300	1400	1680	Qvlc	
	0	600	2000	2400	Qpf	
Unit 18 - 5m Qvr, 15m Qva, Qpf						
1	1	100	1280	1536	soil	386
3	2	250	1450	1740	Qvr	
5	2	350	1500	1800	Qvr	
9	4	350	1680	2016	Qva	
14	5	400	1700	2040	Qva	
20	6	450	1740	2088	Qva	
	0	600	2000	2400	Qpf	
Unit 19 - 10m Qp, Qpf						
10	10	60	1050	1260	Peat	147
15	5	450	1800	2160	Qpf	
20	5	550	1900	2280	Qpf	
	0	600	2000	2400	Qpf	
Unit 20 - 5m Fill, 8m Qvt, 50m Qva, 30m Qvlc, Qpf						
1	1	100	1200	1440	soil	283
3	2	120	1200	1440	Fill	
5	2	130	1200	1440	Fill	
7	2	400	1800	2160	Qvt	
9	2	475	1875	2250	Qvt	
11	2	550	1950	2340	Qvt	
13	2	600	2000	2400	Qvt	
17	4	300	1600	1920	Qva	
22	5	350	1680	2016	Qva	
30	8	400	1700	2040	Qva	
40	10	450	1740	2088	Qva	
50	10	500	1760	2112	Qva	
55	5	550	1780	2136	Qva	
63	8	600	1800	2160	Qva	
73	10	400	1500	1800	Qvlc	
83	10	450	1550	1860	Qvlc	
88	5	500	1600	1920	Qvlc	
93	5	550	1650	1980	Qvlc	
	0	600	2000	2400	Qpf	
Unit 21 - 6m Qt/Qal,8m Qvt, 50m Qva, 30m Qvlc, Qpf						
1	1	100	1200	1440	soil	259

Depth to bottom (m)	Thickness (m)	Vs (m/s)	Dry density (kg/m^3)	Wet density (kg/m^3)	Description	Vs30 (m/s)
3	2	120	1200	1440	Qt/Qal	
6	3	130	1200	1440	Qt/Qal	
8	2	400	1800	2160	Qvt	
10	2	475	1875	2250	Qvt	
12	2	550	1950	2340	Qvt	
14	2	600	2000	2400	Qvt	
18	4	300	1600	1920	Qva	
23	5	350	1680	2016	Qva	
31	8	400	1700	2040	Qva	
41	10	450	1740	2088	Qva	
51	10	500	1760	2112	Qva	
56	5	550	1780	2136	Qva	
64	8	600	1800	2160	Qva	
74	10	400	1500	1800	Qvlc	
84	10	450	1550	1860	Qvlc	
89	5	500	1600	1920	Qvlc	
94	5	550	1650	1980	Qvlc	
	0	600	2000	2400	Qpf	
Unit 22 - 10m Qls, Qpf						
1	1	100	1200	1440	soil	262
3	2	120	1200	1440	Landslide	
5	2	130	1200	1440	Landslide	
10	5	140	1250	1500	Landslide	
15	5	450	1800	2160	Qpf	
20	5	550	1900	2280	Qpf	
	0	600	2000	2400	Qpf	
Unit 23 - 5m Qls, Qpf						
1	1	100	1200	1440	soil	344
3	2	120	1200	1440	Landslide	
5	2	130	1200	1440	Landslide	
10	5	450	1800	2160	Qpf	
15	5	550	1900	2280	Qpf	
	0	600	2000	2400	Qpf	
Unit 24 - 3m Qls, 25m Qvlc, Qpf						
1	1	100	1200	1440	soil	220
3	2	120	1200	1440	Landslide	
13	10	200	1300	1560	Qvlc	
23	10	250	1350	1620	Qvlc	
28	5	300	1400	1680	Qvlc	
	0	600	2000	2400	Qpf	
Unit 25 - 3m Qls, 15m Qva, 25m Qvlc, Qpf						
1	1	100	1200	1440	soil	289
3	2	120	1200	1440	Landslide	
13	10	300	1600	1920	Qva	
18	5	350	1680	2016	Qva	
26	8	400	1700	2040	Qva	
28	2	450	1740	2088	Qva	
38	10	400	1500	1800	Qvlc	
48	10	450	1550	1860	Qvlc	
53	5	500	1600	1920	Qvlc	
	0	600	2000	2400	Qpf	
Unit 26 - 10m Fill, 5m Qvr, Qpf						
1	1	100	1200	1440	soil	244
3	2	120	1200	1440	Fill	
5	2	130	1200	1440	Fill	
10	5	140	1250	1500	Fill	
12	2	250	1400	1680	Qvr	
15	3	350	1500	1800	Qvr	
20	5	450	1800	2160	Qpf	
25	5	550	1900	2280	Qpf	
	0	600	2000	2400	Qpf	
Unit 27 - 10m Fill, Qpf						
1	1	100	1200	1440	soil	262
3	2	120	1200	1440	Fill	
5	2	130	1200	1440	Fill	
10	5	140	1250	1500	Fill	
15	5	450	1800	2160	Qpf	
20	5	550	1900	2280	Qpf	
	0	600	2000	2400	Qpf	
Unit 28 - 10m Fill, 50m Qtf, Qpf						
1	1	100	1200	1440	soil	130
3	2	120	1200	1440	Fill	
5	2	130	1200	1440	Fill	

Depth to bottom (m)	Thickness (m)	Vs (m/s)	Dry density (kg/m^3)	Wet density (kg/m^3)	Description	Vs30 (m/s)
10	5	140	1250	1500	Fill	
30	20	130	1280	1536	Qtf	
60	30	170	1300	1560	Qtf	
	0	600	2000	2400	Qpf	
Unit 29-31 - 4m Fill, 30m Qal, Qva (Duwamish area)						
2	2	100	1200	1440	Fill	142
4	2	110	1200	1440	Fill	
9	5	125	1200	1440	Qal	
14	5	135	1200	1440	Qal	
24	10	160	1300	1560	Qal	
34	10	180	1350	1620	Qal	
38	4	300	1600	1920	Qva	
43	5	350	1680	2016	Qva	
51	8	400	1700	2040	Qva	
61	10	450	1740	2088	Qva	
71	10	500	1760	2112	Qva	
76	5	550	1780	2136	Qva	
	0	600	1800	2160	Qva	
Unit 32 - 3m Fill, 8m Qvt, 50m Qva, 30m Qvlc, Qpf						
1	1	100	1200	1440	soil	316
3	2	120	1200	1440	Fill	
5	2	400	1800	2160	Qvt	
7	2	475	1875	2250	Qvt	
9	2	550	1950	2340	Qvt	
11	2	600	2000	2400	Qvt	
15	4	300	1600	1920	Qva	
20	5	350	1680	2016	Qva	
28	8	400	1700	2040	Qva	
38	10	450	1740	2088	Qva	
48	10	500	1760	2112	Qva	
53	5	550	1780	2136	Qva	
61	8	600	1800	2160	Qva	
71	10	400	1500	1800	Qvlc	
81	10	450	1550	1860	Qvlc	
86	5	500	1600	1920	Qvlc	
91	5	550	1650	1980	Qvlc	
	0	600	2000	2400	Qpf	
Unit 33 - 5m Fill, 5m Qvr, 8m Qvt, 50m Qva, 30m Qvlc, Qpf						
1	1	100	1200	1440	soil	273
3	2	120	1200	1440	Fill	
5	2	130	1200	1440	Fill	
7	2	250	1400	1680	Qvr	
10	3	350	1500	1800	Qvr	
12	2	400	1800	2160	Qvt	
14	2	475	1875	2250	Qvt	
16	2	550	1950	2340	Qvt	
18	2	600	2000	2400	Qvt	
22	4	300	1600	1920	Qva	
27	5	350	1680	2016	Qva	
35	8	400	1700	2040	Qva	
45	10	450	1740	2088	Qva	
55	10	500	1760	2112	Qva	
60	5	550	1780	2136	Qva	
68	8	600	1800	2160	Qva	
78	10	400	1500	1800	Qvlc	
88	10	450	1550	1860	Qvlc	
93	5	500	1600	1920	Qvlc	
98	5	550	1650	1980	Qvlc	
	0	600	2000	2400	Qpf	
Unit 34 - 6m Qt/Qal, Qpf						
1	1	100	1200	1440	soil	322
3	2	120	1200	1440	Qt/Qal	
6	3	130	1200	1440	Qt/Qal	
11	5	450	1800	2160	Qpf	
16	5	550	1900	2280	Qpf	
	0	600	2000	2400	Qpf	
Unit 35 - 3m Fill, 50m Qva, 30m Qvlc, Qpf						
1	1	100	1200	1440	soil	311
3	2	120	1200	1440	Fill	
7	4	300	1600	1920	Qva	
12	5	350	1680	2016	Qva	
20	8	400	1700	2040	Qva	
30	10	450	1740	2088	Qva	
40	10	500	1760	2112	Qva	
45	5	550	1780	2136	Qva	

Depth to bottom (m)	Thickness (m)	Vs (m/s)	Dry density (kg/m^3)	Wet density (kg/m^3)	Description	Vs30 (m/s)
53	8	600	1800	2160	Qva	
63	10	400	1500	1800	Qvlc	
73	10	450	1550	1860	Qvlc	
78	5	500	1600	1920	Qvlc	
83	5	550	1650	1980	Qvlc	
	0	600	2000	2400	Qpf	
Unit 36 - Qpf						
1	1	100	1280	1536	soil	485
6	5	450	1800	2160	Qpf	
11	5	550	1900	2280	Qpf	
	0	600	2000	2400	Qpf	
Unit 37 - 5m Qvr, Qpf						
1	1	100	1280	1536	soil	435
3	2	250	1450	1740	Qvr	
5	2	350	1500	1800	Qvr	
10	5	450	1800	2160	Qpf	
15	5	550	1900	2280	Qpf	
	0	600	2000	2400	Qpf	
Unit 39 - 8m Qvt, 50m Qva, Qpf						
1	1	150	1280	1536	soil	
3	2	400	1800	2160	Qvt	413
5	2	475	1875	2250	Qvt	
7	2	550	1950	2340	Qvt	
8	1	600	2000	2400	Qvt	
16	8	350	1740	2088	Qva	
24	8	450	1760	2112	Qva	
32	8	550	1780	2136	Qva	
	0	600	1800	2160	Qva	
Unit 40 - 8m Qvt, 15m Qva, Qpf (identical to Unit 3)						
1	1	150	1280	1536	soil	
3	2	400	1800	2160	Qvt	421
5	2	475	1875	2250	Qvt	
7	2	550	1950	2340	Qvt	
8	1	600	2000	2400	Qvt	
16	8	350	1740	2088	Qva	
23	7	450	1760	2112	Qva	
	0	600	2000	2400	Qpf	
Unit 41 - 8m Qvt, 30m Qva, 20m Qvlc, Qpf						
1	1	150	1280	1536	soil	
3	2	400	1800	2160	Qvt	413
5	2	475	1875	2250	Qvt	
7	2	550	1950	2340	Qvt	
8	1	600	2000	2400	Qvt	
16	8	350	1740	2088	Qva	
24	8	450	1760	2112	Qva	
32	8	550	1780	2136	Qva	
38	6	600	1800	2160	Qva	
48	10	400	1500	1800	Qvlc	
58	10	450	1550	1860	Qvlc	
	0	600	2000	2400	Qpf	
Unit 42 - 8m Qvt, 15m Qva, Qpf						
1	1	150	1280	1536	soil	421
3	2	400	1800	2160	Qvt	
5	2	475	1875	2250	Qvt	
7	2	550	1950	2340	Qvt	
8	1	600	2000	2400	Qvt	
16	8	350	1740	2088	Qva	
23	7	450	1760	2112	Qva	
	0	600	2000	2400	Qpf	
Unit 43 - 8m Qvt, Qpf						
1	1	150	1280	1536	soil	489
3	2	400	1800	2160	Qvt	
5	2	475	1875	2250	Qvt	
7	2	550	1950	2340	Qvt	
8	1	600	2000	2400	Qvt	
13	5	450	1800	2160	Qpf	
18	5	550	1900	2280	Qpf	
	0	600	2000	2400	Qpf	
Unit 44 - 5m Fill, 5m Qvr, Qpf						
1	1	100	1200	1440	soil	314
3	2	120	1200	1440	Fill	
5	2	130	1200	1440	Fill	

Depth to bottom (m)	Thickness (m)	Vs (m/s)	Dry density (kg/m^3)	Wet density (kg/m^3)	Description	Vs30 (m/s)
7	2	250	1450	1740	Qvr	
10	3	350	1500	1800	Qvr	
15	5	450	1800	2160	Qpf	
20	5	550	1900	2280	Qpf	
	0	600	2000	2400	Qpf	
Unit 45 - 5m Fill, 5m Qal, Qpf						
1	1	100	1200	1440	soil	253
3	2	120	1200	1440	Fill	
5	2	130	1200	1440	Fill	
7	2	120	1200	1440	Qt/Qal	
10	3	130	1200	1440	Qt/Qal	
15	5	450	1800	2160	Qpf	
20	5	550	1900	2280	Qpf	
	0	600	2000	2400	Qpf	
Unit 46 - 5m Fill, 5m Qvt, Qpf						
1	1	100	1200	1440	soil	334
3	2	120	1200	1440	Fill	
5	2	130	1200	1440	Fill	
7	2	400	1800	2160	Qvt	
9	2	475	1875	2250	Qvt	
10	1	550	1950	2340	Qvt	
15	5	450	1800	2160	Qpf	
20	5	550	1900	2280	Qpf	
	0	600	2000	2400	Qpf	
Unit 47 - 5m Qvr, 8m Qvt, 15m Qva, Qpf						
1	1	100	1280	1536	soil	373
3	2	250	1450	1740	Qvr	
5	2	350	1500	1800	Qvr	
7	2	400	1800	2160	Qvt	
9	2	475	1875	2250	Qvt	
11	2	550	1950	2340	Qvt	
13	2	600	2000	2400	Qvt	
17	4	350	1680	2016	Qva	
22	5	400	1700	2040	Qva	
28	6	450	1740	2088	Qva	
	0	600	2000	2400	Qpf	
Unit 48 - 3m Qls, 15m Qva, Qpf						
1	1	100	1200	1440	soil	323
3	2	120	1200	1440	Landslide	
7	4	300	1600	1920	Qva	
12	5	350	1680	2016	Qva	
18	6	400	1700	2040	Qva	
23	5	450	1800	2160	Qpf	
28	5	550	1900	2280	Qpf	
	0	600	2000	2400	Qpf	
Unit 49 - 3m Qls, 5m Qvr, Qpf						
1	1	100	1200	1440	soil	360
3	2	120	1200	1440	Landslide	
5	2	250	1450	1740	Qvr	
8	3	350	1500	1800	Qvr	
13	5	450	1800	2160	Qpf	
18	5	550	1900	2280	Qpf	
	0	600	2000	2400	Qpf	
Unit 50 - 5m alluvium, Qpf						
1	1	100	1200	1440	soil	344
3	2	120	1200	1440	Qt/Qal	
5	2	130	1200	1440	Qt/Qal	
10	5	450	1800	2160	Qpf	
15	5	550	1900	2280	Qpf	
	0	600	2000	2400	Qpf	
Unit 51 - 8m Qb, Qpf						
2	2	120	1200	1440	Beach	298
4	2	130	1200	1440	Beach	
8	4	140	1250	1500	Beach	
13	5	450	1800	2160	Qpf	
18	5	550	1900	2280	Qpf	
	0	600	2000	2400	Qpf	
Unit 52 - 3m Ql, Qpf						
2	2	130	1300	1560	Ql	425
3	1	150	1400	1680	Ql	
8	5	450	1800	2160	Qpf	
13	5	550	1900	2280	Qpf	

Depth to bottom (m)	Thickness (m)	Vs (m/s)	Dry density (kg/m^3)	Wet density (kg/m^3)	Description	Vs30 (m/s)
	0	600	2000	2400	Qpf	
Unit 53 - 2m Fill, 3m Ql,Qpf						
2	2	120	1200	1440	Fill	357
4	2	130	1300	1560	Ql	
5	1	150	1400	1680	Ql	
10	5	450	1800	2160	Qpf	
15	5	550	1900	2280	Qpf	
	0	600	2000	2400	Qpf	
Unit 54 - 3m Qls, 30m Qva, 25m Qvlc, Qpf						
1	1	100	1200	1440	soil	311
3	2	120	1200	1440	Landslide	
7	4	300	1600	1920	Qva	
12	5	350	1680	2016	Qva	
20	8	400	1700	2040	Qva	
30	10	450	1740	2088	Qva	
33	3	500	1760	2112	Qva	
43	10	400	1500	1800	Qvlc	
53	10	450	1550	1860	Qvlc	
58	5	500	1600	1920	Qvlc	
	0	600	2000	2400	Qpf	
Unit 55 -Tb						
2	2	350	1920	2304	Weathered rock	552
4	2	400	1950	2340	Weathered rock	
5	1	500	1970	2364	Weathered rock	
	0	600	2000	2400	Tb or other rock	
Unit 56 - 3m Qls, Tb						
1	1	100	1200	1440	soil	394
3	2	120	1200	1440	Landslide	
5	2	350	1920	2304	Crap	
7	2	400	1950	2340	Crap	
8	1	500	1970	2364	Crap	
	0	600	2000	2400	Tb or other rock	
Unit 57 - 6m Fill, Tb						
1	1	100	1200	1440	soil	321
3	2	120	1200	1440	Fill	
5	2	130	1200	1440	Fill	
6	1	140	1250	1500	Fill	
8	2	350	1920	2304	Crap	
10	2	400	1950	2340	Crap	
11	1	500	1970	2364	Crap	
	0	600	2000	2400	Tb or other rock	
Unit 58 - 8m Qvt, Tb						
1	1	100	1200	1440	soil	490
3	2	400	1800	2160	Qvt	
5	2	475	1875	2250	Qvt	
7	2	550	1950	2340	Qvt	
8	1	600	2000	2400	Qvt	
	0	600	2000	2400	Tb or other rock	
Unit 59 - 3m Qls, 8m Qvt, Tb						
1	1	100	1200	1440	soil	403
3	2	120	1200	1440	Landslide	
5	2	400	1800	2160	Qvt	
7	2	475	1875	2250	Qvt	
9	2	550	1950	2340	Qvt	
11	2	600	2000	2400	Qvt	
	0	600	2000	2400	Tb or other rock	
Unit 60 - 8m Qb,Tb						
2	2	120	1200	1440	Beach	295
4	2	130	1200	1440	Beach	
8	4	140	1250	1500	Beach	
10	2	350	1920	2304	Weathered rock	
12	2	400	1950	2340	Weathered rock	
13	1	500	1970	2364	Weathered rock	
	0	600	2000	2400	Tb or other rock	
Unit 61 - 8m Qvt, 30m Qvlc, Qpf						
1	1	100	1200	1440	soil	251
3	2	400	1800	2160	Qvt	
5	2	475	1875	2250	Qvt	
7	2	550	1950	2340	Qvt	
9	2	600	2000	2400	Qvt	
19	10	200	1300	1560	Qvlc	

Depth to bottom (m)	Thickness (m)	Vs (m/s)	Dry density (kg/m^3)	Wet density (kg/m^3)	Description	Vs30 (m/s)
29	10	250	1350	1620	Qvlc	
34	5	300	1400	1680	Qvlc	
39	5	350	1500	1800	Qvlc	
	0	600	2000	2400	Qpf	
Unit 62 - 5m Qvrl, 15m Qva, 25m Qvlc, Qpf						
1	1	100	1200	1440	soil	327
3	2	250	1450	1740	Qvrl	
6	3	350	1500	1800	Qvrl	
10	4	300	1600	1920	Qva	
15	5	350	1680	2016	Qva	
21	6	400	1700	2040	Qva	
31	10	400	1500	1800	Qvlc	
41	10	450	1550	1860	Qvlc	
46	5	500	1600	1920	Qvlc	
	0	600	2000	2400	Qpf	
Unit 63 - 2m fill, 13m Qvrl, Qpf						
1	1	100	1200	1440	soil	382
2	1	120	1200	1440	Fill	
4	2	250	1450	1740	Qvrl	
7	3	350	1500	1800	Qvrl	
10	3	400	1600	1920	Qvrl	
15	5	450	1650	1980	Qvrl	
	0	600	2000	2400	Qpf	
Unit 64 - 5m Qvrl, Qpf or Tb						
1	1	100	1200	1440	soil	435
3	2	250	1450	1740	Qvrl	
5	2	350	1500	1800	Qvrl	
10	5	450	1800	2160	Qpf/Tb	
15	5	550	1900	2280	Qpf/Tb	
	0	600	2000	2400	Qpf/Tb	
Unit 65 - 8m Qvt, 30m Qvlc, Qpf						
1	1	100	1200	1440	soil	251
3	2	400	1800	2160	Qvt	
5	2	475	1875	2250	Qvt	
7	2	550	1950	2340	Qvt	
9	2	600	2000	2400	Qvt	
19	10	200	1300	1560	Qvlc	
29	10	250	1350	1620	Qvlc	
34	5	300	1400	1680	Qvlc	
39	5	350	1500	1800	Qvlc	
	0	600	2000	2400	Qpf	
Unit 66 - 3m Fill, 8m Qvt, 20m Qva, Qpf						
1	1	100	1200	1440	soil	316
3	2	120	1200	1440	Fill	
5	2	400	1800	2160	Qvt	
7	2	475	1875	2250	Qvt	
9	2	550	1950	2340	Qvt	
11	2	600	2000	2400	Qvt	
15	4	300	1600	1920	Qva	
20	5	350	1680	2016	Qva	
28	8	400	1700	2040	Qva	
31	3	450	1740	2088	Qva	
	0	600	2000	2400	Qpf	
Unit 67 - 5m Qvr, Tb						
2	2	250	1450	1740	Qvr	479
5	3	350	1500	1800	Qvr	
7	2	350	1920	2304	Weathered rock	
9	2	400	1950	2340	Weathered rock	
10	1	500	1970	2364	Weathered rock	
	0	600	2000	2400	Tb or other rock	

Figure A1-1

Map of Representative Shear Wave Velocity Profile Units

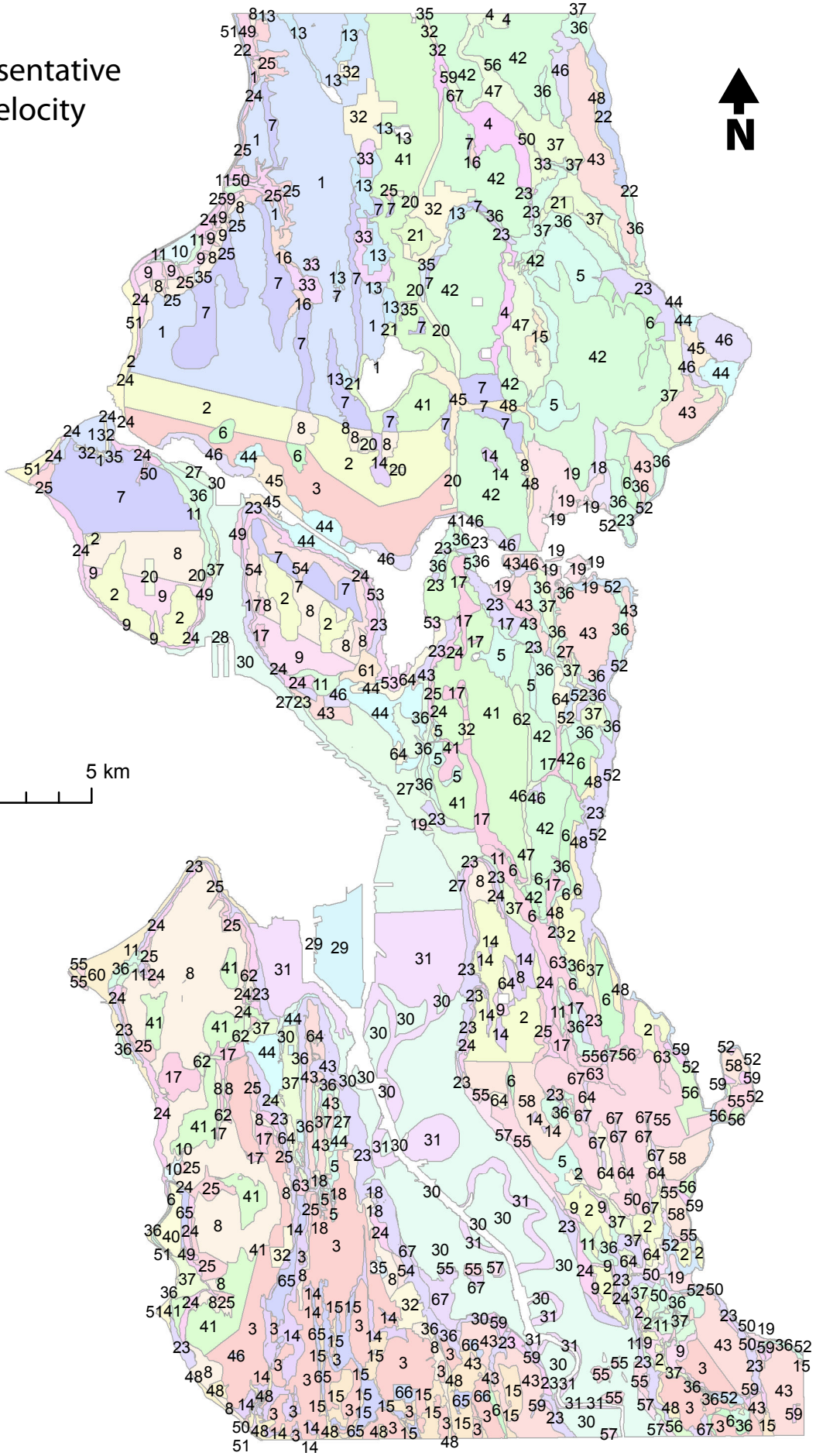

Appendix 2

High resolution maps (2) of relative seismically induced landslide hazard for a M_w 7.0 Seattle fault earthquake for dry and saturated soil conditions.

Figures:

Figure A2-1: Landslide hazard zones for Seattle based on newmark displacement induced by the Mw 7.0 Seattle Fault scenario earthquake under dry soil conditions.

Figure A2-2: Landslide hazard zones for Seattle based on newmark displacement induced by the Mw 7.0 Seattle Fault scenario earthquake under saturated soil conditions.

Figure A2-2

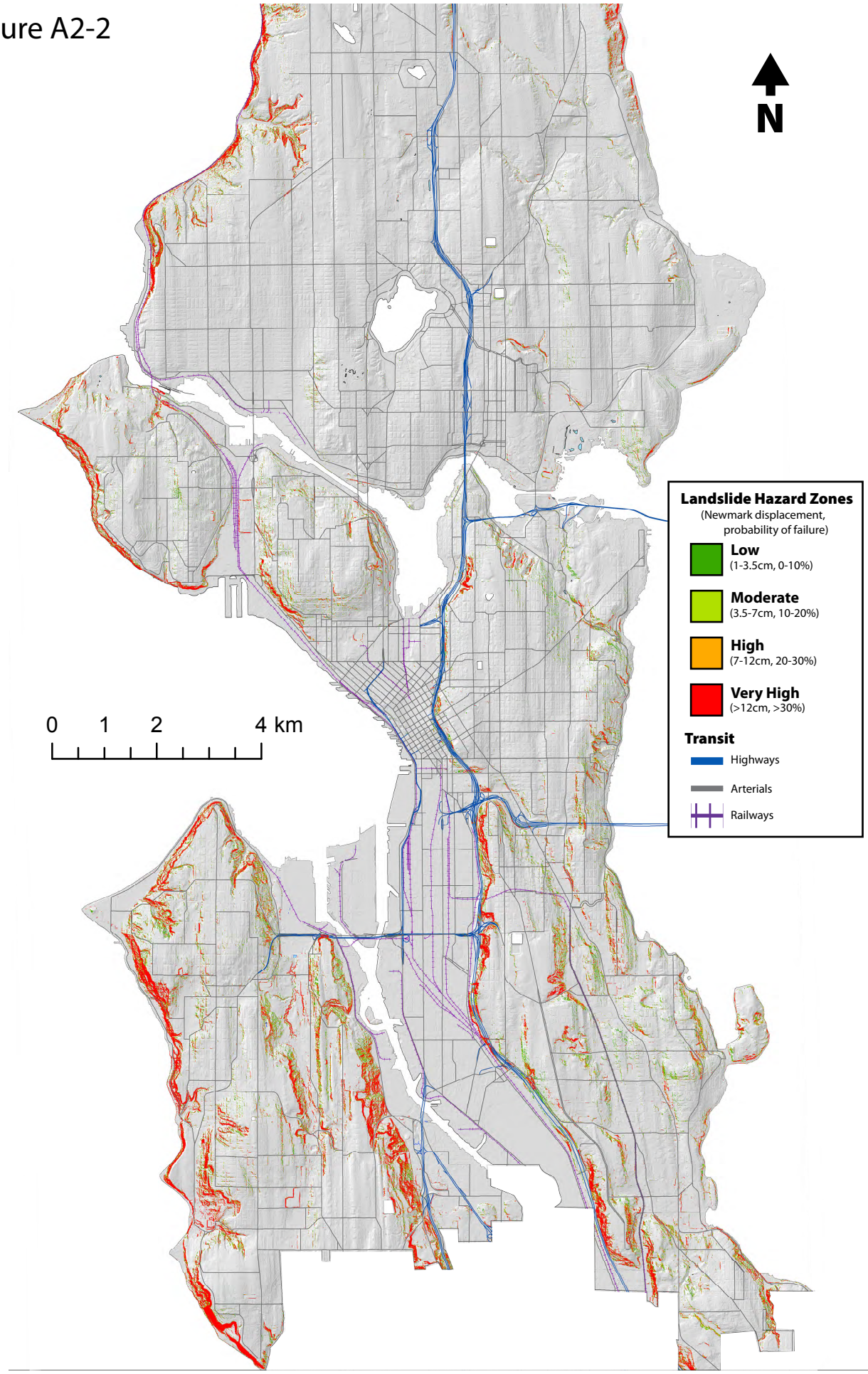
N
Landslide Hazard Zones
(Newmark displacement, probability of failure)
Low
(1-3.5cm, 0-10%)
Moderate
(3.5-7cm, 10-20%)
High
(7-12cm, 20-30%)
Very High
(>12cm, >30%)
Transit
Highways
Arterials
Railways
0 1 2 4 km

Figure A2-1

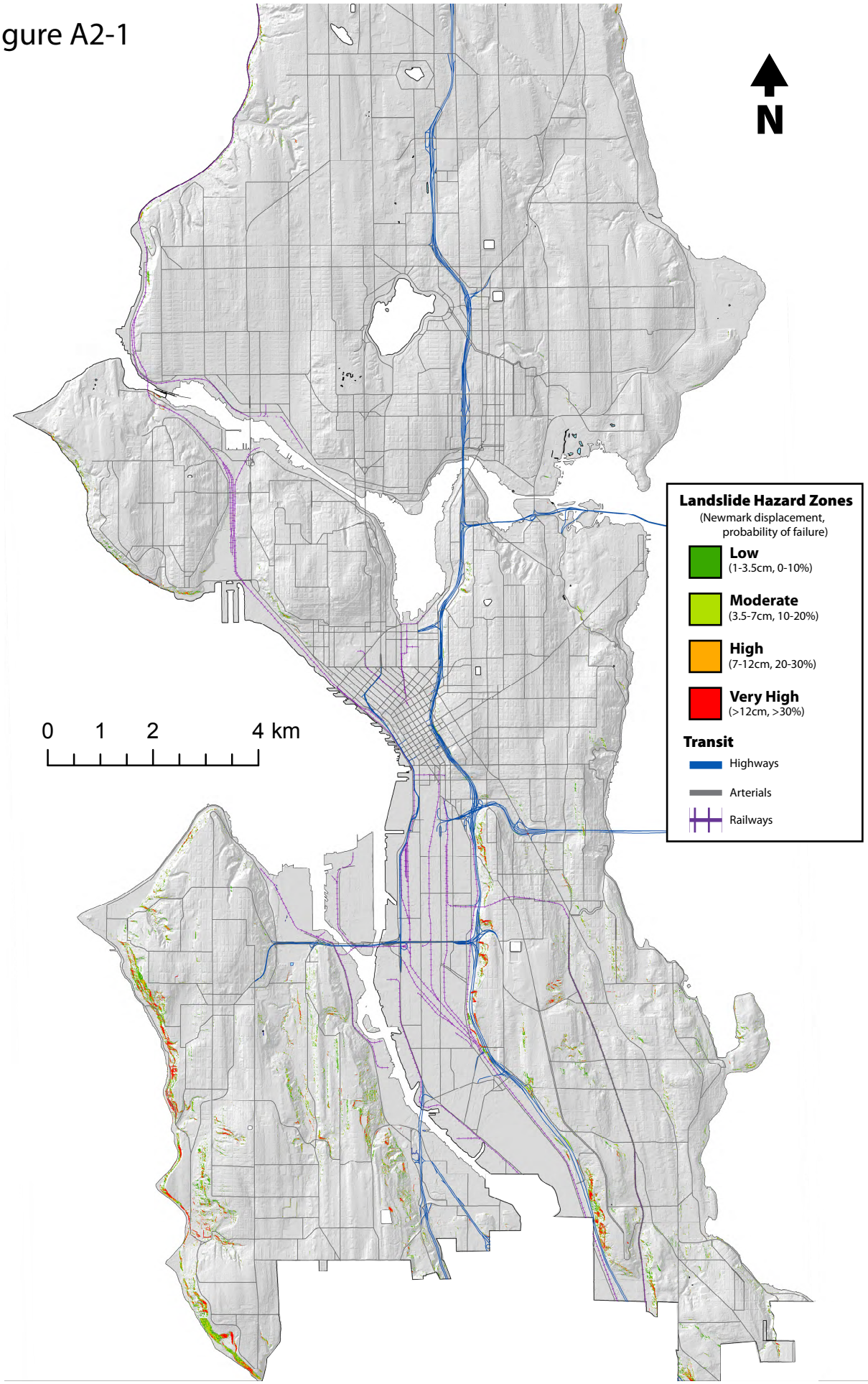
N
0 1 2 4 km
Landslide Hazard Zones
(Newmark displacement, probability of failure)
Low
(1-3.5cm, 0-10%)
Moderate
(3.5-7cm, 10-20%)
High
(7-12cm, 20-30%)
Very High
(>12cm, >30%)
Transit
Highways
Arterials
Railways

Appendix 3 Details of Inversion Methods

This section details the inversion process used to obtain the force-time function in Chapter 2a. The forward problem to obtain the displacement seismograms generated by a single force applied at the source location is:

$$\boldsymbol{d}_i(t) = \boldsymbol{G}_{ij}(t) * \boldsymbol{m}_j(t) \qquad \text{(A1)}$$

where the seismogram $\boldsymbol{d}_i(t)$ at each component of each station (i) is equal to the Green's functions $\boldsymbol{G}_{ij}(t)$ for station component i for an impulse force applied at the source location in direction j convolved (*) with the force-time function of the source, $\boldsymbol{m}_j(t)$, where j is the directional component of the force (Up, North, East). Note that $\boldsymbol{m}_j(t)$ is equivalent to $\boldsymbol{F}_e(t)$ - the change in notation is for consistency with inverse theory conventions, where $\boldsymbol{m}$ refers to 'model.' Equation A1 assumes a stationary force vector applied to a single point on the surface of the earth. Though the landslide is moving, it can be approximated as a stationary point force for the long period wavelengths used in the inversion, as explained in the methods section.

Green's functions are the response of the earth to an impulse source. In this study I calculated the Green's functions relating an impulse force at the source location to the response at the distance and azimuth corresponding to each seismic station. I computed these using the wavenumber integration method [*Bouchon,* 1981] as implemented in Computer Programs in Seismology (CPS) [*Hermann*, 2002]. The velocity model used for these calculations was ak135Q [*Kennett et al.*, 1995]. This is a one-dimensional radially stratified global earth velocity model and does not account for regional or smaller scale variations. However, it was sufficient for this study because the long period waves (T = 30 – 150 s) used in the inversion are not sensitive to smaller scale variability.

Using CPS, I computed the Green's functions corresponding to each seismic station used in the inversion for a Dirac delta function impulse force applied to the surface of the earth at the location of the landslide. Five Green's functions are required for each station used in order to calculate three-component synthetic time histories for a single force mechanism applied in any direction at the source [*Hermann*, 2002]. The radial component of the seismogram is positive in the direction pointing directly away from the source. The transverse component is perpendicular to the radial direction, positive in the direction clockwise from north. Vertical is positive upwards. The five Green's functions are abbreviated as follows:

ZVF = Vertical component of the seismogram for a downward vertical force

RVF = Radial component for a downward vertical force

ZHF = Vertical component for a horizontal force in radial direction

RHF = Radial component for a horizontal force in radial direction

THF = Transverse component for a horizontal force in transverse direction

The first four Green's functions correspond to the P-SV system, while THF corresponds to the SH system. The Green's functions calculated for station SHB, 118 km from the source, are shown on Figure 2a-A1. These illustrate the role of the earth's structure in the waveforms observed at station SHB due an impulse force of 1 N at the source. The Rayleigh wave dwarfs the P and S arrivals on the top four Green's functions, but has not moved out and dispersed much yet because of SHB's proximity to the source. Note that due to the nature of causal filters, the relatively compact unfiltered Green's function becomes distorted when filtered; the energy is smeared out later in time. This is not a problem in the inversion because identical filters are applied to the data so it is distorted in the same way. This is confirmed in that a nearly identical force-time function is obtained when a zero-phase (acausal) filter is used. Also note that the

duration of the source (force-time function) is much longer than the Green's functions, unlike for most regular earthquakes, which is why such a detailed force-time function can be derived from the seismograms.

These Green's functions can be used to calculate synthetic ground displacement seismograms for any single force vector impulse or time series by:

$$\boldsymbol{u_z}=(\boldsymbol{f_1}\cos\phi+\boldsymbol{f_2}\sin\phi)\boldsymbol{ZHF}+\boldsymbol{f_3ZVF} \quad \text{(A2)}$$

$$\boldsymbol{u_r}=(\boldsymbol{f_1}\cos\phi+\boldsymbol{f_2}\sin\phi)\boldsymbol{RHF}+\boldsymbol{f_3RVF} \quad \text{(A3)}$$

$$\boldsymbol{u_t}=(\boldsymbol{f_1}\sin\phi-\boldsymbol{f_2}\cos\phi)\boldsymbol{THF} \quad \text{(A4)}$$

[*Hermann*, 2002] where ϕ is the source to station azimuth measured clockwise from north. The single force $\boldsymbol{f}=(\boldsymbol{f_1}, \boldsymbol{f_2}, \boldsymbol{f_3})$ is in a north (N), east (E), vertical (Z), respectively, Cartesian coordinate system, where Z is positive down (note, however, that Z was switched to positive up in the force-time function plots in this paper to be more intuitive). The ground displacement seismograms are in spherical coordinates local to each source-station pair, where vertical is positive up ($\boldsymbol{u_z}$), radial ($\boldsymbol{u_r}$) is positive in the direction away from the source and tangential ($\boldsymbol{u_t}$) is positive at a right angle clockwise from $\boldsymbol{u_r}$.

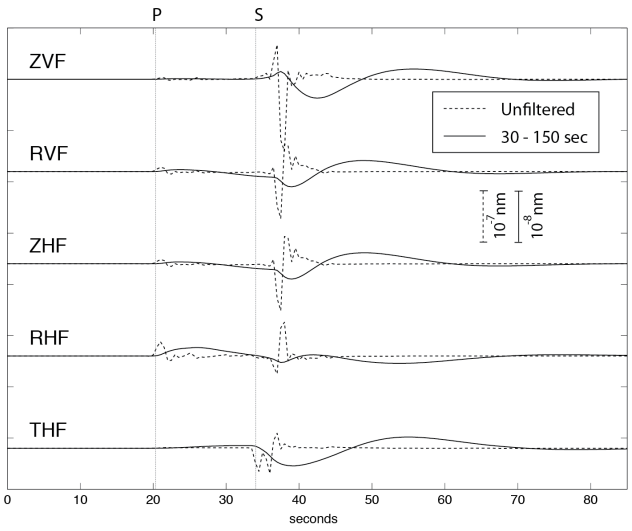

Figure 2a-A1 Green's functions calculated for this study for station SHB located 118 km from the source for a impulse force of 1 N. The functions are shown unfiltered (0.5 Hz sample rate) and bandpass filtered between periods of 30 to 150 seconds using the same causal (minimum phase) butterworth filter applied to the data and Green's functions prior to inversion. The amplitude of the filtered Green's functions is amplified by a factor of ten relative to the unfiltered version. See text for discussion.

In order to do the inversion, the forward problem (equation A1) was rewritten as matrix multiplication rather than a convolution. A convolution is equivalent to reversing one of the two signals being convolved in time and passing them by each other, multiplying all points and summing them up at each time interval. To convolve a Green's function with a force vector via matrix multiplication, the Green's functions were reversed in time and staggered by shifting the Green's function by one sample in each successive row to produce a convolution matrix. To illustrate this setup, Equation A5 shows the convolution via matrix multiplication between a 4-sample Green's function g and a 3-sample force-time function $\boldsymbol{m}$ to obtain the seismogram $\boldsymbol{d}$ that is 6 samples long:

$$\begin{bmatrix} d_1 \\ d_2 \\ d_3 \\ d_4 \\ d_5 \\ d_6 \end{bmatrix} = \begin{bmatrix} g_1 & 0 & 0 \\ g_2 & g_1 & 0 \\ g_3 & g_2 & g_1 \\ g_4 & g_3 & g_2 \\ 0 & g_4 & g_3 \\ 0 & 0 & g_4 \end{bmatrix} \times \begin{bmatrix} m_1 \\ m_2 \\ m_3 \end{bmatrix} \qquad \text{(A5)}$$

Equation A5 illustrates the convolution with just one Green's function for one station and one component of the force-time function. The actual Green's function convolution matrix must be set up to include all the Green's functions corresponding to each component of each seismic station used and to incorporate the equations that relate the source to station azimuth to account

for the radiation patterns of each type of wave (equations A2-A4). This setup can be illustrated for two three-component stations by:

$$\begin{bmatrix} \underline{d}_z^1 \\ \underline{d}_r^1 \\ \underline{d}_t^1 \\ \underline{d}_z^2 \\ \underline{d}_r^2 \\ \underline{d}_t^2 \end{bmatrix} = \begin{bmatrix} \underline{\underline{ZVF}}^{1*} & \underline{\underline{ZHF}}^{1*}\cos\phi & \underline{\underline{ZHF}}^{1*}\sin\phi \\ \underline{\underline{RVF}}^{1*} & \underline{\underline{RHF}}^{1*}\cos\phi & \underline{\underline{RHF}}^{1*}\sin\phi \\ \underline{\underline{0}} & \underline{\underline{THF}}^{1*}\sin\phi & -\underline{\underline{THF}}^{1*}\cos\phi \\ \underline{\underline{ZVF}}^{2*} & \underline{\underline{ZHF}}^{2*}\cos\phi & \underline{\underline{ZHF}}^{2*}\sin\phi \\ \underline{\underline{RVF}}^{2*} & \underline{\underline{RHF}}^{2*}\cos\phi & \underline{\underline{RHF}}^{2*}\sin\phi \\ \underline{\underline{0}} & \underline{\underline{THF}}^{2*}\sin\phi & -\underline{\underline{THF}}^{2*}\cos\phi \end{bmatrix} \times \begin{bmatrix} \underline{m}_Z \\ \underline{m}_N \\ \underline{m}_E \end{bmatrix} \qquad \text{(A6)}$$

Each $\underline{d}^i_c$ in Equation A6 is a column vector that contains the seismogram for the station (i) and component (c) (z vertical, r radial and t transverse). The left side of Equation A6 is a column vector consisting of all the data (displacement seismograms) concatenated end to end. Each entry in the G matrix is a Green's function convolution matrix (indicated by * superscript) for the Green's function specified by its abbreviation for each station (indicated by the superscript). Each $\boldsymbol{m}_j$ is a column vector containing the force-time function for each component (j) of force. The sines and cosines come from equation A2-A4.

For this study, as described in the text, I downweighted the noisy data based on the inverse of the root mean squared value of the noise before the signal at each component of each station. To include this in the inversion I constructed a weighting matrix, $\boldsymbol{W}$. $\boldsymbol{W}$ was built by filling the weights in along the diagonal of $\boldsymbol{W}$, organized so that the correct scalar weight value multiplied the entire seismic signal of the corresponding component of each station when $\boldsymbol{W}$ is multiplied with the data vector. For example, the weight for the vertical component of the first station, $\underline{d}^1_z$, fills in the diagonal of $\boldsymbol{W}$ from W_{11} to W_{ii}, where i is the length of $\underline{d}^1_z$. $\boldsymbol{W}$ weights both the data vector $\boldsymbol{d}$ and the Green's functions matrix, $\boldsymbol{G}$, (which, when weighted are denoted as $\boldsymbol{d}_w$ and $\boldsymbol{G}_w$ respectively) because the same processing must be done to both sides of the equation. For the same reason, the individual Green's functions and the seismograms were bandpass

filtered identically as well prior to building the matrix $\boldsymbol{G}$. In this study I used a minimum phase (causal) Butterworth filter, but a nearly identical result is obtained when using a zero phase (acausal) filter because the same filtering is applied to both sides of the equation.

The next step was to solve the damped least squares problem to invert for m:

$$\boldsymbol{m}=(\boldsymbol{G}_w^T\boldsymbol{G}_w + \alpha^2\boldsymbol{I})^{-1}\boldsymbol{G}_w^T\boldsymbol{d}_w \qquad \text{(A7)}$$

where superscript T indicates the transpose, $\boldsymbol{I}$ is the identity matrix and α is the regularization parameter chosen as the trade-off between keeping the model small while still fitting the data well. The matrix setup of the forward problem using data from five seismic stations with three components of motion each becomes very large, but the inversion was still manageable: it took less than a minute to run in MATLAB on a desktop computer.

An additional step I took in this study was to constrain that all components of the single force must add to zero in the end because the total momentum of the earth must remain stable [*Fukao,* 1995]. This did not significantly change the solution, but is more physically correct. To constrain this in the solution, I added equations to the forward problem by concatenating matrix, $\boldsymbol{A}$, a 3x3N matrix, where N is the length of the data from one component of one station, to the bottom of the Green's function matrix, $\boldsymbol{G}$. $\boldsymbol{A}$ was constructed so that the first third of the first row was ones and the rest was zeros so that it multiplied and added up just the z component of $\boldsymbol{m}$, a corresponding zero is added to the bottom of the data vector $\boldsymbol{d}$ to constrain that these forces add to zero. The same was done for the next two rows to multiply and add up the north and east components of $\boldsymbol{m}$ to equal zero. The $\boldsymbol{A}$ matrix was scaled up to the same magnitude as the weighted Green's functions so that it influenced the final solution.